

**DEVELOPMENT OF H_∞ CONTROL STRATEGY FOR A MULTI-WHEELED
COMBAT VEHICLE**

By

Peter D'Urso

A Thesis Presented in Partial Fulfillment
of the Requirements for the Degree of

Master of Applied Science

In

Automotive Engineering

Faculty of Engineering and Applied Science
University of Ontario Institute of Technology
Oshawa, Ontario, Canada

AUGUST 2016

© 2016 Peter D'Urso

ABSTRACT

This thesis proposes a vehicle dynamics controller for vehicle stability, maneuverability and turning circle reduction for an 8 x 8 heavy combat vehicle utilising both torque vectoring and third and fourth axle steering. The proposed control scheme is composed of two distinct controllers, each with their own range of operation based on vehicle speed. A feedforward zero side slip (ZSS) controller actuates the third and fourth axle steering angles. It is used for maneuvering at speeds of 30 kph and below and for turning circle reduction. A two DOF LPV H_∞ controller that monitors steering wheel angle and yaw rate error and uses both the rear axle steering and torque vectoring is used at speeds above 40 kph. Gaussian distribution functions are used to switch from one controller to the other. The proposed control scheme is evaluated by running simulations using a validated TruckSim full vehicle model in co-simulation with the controller and developed electric powertrain in Simulink. Events used for testing include NATO double lane change, NATO constant step slalom, FMVSS 126 ESC, J-Turn and constant radius circle. Two road friction coefficients are used, 0.35 and 0.85 μ at speeds between 40 and 100 kph. The proposed control system is able to greatly improve vehicle stability at high speeds and/or low friction surfaces by damping vehicle yaw rate, lateral acceleration and vehicle side slip response. The controller is also able to increase maneuverability at lower speeds and/or higher friction surfaces by decreasing vehicle response time delays and reducing steering wheel effort. A turning circle reduction of 30% is obtained using the ZSS feedforward method.

TABLE OF CONTENTS

ABSTRACT	ii
TABLE OF CONTENTS	iii
LIST OF FIGURES	viii
LIST OF TABLES	xvi
NOMENCLATURE.....	xvii
ABBREVIATIONS.....	xix
ACKNOWLEDGEMENTS	xxi
CHAPTER 1 INTRODUCTION	1
1.1 MOTIVATION	1
1.2 SCOPE AND OBJECTIVE	2
1.2.1 Scope.....	2
1.2.2 Objectives	2
1.3 OUTLINE OF THESIS	3
1.4 WORKING FOUNDATIONS	4
1.4.1 Vehicle Dynamics Theory	4
1.4.1.1 Tire Dynamics	6
1.4.1.2 Vehicle Lateral Dynamics	11
1.4.2 Control Systems Theory	16
1.4.2.1 System Configurations	17
CHAPTER 2 LITERATURE REVIEW.....	20
2.1 VEHICLE DYNAMICS CONTROL SYSTEMS.....	20
2.1.1 Basic Principles of Torque Vectoring.....	21
2.1.2 Basic Principles of Rear Wheel Steering	22
2.2 FOUR-WHEELED VEHICLE CONTROL.....	23
2.3 ELECTRIC VEHICLE CONTROL.....	26

2.4	MULTI-WHEELED VEHICLE CONTROL.....	30
2.5	H_∞ CONTROL	31
2.5.1	H_∞ Active Steering	33
2.5.2	H_∞ Torque Vectoring.....	33
2.5.3	H_∞ Integrated Control.....	34
2.6	FEEDFORWARD REAR WHEEL STEERING.....	36
2.6.1	Zero Side Slip (ZSS) Method	36
2.6.2	Steer Angle Dependent 4WS	37
2.7	SUMMARY	39
CHAPTER 3 VEHICLE MODELS AND SIMULATION ENVIRONMENT		42
3.1	INTRODUCTION.....	42
3.2	TRUCKSIM FULL VEHICLE MODEL.....	42
3.2.1	Vehicle Parameters	42
3.2.2	Vehicle Model Validation.....	45
3.2.3	Electric Powertrain.....	46
3.2.3.1	Electric Motor Lookup Table	46
3.2.4	MATLAB/Simulink - TruckSim Co-Simulation.....	48
3.3	LINEAR BICYCLE MODEL - H_∞ CONTROLLER SYNTHESIS	50
3.4	LINEAR BICYCLE MODEL - REFERENCE YAW RATE.....	54
3.4.1	Reference Yaw Rate, r_{desired}	54
3.4.2	Steady State Bicycle Model for Desired Yaw Rate	56
3.5	LINEAR BICYCLE MODEL - ZSS CONTROLLER	57
3.6	SUMMARY	59
CHAPTER 4 LPV H_∞ CONTROLLER DESIGN		60
4.1	INTRODUCTION.....	60
4.2	LPV H_∞ CONTROLLER DESIGN - THEORY	60
4.2.1	LPV Plant Modeling - Theory	60
4.2.2	H_∞ Controller Synthesis – Theory	62
4.3	LPV TWO DOF H_∞ CONTROLLER DESIGN	64

4.3.1	LPV Two DOF Plant Modeling	64
4.3.1.1	Scheduling Parameters.....	64
4.3.1.2	Linear Parameter Dependent Plant	65
4.3.2	LPV TWO DOF H_∞ Controller Synthesis	66
4.3.2.1	H_∞ Controller Synthesis.....	66
4.3.2.2	Weighting Functions.....	68
4.4	SUMMARY	69
CHAPTER 5 VEHICLE DYNAMIC CONTROL SYSTEM.....		71
5.1	PROPOSED CONTROL SYSTEM ARCHITECTURE	71
5.2	VEHICLE FORWARD SPEED CONTROLLER	72
5.3	REFERENCE MODEL.....	72
5.4	ELECTRIC POWERTRAIN.....	73
5.5	UPPER CONTROLLER	74
5.5.1	2 DOF LPV H_∞ Controller, $K(\theta)$	74
5.5.2	ZSS Turning Circle Reduction Controller, $\delta_{4, ZSS}$	75
5.5.3	Switching between ZSS and H_∞ Control	75
5.6	LOWER CONTROLLER	77
5.6.1	Control Allocation – Torque Vectoring Wheel Distribution	77
5.6.2	Control Allocation – Rear Wheel Steer Angle Distribution	80
5.6.3	Slip Controller.....	80
5.7	SUMMARY	81
CHAPTER 6 RESULTS AND DISCUSSION.....		83
6.1	CONTROLLER PERFORMANCE EVALUATION METHODOLOGY	83
6.2	DYNAMIC TESTING OF THE TWO DOF H_∞ CONTROLLER.....	85
6.2.1	Double Lane Change (NATO AVTP-1 03-160W).....	85
6.2.1.1	Results – Double Lane Change (100 kph; $\mu=0.85$).....	85
6.2.1.2	Results – Double Lane Change (80 kph; $\mu=0.85$).....	89
6.2.1.3	Results – Double Lane Change (80 kph; $\mu=0.35$).....	93

6.2.2	30m Constant Step Slalom (NATO AVTP-1 03-30).....	97
6.2.2.1	Results - Constant Step Slalom (65 kph; $\mu=0.85$).....	98
6.2.2.2	Results - Constant Step Slalom (40 kph; $\mu=0.85$).....	103
6.2.2.3	Results - Constant Step Slalom (40 kph; $\mu=0.35$).....	106
6.2.3	FMVSS 126 ESC.....	110
6.2.3.1	Results - FMVSS 126 ESC (80 kph; $\mu=0.85$).....	110
6.2.3.2	Results - FMVSS 126 ESC (80 kph; $\mu=0.35$).....	113
6.2.4	J-Turn (120 deg step steer input).....	116
6.2.4.1	Results – J-Turn (80 kph; $\mu=0.85$).....	117
6.2.4.2	Results – J-Turn (50 kph; $\mu=0.85$).....	121
6.2.4.3	Results – J-Turn (50 kph; $\mu=0.35$).....	125
6.2.5	Constant Radius Circle (100 ft).....	128
6.2.5.1	Results – Constant Radius Circle (50 kph; $\mu=0.85$).....	129
6.3	TURNING CIRCLE EVALUATION OF ZSS CONTROLLER.....	132
6.3.1	Turning Circle Test - Methodology.....	133
6.3.2	Maximum Rear Steer Angle.....	133
6.3.3	Results – Turning Circle Reduction Test.....	134
6.4	SWITCHING SPEED EVALUATION.....	135
6.4.1	Results – H_∞ vs ZSS Ctrl - Double Lane Change (80 kph; $\mu=0.85$).....	136
6.4.2	Results – H_∞ vs ZSS Ctrl - Double Lane Change (60 kph; $\mu=0.85$).....	139
6.4.3	Results – H_∞ vs ZSS Ctrl - Double Lane Change (40 kph; $\mu=0.85$).....	142
6.4.4	Results – H_∞ vs ZSS Ctrl – Const. Step Slalom (40 kph; $\mu=0.85$).....	145
6.5	LOW SPEED DYNAMIC EVALUATION OF ZSS CONTROLLER.....	148
6.5.1	Results –ZSS Controller – Double Lane Change (30 kph; $\mu=0.85$).....	148
6.5.2	Results –ZSS Controller – Double Lane Change (30 kph; $\mu=0.35$).....	151
6.5.3	Results –ZSS Controller – Slalom (30 kph; $\mu=0.85$).....	153
6.5.4	Results –ZSS Controller – Slalom (30 kph; $\mu=0.35$).....	156
6.6	SUMMARY.....	159
6.6.1	Conclusions - H_∞ Controller Dynamic Performance.....	159

6.6.2	Conclusions – Turning Circle Reduction Performance	161
6.6.3	Conclusions – Switching Speed Evaluation	161
6.6.4	Conclusions – Low Speed Dynamic Evaluation of ZSS Controller	162
CHAPTER 7 CONCLUSIONS & FUTURE WORK.....		164
7.1	ACCOMPLISHMENTS.....	164
7.2	GENERAL CONCLUSIONS	166
7.3	FUTURE WORK.....	169
PUBLICATIONS		171
REFERENCES.....		172

LIST OF FIGURES

Figure 1-1 Vehicle Dynamics Interactions [3].....	5
Figure 1-2 Vehicle/Driver Control Loop [5]	6
Figure 1-3 SAE Tire Axis System [6].....	7
Figure 1-4 Tractive Force Generation Due to Longitudinal Slip of a Tire [6]	8
Figure 1-5 Behaviour of a Tire Subjected to a Cornering Maneuver (Top View (Left); Front View (Right)) [7].....	8
Figure 1-6 Cornering Characteristics of a Bias-Ply and Radial-ply Car Tire [6]	9
Figure 1-7 Effect of Load Transfer on an Axle [6].....	9
Figure 1-8 Tire Friction Ellipse for Fixed Normal Load, Slip Angle & Inflation Pressure [6]	10
Figure 1-9 Tire Friction Ellipses of a Vehicle Executing a Left Hand Turn [9]	11
Figure 1-10 Vector Velocity (TOP) and Acceleration (BOTTOM) [10].....	12
Figure 1-11 SAE Vehicle Axis System [11].....	13
Figure 1-12 Heading, Side slip, Course and Steer Angles [11]	14
Figure 1-13 Rise Time and Peak Response Time [10]	15
Figure 1-14 Transient Response of FWS Vehicle to Stepwise Steering Input [12]	16
Figure 1-15 Typical System Response to Step Input [14]	16
Figure 1-16 Open Loop Control System Structure	17
Figure 1-17 Closed Loop Control System Structure.....	18
Figure 1-18 Combined Feedback and Feedforward System.....	18
Figure 1-19 Model Reference Control [4]	19
Figure 2-1 Torque Vectoring Schematic [15].....	21
Figure 2-2 Area of Effectiveness of DYC and 4WS [20].....	23
Figure 2-3 Cornering Force Improvement vs Torque Differential Between Left and Right Wheels [16]	24
Figure 2-4 Active Chassis Control [24]	25
Figure 2-5 Activation function for Torque Vectoring as a Function of Active Steering Angle [28]	27

Figure 2-6 Potential Understeer Gradient Alternatives through torque vectoring via individual electric motors [34].....	29
Figure 2-7 Zero Side Slip (ZSS) 4WS Relationship [64]	37
Figure 2-8 Steer Angle Dependent 4WS Relationship [64].....	37
Figure 2-9 Yaw Velocity Feedback for Four Axle Vehicle While Varying the Middle Axle Steering Angle Ratio as a Function of Front Steering Angle [66]	39
Figure 3-1 (a) Actual Vehicle [69] (b) TruckSim Model	43
Figure 3-2 F_x vs Slip Ratio (a) and F_y vs Slip Angle (b)	44
Figure 3-3 Hydropneumatic Suspension Force Deflection Curve	45
Figure 3-4 Electric Motor Specification Curve.....	47
Figure 3-5 Electric Motor Diagram	48
Figure 3-6 TruckSim Vehicle Model (a) with fixed 3rd and 4th axles (b) with steerable 3rd and 4th axles	48
Figure 3-7 Simulink Control Architecture with TruckSim S-function.....	49
Figure 3-8 Trucksim User Interface.....	49
Figure 3-9 Two DOF Bicycle Model with Rear Steering and External Yaw Moment	50
Figure 3-10 Yaw Rate Reference signal for NATO DLC at 40 kph ($\mu=0.85$)	55
Figure 3-11 Yaw Rate Reference Signal for a J-Turn at 20 kph (120 deg steering wheel input) ($\mu=0.85$).....	55
Figure 3-12 Two DOF Bicycle Model for Steady State Desired Yaw Rate	56
Figure 3-13 ZSS Turning Circle Reduction Ratio, k_{ZSS} as a Function of Vehicle Forward Speed	58
Figure 4-1 Polytope of Scheduling Parameters (θ_1 and θ_2).....	61
Figure 4-2 Mixed Sensitivity Feedback System (a) Standard H_∞ Layout (b).....	63
Figure 4-3 Polytopic Controller Convex Combination Visualisation.....	64
Figure 4-4 Expanded Augmented Plant Layout.....	67
Figure 4-5 Standard H_∞ Layout for Vehicle Dynamic Controller	67
Figure 5-1 Controller Architecture Diagram	71
Figure 5-2 PI Speed Controller Diagram	72
Figure 5-3 Reference Model Diagram	73
Figure 5-4 Simulink Electric Powertrain Diagram (One Motor).....	73

Figure 5-5 Calculation of the H_{∞} Controller State Space Matrices	74
Figure 5-6 ZSS Turning Circle Reduction Controller Simulink Implementation	75
Figure 5-7 Activation Functions for RWS (top) and Torque Vectoring (bottom).....	76
Figure 5-8 Lower Controller Architecture	77
Figure 5-9 Torque Vectoring Control Allocation Schematic.....	78
Figure 5-10 Slip Controller Architecture	81
Figure 6-1 NATO AVTP-1 03-160W Double Lane Change (Courtesy GDLS-C)	85
Figure 6-2 Vehicle Speeds during DLC at 100 kph ($\mu=0.85$)	86
Figure 6-3 Steering Wheel Angles during DLC at 100 kph ($\mu=0.85$)	86
Figure 6-4 Yaw Rate (a) Lateral Acceleration (b) and Vehicle Side Slip Angle (c) during DLC at 100 kph ($\mu=0.85$)	87
Figure 6-5 Uncontrolled (dark green) vs Controlled (light green) Vehicle during DLC at 100 kph ($\mu=0.85$) [Gate 1, 2 and 3 from Top Left to Bottom]	88
Figure 6-6 H_{∞} Yaw Rate Reference Signal Tracking during DLC at 100 kph ($\mu=0.85$)	88
Figure 6-7 Wheel Torque (a) and Rear Steer Angles (b) during DLC at 100 kph ($\mu=0.85$)	89
Figure 6-8 Vehicle Speeds during DLC at 80 kph ($\mu=0.85$)	90
Figure 6-9 Steering Wheel Angles during DLC at 80 kph ($\mu=0.85$)	90
Figure 6-10 Yaw Rate (a) Lateral Acceleration (b) and Vehicle Side Slip Angle (c) during DLC at 80 kph ($\mu=0.85$)	91
Figure 6-11 H_{∞} Yaw Rate Reference Signal Tracking during DLC at 80 kph ($\mu=0.85$)	92
Figure 6-12 Wheel Torque (a) and Rear Steer Angles (b) during DLC at 80 kph ($\mu=0.85$)	93
Figure 6-13 Vehicle Speeds during DLC at 80 kph ($\mu=0.35$)	94
Figure 6-14 Steering Wheel Angles during DLC at 80 kph ($\mu=0.35$)	94
Figure 6-15 Yaw Rate (a) Lateral Acceleration (b) and Vehicle Side Slip Angle (c) during DLC at 80 kph ($\mu=0.35$)	95
Figure 6-16 Uncontrolled (dark green) vs Controlled (light green) Vehicle during DLC at 80 kph ($\mu=0.35$) [Gate 2 and 3 from Left to Right]	96

Figure 6-17 H_{∞} Yaw Rate Reference Tracking during DLC at 80 kph ($\mu=0.35$).....	96
Figure 6-18 Wheel Torque (a) and Rear Steer Angles (b) during DLC at 80 kph ($\mu=0.35$)	97
Figure 6-19 NATO AVTP-1 03-30 Constant Step Slalom Test Course Specifications ...	98
Figure 6-20 Vehicle Speeds during Slalom at 65 kph ($\mu=0.85$)	98
Figure 6-21 Steering Wheel Angles during Slalom at 65 kph ($\mu=0.85$).....	99
Figure 6-22 Vehicle Trajectory during Slalom at 65 kph ($\mu=0.85$).....	99
Figure 6-23 Yaw Rate (a) Lateral Acceleration (b) and Vehicle Side Slip Angle (c) during Slalom at 65 kph ($\mu=0.85$).....	100
Figure 6-24 Uncontrolled (dark green) vs Controlled (light green) Vehicle during Slalom at 65 kph ($\mu=0.85$)	101
Figure 6-25 H_{∞} Yaw Rate Reference Tracking during Slalom at 65 kph ($\mu=0.85$).....	101
Figure 6-26 Wheel Torque (a) and Rear Steer Angles (b) during Slalom at 65 kph ($\mu=0.85$)	102
Figure 6-27 Vehicle Speeds during Slalom at 40 kph ($\mu=0.85$)	103
Figure 6-28 Steering Wheel Angles during Slalom at 40 kph ($\mu=0.85$).....	103
Figure 6-29 Yaw Rate (a) Lateral Acceleration (b) and Vehicle Side Slip Angle (c) during Slalom at 40 kph ($\mu=0.85$).....	104
Figure 6-30 H_{∞} Yaw Rate Reference Tracking during Slalom at 40 kph ($\mu=0.85$).....	105
Figure 6-31 Wheel Torque (a) and Rear Steer Angles (b) during Slalom at 40 kph ($\mu=0.85$)	106
Figure 6-32 Vehicle Speeds during Slalom at 40 kph ($\mu=0.35$)	106
Figure 6-33 Steering Wheel Angles during Slalom at 40 kph ($\mu=0.35$).....	107
Figure 6-34 Yaw Rate (a) Lateral Acceleration (b) Vehicle Side Slip Angle (c) during Slalom at 40 kph ($\mu=0.35$)	108
Figure 6-35 H_{∞} Yaw Rate Reference Tracking during Slalom at 40 kph ($\mu=0.35$).....	108
Figure 6-36 Wheel Torque (a) and Rear Steer Angle (b) during Slalom at 40 kph ($\mu=0.35$)	109
Figure 6-37 Steering Wheel Input during FMVSS Maneuvers	110
Figure 6-38 Vehicle Speeds during FMVSS at 80 kph ($\mu=0.85$)	110

Figure 6-39 Yaw Rate (a) Lateral Acceleration (b) and Vehicle Side Slip Angle (c) during FMVSS at 80 kph ($\mu=0.85$).....	111
Figure 6-40 H_{∞} Yaw Rate Reference Tracking during FMVSS at 80 kph ($\mu=0.85$).....	112
Figure 6-41 Wheel Torque (a) and Rear Steer Angles (b) during FMVSS at 80 kph ($\mu=0.85$)	113
Figure 6-42 Vehicle Speeds during FMVSS at 80 kph ($\mu=0.35$)	113
Figure 6-43 Yaw Rate (a) Lateral Acceleration (b) and Vehicle Side Slip Angle (c) during FMVSS at 80 kph ($\mu=0.35$).....	114
Figure 6-44 H_{∞} Yaw Rate Reference Tracking during FMVSS at 80 kph ($\mu=0.35$).....	115
Figure 6-45 Wheel Torque (a) and Rear Steer Angles (b) during FMVSS at 80 kph ($\mu=0.85$)	116
Figure 6-46 Step Steering Wheel Input for J-Turn Maneuver	117
Figure 6-47 Vehicle Speeds during J-Turn at 80 kph ($\mu=0.85$).....	117
Figure 6-48 Vehicle Trajectory during J-Turn at 80 kph ($\mu=0.85$)	118
Figure 6-49 Turning Radius of the uncontrolled (dark green) and controlled (light green) vehicles during J-Turn at 80 kph ($\mu=0.85$).....	118
Figure 6-50 Yaw Rate (a) Lateral Acceleration and Vehicle Side Slip Angle (c) during J-Turn at 80 kph ($\mu=0.85$).....	119
Figure 6-51 H_{∞} Yaw Rate Reference Tracking during J-Turn at 80 kph ($\mu=0.85$)	120
Figure 6-52 Wheel Torque (a) and Rear Steer Angles (b) during J-Turn at 80 kph ($\mu=0.85$)	121
Figure 6-53 Vehicle Speeds during J-Turn at 50 kph ($\mu=0.85$).....	121
Figure 6-54 Vehicle Trajectory during J-Turn at 50 kph ($\mu=0.85$)	122
Figure 6-55 Turning Radius of the uncontrolled (dark green) and controlled (light green) vehicles during J-Turn at 50 kph ($\mu=0.85$).....	122
Figure 6-56 Yaw Rate (a) Lateral Acceleration and Vehicle Side Slip Angle (c) during J-Turn at 50 kph ($\mu=0.85$).....	123
Figure 6-57 H_{∞} Yaw Rate Reference Tracking during J-Turn at 50 kph ($\mu=0.85$)	124
Figure 6-58 Wheel Torque (a) and Rear Steer Angles (b) during J-Turn at 50 kph ($\mu=0.85$)	125
Figure 6-59 Vehicle Speeds during J-Turn at 50 kph ($\mu=0.35$).....	125

Figure 6-60 Vehicle Trajectory during J-Turn at 50 kph ($\mu=0.35$)	126
Figure 6-61 Yaw Rate (a) Lateral Acceleration (b) and Vehicle Side Slip Angle (c) during J-Turn at 50 kph ($\mu=0.35$)	127
Figure 6-62 H_{∞} Yaw Rate Reference Tracking during J-Turn at 50 kph ($\mu=0.35$)	127
Figure 6-63 Wheel Torque (a) and Rear Steer Angles (b) during J-Turn at 50 kph ($\mu=0.35$)	128
Figure 6-64 100 ft Constant Radius Circle Test Track	129
Figure 6-65 Vehicle Speeds during Constant Radius Turn at 50 kph ($\mu=0.85$)	129
Figure 6-66 Yaw Rate (a) Lateral Acceleration (b) and Vehicle Side Slip Angle (c) during Constant Radius Circle at 50 kph ($\mu=0.85$)	130
Figure 6-67 Uncontrolled (dark green) Vehicle leaving Test Track during maneuver ..	131
Figure 6-68 H_{∞} Yaw Rate Reference Tracking during Constant Radius Circle at 50 kph ($\mu=0.85$)	131
Figure 6-69 Wheel Torque (a) and Rear Steer Angles (b) during Constant Radius Circle at 50 kph ($\mu=0.85$)	132
Figure 6-70 Turning Circle Reduction Evaluation Test (uncontrolled vehicle (dark green) controlled (light green))	133
Figure 6-71 ZSS - No Limit Rear Wheel Angles	134
Figure 6-72 Turning Circle Diameter Reduction Results for Various Maximum Rear Wheel Steer Angles	135
Figure 6-73 Vehicle Speeds during DLC at 80 kph ($\mu=0.85$)	136
Figure 6-74 Steering Wheel Angles during DLC at 80 kph ($\mu=0.85$)	136
Figure 6-75 ZSS Controlled Vehicle Failing by Cone Contact during DLC at 80 kph ($\mu=0.85$)	137
Figure 6-76 Yaw Rate (a) Lateral Acceleration (b) and Vehicle Side Slip Angle (c) during DLC at 80 kph ($\mu=0.85$)	138
Figure 6-77 Rear Steer Angles of ZSS and H_{∞} Controllers during DLC at 80 kph ($\mu=0.85$)	139
Figure 6-78 Vehicle Speeds during DLC at 60 kph ($\mu=0.85$)	139
Figure 6-79 Steering Wheel Angles during DLC at 60 kph ($\mu=0.85$)	140

Figure 6-80 Yaw Rate (a) Lateral Acceleration (b) and Vehicle Side Slip Angle during DLC at 60 kph ($\mu=0.85$)	141
Figure 6-81 Rear Steer Angles of ZSS and H_∞ Controllers during DLC at 60 kph ($\mu=0.85$)	142
Figure 6-82 Vehicle Speeds during DLC at 40 kph ($\mu=0.85$)	142
Figure 6-83 Steering Wheel Angles during DLC at 40 kph ($\mu=0.85$)	143
Figure 6-84 Yaw Rate (a) Lateral Acceleration (b) Vehicle Side Slip Angle (c) during DLC at 40 kph ($\mu=0.85$)	144
Figure 6-85 Rear Steer Angles of ZSS and H_∞ Controllers during DLC at 40 kph ($\mu=0.85$)	145
Figure 6-86 Vehicle Speeds during Slalom at 40 kph ($\mu=0.85$)	145
Figure 6-87 Steering Wheel Angles during Slalom at 40 kph ($\mu=0.85$)	146
Figure 6-88 Yaw Rate (a) Lateral Acceleration (b) and Vehicle Side Slip Angle (c) during Slalom at 40 kph ($\mu=0.85$)	147
Figure 6-89 Rear Steer Angles of ZSS and H_∞ Controllers during Slalom at 40 kph ($\mu=0.85$)	148
Figure 6-90 Vehicle Speeds during DLC at 30 kph ($\mu=0.85$)	149
Figure 6-91 Steering Wheel Angles during DLC at 30 kph ($\mu=0.85$)	149
Figure 6-92 Yaw rate (a) and Lateral Acceleration (b) during DLC at 30 ($\mu=0.85$)	150
Figure 6-93 Rear Steer Angles during DLC at 30 kph ($\mu=0.85$)	151
Figure 6-94 Vehicle Speeds during DLC at 30 kph ($\mu=0.35$)	151
Figure 6-95 Steering Wheel Angles during DLC at 30 kph ($\mu=0.35$)	152
Figure 6-96 Yaw rate (a) and Lateral Acceleration (b) during DLC at 30 kph ($\mu=0.35$)	153
Figure 6-97 Rear Steer Angles during DLC at 30 kph ($\mu=0.35$)	153
Figure 6-98 Vehicle Speeds during Slalom at 30 kph ($\mu=0.85$)	154
Figure 6-99 Steering Wheel Angles during Slalom at 30 kph ($\mu=0.85$)	154
Figure 6-100 Yaw Rate (a) and Lateral Acceleration (b) during Slalom at 30 kph ($\mu=0.85$)	155
Figure 6-101 Rear Steer Angles during Slalom at 30 kph ($\mu=0.85$)	156
Figure 6-102 Vehicle Speeds during Slalom at 30 kph ($\mu=0.35$)	156

Figure 6-103 Steering Wheel Angles during Slalom at 30 kph ($\mu=0.35$)..... 157

Figure 6-104 Yaw rate (a) and Lateral Acceleration (b) during Slalom at 30 kph
($\mu=0.35$) 158

Figure 6-105 Rear Steer Angles during Slalom at 30 kph ($\mu=0.35$)..... 158

LIST OF TABLES

Table 3-1 Summary of Vehicle Models	42
Table 3-2 Test Courses Used for Validation in [46]	45
Table 3-3 Electric Powertrain Parameters	46
Table 5-1 Proportional-Integral Controller Gains	72
Table 6-1 Event List for Controller Evaluation	84

NOMENCLATURE

a_y	Lateral acceleration, m/s^2
C_α	Tire cornering stiffness, N/rad
F_x	Tire longitudinal forces, N
F_y	Tire lateral forces, N
$F_{y\alpha}$	Tire lateral cornering forces, N
F_{yy}	Tire lateral camber thrust forces, N
g	Acceleration due to gravity, m/s^2
G	Plant model
G_{aug}	Interconnected/augmented system for H_∞ synthesis
GR	Electric motor gear reduction ratio
I_{xx}	Vehicle roll inertia, $kg \cdot m^2$
I_{yy}	Vehicle pitch inertia, $kg \cdot m^2$
I_{zz}	Vehicle yaw inertia, $kg \cdot m^2$
I_{motor}	Spin inertia electric motor, $kg \cdot m^2$
I_{wheel}	Spin inertia wheel, $kg \cdot m^2$
i	Longitudinal slip of the tire, %
K	Controller
$k_{SW \rightarrow 1}$	Steering wheel ratio ($\delta_1 : \delta_{SW}$)
$k_{1 \rightarrow 2}$	Wheel steer angle ratio ($\delta_2 : \delta_1$)
k_{zss}	ZSS Turning circle reduction ratio ($\delta_4 : \delta_1$)
l	Vehicle wheelbase, mm
m	Vehicle mass, kg
N	Torque vectoring yaw moment, N
p	Vehicle roll velocity, rad/s
q	Vehicle pitch velocity, rad/s
r	Vehicle yaw rate, rad/s
$r_{desired}$	Desired vehicle yaw rate, rad/s
$r_{effective}$	Effective rolling radius of the tire, m
r_{ss}	Steady state vehicle yaw rate, rad/s

T_{motor}	Electric motor torque, N
t_w	Vehicle Track Width, m
U	Vehicle forward speed, m/s
V	Vehicle lateral speed, m/s
V_t	Speed of the tire, m/s
w	Vehicle normal velocity, rad/s
X	Gaussian activation functions

Greek Letters

α	Tire slip angle, rad
$\alpha_{\text{subscript}}$	Angular velocity, rad/s (subscript is place holder)
β	Vehicle side slip angle, rad
δ	Steering wheel angle, rad
θ	Scheduling Parameter for LPV plant
μ	Road friction coefficient
$\omega_{\text{subscript}}$	Angular speed, rad/s (subscript used as place holder)
Π	Vertices of scheduling parameter polytope
ρ	Radius of curvature, m
σ	Standard deviation for Gaussian activation functions
τ_{yaw}	Desired vehicle yaw response time delay, s

ABBREVIATIONS

4WS	Four-wheel steering
ABS	Anti-lock braking system
AC	Alternating current
AFS	Active Front Steering
AVTP	Allied vehicle testing publications
AWD	All-wheel drive
DEG	Degree(s)
DOF	Degree(s) of freedom
ESC	Electronic stability control
EQN	Equation
FMVSS	Federal motor vehicle safety standards
FWD	Front wheel drive
FWS	Front wheel steering
HZ	Hertz
ICE	Internal combustion engine
ISO	International Organization for Standardization
KPH	Kilometers per hour
LPV	Linear parameter varying
LQG	Linear quadratic Gaussian
LQR	Linear quadratic regulator
LMI	Linear matrix inequality
MIMO	Multi input multi output
MPC	Model predictive control
MR	Magnetorheological fluid
NATO	North Atlantic treaty organization
OGCC	Optimal guaranteed cost coordination
PID	Proportional-Derivative-Integral
QFT	Quantitative feedback theory
RPM	Revolutions per minute

RWD	Rear wheel drive
RWS	Rear wheel steering
SAE	Society of Automotive Engineers
TCS	Traction control system
VDC	Vehicle dynamics controller
ZSS	Zero side slip

ACKNOWLEDGEMENTS

I would like to express my gratitude to General Dynamics Land Systems-Canada for their financial and technical support during the course of my research.

I wish to express my sincere thanks to my thesis supervisor Dr. Moustafa El-Gindy for his support, guidance and for giving me the opportunity to work on this very interesting thesis in the first place.

I would also like to thank my family and friends for their continual love and support.

CHAPTER 1

INTRODUCTION

1.1 MOTIVATION

Multi-wheeled combat vehicles are utilized by various armed forces around the world in multiple roles. They often serve as modular platforms on which many configurations are based including: infantry section carriers, command posts and remote weapons systems [1]. The vehicles offer advantages over more traditional battle tanks and four-wheeled vehicles. Unlike tanks, they are able to maneuver at relatively high speeds in road and off road applications. Unlike traditional four-wheeled armoured vehicles, additional wheels allow for a uniform distribution of vehicle weight across the entire wheelbase offering mobility advantages in softer soils.

Combat vehicle payload and protection requirements continue to increase leading to higher vehicle weight, inertia and center of gravity height adversely affecting vehicle maneuverability and stability.

Drivers are faced with unexpected obstacles and changes in road friction coefficients. In these situations, they must make split-second inputs to a combination of steering, throttle and/or brake. Although a vehicle can be designed to be stable and predictable, a driver's inputs cannot. These sudden disturbances are contributing factors in a vehicle reaching the limits of its dynamic capabilities leading to loss of directional stability or even roll over.

The widespread adoption of active safety control systems in automotive applications in the last several decades including anti-lock braking (ABS) systems, traction control systems (TCS) and electronic stability control systems (ESC) has led to a decrease in the likelihood of single-vehicle crashes by upwards of 40% [2]. Advancements in powertrain and control systems technologies have led to the rise of more complex and effective systems including torque vectoring and rear wheel steering.

The above control systems have been proven in real life applications and are currently in production in passenger vehicles. Multi-wheeled heavy vehicles require special driver training and are unique dynamically as compared to passenger vehicles. However, there is no indication that torque vectoring and rear wheel steering cannot offer similar benefits when applied to multi-wheeled combat vehicles.

1.2 SCOPE AND OBJECTIVE

1.2.1 Scope

This research work is focused on exploring the benefits of modern control systems, particularly, torque vectoring and rear wheel steering (RWS) on an electrically driven armoured vehicle equipped with eight independently controlled wheel drive motors. Effects on stability and maneuverability at various speeds and maneuvers are to be investigated. Active front steering and active suspension are not options that can be implemented on the vehicle at this time and will therefore not be part of this study.

1.2.2 Objectives

The aim of this thesis is to provide insight into an advanced torque vectoring and rear steer controller and investigate the benefits when applied to an electrically driven 8 x 8 heavy combat vehicle. Simulations are to be conducted with a validated multi-wheeled combat vehicle TruckSim model in co-simulation with a controller in MATLAB/Simulink. Objectives include:

- Replace combustion engine powertrain with simplified electric motors and gear reducers (full details on the electric powertrain are classified)
- Design an H_∞ controller utilizing torque vectoring and rear steering as controller outputs
- Perform simulations to investigate the performance of the developed controller in various dynamic events using non-linear TruckSim vehicle model
- Investigate feedforward rear steering control for reduction of vehicle curb-to-curb turning circle at low speeds

- Propose a combined vehicle dynamics control system integrating both H_∞ controller and feedforward rear steering controller with seamless switching between control strategies
- Draw conclusions about the capabilities of the systems to improve vehicle performance and mobility

1.3 OUTLINE OF THESIS

The thesis is structured as follows:

Chapter 1 outlines the motivation, scope, outline and objective of this work. Working foundations of vehicle dynamics and control systems theory are introduced.

Chapter 2 provides a literature review of torque vectoring and rear steering with an emphasis on multi-wheeled vehicles, electric vehicle torque vectoring and H_∞ implementations. Feedforward turning circle reduction strategies are also reviewed.

Chapter 3 introduces the various vehicle models used and their purpose. The full vehicle TruckSim model, bicycle model used as the H_∞ plant, yaw rate reference model and the zero side slip (ZSS) feedforward control equation for turning circle reduction are derived. The co-simulation environment is also explained.

Chapter 4 details the theory behind linear parameter-varying (LPV) H_∞ plant modeling, structure and synthesis. The proposed LPV H_∞ controller for the 8 x 8 combat vehicle used during this work is developed using the theory presented.

Chapter 5 describes the proposed vehicle dynamics control system architecture. The interaction of all the different blocks including the PI speed controller, upper and lower controllers and on/off slip controller is covered.

Chapter 6 presents the results of the performance of the developed control system. Simulations are conducted on the full TruckSim vehicle model in co-simulation with MATLAB/Simulink. Various events, road friction coefficients and vehicle speeds are used to fully test the proposed systems performance.

Chapter 7 draws conclusions and presents future work regarding the proposed vehicle dynamic control strategy for an 8 x 8 heavy combat vehicle.

1.4 WORKING FOUNDATIONS

This chapter is meant to introduce the main concepts relevant to the work conducted.

The review is divided into the following areas:

- Vehicle Dynamics Theory
- Control Systems Theory

1.4.1 Vehicle Dynamics Theory

The field of vehicle dynamics involves the complex interactions between driver, vehicle and the environment (road and weather). Vehicle dynamics can be separated into two distinct categories; Isolation and Control as illustrated in Figure 1-1 [3]. Isolation deals with the attenuation of internal and external disturbances and will not be covered here. Control, the main focus of this work, deals with the vehicle's response to driver commands.

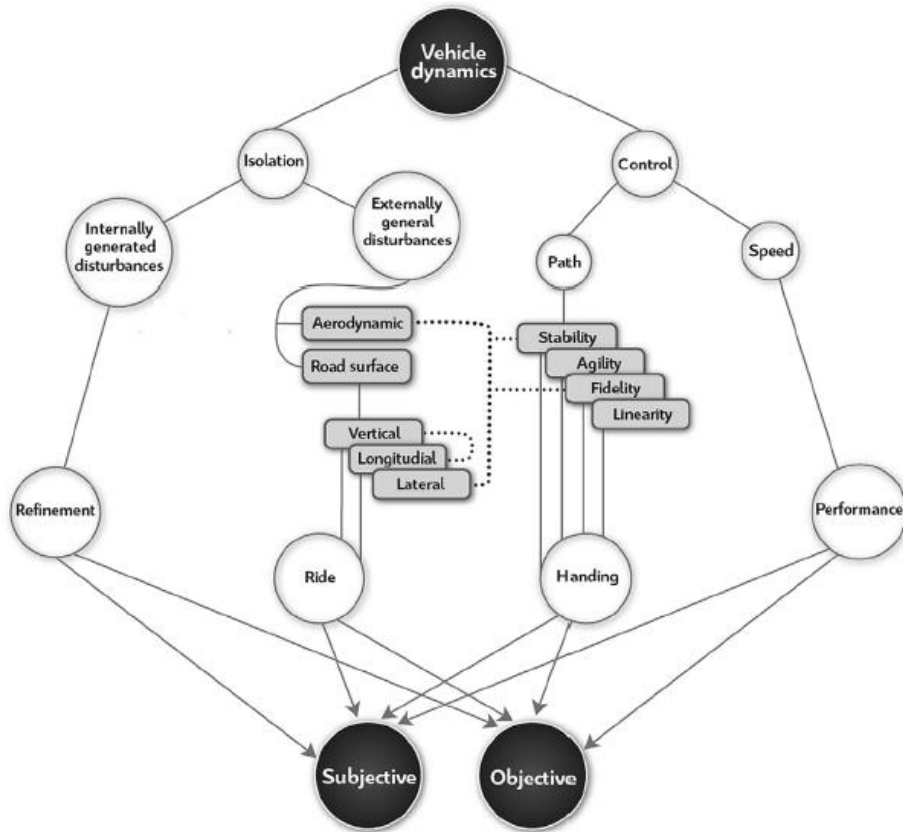


Figure 1-1 Vehicle Dynamics Interactions [3]

A vehicle's main objective is to transport driver, passengers and cargo in a safe and efficient manner [4]. In order to design a vehicle that can accomplish this task an in-depth understanding of control is critical. A driver has active control of a vehicle's heading angle, road position (path) and speed. The driver makes use of the steering system, brake and accelerator pedals in order to control the vehicle as seen in Figure 1-2.

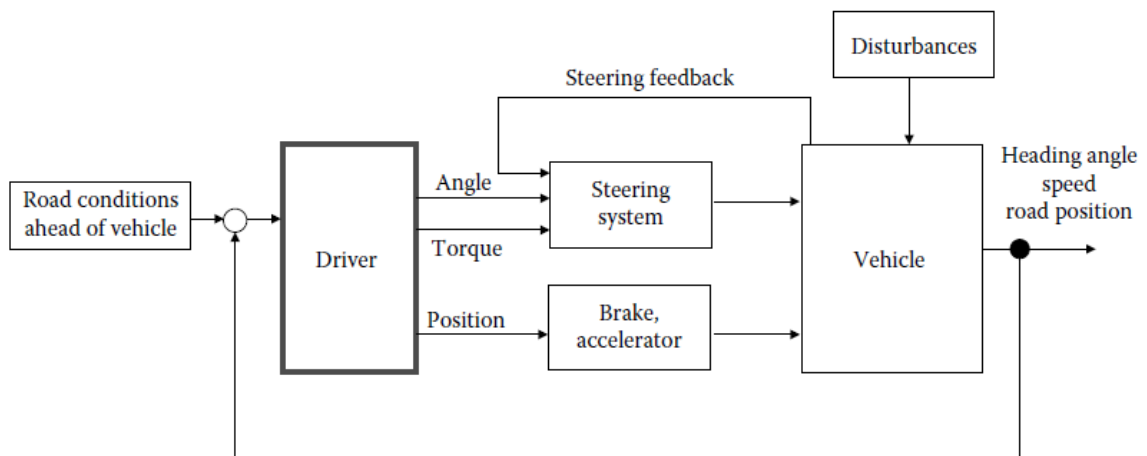


Figure 1-2 Vehicle/Driver Control Loop [5]

1.4.1.1 Tire Dynamics

The driver's steering wheel angle is translated to wheel angles via the steering system. A vehicle's behaviour is a direct product of the dynamics of its tires. Tires provide traction, steering control and directional stability to a vehicle through the generation of longitudinal and lateral forces [6].

SAE Tire Axis System

The axis system recommended by the Society of Automotive Engineers (SAE) is shown in Figure 1-3. The origin of the SAE tire coordinate system is located at the center of the contact patch where the tire makes contact with the ground. The x axis is aligned with the tire/wheel heading. Longitudinal forces, F_x , are generated on this axis. The y axis is located on the ground and perpendicular to the other two axes. It is also located on the right hand side of the reference frame and lateral forces, F_y , are generated on this axis. The z axis is perpendicular to the ground and is pointed upward. It should be noted it is not located in the wheel plane and normal forces act on this axis.

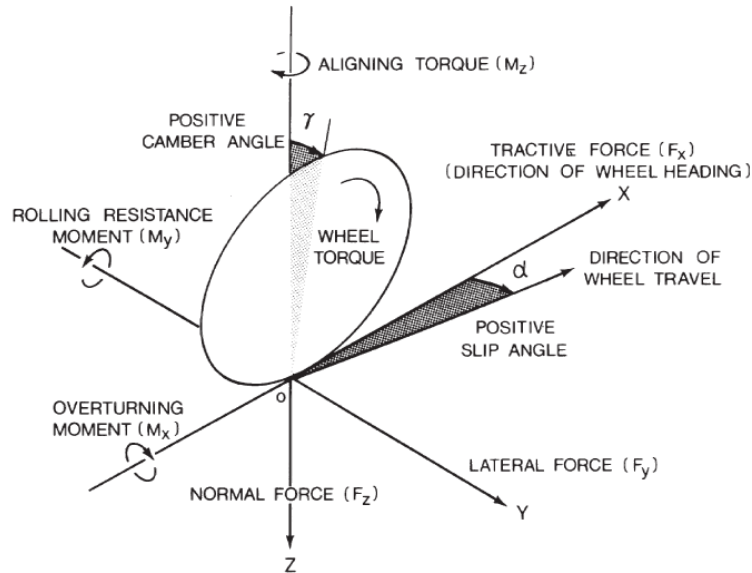


Figure 1-3 SAE Tire Axis System [6]

It should be noted that each axis has an associated moment. For the purposes of this work only longitudinal and lateral forces will be covered as they are the most critical to torque vectoring and rear steering.

Longitudinal Forces, F_x

Tire longitudinal forces are generated at the tire-ground contact patch in line with the wheel heading and SAE x axis. They are a function of longitudinal slip, i , defined as:

$$i = \left(1 - \frac{V_t}{r_{effective} \omega_{tire}} \right) * 100\% \quad 1-1$$

where V_t is the speed of the tire, ω_{tire} , is the angular speed of the tire, $r_{effective}$ is the effective rolling radius of the tire. Figure 1-4 demonstrates the relationship between tractive effort and longitudinal slip graphically. Initially, tractive forces build linearly with increasing slip and gradually begin to saturate. At approximately 20% slip (for dry pavement) tractive forces reach their peak value and any increase in longitudinal slip will cause a decrease in tractive force. It should be noted that this relationship is highly dependent on tire normal force, inflation pressure, tire construction and road surface.

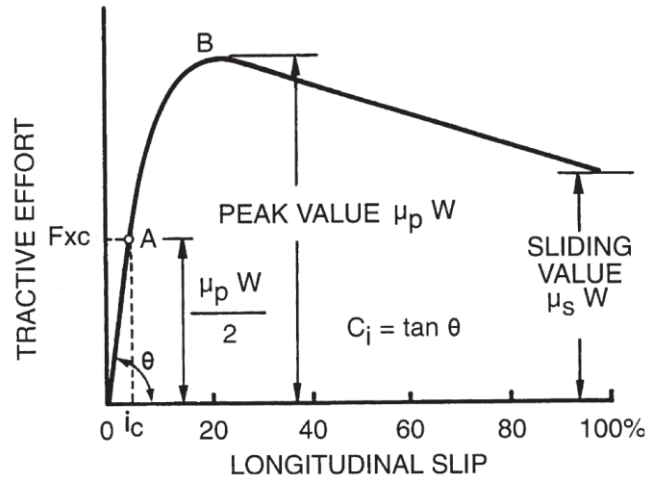


Figure 1-4 Tractive Force Generation Due to Longitudinal Slip of a Tire [6]

Lateral Forces, F_y

Tire lateral forces are generated at the tire contact patch parallel to the wheel heading in the SAE y axis. Total lateral force is a combination of cornering force, $F_{y\alpha}$, and camber thrust, $F_{y\gamma}$ [6]. Camber thrust will not be covered here.

Tire cornering force, $F_{y\alpha}$, is generated when a side force is applied to a tire causing the tire to move along a path at a slip angle, α , with the wheel plane as seen in Figure 1-5 [6].

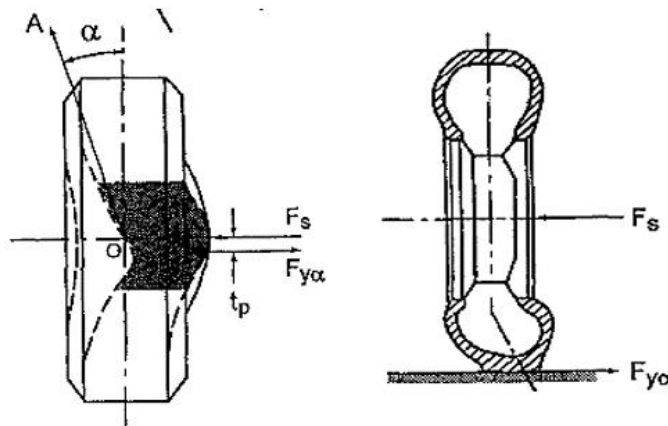


Figure 1-5 Behaviour of a Tire Subjected to a Cornering Maneuver (Top View (Left); Front View (Right)) [7]

Initially, tire cornering forces build linearly with increasing slip angle and gradually begin to saturate at high values of slip angle as in Figure 1-6. When the road adhesion limit is reached, the tire will begin to slide.

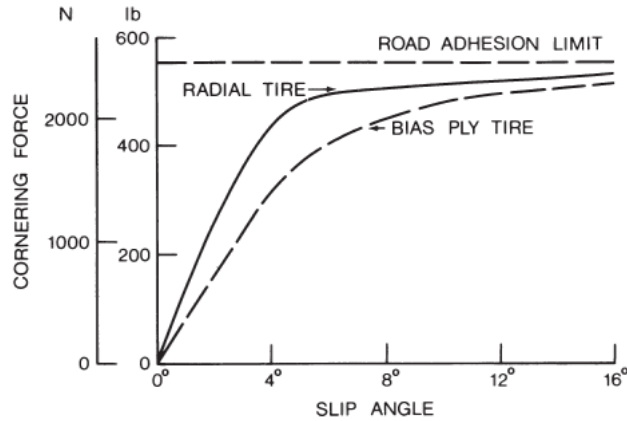


Figure 1-6 Cornering Characteristics of a Bias-Ply and Radial-ply Car Tire [6]

Tire cornering stiffness, C_α , is commonly used to define a tire's capacity to generate cornering force at low slip angle values. It is defined as the slope of tire cornering force at zero side slip angle [6]:

$$C_\alpha = \frac{\partial F_{y\alpha}}{\partial \alpha} \Big|_{\alpha=0} \quad 1-2$$

Tire normal force has a significant effect on cornering force. For a given slip angle, tire cornering force generally increases with increasing normal load [6]. Load transfer on an axle will reduce the overall cornering force of the pair of tires as seen in Figure 1-7.

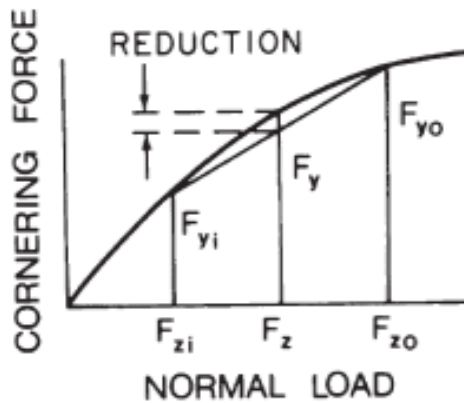


Figure 1-7 Effect of Load Transfer on an Axle [6]

Combined Longitudinal and Lateral Tire Force Relationship

A vehicle's tire characteristics are crucial to its overall dynamic behaviour. A friction ellipse is used to graphically represent a tire's force generation capability as in Figure 1-8.

The shape and overall area of the ellipse is a function of tire slip angle, normal load, inflation pressure and tire type.

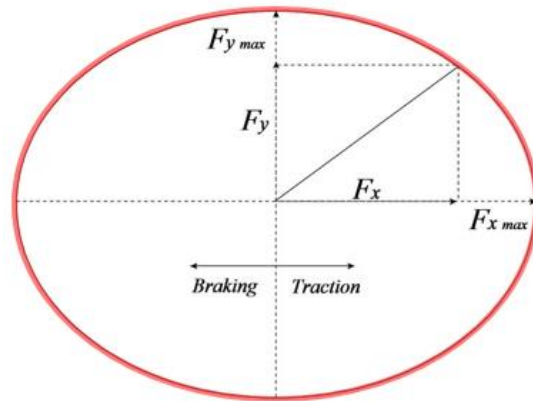


Figure 1-8 Tire Friction Ellipse for Fixed Normal Load, Slip Angle & Inflation Pressure [6]

The horizontal axis represents the magnitude of longitudinal force being generated (traction & braking). The vertical axis represents the magnitude of lateral cornering force. The boundary of the ellipse (red) is the ultimate force generation limit of a tire. A tire can generate purely longitudinal force (vector along x axis), pure cornering force (vector along y axis) or a combination of the two. It is important to note that as tire longitudinal force, F_x , increases, tire cornering force, $F_{y\alpha}$, decreases. This relationship is defined as:

$$\frac{F_{y\alpha}^2}{F_{y\alpha\max}^2} + \frac{F_x^2}{F_{x\max}^2} = 1 \quad 1-3$$

It should be noted that at low lateral acceleration levels, the resultant tire force vector may not reach the limits of the friction ellipse. In this case, the longitudinal and lateral tire forces are considered almost independent of each other [8]. Near the friction ellipse limit however, at high lateral accelerations, a reduction in one component can lead to the increase in the other.

Figure 1-9 illustrates this point. A passenger car is executing a left hand turn. Due to roll (load transfer to outside tire) and squat (load transfer to rear tires) the outside tires have larger friction ellipse boundaries (larger force generation potential) than the inside tires.

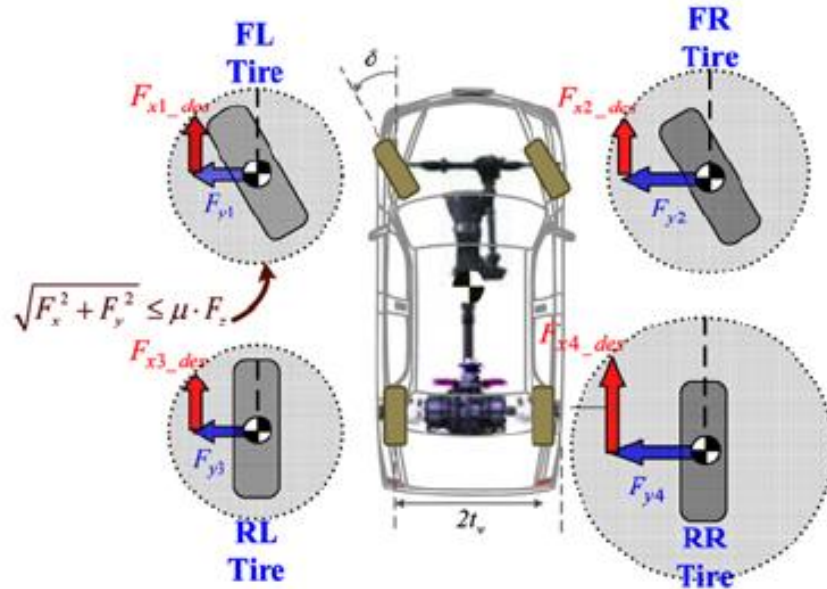


Figure 1-9 Tire Friction Ellipses of a Vehicle Executing a Left Hand Turn [9]

When the resultant tire force vector reaches the boundary of the friction ellipse the tire has reached its force generation limit. Any increase in longitudinal or lateral force will cause the tire to slip causing understeer or oversteer. Vehicle load transfer due to pitch and roll during maneuvers creates variations in wheel normal loads and results in different force generation limits for each tire.

1.4.1.2 Vehicle Lateral Dynamics

In simplest terms, a vehicle can be approximated as a point mass traveling along a path of varying curvature. It is useful to represent its velocity and acceleration components as vectors as in Figure 1-10. It is easy to see that the velocity vector is always tangent to the curved path. Lateral acceleration is composed of longitudinal and lateral components.

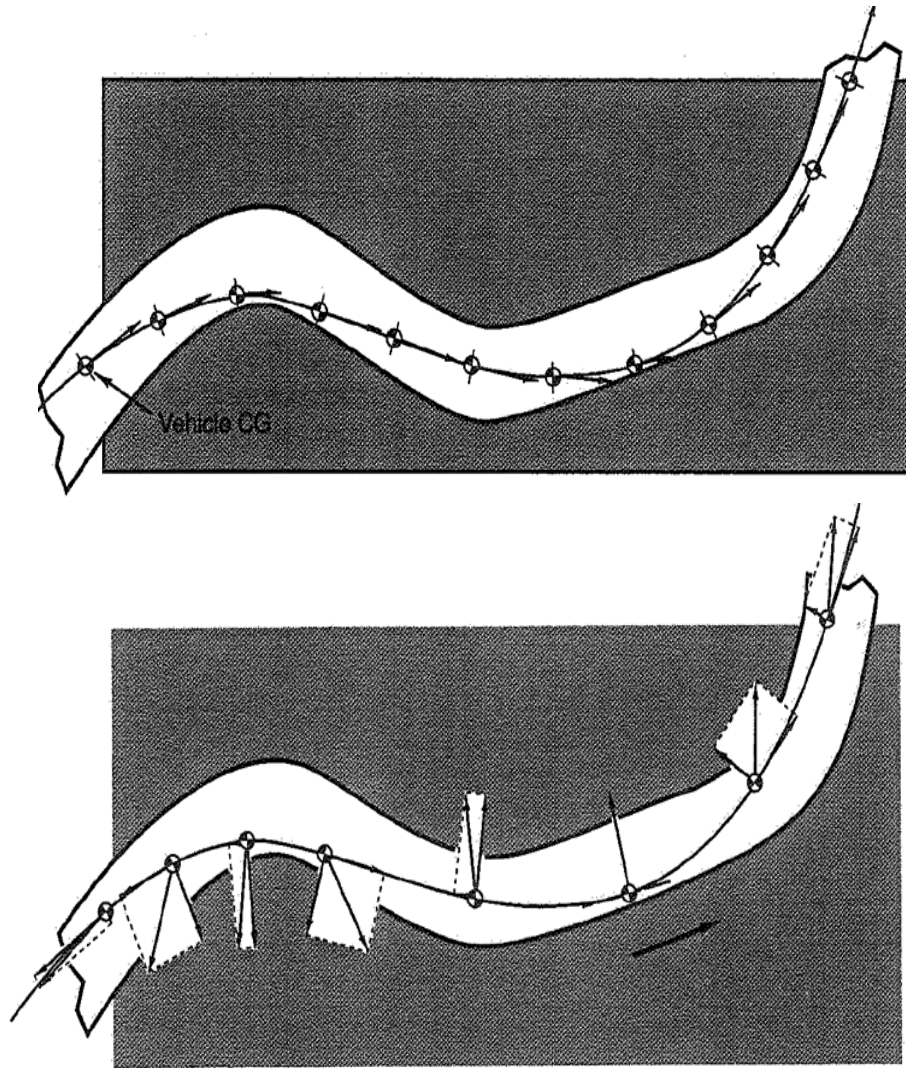


Figure 1-10 Vector Velocity (TOP) and Acceleration (BOTTOM) [10]

The lateral component of acceleration is more commonly referred to as centripetal acceleration and lateral acceleration within the field of vehicle dynamics. It acts to accelerate the point's mass towards the center of the turn. Lateral acceleration i.e. centripetal acceleration, a_y , is a function of path curvature, ρ , and forward speed, U , and yaw rate, r :

$$a_y = \frac{U^2}{\rho} = rU = r^2\rho \quad 1-4$$

This acceleration is generated by a vehicle's tire forces. Although a point mass representation is useful to understand basic concepts, a vehicle is not so simple.

SAE Vehicle Axis System

The Society of Automotive Engineers (SAE) have defined a vehicle axis system as seen in Figure 1-11. The axis system is orthogonal similar to the tire axis system. The origin of the axis system is located at the intersection of the vehicle roll axis and line perpendicular to the ground and passing through the vehicle center of gravity [10]. The x and y axis are parallel to the ground. The y axis is positive to the passenger side of the vehicle. The z axis is perpendicular to the plane formed by the x and y axis. All vectors point in the positive direction. The right hand rule is used to define the direction of positives moments as shown. The coordinate system moves with the vehicle.

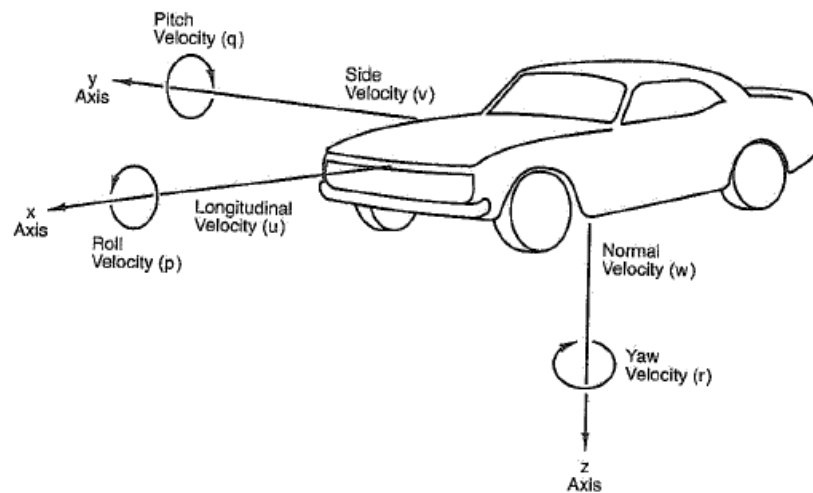


Figure 1-11 SAE Vehicle Axis System [11]

The x axis defines longitudinal velocity, u , and roll velocity, p . The y axis defines lateral velocity, v , and pitch velocity, q . The z axis defines normal velocity, w , and yaw rate/velocity, r .

Vehicle and Tire Side Slip Angle Generation

Figure 1-12 shows a vehicle performing a right turn at speed. During the maneuver an angle forms between the heading of the vehicle and the velocity vector of the center of gravity. This angle is known as the vehicle side slip angle, β . A similar angle is formed between the heading of each wheel and each wheel's velocity vector. This angle is known as the tire

slip angle, α . The generation of these forces can be dealt with in two separate phases. The transient and steady state phases.

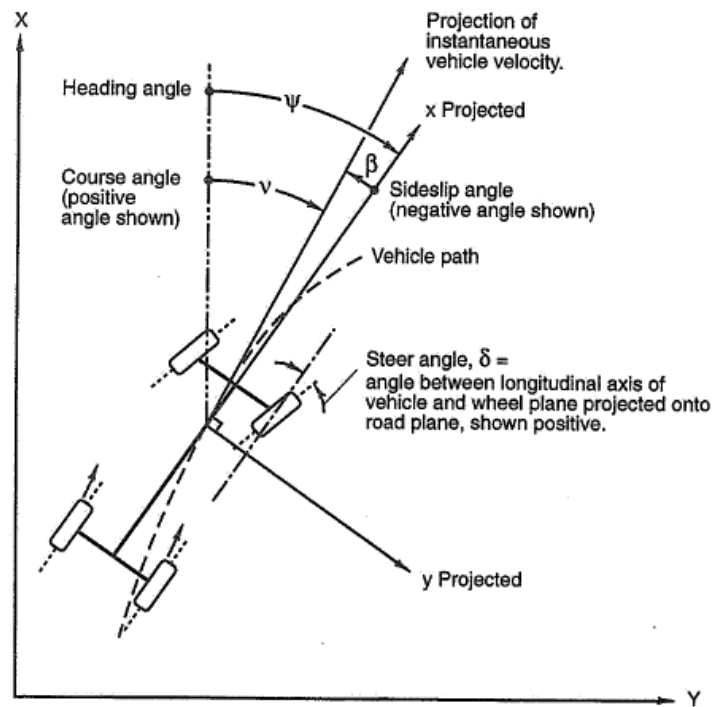


Figure 1-12 Heading, Side slip, Course and Steer Angles [11]

Lateral Force Generation - Transient Dynamics

During initial turn in (transient phase) of a step steering wheel input angle, the generation of cornering forces is not instantaneous. Figure 1-13 shows the relationship between a ramp steering wheel input and a generic vehicle's motion response. An offset in time can be observed between the point when the steering wheel reaches its final value and the time the vehicle's response reaches steady state. Common responses of interest in vehicle dynamics include yaw rate, lateral acceleration, side slip angle and roll angle [10]. The time required to reach 90% of the final steady state value is defined as the rise time and is unique to each vehicle.

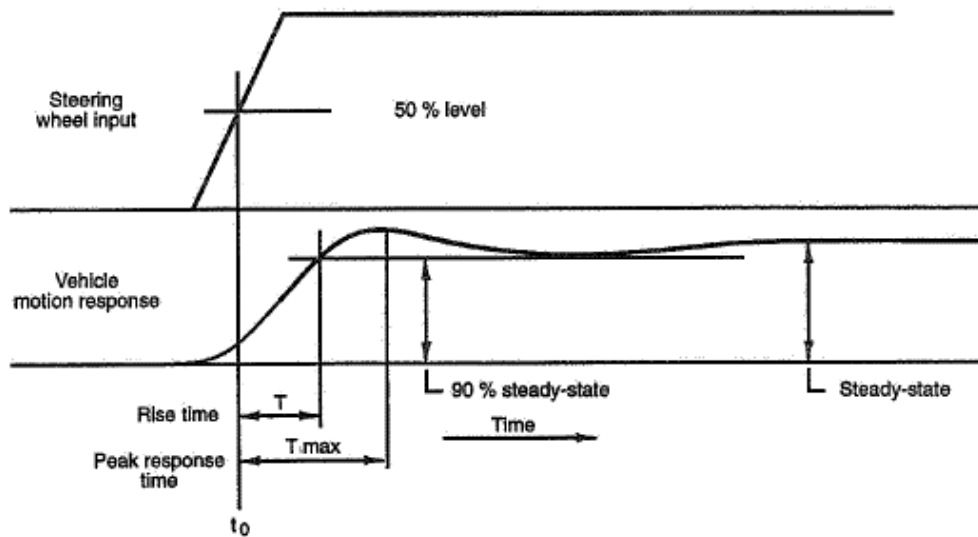


Figure 1-13 Rise Time and Peak Response Time [10]

The transient sequence of force generation is detailed in Figure 1-14. The driver turns the steering wheel causing an initial yaw response about the center of gravity of the vehicle. This is accomplished through the establishment of a front tire slip angle and resultant cornering force. The initial yaw response causes a difference between the vehicle heading angle and velocity vector of the center of gravity leading to a vehicle side slip angle and rear tire slip angles. Front and rear centripetal tire forces are established resulting in lateral acceleration and the vehicle cornering. It should be noted that the entire process takes place in fractions of a second. It should be noted that his initial yaw response is even more pronounced in vehicles with high moments of inertia as is the case in this work [4].

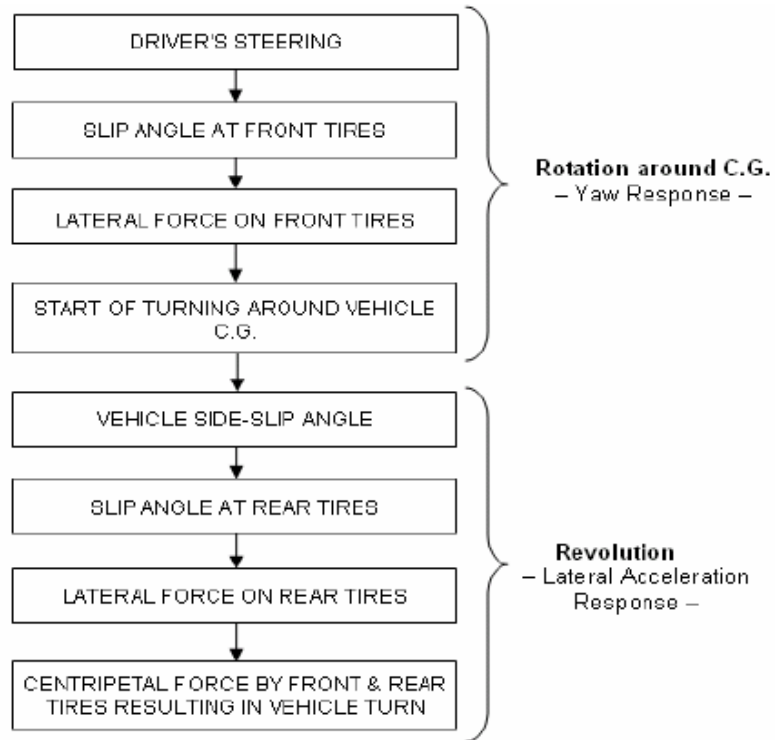


Figure 1-14 Transient Response of FWS Vehicle to Stepwise Steering Input [12]

1.4.2 Control Systems Theory

A control system is defined as a group of interconnected subsystems and one or more plants used to obtain a desired output, y , by manipulating the plant input, u [13]. Figure 1-15 illustrates a typical system response to a step input. The response is composed of a transient component and a steady-state component. Two widely accepted measures of controller performance are transient response and steady-state error.

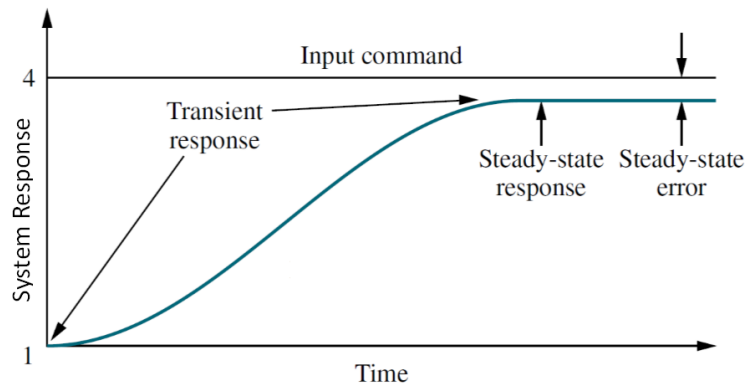


Figure 1-15 Typical System Response to Step Input [14]

1.4.2.1 System Configurations

There are two widely accepted control system configurations: open loop and closed loop systems [14]. Each has advantages and disadvantages and has been used for vehicle dynamics control. Combinations of both systems have also been used.

Open Loop (Feedforward) Systems

Open loop controllers are composed of a controller, K , that uses the input or reference signal to produce a control signal, u , that is sent to the plant, G , as illustrated in Figure 1-16. The controller in an open loop system is often referred to as feedforward controller. The response to changes in the input or reference signal is predefined and is often based on an inverse model of the plant to be controlled.

Open loop systems are simple and cost effective. However, they do not have the ability to compensate for any disturbances in the system that may affect the output of the plant. Inverse model based systems may have difficulty if the plant dynamics change over time.

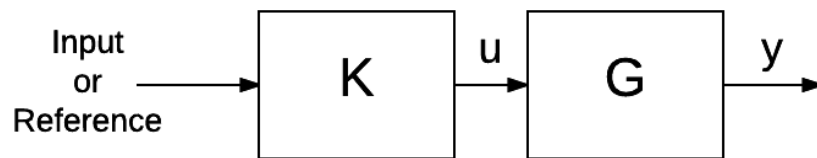


Figure 1-16 Open Loop Control System Structure

Closed Loop (Feedback) Systems

Closed loop controllers are also composed of a controller, K , and plant, G as shown in Figure 1-17. The controller in a closed loop system is often referred to as a feedback controller. Closed loop systems differ in the signal received by the controller. Instead of directly reading the input or reference signal, a feedback controller receives the error between the input or reference signal and the actual output of the plant in order to generate a control signal. Due to this, a feedback controller inherently reacts and adjusts to disturbances. This allows for greater accuracy than an open loop system at the expense of greater complexity and cost [14]. The drawback with closed loop systems is that error must be present before the controller can take action.

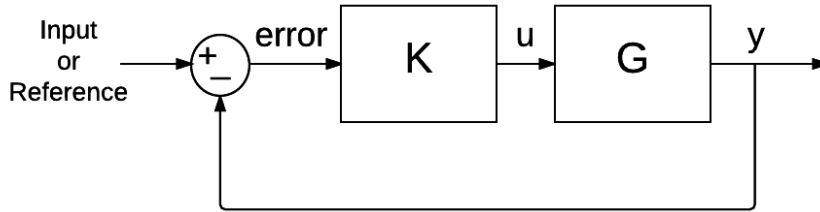


Figure 1-17 Closed Loop Control System Structure

Combined Systems

Feedforward and feedback controllers can also be used simultaneously in a combined system. A closed loop system alone cannot satisfy both disturbance rejection and reference tracking [13]. A combined system uses a feedforward controller to provide a rapid response and a feedback controller to fine tune the response ensuring the error between the desired and actual system response is minimized.

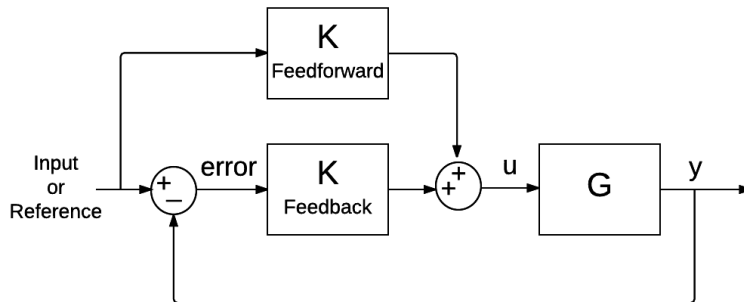


Figure 1-18 Combined Feedback and Feedforward System

Application to Vehicle Dynamics Using a Reference Model

Closed loop vehicle dynamics control systems actively monitor the error between the response of an internal reference model of the vehicle and the actual vehicle response as shown in Figure 1-19.

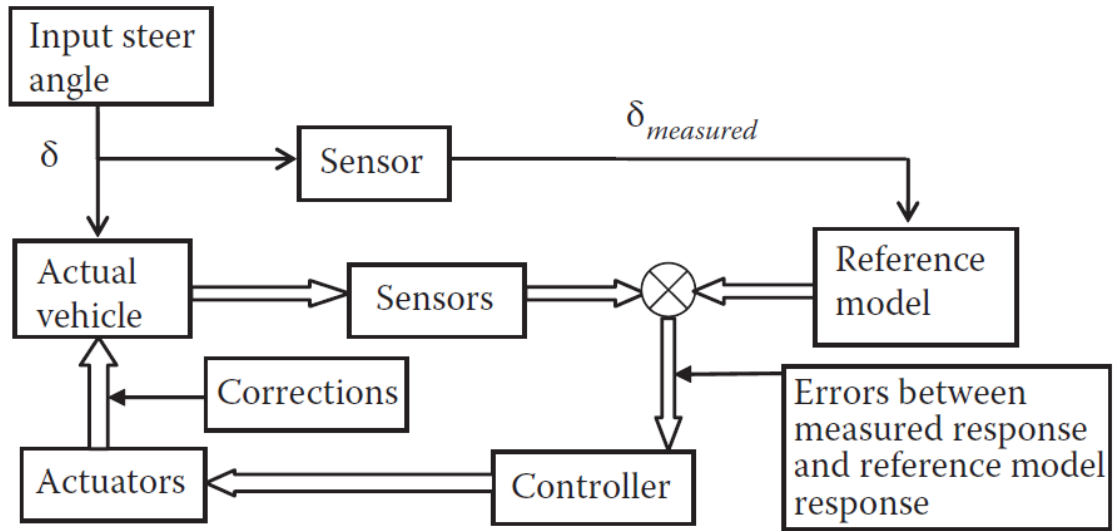


Figure 1-19 Model Reference Control [4]

Common sensors available on the vehicle for this type of control include yaw rate sensor, steering wheel position sensor, lateral acceleration sensor as well as longitudinal acceleration sensor already present for use by the ABS system [4].

CHAPTER 2

LITERATURE REVIEW

A general survey of torque vectoring and rear steer will be conducted with an emphasis on multi-wheeled vehicles, electric vehicle torque vectoring and H_{∞} implementations. Active front steering and torque vectoring other than through electric motors is not in the scope of this work.

2.1 VEHICLE DYNAMICS CONTROL SYSTEMS

The past several decades have brought innovations within the automotive industry that have led to significant increases in performance and safety. These advances can be attributed to the introduction of computer control to vehicle dynamics. Computer control has allowed for the mass implementation of control based stability systems which are now mandatory in many jurisdictions.

Stability systems are tasked with preventing a vehicle from reaching its handling limits and thus safeguarding the driver from loss of control. Modern stability control systems have their root in antilock braking systems (ABS) and traction control systems (TCS). ABS and TCS were developed to enhance vehicle safety by limiting wheel lock up and wheel slip respectively through actuation of the brakes and control of the throttle. Excessive braking or tractive forces can cause wheel lockup or slip. Locked and slipping wheels have their lateral force generation potential decreased which can lead to a loss of directional stability.

A natural progression was made from standalone ABS and TCS systems to electronic stability control (ESC). ESC systems compare desired vehicle direction against actual vehicle direction. When a discrepancy is detected, one of the four brakes is suddenly actuated in order to correct the error. As technology has progressed, it is now possible to actively enhance vehicle performance and mobility as well. These systems are based on the same basic control principles as ESC systems but the main objective is to enhance performance rather than intervene in emergency situations. Torque vectoring and rear

steering are just two of several techniques used to manipulate a vehicle's dynamic behaviour and are becoming more and more common.

2.1.1 Basic Principles of Torque Vectoring

Torque vectoring systems have the ability to control torque distribution between driven wheels as shown in Figure 2-1. Several methods are used to achieve this torque distribution. The vast majority of implemented torque vectoring systems employ either differential braking or torque vectoring differentials.

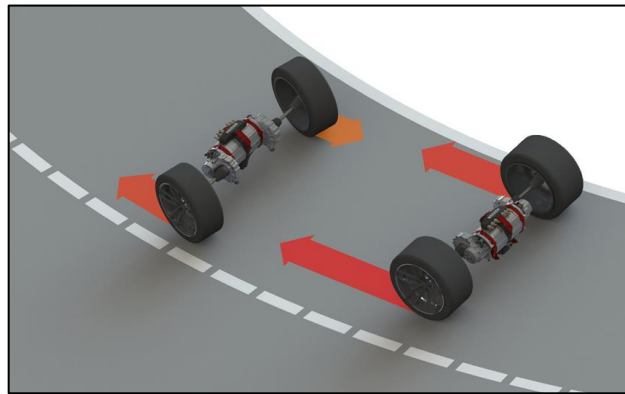


Figure 2-1 Torque Vectoring Schematic [15]

Differential braking takes advantage of the existing brake system. It is a cost effective way to implement torque vectoring. However, the braking system inherently reacts slower than other mechanisms and is less sensitive than a torque vectoring differential. Additionally, the strategy is intrusive as it interferes with driver intended acceleration & slows vehicle speed during operation [16]. Active differential braking systems are considerably less efficient than torque vectoring differential systems [17]. Hancock et al. [17] found energy dissipation to be up to 10 times higher in a brake based system for certain maneuvers as compared to a system with torque vectoring differentials.

Torque vectoring differentials allow for flexibility and near total control over torque distribution at each wheel on an axle. The system is not intrusive as there is no change in applied torque just a redistribution of the available input torque. Added complexity and vehicle weight are the major drawbacks.

Individual electric motors at each wheel represent the state of the art torque vectoring application. The most appropriate torque distribution under any circumstance can be achieved. Such a system exhibits the same advantages as an active torque vectoring differential except that in the case of electric motors each motor can produce any magnitude and direction of torque independent of each other.

2.1.2 Basic Principles of Rear Wheel Steering

Rear wheel steering, sometimes referred to as four-wheel steering, is defined as the ability to manipulate rear tire slip angles through an additional rear steering angle. This allows for the direct control over rear tire lateral forces. Rear wheel steering has a critical effect on a driver's impression of a vehicle's dynamics [3]. The addition of rear wheel steering can achieve one of several objectives [18]:

- Vehicle side slip angle reduction
- Reduction in yaw rate and lateral acceleration phase difference
- Turning circle reduction at low speed
- Model matching steering response
- Tire force limit increase (low friction surfaces)

Ulsoy et al. [18] showed that the rear wheels are just as effective as the front wheels at generating a yaw moment about the center of gravity of a vehicle. The ability to control the lateral forces at the rear axle through the inclusion of a rear steering angle in the same direction of the front tires could reduce the lag in lateral motion response of the rear axle proving quite useful in emergency lane change maneuvers [4]. Rear axle steering in the opposite direction of the front tires proves quite difficult for a human driver at high speeds as transient force generation is in the opposite direction of the steady state [18]. Rear wheel steering has been a controversial topic due to the fact that, *“as the handling limit approaches the flat nature of the tyre side-force-versus-slip-angle curve means that its ability to improve vehicle control disappears. In this sense, it is possibly the worst type of system - enhancing driver confidence without actually improving limit capability”* [3].

Several methods can be used to steer the rear wheels. A central steering rack can be used to duplicate the front steering system in the rear. The disadvantage of this system is that

active control of the rear steering angle is not possible as the relationship between steering wheel and rear axle angle is dictated by the mechanical composition of the rack itself. Hydraulic and electromechanical actuators can also be used.

2.2 FOUR-WHEELED VEHICLE CONTROL

Extensive work has been conducted in the area of vehicle dynamic controls pertaining to four-wheeled vehicles. A brief review here will highlight the major contributions in this area.

Furukawa and Abe [19] conducted a study on advanced chassis control systems for vehicle handling and active safety. They concluded that direct yaw moment control (torque vectoring) is more effective in vehicle motion at large side slip angles and high lateral accelerations and that four-wheel steer (rear wheel steering) and direct yaw moment control could be used together in order to complement each other. Nagai et al. [20] and Yamamoto [21] agreed with the region of effectiveness of direct yaw moment control as illustrated in Figure 2-2.

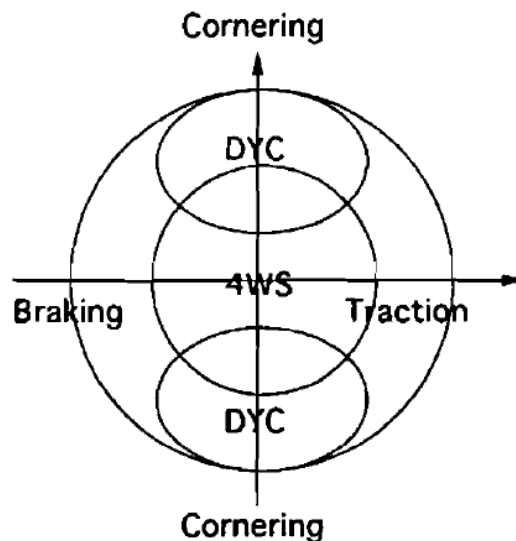


Figure 2-2 Area of Effectiveness of DYC and 4WS [20]

Shimada and Shibahata [22] used stabilizing moment diagrams to analyze three control methods: lateral torque vectoring through driving and braking forces, roll stiffness control, rear wheel steering angle control. The study concluded that torque vectoring was effective

at negating the changes in a vehicle's dynamic behaviour caused by acceleration and deceleration. Roll stiffness control was found to only be effective at high lateral accelerations and rear wheel steering was most effective at small vehicle side slip angles.

Sawase and Ushiroda [23] studied the improvement that right and left torque vectoring systems had on vehicle dynamics for front, rear and all-wheel drive vehicles. The study applied torque vectoring to the front axle only, the rear axle only and both axles on FWD, RWD and AWD vehicles. They concluded that torque vectoring is most effective when applied to the front wheels on FWD vehicles and to the rear wheels on RWD and AWD vehicles.

Sawase et al. [16] published results relating rear cornering force margin as a function of torque difference between the left and right wheels. Results showed that as the torque differential between left and right wheels increased so did the rear tire cornering force margin. They identified a range of torque difference between left and right rear wheels where the rear tire cornering force margin effectively saturated as illustrated in Figure 2-3.

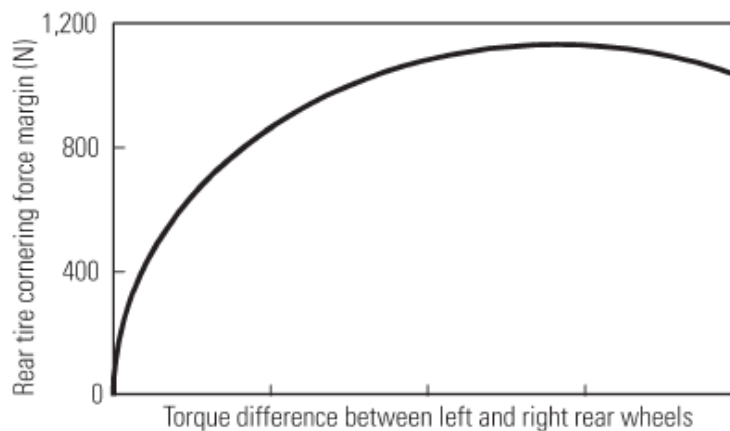


Figure 2-3 Cornering Force Improvement vs Torque Differential Between Left and Right Wheels [16]

Nagai et al. [20] proposed a feedforward and feedback controller tracking both yaw rate and vehicle side slip angle to control torque vectoring and rear steering angle. The work demonstrated the ability of model matching control systems based on linear methods to improve vehicle performance in non-linear range of tire operation.

Aripin et al. [24] conducted a review of active yaw control systems for vehicle handling and stability enhancement in four-wheeled vehicles. The survey covered the vehicle models in use, the control objectives, the various active systems as well as the control strategies. The study explained that multiple degrees of freedom (DOF) vehicle models have been used to evaluate controller performance. The reviewer stated that the classical bicycle model has been used prominently for yaw control design and is regularly used as a reference model to generate desired yaw rate and side slip angle using steady state assumptions or approximated as a first order response. Control objectives of yaw stability control systems were classified into three categories: yaw rate control, side slip control and a combination of yaw rate and side slip. Active chassis control systems were classified into three major categories each with its own set of possible actuators as illustrated in Figure 2-4.

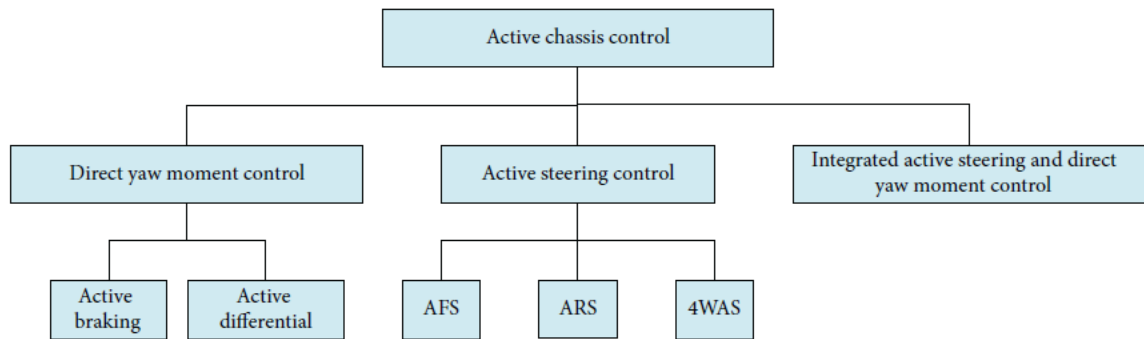


Figure 2-4 Active Chassis Control [24]

Active rear steering (ARS) is described as being used to “*improve the vehicle response for low speed cornering maneuvers*”. Integrated active chassis control is covered in several papers by combining active steering, active braking and active suspension or stabiliser. The most common was identified as the combination of AFS and direct yaw moment control through active braking. The review of control strategies included one PID, two PI, several linear matrix inversion based and static based feedback, several H_{∞} controllers, several sliding mode control papers, one optimal guaranteed cost coordination controller (OGCC), an adaptive based control paper, an internal model control paper, a quantitative feedback theory (QFT) and a μ -synthesis control paper. Several other less common combinations are discussed. A table is constructed to summarise the various systems and their advantages

and disadvantages. The study concludes that due to uncertainties in real driving conditions, such as surface friction, varying vehicle parameters (weights, inertia, tire wear, tire cornering stiffness, vehicle speed, etc.) and crosswinds, use of a robust control strategy is essential. The survey does not include electric motor drives at each wheel as a direct yaw moment control option and all papers mentioned in the survey are specific to four-wheeled vehicles.

Hac et al. [25] identified regions of effectiveness in yaw control for each chassis subsystem. Handling tests were run for a preliminary control algorithm integrating the control of brakes and magneto-rheological (MR) dampers on various events (track, double lane change, circular track, J-turn and sinusoidal steer). Using the integrated control there was a reduction in the time the brake system was active during the various events ranging from approximately 20 to 70 percent. The study concluded that in maneuvers performed close to the limits of adhesion, relatively minor changes in the tyre force characteristics, driver inputs, disturbances, etc. can have an effect on vehicle stability making vehicle response due to driver inputs unpredictable. It was determined that closed loop control was critical for vehicle dynamics systems at high speeds.

Integrated vehicle dynamics control involving several active chassis control systems is now the focus of work in vehicle dynamics control systems. Most systems involve the integration of the available active control components under the authority of a supervisory controller. The goal is to determine the optimal coordination of the different actuators on a vehicle [26].

2.3 ELECTRIC VEHICLE CONTROL

Electric vehicles present a unique opportunity for the application of torque vectoring. Where previously tractive and braking torques were generated by separate actuation systems i.e. the engine and the braking system respectively, electric motors can produce both types of torque. Novel powertrain layouts are being proposed utilizing individually controlled motors for each wheel station. These architectures are enabling innovation in the field of electric vehicle torque vectoring and a great deal of work is being conducted

with implementations on several experimental vehicles. With this new found freedom in torque distribution optimal distribution of driving and braking torque has been the focus of many studies.

Yamakawa and Watanabe [27] presented an optimal method for determination of electric motor torque for electric vehicles with independent motors at each wheel station under steady state conditions. Optimal torque on each wheel for a four-wheeled vehicle was obtained for several driving conditions. The authors observed that optimal torque distribution improved driving on an incline and that a combination of steering angles and torque distribution has the potential to reduce energy consumption while cornering. It was also concluded that straight motion over flat ground did not require optimal torque distribution as driving all wheels at the same velocity ensured this automatically and that distributing wheel torque based on vertical load ratio provided proper torque to each wheel.

Jalali et al. [28] developed an integrated control strategy utilizing a torque vectoring controller (developed in [29]) and genetic fuzzy active steering controller for four-wheeled electric vehicle equipped with directly driven in-wheel hub motors. The active steering controller first attempts to stabilize the vehicle without the use of the torque vectoring controller. Torque vectoring support is gradually activated as the active steering angle reaches its maximum value of three degrees as in Figure 2-5 using a Gaussian activation function.

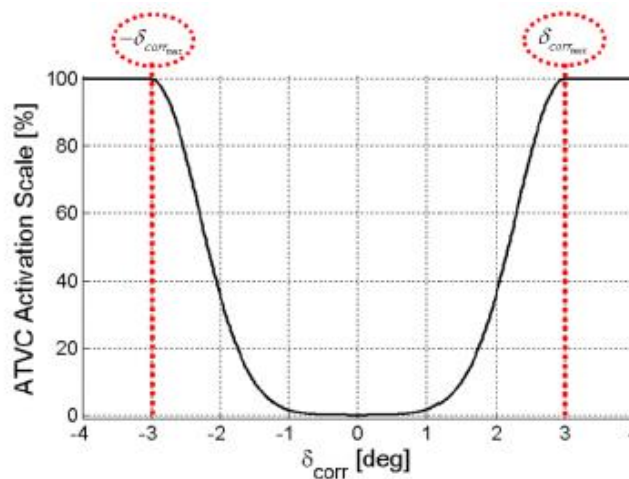


Figure 2-5 Activation function for Torque Vectoring as a Function of Active Steering Angle [28]

The study concluded that the continuously active front steering controller was not disruptive to the driver. The combined control strategy implementing the proposed activation function was proven effective as compared to individual actuation of each control system.

Siampis et al. [30] proposed a constrained optimal control method to control vehicle speed yaw rate and side slip for vehicle stability using rear wheel torque for an electric vehicle. Two model predictive control (MPC) strategies are proposed. One which uses left and right rear wheel torques as inputs and one that uses rear wheel slips as inputs. These two strategies are evaluated against a linear quadratic regulator strategy. The study concluded that there was no visible performance increase when including wheel torque as an input as opposed to wheel slip controller even though there was a noticeable increase in computation time. The MPC controller achieved significantly lower side slip angle and yaw rate values.

Li et al. [31] proposed a tyre force distribution for yaw rate and vehicle side slip angle control. The upper controller determined the desired longitudinal and lateral forces for each wheel. The lower controller distributed the desired forces between the individual steering actuator and motor for each wheel. An inverse Dugoff tire model is used to calculate the desired slip angle and longitudinal slip values. Individual proportional-integral (PI) controllers are used to control the individual actuators using the error between actual and desired values. The gains of the PI controllers are optimized using a genetic algorithm.

Bünthe et al. [32] presented a concept for an electric vehicle with two independent electric motors to power the two rear wheels independently. Yaw rate feedforward and feedback control is used to obtain a neutral steering vehicle. Yaw rate feedback is based on the inverse disturbance observer design developed in [33]. Anti-windup compensation is included in the feedback portion of the controller. The system was tested on an actual vehicle on dry asphalt and a frozen lake. Good performance is claimed although only a small portion of the results are included.

A review of individually controlled electric motors for torque vectoring and its effect on a baseline all-wheel drive (AWD) four-wheeled vehicle was conducted in [34]. The possibility of controlling a vehicle's dynamic characteristics in steady-state and transient

conditions is explored. Figure 2-6 represents two possible modifications to a baseline vehicle through torque vectoring of individual wheels.

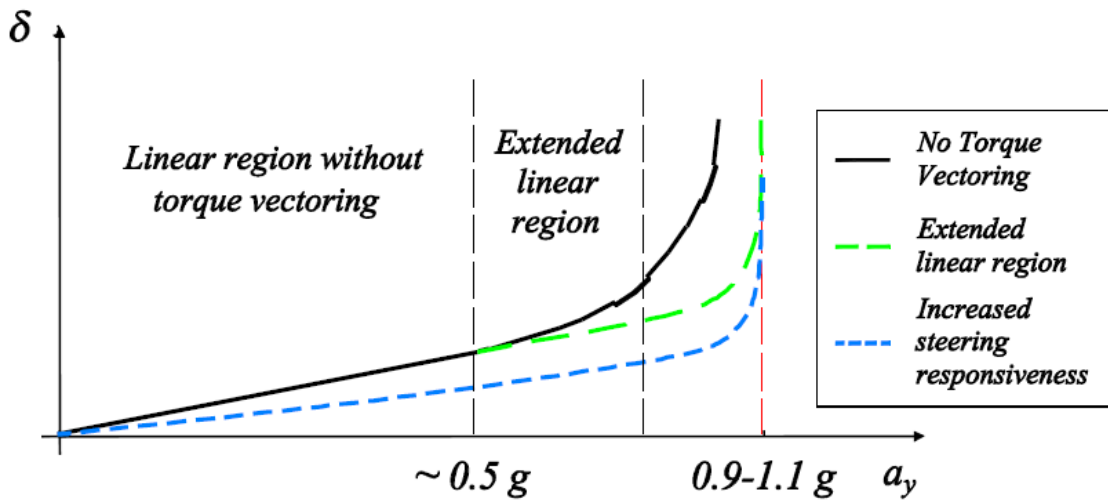


Figure 2-6 Potential Understeer Gradient Alternatives through torque vectoring via individual electric motors [34]

The linear response of the vehicle can be extended as shown with the green dashed line. Conversely, the understeer gradient can be reduced to enhance vehicle responsiveness (blue dashed line). In both cases, the maximum achievable lateral acceleration is increased for both torque vectoring options. The authors suggested that individual motor control could minimize the variation of vehicle cornering behaviour while accelerating and braking at different rates. The study concluded that individual electric motor control on an AWD vehicle allows for the design of the vehicle transient and dynamic behaviour through active control as opposed to classic physical vehicle parameters such as weight distribution and suspension properties.

Ivanov et al. [35] drew the similar conclusions as [34] with emphasis on all terrain electric vehicles. An offline optimization strategy was proposed for generation of the target understeer gradient. The work showed that torque vectoring control can provide positive results to issues of off road mobility such as “*minimization of the kinematic discrepancy, the reduction of slip losses and the improvement of rolling and obstacle resistance*”.

De Novellis, Sorniotti et al. [36] presented a feedback and feedforward direct yaw moment controller for continuous yaw moment control. A side slip based yaw moment contribution

was activated when vehicle side slip passed a certain threshold. The goal was to allow for the continuous modification of the vehicle understeer characteristic and increase yaw and side slip damping during transients. Experimental results were conducted on a fully electric vehicle demonstrator with two independent front axle electric motors. Results were compared to those of a friction brake-based system using the same control algorithm. The study concluded that direct yaw moment control allows for important changes to vehicle cornering behaviour.

2.4 MULTI-WHEELED VEHICLE CONTROL

Work related to multi-wheeled vehicles is far less developed than four-wheeled vehicle studies. Similar principles to those used in four-wheel vehicles are used in the application of active steering and torque vectoring control for multi-wheeled work. A desired model is used for reference values and the various control strategies used in four-wheeled work including fuzzy logic, PID, LQR and sliding mode control are developed for use in the multi-wheeled case. Lower controller allocation strategies include simple differential distribution to advanced optimal control strategies.

Jackson and Crolla [37] presented a controller for a 6 x 6 hybrid electric off road vehicle with hub mounted electric motors at each wheel. Individual wheel torque control was implemented to improve vehicle stability while cornering through fuzzy logic yaw rate control. Proportional-derivative traction and anti-lock braking controllers were also implemented.

Chen et al. [38] developed an active second and third axle steering linear quadratic regulator (LQR) controller for a six-wheeled vehicle. An et al. [39] proposed a LQR to control all three axles based on steering wheel angle and vehicle speed. This LQR work was continued in [40], where the desired yaw rate was based on a six-wheeled vehicle and not a four-wheeled vehicle as in [39]. The continued work included yaw rate and side slip angle control to improve cornering through independent control of all six wheel angles. The controller was implemented on a scale six-wheeled vehicle.

Kim et al. [41] and [42] presented a controller for a six-wheeled vehicle. The vehicle was powered by in-wheel motors at all wheel stations. The front and middle wheels were equipped with steer-by-wire systems. Sliding mode control was used for yaw rate control based on a reference model. Optimal control theory based on individual tire friction ellipses was used to distribute tire longitudinal and lateral forces in order to apply the yaw moment and desired longitudinal force from the upper controller. A 24 degree of freedom full vehicle model was used to evaluate controller performance. Desired yaw rate was determined using a steady state bicycle model of the vehicle in question combined with a first order transfer function. Desired yaw rate was constrained as a function of the tire-road friction relationship as proposed in [43]. Friction circle and tire force estimation were developed. Simulation of a double lane change was conducted. Improvement in vehicle yaw rate error and side slip angle were observed. Lee [44] conducted simulations using the developed controller with model and hardware in the loop on double lane change, fishhook and slalom tests. In all cases, stability was improved. Kim et al. [45] applied the controller to an eight-wheeled vehicle. Steering control was applied to the first and second axles and torque distribution was controlled at all eight wheels.

Ragheb [46] developed a torque distribution controller for an eight-wheeled off road vehicle equipped with a combustion engine and mechanical torque vectoring differentials. A finite element tire model was developed and the TruckSim full vehicle model was validated against actual vehicle data. PID feedback control was used to track yaw rate and lateral acceleration error to determine the total inter-axle (left-right side) torque differential required. A fuzzy slip control system was also proposed. Simulations of several standard maneuvers were conducted. In all cases, vehicle stability was improved.

2.5 H_∞ CONTROL

Robustness to external disturbances, signal noise and modeling inaccuracies is critical in control system design [47]. Classic control theory often refers to single input single output systems where robustness is achieved through the design of proper phase and gain margins [47]. In real applications, often the plant to be controlled is non-linear and consists of multiple inputs and multiple outputs (MIMO). Non-linear control techniques, such as

sliding mode, exist but they are often difficult to tune for good performance [48]. Linear control methods are more commonly used to control non-linear systems [48]. H_∞ control is a linear control technique that can be used for MIMO systems. H_∞ controller synthesis involves an optimization problem cast in the frequency domain. Frequency dependent weighting functions are used to shape the cost functions for various closed loops transfer functions of a particular plant to be controlled. Once synthesis is complete, an H_∞ controller based on the weighting functions is obtained. H_∞ was seen as an alternative to linear quadratic Gaussian controllers (LQG) which could sometimes not be robust enough for practical use [13]. Robustness to unmodeled dynamics in vehicle control systems is critical [49]. Goggia et al. [50] discussed the importance of stability and noise rejection in vehicle dynamic control claiming that PID was not well suited for active torque vectoring because it could not provide precision reference tracking while simultaneously ensuring stability and disturbance/noise rejection. H_∞ control has the ability to be robust to uncertainties while guaranteeing system stability and disturbance/noise rejection. Mixed sensitivity H_∞ synthesis can be employed for good reference tracking and limiting control signal magnitudes [47]. This strategy is used extensively in vehicle control studies.

A vehicle is a system whose dynamics are non-linear. Tire characteristic, road surface, physical vehicle properties (suspension, mass, inertia, etc...) and forward speed of the vehicle in question are all sources that contribute to the non-linear nature of a vehicle's behaviour. The dependence of a vehicle's response on these parameters make vehicle control systems good candidates for linear parameter varying (LPV) H_∞ techniques. LPV methods are appropriate for use in cases where parameter uncertainties are large [47]. Gain scheduling LPV control formulate the stability and performance of the closed-loop system (plant and H_∞ controller) as convex optimisation problems defined as linear matrix inequalities [48]. This is of particular interest as vehicle yaw damping varies with vehicle speed [49].

A great deal of work has been conducted using H_∞ control, including LPV methods, in the field of vehicle dynamic control particularly when the coordination of multiple actuators is required. Good results have been obtained for active steering, torque vectoring and integrated controllers.

2.5.1 H_∞ Active Steering

Horiuchi et al. [51] proposed a two degree of freedom active front and rear wheel steering controller to match desired yaw rate and lateral acceleration responses for a four-wheeled vehicle. Feedback control was achieved using a mixed sensitivity H_∞ controller. Feedforward control was designed based on a neutral steering vehicle to obtain the desired responses to the command signal. The proposed controller was installed on a test vehicle and good referencing tracking was observed.

Lv et al. [52] proposed a yaw rate tracking controller that specified the front and rear steering angle for a four-wheeled vehicle. The objective of the controller synthesis was to reduce peak values of yaw rate, side slip angle and lateral acceleration. The H_∞ controller was compared to a zero side slip feedforward only controller. The feedforward controller exhibited understeer.

Güvenç et al. [53] developed a two degree of freedom robust steering controller for yaw rate tracking. An additional front steering angle was added mechanically to the driver front steering angle. Corrective steering action was only taken at high frequency. Low frequency driving is left to the driver. A LPV H_∞ controller scheduled using vehicle forward speed and road friction coefficient is developed. Mixed sensitivity weighting functions were used. Controller performance was demonstrated using split μ braking maneuver. Hardware in the loop simulation performance of the proposed controller was presented in [54].

2.5.2 H_∞ Torque Vectoring

Canale et al. [55] proposed a H_∞ controller for a four-wheeled vehicle equipped with an active differential that tracked desired yaw rate only. The two-part controller was composed of feedforward (to enhance system transient performance) and feedback (to guarantee robust stability) components. An additive uncertainty model was added to the nominal plant during controller synthesis. It was generated by running simulations of a fourteen DOF vehicle model in various events while varying different vehicle parameters. The developed controller was tested on various maneuvers. The effectiveness of the proposed controller was demonstrated.

Kaiser et al. [56] proposed a LPV gain scheduled H_∞ controller for a four-wheeled electric vehicle with two independent electric motors on the front axle with yaw rate tracking. The LPV controller was scheduled using vehicle speed and yaw rate. The focus of the work was the implementation of an integrated torque slip limiter and comparison between two such strategies was done on a modified ISO maneuver. This work was continued in [48] where the controller was implemented on a test vehicle. Test vehicle results concluded that the controlled vehicle displayed faster reaction times and that the oversteering tendency of the vehicle was reduced.

Liu et al. [57] presented a mixed sensitivity LPV H_∞ controller for a hybrid electric vehicle. A two DOF controller gain scheduled using vehicle speed and vehicle speed squared was developed. Yaw rate tracking was used for feedback control. The controller was compared to a LQG controller in two different maneuvers to measure reference tracking and disturbance rejection. The H_∞ controller demonstrated superior performance to that of the LQG controller.

Recently, two other types of H_∞ controllers have been implemented for torque vectoring on four-wheeled vehicles. Yin et al. [58] presented a robust controller for independent torque control of a four-wheeled electric vehicle. A different type of H_∞ control, μ synthesis control, was proposed. CarSim simulations were conducted to demonstrate the effectiveness of the controller when vehicle weight and inertia were varied by 20%. Lu et al. [49] proposed H_∞ loop shaping for the torque vectoring control of a four-wheeled electric vehicle with four individually controller electric motors. Experimental results were demonstrated on a test vehicle. H_∞ control was compared to PI control. H_∞ control was shown to be more robust to a variety of operating conditions. It remains to be seen if these and other H_∞ techniques become widely adopted in the future.

2.5.3 H_∞ Integrated Control

Gaspar et al. [59] presented an integrated fault tolerant LPV H_∞ controller for a heavy vehicle. Active braking, active suspension and active anti-roll bars were coordinated. Two separate closed loop controllers are proposed. The roll prevention controller monitors yaw and roll and utilized the braking, anti-roll bars and suspension forces as controller outputs.

The active suspension controller utilized suspension forces to control ride quality. Scheduling parameters used were forward vehicle speed (active suspension controller), lateral load transfer (roll prevention controller) and a fault parameter. Results with the proposed controller with and without a fault in the active anti-roll bars are published for a 70 kph step steer maneuver with a ten centimeters bump in the middle of the maneuver. No comparison was made with the uncontrolled vehicle to demonstrate improvement in vehicle dynamics.

Poussot-Vassal et al. published a paper [60] which presented two variations of an approach to design an LPV gain scheduled feedback H_∞ controller used active additive front steering and brake torque vectoring to control yaw rate. The first strategy involved using the braking actuator as the primary means for yaw rate control and only involving the steering actuator when necessary. The controller was gain scheduled using steering monitor and braking torque parameters. The second strategy aimed at using the steering action and limiting the use of the braking actuator only when the vehicle limits were reached using a braking activation parameter. This parameter was determined using the phase plane of β and $\dot{\beta}$. Brake torque was distributed by transferring brake force between the wheels on the rear axle. Simulations were conducted in single lane change and double lane change maneuvers comparing a non-gain scheduled version of the developed controller against the gain scheduled controller. The gain scheduled controller demonstrated superior performance. This work was extended by Selmanaj et al. [61] to include rear steering with active brake torque vectoring and, when necessary, front steering. It was found that rear steering became more relevant in low friction situations.

Doumiati et al. [62] developed a gain scheduled H_∞ controller controlling vehicle yaw rate through actuation of the front steering and rear brakes. Active steering was involved at all times for steerability enhancement and differential braking was actuated when the vehicle reached its handling limits. The scheduling parameter were a function of the vehicle side slip angle and rate. The desired yaw rate signal was limited according to [43].

Poussot-Vassal [63] proposed several LPV gain scheduled based methodologies to improve vehicle comfort and safety using suspension, braking and front steering control. A novel LPV semi-active suspension strategy was proposed. Several coordinated controller

frameworks were also proposed involving different combinations of suspension, braking and steering actuation. Simulations were conducted for the different proposed coordinated controllers.

2.6 FEEDFORWARD REAR WHEEL STEERING

Feedforward rear wheel steering control as discussed in this thesis refers to a control algorithm that outputs a rear wheel steering angle as a function of the front steering wheel angle. Feedback control will be accomplished using the proposed H_∞ controller and will not be covered in this section. Instead, the focus will be on feedforward methods, specifically, those applied to increase vehicle maneuverability at low speeds. The chosen control system will be used to reduce vehicle turning circle.

Furukawa et al. [64] conducted a review of four-wheel steering (4WS) studies in 1989. 4WS feedforward and feedback control configurations were reviewed. Although much work has been conducted since then with respect to feedback control, the feedforward portion of the review remains relevant. The study specifically addresses the improvement of vehicle maneuverability at low speed. Two methods are covered: the zero side slip method (ZSS) and steer angle dependent 4WS.

2.6.1 Zero Side Slip (ZSS) Method

The transfer function of a steady state two DOF bicycle model with front and rear wheel steer angles is derived. By eliminating yaw rate and setting the steady state side slip angle to zero, a speed dependent ratio relating the front and rear steering angles defined as the zero side slip method is obtained:

$$k = \frac{-b - \frac{ma}{C_r l} U^2}{a + \frac{mb}{C_f l} U^2} \quad 2-1$$

U is the vehicle forward speed, C_f and C_r are the front and rear tire cornering stiffnesses, a and b represent the distance of the front and rear axle from the center of gravity respectively and l is the wheelbase of the vehicle. This relationship is visualised in Figure 2-7.

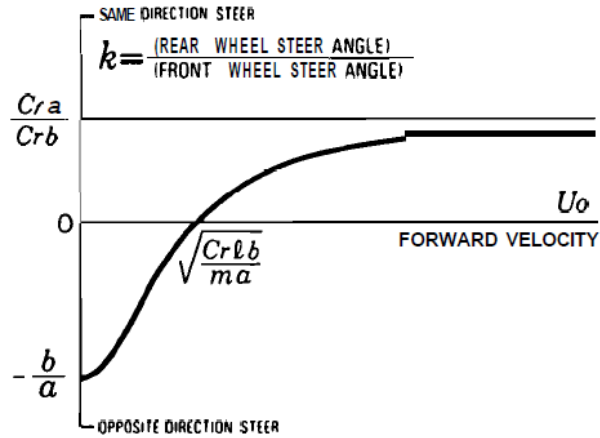


Figure 2-7 Zero Side Slip (ZSS) 4WS Relationship [64]

2.6.2 Steer Angle Dependent 4WS

The steer angle dependent 4WS system determines the steering direction of the rear wheels based on the magnitude of the steering wheel angle. When a small front steering angle is detected, the rear wheels are turned in the opposite direction of the front wheels. A large front steering angle results in the rear wheels being turned in the same direction as the front wheels [64]. This relationship is shown in Figure 2-8. There is substantial risk in using steer angle dependent 4WS relationship in high speed limit cornering maneuvers where large steering inputs may be requested by the driver.

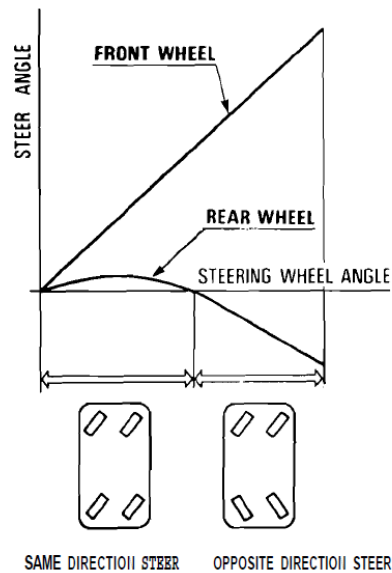


Figure 2-8 Steer Angle Dependent 4WS Relationship [64]

Lin [65] classified rear steering control algorithms into several categories: proportional control, first-order delay control, first-order lead control, zero side slip control and ideal/advanced four-wheel steer control where both front and rear wheels are controlled. At the time, the author claimed that the zero side slip steering controller provided superior results except for its understeer characteristic at high speeds.

Bayar and Unlusoy [66] applied zero side slip 4WS [12] and yaw velocity feedback [67] four-wheel steering strategies to vehicles with three and four axles. It should be noted that the center of gravity of the models used in the study was located between the first and second axles in all cases. Step steer simulations conducted at speeds between 60 and 90 kph for the three and four axle vehicles supported previous findings in the literature for two axle vehicles that ZSS and yaw velocity feedback strategies both promote heavy understeer at higher speeds resulting from low lateral acceleration and yaw rate response when only the first and last axles were steered. At all speeds, the yaw velocity feedback method resulted in lower yaw rate and lateral acceleration responses than the zero side slip 4WS strategy for the three axle vehicle. A strategy of steering the middle axles as a function of the front steering angle in tandem with the yaw velocity feedback method was proposed which greatly increased the lateral acceleration and yaw rate responses with both the three and four axle vehicles. Results at all simulated vehicle speeds for the four axle vehicle are shown in Figure 2-9.

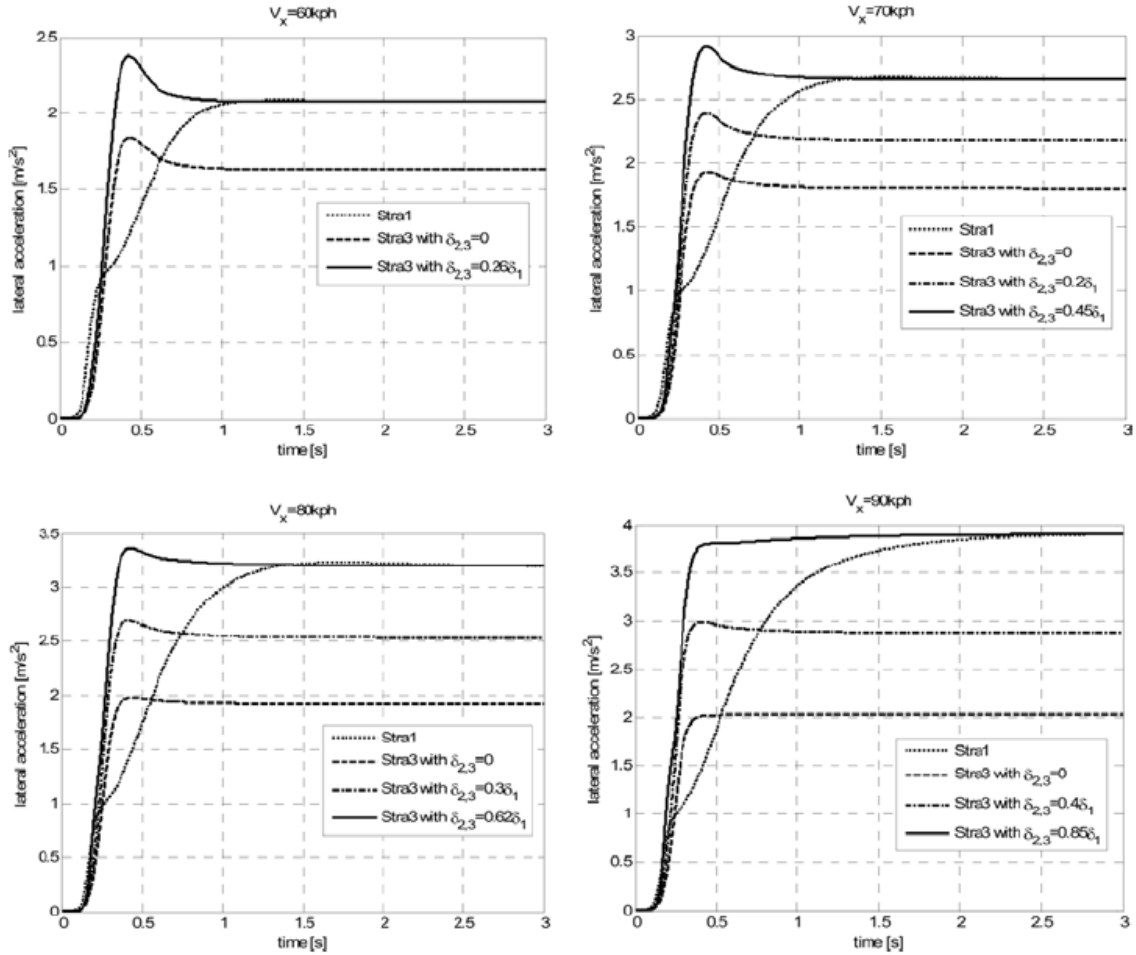


Figure 2-9 Yaw Velocity Feedback for Four Axle Vehicle While Varying the Middle Axle Steering Angle Ratio as a Function of Front Steering Angle [66]

2.7 SUMMARY

Torque vectoring and rear wheel steering have been successfully implemented in production vehicles and multiple researchers have confirmed the dynamic improvements offered by the two systems. The most common actuation methods have traditionally been brake torque vectoring and active front steering as these systems are more easily incorporated on traditional vehicles. As electric vehicles become more popular, individual wheel torque manipulation has become the focus of much research. A great deal of work has been conducted showcasing the dynamic improvements offered by the active torque vectoring and active steering systems regardless of actuation method used. It is clear that the two systems can have a positive effect on vehicle stability and maneuverability on

vehicles with multiple axles though the majority of work has been conducted using four-wheeled vehicle models [37]-[46].

Various linear control methods have been proposed to control non-linear vehicle responses utilizing feedforward, feedback control or both. Positive results have been demonstrated by all studies. The most popular methods of control include PID, fuzzy logic, MPC, LQR, sliding mode and H_∞ . Several other methods have been studied including combinations of those mentioned above. Incorporation of both feedforward and feedback control has been found to improve controller transient response. Feedforward and feedback control will be incorporated in this work. The literature still has not explicitly identified the “best” control system for vehicle dynamic control. There remains no clear all-encompassing study comparing all the different controllers at once demonstrating simulation or experimental results on one particular vehicle. However, several studies conclude that due to the uncertainties involved with vehicle dynamics, robust control strategies should be used.

H_∞ control is well suited to the control of multiple actuation systems and exhibits the robustness and disturbance rejection required for this application. LPV H_∞ control has been widely used for multiple input multiple output systems with good results. A vehicle speed scheduled LPV H_∞ controller is appropriate in this application as it will directly address the non-linear and speed dependent nature of vehicle dynamic responses and has been proposed for this reason.

Due to the fact that active steering is not effective at high lateral accelerations, torque vectoring will be used as the main actuation system for while rear wheel steering will intervene at higher frequencies as proposed by [53, 60]. This strategy has shown good results and allows for an elegant solution to control allocation of an over actuated system avoiding the use of complex online optimization to distribute tractive and steering forces in the lower controller.

The lower controller will remain a simple torque differential distribution between wheels on an axle for ease of implementation and to isolate upper controller performance as the focus of this study. Only the two rear axles will be manipulated by the lower controller to apply torque vectoring to the multi-wheeled vehicle following the findings in [23]. This

strategy does not involve any online optimization process which allows for a low computational cost and is therefore more suitable for real-time control applications [62].

Bicycle models of the vehicle to be controlled are most often used as reference models. Yaw rate, side slip angle, lateral acceleration or a combination of several have been used as controller inputs. An overwhelming amount of studies has successfully implemented controllers utilizing yaw rate tracking including several LPV H_∞ controllers. Yaw rate manipulation directly influences lateral acceleration and can be measured on board a vehicle relatively easily [55]. Yaw rate tracking will be implemented in the proposed controller. Desired yaw rate saturation based on road friction coefficient proposed by [43] and implemented in [41, 45, 55, 57, 68] will be used.

Turning circle reduction will be implemented using the zero side slip speed dependent method. Feedforward control has been proven in production vehicles and steer angle dependent 4WS does not seem appropriate for this application.

CHAPTER 3

VEHICLE MODELS AND SIMULATION ENVIRONMENT

3.1 INTRODUCTION

This chapter will introduce the various vehicle models used. A summary of the models is included in Table 3-1:

Table 3-1 Summary of Vehicle Models

MODEL DESCRIPTION		DOF	USE
1	TruckSim Full Vehicle Model (Non-linear)	23	Simulation of various events to evaluate controller performance
2	Bicycle Model with RWS / External Yaw Moment (Linear)	2	Differential equations for lateral and yaw motion used as plant for H_∞ controller synthesis
3	Bicycle Model no RWS / External Yaw Moment (Linear & Steady State)	2	Desired yaw rate calculation combines steady state yaw rate as a function of vehicle speed and steering angle with a 1 st order lag
4	Bicycle Model with RWS / External Yaw Moment (Linear & Steady State)	2	Steady state side slip angle used in zero side slip (ZSS) method for turning circle reduction and maneuvering at low speeds

3.2 TRUCKSIM FULL VEHICLE MODEL

3.2.1 Vehicle Parameters

A 23 degree of freedom (DOF) full vehicle model is used for dynamic simulation. TruckSim© Mechanical Simulation™ software uses 177 ordinary differential equations to calculate the vehicle's kinematics and dynamics. The model's sprung mass is assumed to be a rigid body with six DOF. The steering system has one DOF. Each wheel has two degrees of freedom, namely vertical and spin, for a total of 16 DOF for the eight wheels

for the fixed third and fourth axle vehicle. The model is based on the actual combat vehicle shown in Figure 3-1.

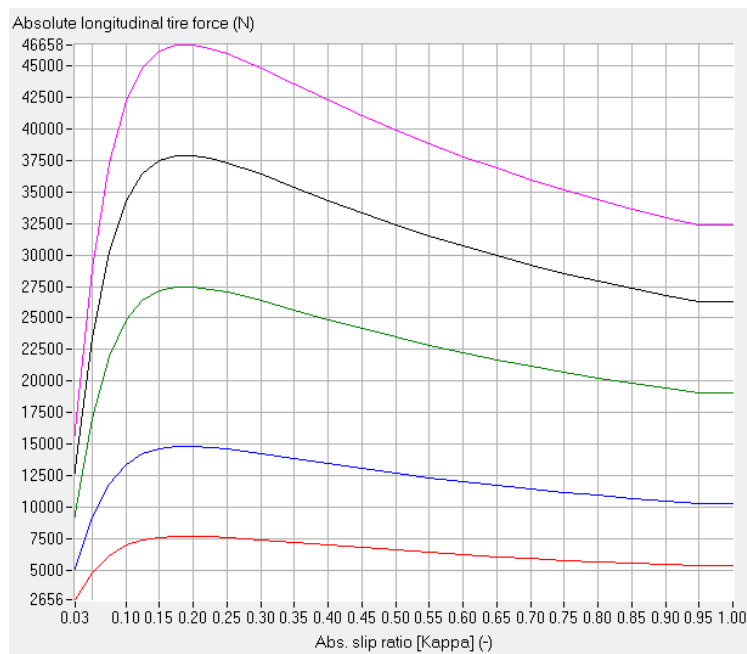


Figure 3-1 (a) Actual Vehicle [69] (b) TruckSim Model

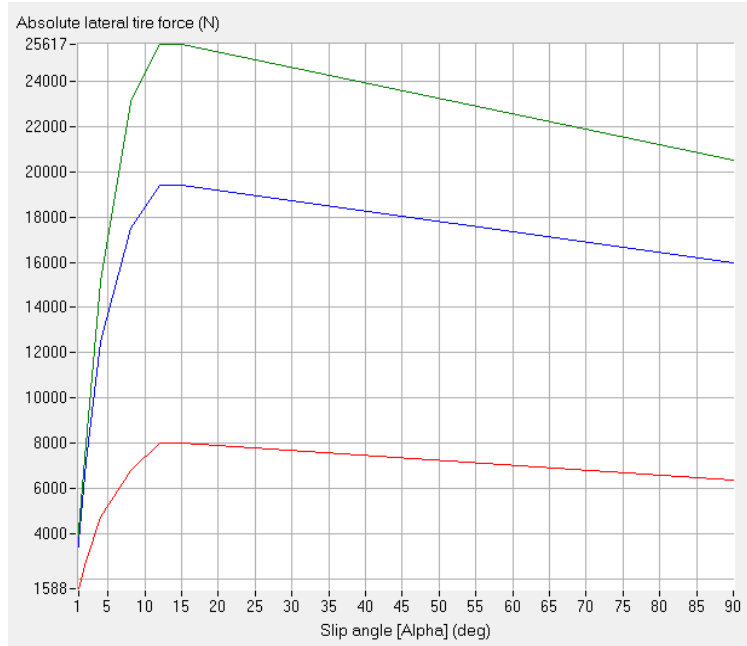
Relevant vehicle parameters are not presented in this thesis as they are considered to be classified information.

Off road tire measured manufacturer data is incorporated in the model via lookup tables. Tire longitudinal forces as a function of slip ratio and tire lateral force as a function of slip angle are shown in

Figure 3-2.



(a)



(b)

Figure 3-2 F_x vs Slip Ratio (a) and F_y vs Slip Angle (b)

The vehicle is equipped with independent hydropneumatic suspension at each wheel station. The corresponding force deflection curve is shown in Figure 3-3. Mechanically linked steering components allow for steering of both the first and second axes of the vehicle. Air brakes are used to slow the vehicle.

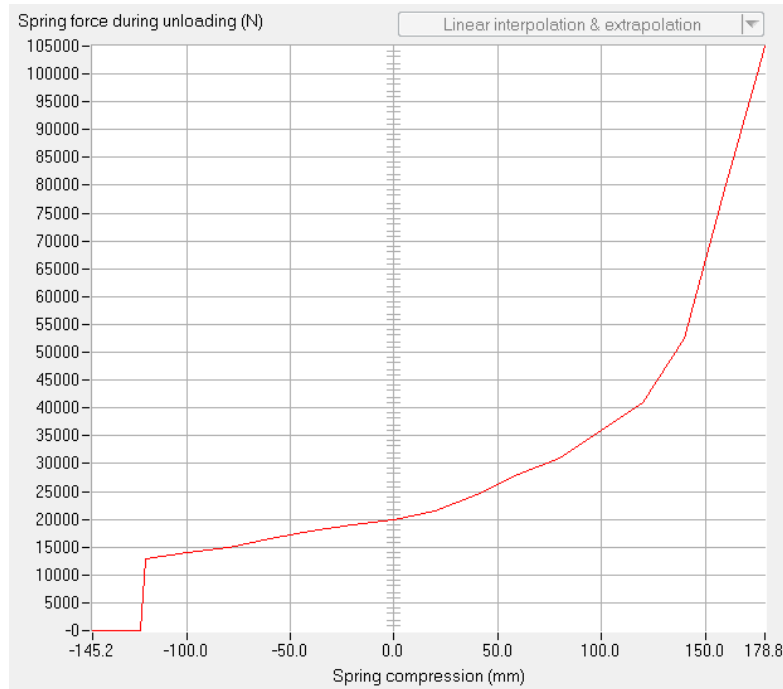


Figure 3-3 Hydropneumatic Suspension Force Deflection Curve

3.2.2 Vehicle Model Validation

Ragheb [46] validated the vehicle model using four different standard test events: double lane change constant step slalom and J-turn at different speeds as shown in Table 3-2. Inputs to the virtual model were the experimentally measured actual vehicle speed and steering wheel angle time histories.

Table 3-2 Test Courses Used for Validation in [46]

No.	Test Course	Vehicle Speed	Additional Test Data
1	Double Lane Change (NATO AVTP-1 03-160W)	40,53,72,81 km/h and maximum	-----
2	Constant Step Slalom (NATO AVTP-1 03-30)	40,53,60 km/h and maximum	30 m cone spacing
3	J-Turn (75ft radius)	30,35,40,45,50km/h	-----
4	Turning Circle (4x8 & 8x8)	Crawling	-----

Note: vehicle model and actual vehicle were both equipped with a standard internal combustion engine (ICE) and conventional powertrain during the validation.

3.2.3 Electric Powertrain

The full vehicle model's engine and powertrain were replaced with an electric powertrain. The electric powertrain is externally modelled in Simulink and has been developed using preliminary parameters. The model consists of eight individual electric motors each coupled to a gear reducer with one fixed gear ratio at each wheel station. Table 3-3 lists the powertrain characteristics used.

Table 3-3 Electric Powertrain Parameters

POWERTRAIN PARAMETERS	VALUE
Battery Voltage	400 V
Motor Type	Permanent Magnet AC
Max Power Draw from Batteries	150 kW
Max Current Draw	375 A
Maximum Motor Speed	6000 rpm
Electric Motor Gear Reduction Ratio, GR	10:1
Motor Spin Inertia, I_{motor}	1 kg·m ²

The assumptions used when modelling the electric powertrain are as follows:

- Max current received by each individual motor
- Torque output identical when motor is run backward (negative current)
- Spin inertia of motor and wheels included in powertrain model
- Unsprung mass unchanged from baseline ICE vehicle

3.2.3.1 Electric Motor Lookup Table

A three dimensional lookup table was developed using the electric powertrain parameters. Motor speed vs torque curves at varying current levels for both negative and positive current signals are shown in Figure 3-4.

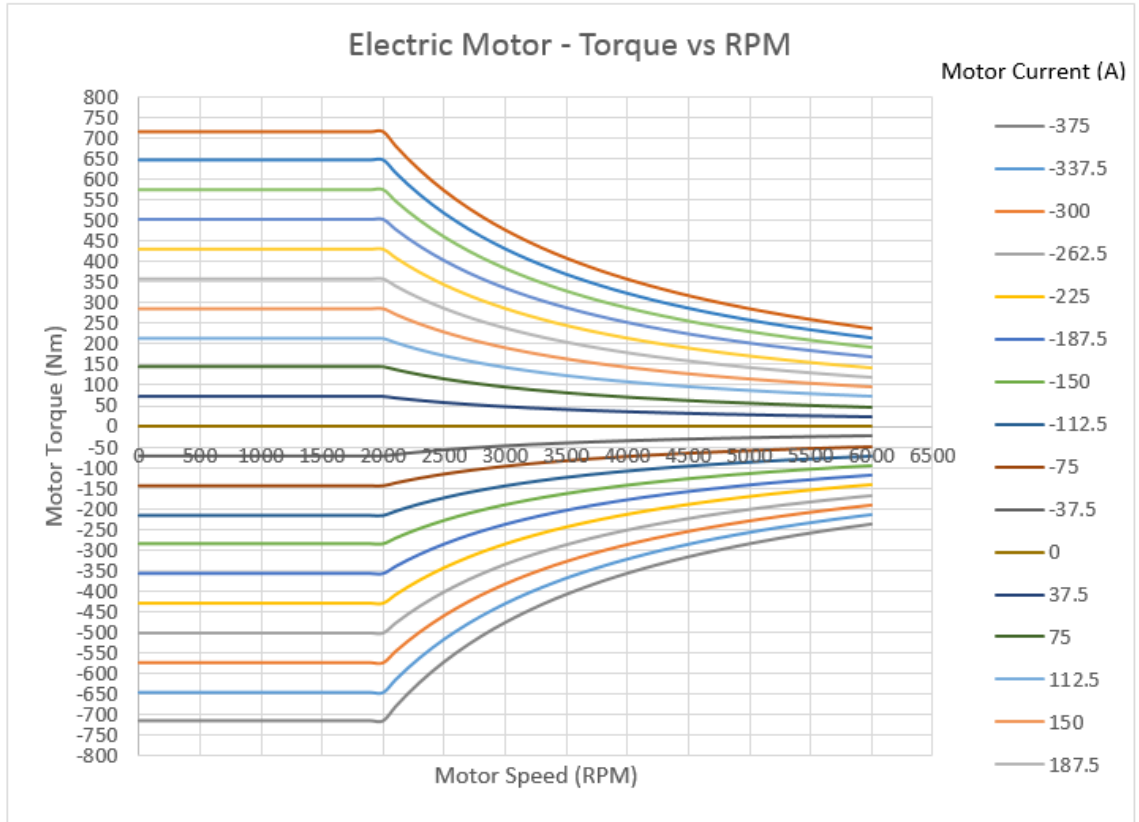


Figure 3-4 Electric Motor Specification Curve

Equations 3-1 to 3-5 are used to model the electric powertrain in Simulink. Electric motor current required and wheel rpm are input to the lookup table to produce a corresponding motor torque:

$$T_{m,NET} = T_{motor} - I_{motor}\alpha_{motor} \quad 3-1$$

$$T_{m,NET} \cdot GR - F_x \cdot r_{effective} = I_{wheel}\alpha_{wheel} \quad 3-2$$

$$\alpha_{wheel} = \frac{T_{m,NET} \cdot GR - F_x \cdot r_{effective}}{I_{wheel}} \quad 3-3$$

$$\int \alpha_{wheel} = \omega_{wheel} \quad 3-4$$

$$\omega_{motor} = \omega_{wheel} \cdot GR \quad 3-5$$

I , α , ω , T represent the spin inertia, angular acceleration, angular speed and torque respectively. Subscripts are used to differentiate each of the values between the electric motor and wheel. GR is the electric motor gear reduction ratio and F_x is the tire longitudinal force. This process is presented for one individual electric powertrain model in Figure 3-5.

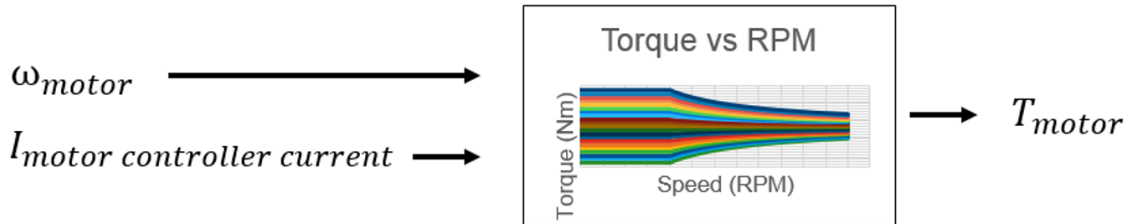
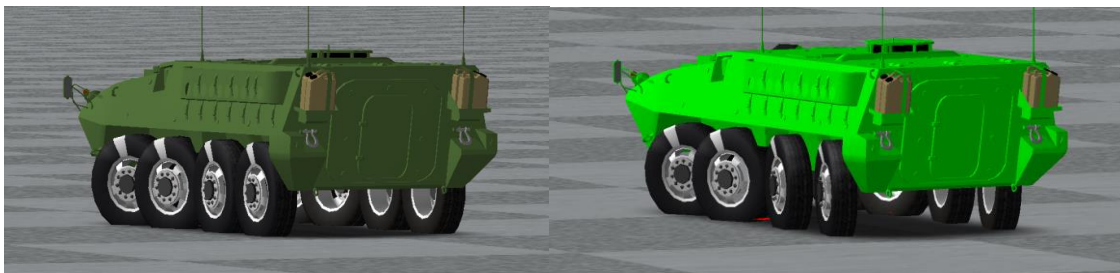


Figure 3-5 Electric Motor Diagram

The full non-linear vehicle model with and without the proposed controller (rear wheel steering (RWS) and torque vectoring capability) are shown in Figure 3-6. They will be compared in various standard test maneuvers in order to evaluate controller performance. The zero side slip (ZSS) turning circle reduction controller will also be tested using this model.



(a)

(b)

Figure 3-6 TruckSim Vehicle Model (a) with fixed 3rd and 4th axles (b) with steerable 3rd and 4th axles

3.2.4 MATLAB/Simulink - TruckSim Co-Simulation

The TruckSim full vehicle model interfaces with the MATLAB/Simulink external powertrain and vehicle dynamics controller in order to conduct simulations of dynamic events. The Trucksim vehicle model is imported into Simulink as an S-function with

various input and output variables specified by the user. Simulink then uses the model output variables calculated by TruckSim at each time step as input signals to the various control blocks as shown in Figure 3-7. The controller block then outputs signals which are fed into the TruckSim model. Vehicle parameters, event settings, Simulink file selection and post processing are performed within TruckSim as shown in Figure 3-8.

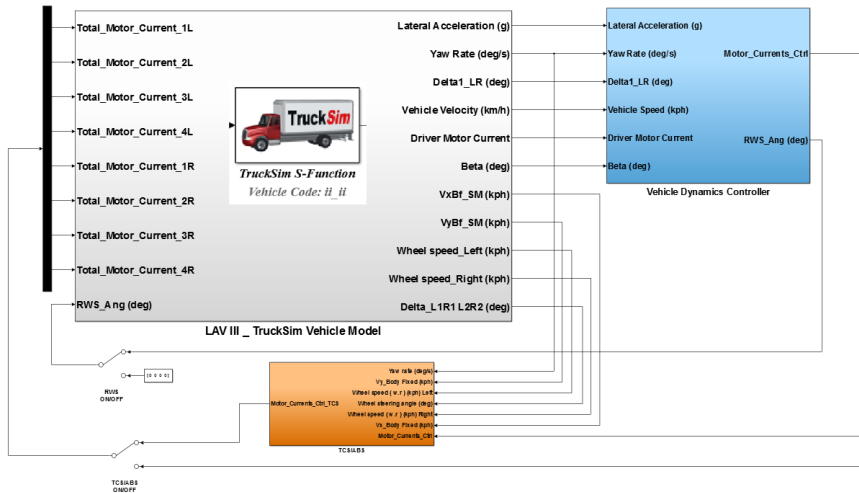


Figure 3-7 Simulink Control Architecture with TruckSim S-function

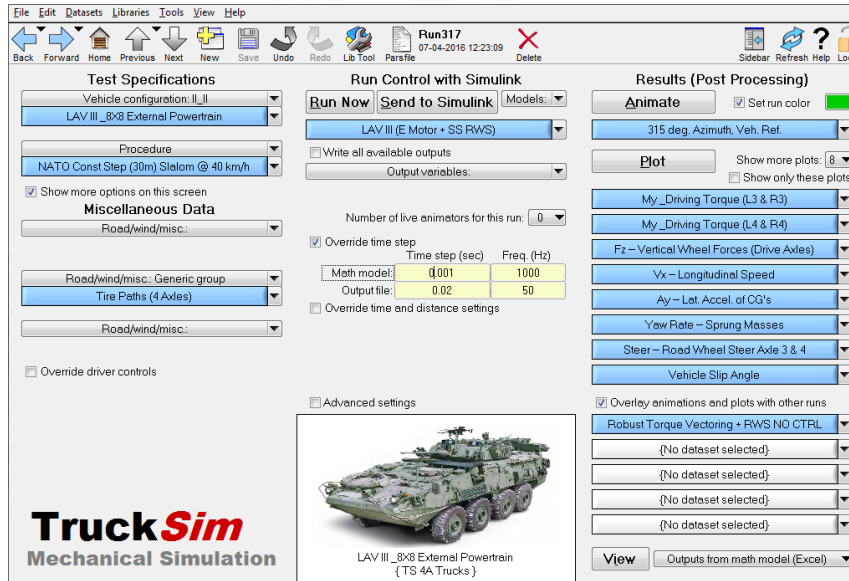


Figure 3-8 Trucksim User Interface

3.3 LINEAR BICYCLE MODEL - H_∞ CONTROLLER SYNTHESIS

A two DOF bicycle model, sometimes referred to as single track model, is used to develop the differential equations defining the linearized plant used for H_∞ controller synthesis. The plant is a simplified version of the actual vehicle and describes the lateral and yaw motion of the 8 x 8 vehicle while neglecting roll dynamics.

Figure 3-9 represents the free body diagram of the model. The left and right sides of the vehicle have been combined into one single track. The center of gravity is represented by a golden circle and is located between the second and third axles. Vehicle forward speed, U , lateral speed, V , and yaw rate, r , are shown acting on the center of gravity. The positive x axis points to the right of the page, the positive y axis points down the page, the positive z axis is directed into the page and yaw moments are clockwise positive as shown in the legend at the top right of Figure 3-9. All forces are depicted in black. Tire slip angles and wheel steer angles are shown in blue and red respectively. Axle distances, $a_{\text{subscript}}$, are measured from the center of gravity to the center of each axle. Third and fourth axle steering, δ_3 and δ_4 , and an external yaw moment at the center of gravity, N , have been included to represent rear axle steering and torque vectoring control systems respectively.

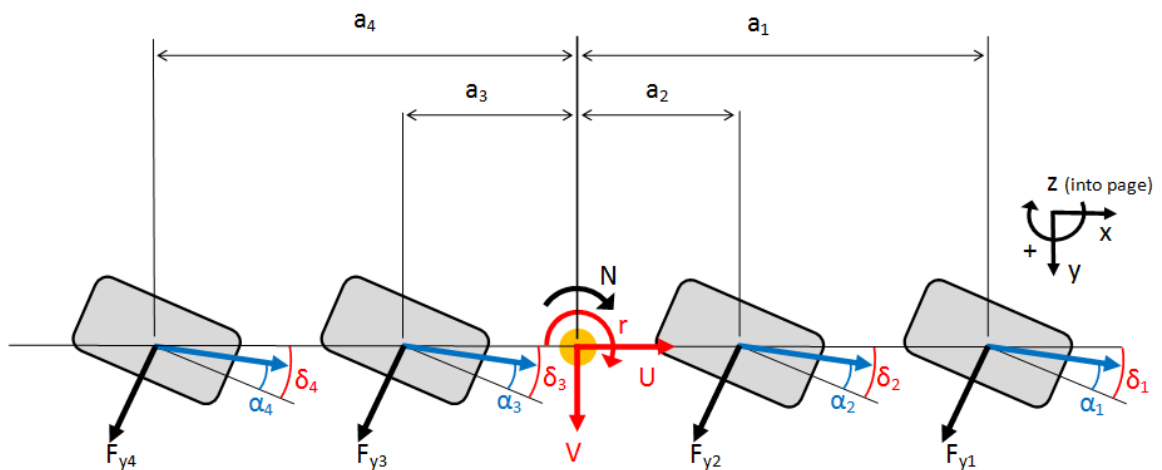


Figure 3-9 Two DOF Bicycle Model with Rear Steering and External Yaw Moment

The assumptions used when constructing the bicycle model are as follows:

- Lateral load transfer is neglected
- Longitudinal load transfer is neglected
- Lateral accelerations are limited to less than 0.4g (tire dynamics assumed linear)
- Effects of suspension geometry are neglected
- Vehicle forward speed is considered a constant ($\sum F_x = 0$)
- Aerodynamic forces are neglected
- Left and right tire cornering stiffnesses are combined for each axle
- Axle steer angles are the average of the left and right wheel steer angles on an axle
- δ_1 represents the average first axle wheel angle and is related to the steering wheel angle through $k_{SW \rightarrow 1}$
- Small-angle approximation is valid for β , all δ and α

Fundamental Equations of Vehicle Motion:

$$\sum F_x = 0 \quad 3-6$$

$$\sum F_y : m(\dot{V} + rU) = F_{y1} + F_{y2} + F_{y3} + F_{y4} \quad 3-7$$

$$\sum M_z : I_{zz}\dot{r} = a_1F_{y1} + a_2F_{y2} - a_3F_{y3} - a_4F_{y4} + N \quad 3-8$$

Tire longitudinal forces and tire slip angle equations are calculated for each axle where $[i = 1:4]$, $[j = 1:2]$ and $[k = 3:4]$:

$$F_{yi} = \alpha_i C_{ai} \quad 3-9$$

$$\alpha_j = \delta_j - \left(\frac{V + a_j r}{U} \right) \quad 3-10$$

$$\alpha_k = \delta_k - \left(\frac{V - a_k r}{U} \right) \quad 3-11$$

Note: C_{ai} represents the axle cornering stiffness and not the individual left or right tire on an axle when used in conjunction with a bicycle model.

Derivation of Lateral Motion Equation

Substituting equations 3-9, 3-10 and 3-11 into 3-7 yields:

$$m(\dot{V} + rU) = C_{\alpha 1} \left[\delta_1 - \left(\frac{V + a_1 r}{U} \right) \right] + C_{\alpha 2} \left[\delta_2 - \left(\frac{V + a_2 r}{U} \right) \right] + C_{\alpha 3} \left[\delta_3 - \left(\frac{V - a_3 r}{U} \right) \right] + C_{\alpha 4} \left[\delta_4 - \left(\frac{V - a_4 r}{U} \right) \right] \quad 3-12$$

$$\dot{V} = -\frac{(C_{\alpha 1} + C_{\alpha 2} + C_{\alpha 3} + C_{\alpha 4})}{mU} V + \left(-\frac{(a_1 C_{\alpha 1} + a_2 C_{\alpha 2} - a_3 C_{\alpha 3} - a_4 C_{\alpha 4})}{mU} - U \right) r + \left(\frac{C_{\alpha 1} \delta_1 + C_{\alpha 2} \delta_2 + C_{\alpha 3} \delta_3 + C_{\alpha 4} \delta_4}{m} \right) \quad 3-13$$

Dividing both sides of equation 3-13 by U and substituting $\dot{\beta} = \frac{\dot{V}}{U}$:

$$\dot{\beta} = -\frac{(C_{\alpha 1} + C_{\alpha 2} + C_{\alpha 3} + C_{\alpha 4})}{mU} \beta + \left(-\frac{(a_1 C_{\alpha 1} + a_2 C_{\alpha 2} - a_3 C_{\alpha 3} - a_4 C_{\alpha 4})}{mU^2} - 1 \right) r + \frac{(C_{\alpha 1} \delta_1 + C_{\alpha 2} \delta_2 + C_{\alpha 3} \delta_3 + C_{\alpha 4} \delta_4)}{mU} \quad 3-14$$

Derivation of Yaw Motion Equation

Substituting equations 3-9, 3-10 and 3-11 into 3-8 yields:

$$\dot{r} = \frac{1}{I_{zz}} \left\{ a_1 C_{\alpha 1} \left[\delta_1 - \left(\frac{V + a_1 r}{U} \right) \right] + a_2 C_{\alpha 2} \left[\delta_2 - \left(\frac{V + a_2 r}{U} \right) \right] - a_3 C_{\alpha 3} \left[\delta_3 - \left(\frac{V - a_3 r}{U} \right) \right] - a_4 C_{\alpha 4} \left[\delta_4 - \left(\frac{V - a_4 r}{U} \right) \right] + N \right\} \quad 3-15$$

Rearranging,

$$\dot{r} = \frac{1}{I_{zz}} \left\{ a_1 C_{\alpha 1} \delta_1 + a_2 C_{\alpha 2} \delta_2 - a_3 C_{\alpha 3} \delta_3 - a_4 C_{\alpha 4} \delta_4 - a_1 C_{\alpha 1} \frac{V}{U} - a_2 C_{\alpha 2} \frac{V}{U} + a_3 C_{\alpha 3} \frac{V}{U} + a_4 C_{\alpha 4} \frac{V}{U} - \frac{a_1^2 C_{\alpha 1} r}{U} - \frac{a_2^2 C_{\alpha 2} r}{U} - \frac{a_3^2 C_{\alpha 3} r}{U} - \frac{a_4^2 C_{\alpha 4} r}{U} + N \right\} \quad 3-16$$

Substituting $\beta = \frac{V}{U}$ and rearranging yields:

$$\begin{aligned} \dot{r} = & -\frac{(a_1 C_{\alpha 1} + a_2 C_{\alpha 2} - a_3 C_{\alpha 3} - a_4 C_{\alpha 4})}{I_{zz}} \beta \\ & - \frac{(a_1^2 C_{\alpha 1} + a_2^2 C_{\alpha 2} + a_3^2 C_{\alpha 3} + a_4^2 C_{\alpha 4})}{I_{zz} U} r \\ & + \frac{a_1 C_{\alpha 1} \delta_1 + a_2 C_{\alpha 2} \delta_2 - a_3 C_{\alpha 3} \delta_3 - a_4 C_{\alpha 4} \delta_4}{I_{zz}} + \frac{N}{I_{zz}} \end{aligned} \quad 3-17$$

The differential equations 3-14 and 3-17 fully describe the motion of the linear bicycle model. The second and third wheel steering angle terms can be eliminated using the following steering relationships:

$$\delta_2 = k_{1 \rightarrow 2} \delta_1 \quad 3-18$$

$$\delta_3 = k_{4 \rightarrow 3} \delta_4 \quad 3-19$$

Substituting equations 3-18 and 3-19 into 3-14 and 3-17 and rearranging into state space form (equation 3-20 and 3-21) yields the H_∞ plant model:

$$\dot{x} = Ax + Bu \quad 3-20$$

$$y = Cx + Du \quad 3-21$$

$$\begin{aligned} \dot{x} &= \begin{bmatrix} \dot{\beta} \\ \dot{r} \end{bmatrix} \\ &= \begin{bmatrix} -\frac{(C_{\alpha 1} + C_{\alpha 2} + C_{\alpha 3} + C_{\alpha 4})}{mU} & -\frac{(a_1 C_{\alpha 1} + a_2 C_{\alpha 2} - a_3 C_{\alpha 3} - a_4 C_{\alpha 4})}{mU^2} - 1 \\ -\frac{(a_1 C_{\alpha 1} + a_2 C_{\alpha 2} - a_3 C_{\alpha 3} - a_4 C_{\alpha 4})}{I_{zz}} & -\frac{(a_1^2 C_{\alpha 1} + a_2^2 C_{\alpha 2} + a_3^2 C_{\alpha 3} + a_4^2 C_{\alpha 4})}{I_{zz} U} \end{bmatrix} \begin{bmatrix} \beta \\ r \end{bmatrix} \\ &+ \begin{bmatrix} \frac{C_{\alpha 1} + k_{1 \rightarrow 2} C_{\alpha 2}}{mU} & \frac{k_{4 \rightarrow 3} C_{\alpha 3} + C_{\alpha 4}}{mU} & 0 \\ \frac{a_1 C_{\alpha 1} + k_{1 \rightarrow 2} a_2 C_{\alpha 2}}{I_{zz}} & \frac{-(k_{4 \rightarrow 3} a_3 C_{\alpha 3} + a_4 C_{\alpha 4})}{I_{zz}} & \frac{1}{I_{zz}} \end{bmatrix} \begin{bmatrix} \delta_1 \\ \delta_4 \\ N \end{bmatrix} \end{aligned} \quad 3-22$$

$$y = r = \begin{bmatrix} 0 & 1 \end{bmatrix} \begin{bmatrix} \beta \\ r \end{bmatrix} + \begin{bmatrix} 0 & 0 & 0 \end{bmatrix} \begin{bmatrix} \delta_1 \\ \delta_4 \\ N \end{bmatrix} \quad 3-23$$

The plant model is composed of two state variables; vehicle side slip angle and yaw rate; $x: [\beta \ r]$; two control variables, fourth axle steering angle and external yaw moment; $u:$

$[\delta_4 \ N]$; plant output, yaw rate; $y: [r]$ and disturbance, front axle steering angle; $w: [\delta_1]$. Vehicle mass, m , yaw moment of inertia, I_{zz} , center of gravity location and steering wheel ratio, $k_{sw \rightarrow 1}$, are identical to the full vehicle model. Due to the linear nature of the model, the tire cornering stiffnesses and the steering kinematic relationship must be linearized. The parameters of the linear bicycle model are not presented as they are considered to be classified information.

3.4 LINEAR BICYCLE MODEL - REFERENCE YAW RATE

3.4.1 Reference Yaw Rate, $r_{desired}$

A first order time delay transfer function in conjunction with a linear two DOF bicycle model's steady state yaw rate response, $\frac{r_{ss}}{\delta_1}$, is used to generate the desired yaw rate, $r_{desired}$. The first order time delay allows control over the vehicle yaw response time through the yaw rate time delay, τ_{yaw} . A time delay of 0.3 seconds was used.

$$r_{desired} = \frac{1}{1 + \tau_{yaw}s} \cdot \frac{r_{ss}}{\delta_1} \cdot \delta_1 \quad 3-24$$

The desired yaw response, $r_{desired}$, is limited using the following relationship presented by [43] and implemented by [41, 45, 55, 57, 68]:

$$r_{desired,bound} = \left| 0.7 \cdot \frac{\mu g}{U} \right| \quad 3-25$$

When the desired yaw rate (equation 3-24) exceeds the yaw rate bound (equation 3-25) the value is saturated to $\pm r_{desired,bound}$. This ensures that the vehicle slip angle does not become too large and that the available grip is considered when generating the desired signal. The desired yaw rate allows the model matching control system to ensure that the vehicle behaves in a predictable manner similar to a conventional vehicle.

In order to demonstrate how the above proposed method modifies the conventional steady state yaw rate signal, two examples of reference signals will be presented. The reference

signal for a NATO double lane change at 40 kph and J-Turn at 20 kph using a 120 degree steering input. The signals are shown in Figure 3-10 and Figure 3-11 respectively.

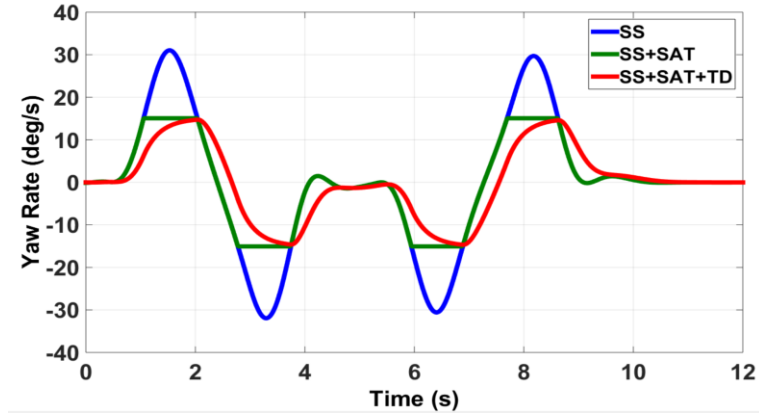


Figure 3-10 Yaw Rate Reference signal for NATO DLC at 40 kph ($\mu=0.85$)

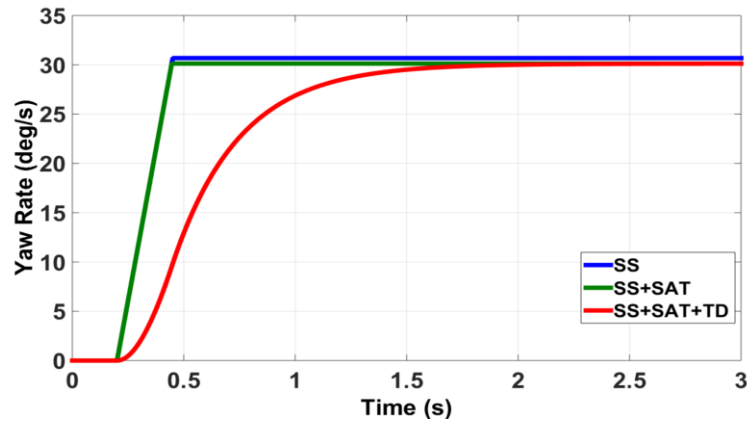


Figure 3-11 Yaw Rate Reference Signal for a J-Turn at 20 kph (120 deg steering wheel input) ($\mu=0.85$)

The blue signals, SS, represent the steady state yaw rate calculated using the steady state bicycle model without any saturation on the desired value or time delay applied. The green signals, SS+SAT, represent the steady state bicycle model with the saturation bound based on vehicle speed and road friction coefficient presented in equation 3-25. The red signals, SS+SAT+TD, represent the steady state bicycle model with the saturation bound and desired time delay applied as presented in equation 3-24. This equation will be used to generate the reference yaw rate signal for the proposed controller.

3.4.2 Steady State Bicycle Model for Desired Yaw Rate

Assumptions used for the bicycle model in section 3.3 are applicable here as well. The model in this section is not equipped with any control systems:

- No external yaw moment ($N = 0$)
- No third or fourth axle steering ($\delta_3, \delta_4 = 0$)

Figure 3-12 displays the free body diagram of the proposed model.

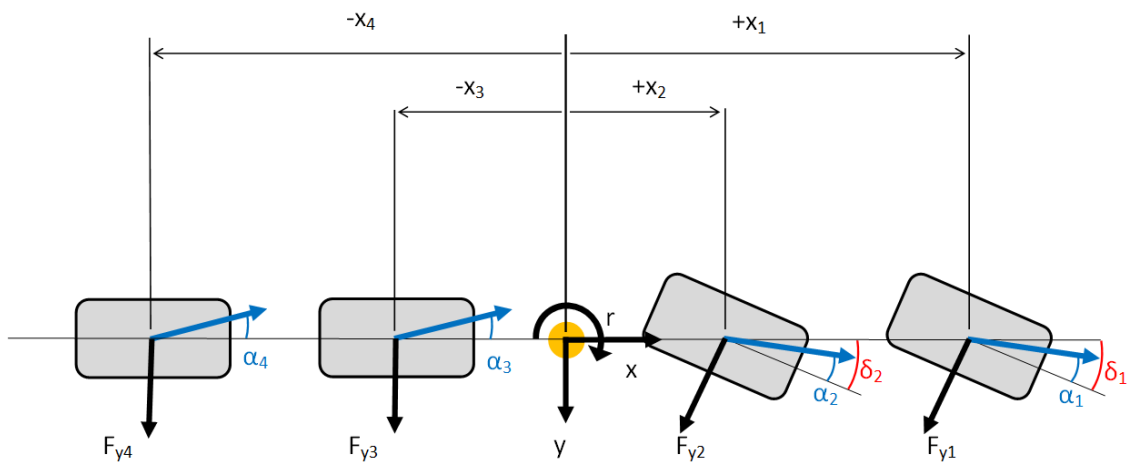


Figure 3-12 Two DOF Bicycle Model for Steady State Desired Yaw Rate

The general form of the steady state yaw rate equation for vehicles with multiple steering axles was presented by Williams, equation (66), in [70] and designated equation [70] 3-26 here:

$$\begin{bmatrix} \beta_{ss} \\ r_{ss} \end{bmatrix} = \frac{\begin{bmatrix} mu \sum_1^n x_n^2 C_n & -I (\sum_1^n x_n C_n + mu^2) \\ -mu^2 \sum_1^n x_n C_n & Iu \sum_1^n C_n \end{bmatrix} \begin{bmatrix} \frac{C_1}{mu} & \dots & \frac{C_n}{mu} \\ \frac{x_1 C_1}{I} & \dots & \frac{x_n C_n}{I} \end{bmatrix} \begin{bmatrix} \delta_1 \\ \vdots \\ \delta_n \end{bmatrix}}{(\sum_1^n C_n)(\sum_1^n x_n^2 C_n) - (\sum_1^n x_n C_n)^2 - mu^2 \sum_1^n x_n C_n} \quad (66) \quad [70] \text{ 3-26}$$

Equation [70] 3-26 will be derived for the particular vehicle in question with four axles ($n=4$) and two front steering axles where $\delta_2 = k_{1 \rightarrow 2} \delta_1$.

Note: a slight change of notation is required. Axles located rearward of the center of gravity have their distances specified as negative values and a change in symbols that designate

axle distances from a to x is required (i.e. $a_1 = x_1$; $a_2 = x_2$; $a_3 = -x_3$ and $a_4 = -x_4$). n is used to represent the number of axles [$n = 1: 4$].

Isolating the steady state yaw rate and substituting $\delta_2 = k_{1 \rightarrow 2} \delta_1$ yields:

$$\frac{r_{ss}}{\delta_1} = \frac{UC_1 \sum_1^n C_n (x_1 - x_n) + k_{1 \rightarrow 2} UC_2 \sum_1^n C_n (x_2 - x_n)}{(\sum_1^n C_n)(\sum_1^n x_n^2 C_n) - (\sum_1^n x_n C_n)^2 - mU^2 \sum_1^n x_n C_n} \quad 3-27$$

Rearranging equation 3-27:

$$\begin{aligned} \frac{r_{ss}}{\delta_1} \\ = \frac{U(1 + k_{1 \rightarrow 2})}{\frac{(\sum_1^n C_n)(\sum_1^n x_n^2 C_n) - (\sum_1^n x_n C_n)^2}{C_1 \sum_1^n C_n (x_1 - x_n) + C_2 \sum_1^n C_n (x_2 - x_n)} - U^2 \frac{m \sum_1^n x_n C_n}{C_1 \sum_1^n C_n (x_1 - x_n) + C_2 \sum_1^n C_n (x_2 - x_n)}} \end{aligned} \quad 3-28$$

3.5 LINEAR BICYCLE MODEL - ZSS CONTROLLER

The zero side slip (ZSS) method is used as a feedforward controller for turning circle reduction and increased maneuverability at low speeds. The method involves obtaining the ratio between fourth and first axle steer angles, k_{ZSS} , as a function of vehicle speed. This is accomplished by setting the steady state vehicle side slip angle, β_{ss} , to zero and isolating for δ_4 / δ_1 .

The portion of equation [70] 3-26 representing the steady state side slip angle is derived with four axles ($n=4$) and four steering axles where $\delta_2 = k_{1 \rightarrow 2} \delta_1$ and $\delta_3 = k_{4 \rightarrow 3} \delta_4$. The same notation modifications discussed in section 3.4.2 apply. The denominator has been omitted for brevity,

$$\beta_{ss} = 0 = \frac{[mU \sum_1^n x_n^2 C_n \quad -I_{zz}(\sum_1^n x_n C_n + mU^2)] \begin{bmatrix} \frac{C_1}{mU} & \frac{C_2}{mU} & \frac{C_3}{mU} & \frac{C_4}{mU} \\ x_1 C_1 & x_2 C_2 & x_3 C_3 & x_4 C_4 \\ \frac{1}{I_{zz}} & \frac{1}{I_{zz}} & \frac{1}{I_{zz}} & \frac{1}{I_{zz}} \end{bmatrix} \begin{bmatrix} \delta_1 \\ \delta_2 \\ \delta_3 \\ \delta_4 \end{bmatrix}}{\text{Denominator (see [70] 3-26)}} \quad 3-29$$

Both side of the equation are multiplied by the denominator which is eliminated from the equation. Eliminating δ_2 and δ_3 by substituting in equations 3-18 and 3-19 yields:

0 =

$$[mU \sum_1^n x_n^2 C_n \quad -I_{zz}(\sum_1^n x_n C_n + mU^2)] \begin{bmatrix} \frac{1}{mU} [(C_1 + k_{1 \rightarrow 2} C_2) \delta_1 + (k_{4 \rightarrow 3} C_3 + C_4) \delta_4] \\ \frac{1}{I_{zz}} [(x_1 C_1 + k_{1 \rightarrow 2} x_2 C_2) \delta_1 + (k_{4 \rightarrow 3} x_3 C_3 + x_4 C_4) \delta_4] \end{bmatrix} \quad 3-30$$

Conducting matrix multiplication on equation 3-30 and isolating for δ_4 / δ_1 yields the ZSS turning circle reduction ratio, k_{ZSS} :

$$k_{ZSS} = \frac{\delta_4}{\delta_1} = \frac{\sum_1^n x_n^2 C_n (C_1 + k_{1 \rightarrow 2} C_2) - \sum_1^n x_n C_n (x_1 C_1 + k_{1 \rightarrow 2} x_2 C_2) - mU^2 (x_1 C_1 + k_{1 \rightarrow 2} x_2 C_2)}{-(x_n^2 C_n) (k_{4 \rightarrow 3} C_3 + C_4) + \sum_1^n x_n C_n (k_{4 \rightarrow 3} x_3 C_3 + x_4 C_4) + mU^2 (k_{4 \rightarrow 3} x_3 C_3 + x_4 C_4)} \quad 3-31$$

Figure 3-13 graphs equation 3-31 for vehicle forward speed, U, ranging from 0 to 30 m/s (0 – 108 kph).

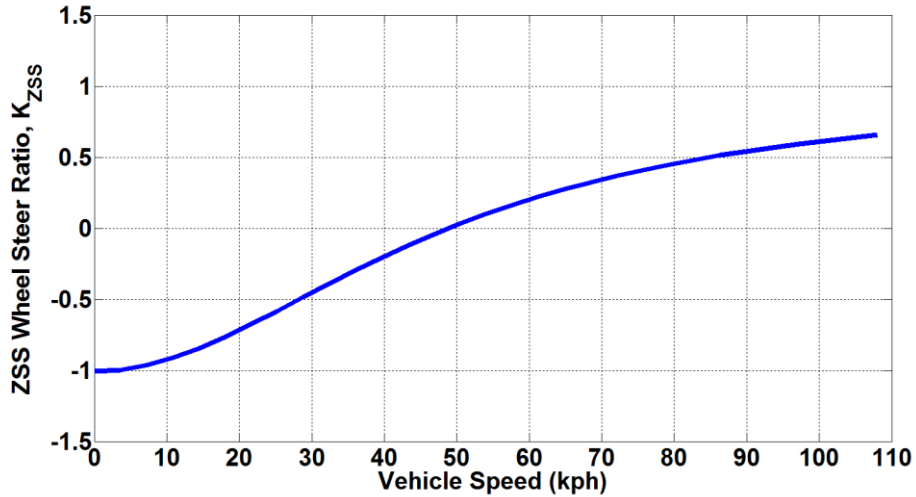


Figure 3-13 ZSS Turning Circle Reduction Ratio, k_{ZSS} as a Function of Vehicle Forward Speed

Multiplying this ratio by the front steering angle yields the speed dependent ZSS rear steer angle controller, $\delta_{4,ZSS}$, for turning circle reduction:

$$\delta_{4,ZSS} = k_{ZSS} \cdot \delta_1 \quad 3-32$$

3.6 SUMMARY

Four different vehicle models have been presented:

Vehicle simulations will be conducted using a non-linear TruckSim vehicle model of the 8 x 8 combat vehicle that has been validated by [46]. The vehicle is equipped with manufacturer tire data, hydropneumatic suspension and steering on the two front axles. An externally modelled powertrain was developed in Simulink for used during simulation. This model will serve as both the controlled and uncontrolled vehicles. When serving as the controlled vehicle the TruckSim model will be run in co-simulation with the proposed controller and external powertrain Simulink model. It will have both rear steering on the third and fourth axle as well as torque vectoring on the two rear axles.

H_∞ controller synthesis requires a linear vehicle model to be used as the plant. For this purpose, a linear bicycle model with external yaw moment (used to represent torque vectoring) and rear axle steering has been proposed in state space form represented by equations 3-22 and 3-23.

The H_∞ controller requires a reference signal to track. A linear steady state bicycle model of a vehicle without any control systems equipped is used as part of a reference model and presented in equation 3-28. This model is combined with a first order time delay and saturation function based on the road friction coefficient to form the yaw rate reference signal.

A feedforward speed sensing rear steer controller is proposed for use at low speeds to reduce the vehicle's turning circle diameter and increase maneuverability. It is based on a steady state bicycle model equipped with rear axle steering on the third and fourth axles. The zero side slip (ZSS) method is used for this control. The method involves setting the differential equation representing the vehicle side slip angle to zero and isolating for the ratio between the first axle wheel angle and fourth axle wheel angles presented in equation 3-31. This expression is then used in equation 3-32 and represents the ZSS turning circle reduction controller.

CHAPTER 4

LPV H_∞ CONTROLLER DESIGN

4.1 INTRODUCTION

If the dynamics of a plant depend heavily on parameters whose ranges are large it is convenient to model it as a linear parameter-varying system (LPV) [47]. These parameters are called scheduling parameters and may vary with time within a range defined by the designer. LPV systems are employed for aerospace, robotics and most recently vehicle control [47].

There are two steps to the design of an LPV H_∞ controller. The first is to create an LPV model of the plant to be controlled. The second step consists of synthesizing an LPV controller dependent on the scheduling parameter using the developed LPV plant. This chapter is presented in two sections. The first will detail the theoretical aspects of LPV H_∞ design and the second will detail the implementation of that theory in this work.

The interested reader is directed toward [13, 47, 71, 72] for in-depth theoretical and practical implementation of H_∞ control theory.

4.2 LPV H_∞ CONTROLLER DESIGN - THEORY

4.2.1 LPV Plant Modeling - Theory

H_∞ control is a linear control method and therefore requires a linear plant model. Once the linear plant model has been obtained, appropriate scheduling parameter(s), θ_n , must be chosen. The plant to be controlled, $G(\theta)$, may then be described as being a function of the scheduling parameter vector, $\theta = [\theta_1 \dots \theta_n]$ where $\underline{\theta}_n \leq \theta_n \leq \overline{\theta}_n$, whose state space form is:

$$\dot{x} = A(\theta)x + B(\theta)u \quad 4-1$$

$$y = C(\theta)x + D(\theta)u \quad 4-2$$

The state space matrices, A, B, C and D are functions of θ and can be expressed as constants multiplied by the scheduling parameters:

$$A(\theta) = A_0 + \theta_1 A_1 + \dots + \theta_n A_n \quad 4-3$$

$$B(\theta) = B_0 + \theta_1 B_1 + \dots + \theta_n B_n \quad 4-4$$

$$C(\theta) = C_0 + \theta_1 C_1 + \dots + \theta_n C_n \quad 4-5$$

$$D(\theta) = D_0 + \theta_1 D_1 + \dots + \theta_n D_n \quad 4-6$$

The plant model, $G(\theta)$, varies with the value of the scheduling parameter. A polytope, whose vertices, Π_q , are combinations of the maximum and minimum values of the scheduling parameters, is constructed as in Figure 4-1 (example of two scheduling parameters shown).

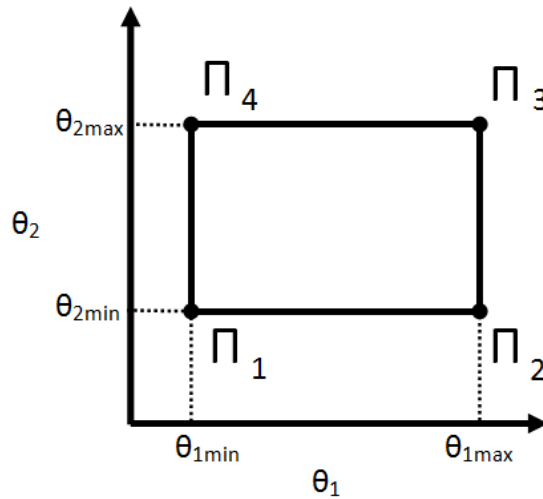


Figure 4-1 Polytope of Scheduling Parameters (θ_1 and θ_2)

The number of vertices, q , of a polytope for a given system can be calculated as, $q = 2^n$, where n is the number of scheduling parameters. In the case of a system with two parameters (the case in this work), q is equal to four.

The plant model varies as a function of these parameters and is a convex linear combination of the LPV state space matrices at the vertices of the polytope and can be referred to as a polytopic system [47] represented by:

$$\begin{bmatrix} A + jE & B \\ C & D \end{bmatrix} = \sum_{i=1}^q \alpha_i \begin{bmatrix} A_i + jE_i & B_i \\ C_i & D_i \end{bmatrix} \quad 4-7$$

where $\alpha_i \geq 0$, $\sum_{i=1}^q \alpha_i = 1$

4.2.2 H_∞ Controller Synthesis – Theory

Various combinations of cost functions can be used for H_∞ controller synthesis. They can be interpreted as design objectives for the transfer functions of the closed loop system (plant and H_∞ controller). H_∞ control synthesis determines a controller K that minimizes the ∞ -norm of the appropriate transfer functions of the closed loop system. The mixed sensitivity formulation is used in this work. It allows for good reference tracking and limits the control signal, u . It can be posed as an minimization problem to find a stabilizing controller K that minimizes the output signal, z , for all external inputs, w , i.e. minimizing the H_∞ -norm of the w to z transfer function [47]:

$$\min_K \left\| \begin{bmatrix} W_e(I + GK)^{-1} \\ W_u K(I + GK)^{-1} \end{bmatrix} \right\|_\infty \quad 4-8$$

The general closed loop feedback mixed sensitivity H_∞ layout is shown in Figure 4-2a. z_e and z_u , the dotted signals, depict the mixed sensitivity weighting functions performance output signals, K represents the H_∞ controller, r is the reference signal, e is the error signal, u the control signal and y the output signals available from the plant. In order to use standard solving techniques, the layout depicted in Figure 4-2a must be combined into an augmented plant, G_{aug} , layout yielding the standard H_∞ form of the closed loop system depicted in Figure 4-2b.

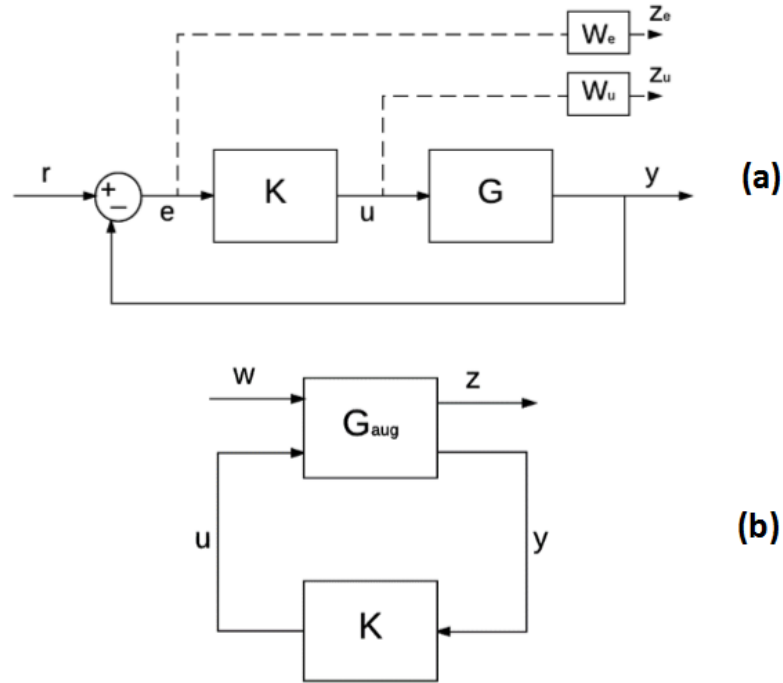


Figure 4-2 Mixed Sensitivity Feedback System (a) Standard H_∞ Layout (b)

External inputs are designated as w and typically include r ; y , in diagram b, represents the error between reference and actual plant output; z represents the previously mentioned performance signals. G_{aug} represents the interconnected/augmented system. It is the concatenation of all the inputs and outputs shown in Figure 4-2a.

The state space description of G_{aug} is as follows:

$$\begin{aligned}\dot{\xi} &= A(\theta)\xi + B_1(\theta)w + B_2u \\ z &= C_1(\theta)\xi + D_{11}(\theta)w + D_{12}u \\ y &= C_2\xi + D_{21}w + D_{22}u\end{aligned}\tag{4-9}$$

Controller synthesis involves obtaining a parameter dependent controller that minimizes the mixed sensitivity weighting functions over the entire range of the scheduling parameters. The final controller, $K(\theta)$, is a convex linear combination of q controllers computed at the vertices of the scheduling parameter polytope:

$$K(\theta) = \begin{cases} \zeta = A_K(\theta)\zeta + B_K(\theta)y \\ u = C_K(\theta)\zeta + D_K(\theta)y \end{cases}\tag{4-10}$$

where

$$A_K(\theta) = \alpha_1 A_1(\Pi_1) + \dots + \alpha_q A_q(\Pi_q) \quad 4-11$$

$$B_K(\theta) = \alpha_1 B_1(\Pi_1) + \dots + \alpha_q B_q(\Pi_q) \quad 4-12$$

$$C_K(\theta) = \alpha_1 C_1(\Pi_1) + \dots + \alpha_q C_q(\Pi_q) \quad 4-13$$

$$D_K(\theta) = \alpha_1 D_1(\Pi_1) + \dots + \alpha_q D_q(\Pi_q) \quad 4-14$$

The controller is obtained offline via the `hinfgs` function in MATLAB which uses the linear matrix inequality (LMI) approach. The controller is then gain scheduled online. α is adjusted at each time step returning a different convex linear combination of the q H_∞ controllers computed for the q vertices of the parameter polytope as shown in Figure 4-3.

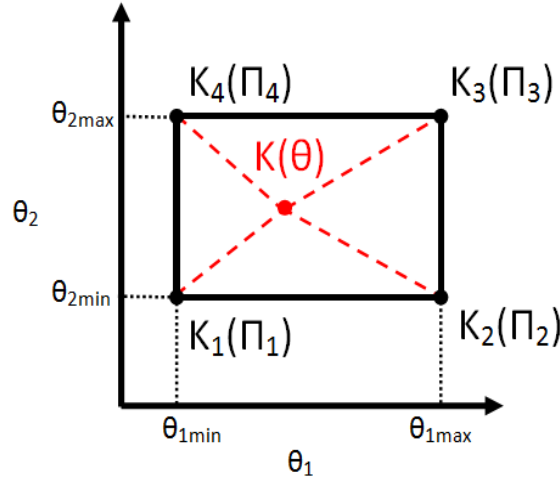


Figure 4-3 Polytopic Controller Convex Combination Visualisation

4.3 LPV TWO DOF H_∞ CONTROLLER DESIGN

4.3.1 LPV Two DOF Plant Modeling

4.3.1.1 Scheduling Parameters

Linearization of the two DOF bicycle model has been presented in CHAPTER 3. Equations 3-22 and 3-23 represent the linear plant model. A vehicle's dynamic response is heavily dependent on vehicle forward speed therefore scheduling parameters based on vehicle

speed will be used as in [53, 56, 57]. Specifically, the strategy proposed by [57]. The two scheduling parameters will be the inverse of vehicle forward speed, $\frac{1}{U}$, and the inverse of vehicle forward speed squared, $\frac{1}{U^2}$, where $9.7 \leq U \leq 30.5 \frac{m}{s}$ (35 – 110 kph):

$$\theta = \begin{bmatrix} \frac{1}{U} & \frac{1}{U^2} \end{bmatrix} \quad 4-15$$

4.3.1.2 Linear Parameter Dependent Plant

The general state space matrices of an LPV plant (equations 4-3 to 4-6) will now be developed for the two DOF bicycle model described by equations 3-22 and 3-23. Because the B matrix of the plant to be controlled is dependent on the scheduling parameters, it must be modified in order for the LPV problem to be solvable. Strictly proper low pass filters for the steering angles (equation 4-16) are applied to the generalized plant to remove the parameter dependence.

$$F_{\delta_1} = F_{\delta_4} = \frac{100}{s + 100} = \frac{1}{\frac{s}{100} + 1} = \begin{bmatrix} a_{fil} & b_{fil} \\ c_{fil} & d_{fil} \end{bmatrix} = \begin{bmatrix} -100 & 1 \\ 100 & 0 \end{bmatrix} \quad 4-16$$

The dependence is rejected into the A state space matrix of the plant [71]. The state space matrices are as follows. **Note:** parameter dependent terms have been highlighted by including the dependent parameters in **red**.

$$A(\theta) = \begin{bmatrix} a_{11}\theta_1 & a_{12}\theta_2 - 1 & c_{fil,\delta 1}a_{13}\theta_1 & c_{fil,\delta 4}a_{14}\theta_1 \\ a_{21} & a_{22}\theta_1 & 0 & 0 \\ 0 & 0 & a_{fil,\delta 1} & 0 \\ 0 & 0 & 0 & a_{fil,\delta 4} \end{bmatrix} \quad 4-17$$

where

$$a_{11} = -\frac{(C_{\alpha 1} + C_{\alpha 2} + C_{\alpha 3} + C_{\alpha 4})}{m}$$

$$a_{12} = -\frac{(a_1 C_{\alpha 1} + a_2 C_{\alpha 2} - a_3 C_{\alpha 3} - a_4 C_{\alpha 4})}{I_{zz}}$$

$$a_{13} = \frac{C_{\alpha 1} + k_{1 \rightarrow 2} C_{\alpha 2}}{m}$$

$$\begin{aligned}
a_{14} &= \frac{k_{4 \rightarrow 3} C_{\alpha 3} + C_{\alpha 4}}{m} \\
a_{21} &= -\frac{(a_1 C_{\alpha 1} + a_2 C_{\alpha 2} - a_3 C_{\alpha 3} - a_4 C_{\alpha 4})}{I_{zz}} \\
a_{22} &= -\frac{(a_1^2 C_{\alpha 1} + a_2^2 C_{\alpha 2} + a_3^2 C_{\alpha 3} + a_4^2 C_{\alpha 4})}{I_{zz}} \\
B(\theta) &= \begin{bmatrix} 0 & 0 & 0 \\ \frac{a_1 C_{\alpha 1} + k_{1 \rightarrow 2} a_2 C_{\alpha 2}}{I_{zz}} & \frac{-(k_{4 \rightarrow 3} a_3 C_{\alpha 3} + a_4 C_{\alpha 4})}{I_{zz}} & \frac{1}{I_{zz}} \\ b_{fil, \delta 1} & 0 & 0 \\ 0 & b_{fil, \delta 4} & 0 \end{bmatrix} \quad 4-18
\end{aligned}$$

$$C(\theta) = \begin{bmatrix} 1 & 0 & 0 & 0 \\ 0 & 1 & 0 & 0 \end{bmatrix} \quad 4-19$$

$$D(\theta) = \begin{bmatrix} 0 & 0 & 0 \\ 0 & 0 & 0 \end{bmatrix} \quad 4-20$$

4.3.2 LPV TWO DOF H_∞ Controller Synthesis

4.3.2.1 H_∞ Controller Synthesis

A two DOF (feedback and feedforward) controller is proposed using the mixed sensitivity formulation. The feedforward controller ensures good reference tracking and the feedback controller is used to minimize the error signal due to disturbances (external inputs) and uncertainties.

The expanded augmented plant, G_{aug} , layout is shown by the dashed red area in Figure 4-4 where the controller outputs are the rear steering angle and the external yaw moment, $u = \begin{bmatrix} \delta_4 \\ N \end{bmatrix}$; the external inputs are the reference yaw rate and front wheel angle, $w = \begin{bmatrix} r^{desired} \\ \delta_1 \end{bmatrix}$; the mixed sensitivity performance signals are an error tracking signal, z_e , and two control signal effort attenuation signals, $z_{u, \delta 4}$ and $z_{u, N}$, each respectively weighted by a unique weighting function, $z =$

$$\begin{bmatrix} z_e \\ z_{u, \delta 4} \\ z_{u, N} \end{bmatrix} = \begin{bmatrix} W_e e \\ W_{u, \delta 4} \delta_4 \\ W_{u, N} N \end{bmatrix}; \text{ the input to the controller is } y = e = r_{desired} - r \text{ and the front wheel angle.}$$

The developed two DOF plant model is represented by $G(\theta)$. W_e , W_{u,δ_4} and $W_{u,N}$ represent the frequency domain weighting functions that determine the behaviour of the obtained H_∞ controllers by shaping the performance output signals during synthesis. They will be discussed in section 4.3.2.2.

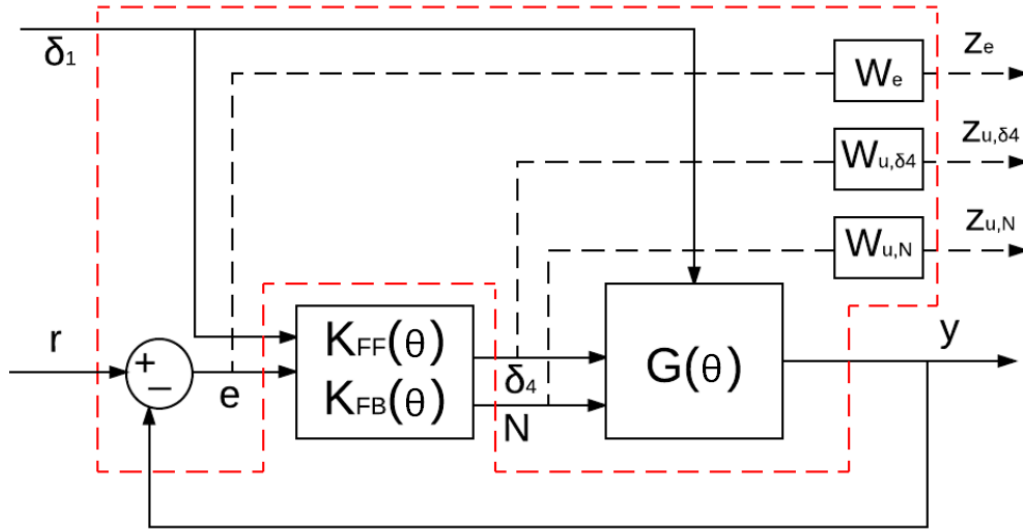


Figure 4-4 Expanded Augmented Plant Layout

The standard H_∞ layout of the augmented plant is shown in Figure 4-5.

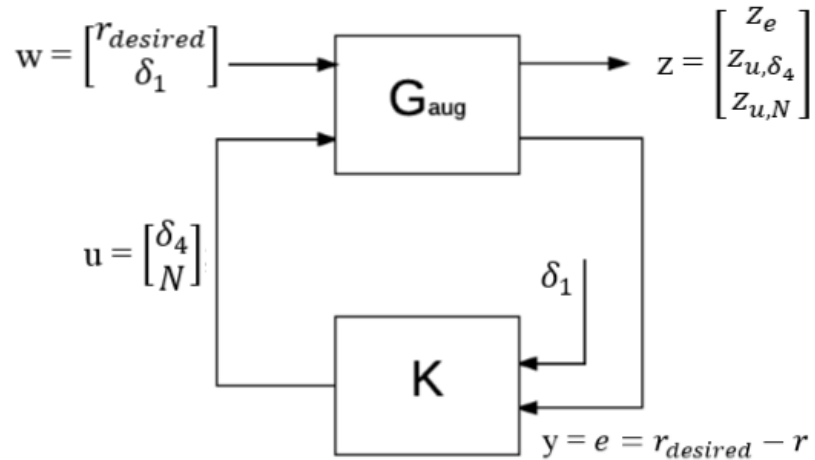


Figure 4-5 Standard H_∞ Layout for Vehicle Dynamic Controller

The state space representation of the augmented plant is:

$$G_{aug} : \begin{cases} \dot{\xi} = A(\theta)\xi + B_1(\theta)w + B_2u \\ z = C_1(\theta)\xi + D_{11}(\theta)w + D_{12}u \\ y = C_2\xi + D_{21}w \end{cases} \quad 4-21$$

ξ includes the state variables of the linearized vehicle model and of the filters. All other variables have already been described.

Both feedforward and feedback controllers are synthesized simultaneously and guarantee performance and stability for all possible combinations of scheduling parameters within the proposed range of 35 to 110 kph. The two DOF controller's state space equation is derived:

$$K(\theta) = \begin{cases} \dot{\zeta} = A_K(\theta)\zeta + B_{Ke}(\theta)e + B_{K\delta_1}(\theta)\delta_1 \\ u = C_K(\theta)\zeta + D_{Ke}(\theta)e + D_{K\delta_1}(\theta)\delta_1 \end{cases} \quad 4-22$$

where ζ is the controller state variable and u the controller output, $\begin{bmatrix} \delta_4 \\ N \end{bmatrix}$.

4.3.2.2 Weighting Functions

Mixed sensitivity weighting functions are used to shape the performance signals, z . The weighting function design is inspired by [60] and has been modified for use in this application. Gain scheduling of the external yaw moment has been removed as the scheduling parameters of the controller and the actuation systems of the simulated vehicle differ. Fine tuning was accomplished through full vehicle simulations with Trucksim in various dynamic events.

- \mathbf{z}_e represents the yaw rate error signal and is weighted by W_e :

$$W_e = \frac{1}{20G_e} \cdot \frac{\frac{G_e}{2\pi f_e} s + 1}{\frac{1}{2\pi f_e} s + 1} \quad [60] \quad 4-23$$

where $f_e = 1 \text{ Hz}$ is the cut-off frequency of the high pass filter. $G_e = 0.15$ is magnitude to which the low frequency signals are attenuated. This ensures that the steady state error is no greater than 15%.

- \mathbf{z}_{u,δ_4} and $\mathbf{z}_{u,N}$ represent the rear wheel steering and torque vectoring yaw moment control signal outputs respectively.

z_{u,δ_4} is weighted by W_{u,δ_4} :

$$W_{u,\delta_4} = G_{\delta_4}^0 \frac{\left(\frac{1}{2\pi f_3} s + 1\right) \left(\frac{1}{2\pi f_4} s + 1\right)}{\left(\frac{1}{40\pi f_4} s + 1\right)^2} \quad [60] \text{ 4-24}$$

$$G_{\delta_4}^0 = G_{\delta_4} \frac{\left(\frac{\Delta f}{40\pi f_4} + 1\right)^2}{\left(\frac{\Delta f}{2\pi f_3} + 1\right) \left(\frac{\Delta f}{2\pi f_4} + 1\right)}$$

$$\Delta f = \frac{2\pi(f_4 + f_3)}{2}$$

where $f_3 = 1 \text{ Hz}$ and $f_4 = 10 \text{ Hz}$ represent the lower and upper limit frequencies of the rear wheels steering actuator bandwidth. $G_{\delta_4} = 3$; represents a bandpass filter that limits the use of the rear wheel steering to frequencies between 1 - 10 Hz where the signal is limited by G_{δ_4} . The purpose is to limit rear steering intervention to frequencies where the driver cannot make corrections on his own.

$z_{u,N}$ is weighted by $W_{u,N}$:

$$W_{u,N} = G_N \frac{\frac{1}{2\pi f_N} s + 1}{\frac{1}{40\pi f_N} s + 1} \quad [60] \text{ 4-25}$$

where $f_N = 10 \text{ Hz}$ represents the bandwidth of the electric motor actuators for yaw moment generation. $G_N = 10^{-4}$ limits the fluctuation in the magnitude of the desired yaw moment signal, N.

4.4 SUMMARY

In this chapter, the theoretical steps used to design an LPV H_∞ controller were introduced and then used to develop the proposed LPV H_∞ controller in the vehicle dynamics control

system. An LPV model of the 8 x 8 combat vehicle plant model was developed using the state space plant model developed in CHAPTER 3 . The scheduling parameters used were the inverse of vehicle speed and the inverse of vehicle speed squared for speed ranges between 35 and 110 kph. A two DOF controller (feedback and feedforward) using the mixed sensitivity formulation is proposed. The feedforward controller ensures good reference tracking and the feedback controller is used to minimize the yaw rate error signal due to disturbances (external inputs) and uncertainties. The controller was synthesized using the parameter dependent LPV plant and the proposed weighting functions. The weighting functions describe the desired performance of the controller. Steady state error is limited to 15%. A bandpass filter is used as the weighting function for the rear steering control signal in order to limit rear steering intervention to frequencies where the driver cannot make correction on his own (1 – 10 Hz).

CHAPTER 5

VEHICLE DYNAMIC CONTROL SYSTEM

5.1 PROPOSED CONTROL SYSTEM ARCHITECTURE

The proposed vehicle dynamics control system is shown in Figure 5-1. The TruckSim full vehicle model is run in co-simulation with Simulink. All blocks are developed within the Simulink environment.

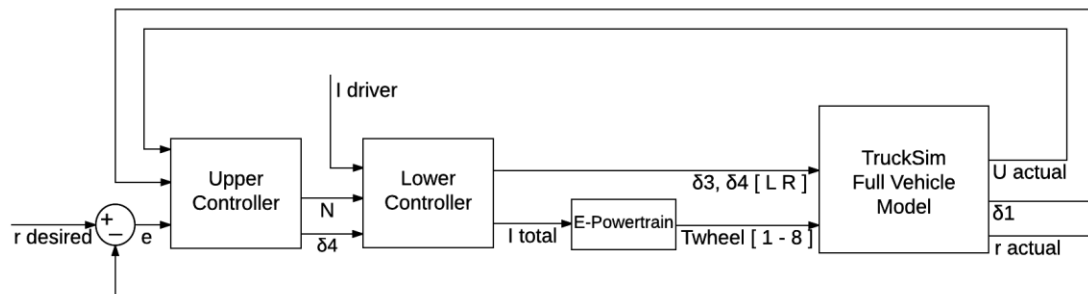


Figure 5-1 Controller Architecture Diagram

Active control is initiated when the vehicle is moving forward between speeds of 0 and 110 kph. The controller is not active when the vehicle is in reverse for safety reasons. The upper controller is composed of two controllers: the LPV two DOF H_{∞} controller, $K(\theta)$, covered in section 4.3.2, equation 4-22 and the speed dependent ZSS rear steer angle controller, δ_4 , zss, presented in section 3.5, equation 3-32.

The lower controller receives the driver motor current, I_{driver} , from a vehicle forward speed controller (omitted for clarity from figure) and the torque vectoring/rear steering commands from the upper controller. These values are converted into vehicle component level commands to achieve active control of the multi-wheeled vehicle, δ_3 , δ_4 and I_{total} . An on/off slip controller is embedded within the lower controller as well.

The desired yaw rate, $r_{desired}$, is generated via equation 3-24 in section 3.4.1 (omitted for clarity from figure). The electric powertrain block is presented in section 3.2.3 by equations 3-1 to 3-5. The eight electric motors each receive the total motor current, $I_{motor,total}$, to

produce output shaft torque applied to each corresponding wheel of the vehicle. The blocks will be presented in more detail in the following sections.

5.2 VEHICLE FORWARD SPEED CONTROLLER

A proportional integral (PI) controller is used for vehicle forward speed control. The system tracks the error, e_U , between the desired vehicle speed, $U_{desired}$, and the actual vehicle speed, U_{actual} , from the Trucksim vehicle model as shown in Figure 5-2. $U_{desired}$ is determined within the TruckSim environment and is dependent on the desired speed for the dynamic event being simulated.



Figure 5-2 PI Speed Controller Diagram

The controller returns the driver motor current, I_{driver} , required for each of the eight electric motors in order to track the reference vehicle speed. All currents are equal to I_{driver} . Controller gains were tuned using the non-linear full vehicle simulations and are listed in Table 5-1.

Table 5-1 Proportional-Integral Controller Gains

PI SPEED CONTROLLER GAINS	
P	8.5
I	10

5.3 REFERENCE MODEL

The reference model is generated using equation 3-24 which consists of a two DOF bicycle model and a first order lag. The block uses the average front axle wheel steering angle, δ_1 , and the actual vehicle forward speed, U_{actual} , to determine the desired yaw rate, $r_{desired}$. The

road friction coefficient, μ , is used in order to limit the required yaw rate to achievable values as described in equation 3-25 and shown in Figure 5-3.

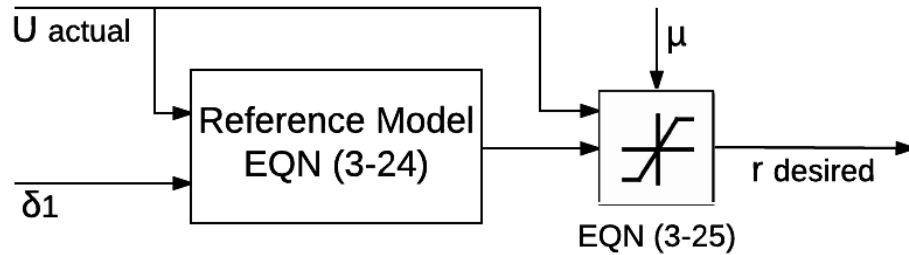


Figure 5-3 Reference Model Diagram

Refer to section 3.4.1 for further details.

Note: The road friction coefficient is directly entered as a constant into the reference model. An online μ estimator can be integrated. Development of this type of estimator was not pursued in order to focus on the performance of the proposed controller without unnecessary added complexity. There has been a great deal of work related to online road friction estimation and the interested reader is directed to [73-77] for further details.

5.4 ELECTRIC POWERTRAIN

Figure 5-4 depicts the integration of the electric powertrain differential equations 3-1 to 3-5 within the Simulink environment. Refer to section 3.2.3 for more detail.

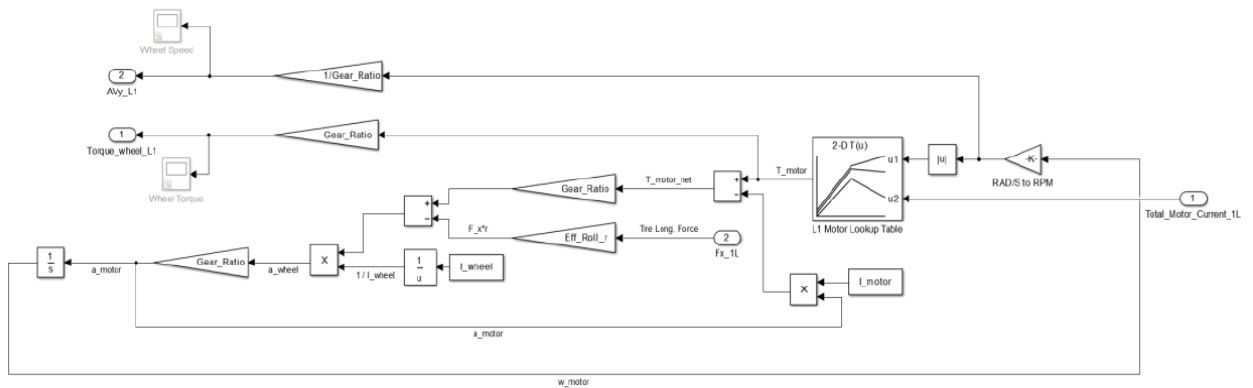


Figure 5-4 Simulink Electric Powertrain Diagram (One Motor)

5.5 UPPER CONTROLLER

The upper controller consists of the two DOF LPV H_∞ controller, $K(\theta)$, which employs torque vectoring and rear steering and the zero side slip (ZSS) turning circle reduction controller, δ_4, z_{SS} , which only employs rear steering. A method is proposed in order to determine how and when to switch between the two different control strategies.

5.5.1 2 DOF LPV H_∞ Controller, $K(\theta)$

After completing synthesis of the H_∞ controller as presented in section 4.3.2. The controller is implemented online in Simulink using its state space matrices and matrix multiplication. The polytopic coordinates, α_1 through α_4 , are evaluated using the online values of the scheduling parameters, $\theta = \left[\frac{1}{U} \quad \frac{1}{U^2} \right]$. The convex linear combination of the four H_∞ controller's state space matrices is computed by multiplying each vertex controller by its corresponding α value using equations 4-11 through 4-14 as shown in Figure 5-5.

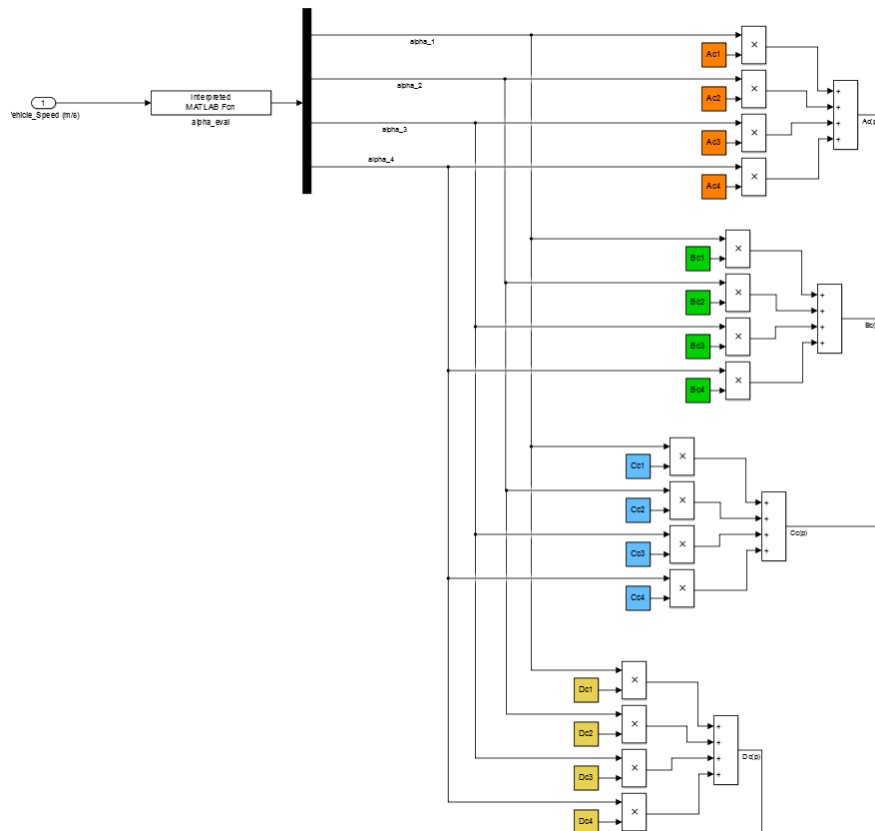


Figure 5-5 Calculation of the H_∞ Controller State Space Matrices

The convex linear combination of state space matrices is then used to recreate equation 4-22 (repeated below for continuity) resulting in the Simulink implementation of the H_∞ controller.

$$K(\theta) = \begin{cases} \dot{\zeta} = A_K(\theta)\zeta + B_{Ke}(\theta)e + B_{K\delta_1}(\theta)\delta_1 \\ u = C_K(\theta)\zeta + D_{Ke}(\theta)e + D_{K\delta_1}(\theta)\delta_1 \end{cases} \quad 4-22$$

5.5.2 ZSS Turning Circle Reduction Controller, δ_4 , ZSS

The ZSS turning circle reduction controller is implemented in Simulink using the blocks shown in Figure 5-6. Equation 3-32 is implemented using a MATLAB function block. A saturation block is also included in order to represent the physical constraint on the rear wheel steering angle. This can be attributed to the large diameter tires and the limited space available for the tires before coming into contact with the vehicle hull. In the absence of detailed mechanical design of the rear suspension and steering configuration, several maximum rear steer values will be investigated and can be used as design guides when implementing such a system. See section 6.3 for details and results.

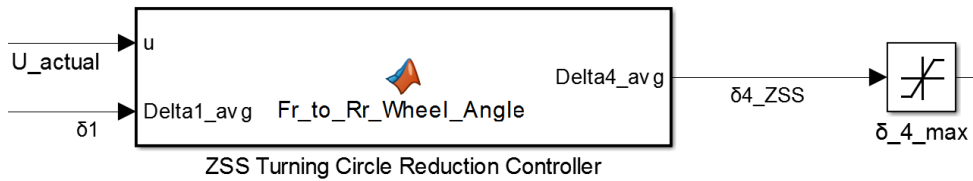


Figure 5-6 ZSS Turning Circle Reduction Controller Simulink Implementation

5.5.3 Switching between ZSS and H_∞ Control

At low vehicle speeds, the ZSS feedforward controller will be active. No torque vectoring will take place. As vehicle speed increases, two Gaussian distribution based activation functions will gradually decrease the ZSS controller rear steering signal and increase the H_∞ controller rear steer control signal as a function of vehicle forward speed, U .

$$X_{actv,RWS}(U) = \begin{cases} e^{\left(\frac{-(|U-35|-5)^2}{2\sigma^2}\right)} \cdot 100\% & |U - 35| \leq 5 \\ 100\% & |U - 35| > 5 \end{cases} \quad 5-1$$

A similar function will be used for the torque vectoring signal however the low speed signal is zero.

$$X_{actv,TV}(U) = \begin{cases} e^{\left(\frac{-(|U-35|-5)^2}{2\sigma^2}\right)} \cdot 100\% & |U - 35| \leq 5 \text{ AND } (U - 35) > 0 \\ 0\% & (U - 35) < 0 \\ 100\% & |U - 35| > 5 \end{cases} \quad 5-2$$

σ is the standard deviation and is set to 0.7 to shape the bell curves of the activation functions as show in Figure 5-7. Switching will take place between 30 and 40 kph. See section 6.4 for justification of vehicle speed range used based on simulations conducted on both ZSS and H_∞ controlled vehicles.

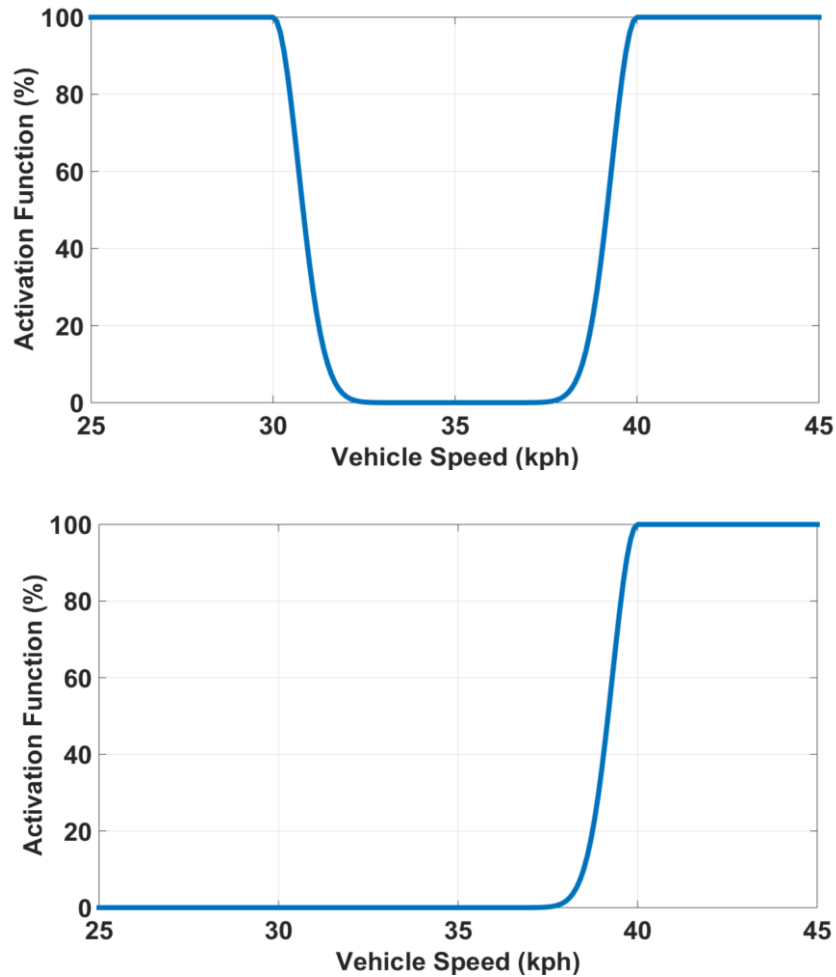


Figure 5-7 Activation Functions for RWS (top) and Torque Vectoring (bottom)

5.6 LOWER CONTROLLER

The lower controller receives the torque vectoring/rear steering commands from the upper controller. These values are converted into vehicle component commands for each of the eight motors, torque vectoring motor current, I_{VDC} , and third and fourth axle wheel steer angles, δ_3 and δ_4 .

The lower controller combines the array of eight driver motor currents, I_{driver} , from the vehicle forward speed controller with the eight element torque vectoring motor current array, I_{VDC} . The array of total current for each motor, I_{total} , is sent to the electric powertrain. An on/off slip controller is embedded within the lower controller as well. The configuration is shown in Figure 5-8.

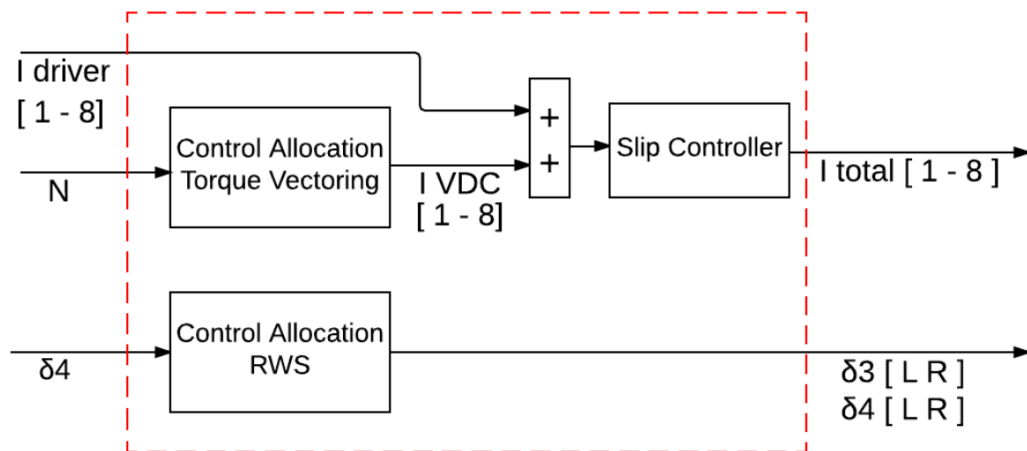


Figure 5-8 Lower Controller Architecture

5.6.1 Control Allocation – Torque Vectoring Wheel Distribution

Torque vectoring capabilities are limited to the two rear axles of the 8 x 8 vehicle as shown in Figure 5-9. In the case of a positive desired yaw moment command from the upper controller, positive current (torque increase) is applied to the two left rear motors and negative current is applied to the two right rear motors and vice versa for a negative yaw moment command.

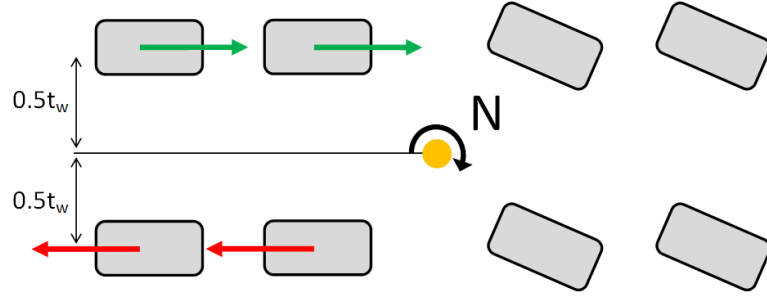


Figure 5-9 Torque Vectoring Control Allocation Schematic

Note: Torque vectoring has been limited to the two rear axles of the vehicle as [23] concluded that torque vectoring was most effective when applied to the rear axle of AWD and RWD vehicles. This can also be observed in implementations of torque vectoring systems in commercialized systems.

Equations 5-3 through 5-9 describe the calculations used to convert the external yaw moment signal from the upper controller, N , to individual vehicle dynamics controller motor currents, $I_{VDC,motor}$.

The total force required to apply the desired yaw moment about the center of gravity of the vehicle is described as:

$$F_{tire,total} = \frac{N}{0.5t_w} \quad 5-3$$

where t_w is the vehicle track width. The total tire force, $F_{tire,total}$, is then divided evenly between the four rear tires. Negative signs are assigned to the wheels on the right side of the vehicle for sign convention purposes:

$$F_{individual\ tire} = F_{L3} = F_{L4} = -F_{R3} = -F_{R4} = \frac{F_{tire,total}}{4\ tires} = \frac{N}{4} \quad 5-4$$

The individual tire force is then converted into the corresponding motor current through the following equations:

$$P_{motor} = T_{motor}\omega_{motor} = V_{motor}I_{motor} \quad 5-5$$

$$T_{motor} = \frac{V_{motor} I_{motor}}{\omega_{motor}} \quad 5-6$$

Substituting $V_{motor} = 400$ V and rearranging for I_{motor} yields the vehicle dynamics controller current signal for a particular motor, $I_{VDC,motor}$:

$$I_{VDC,motor} = I_{motor} = \frac{T_{motor} \omega_{motor}}{400} \cdot \left(\frac{2\pi}{60} \right)_{RPM \rightarrow Radians} \quad 5-7$$

where

$$T_{motor} = \frac{T_{tire,total}}{GR} = \frac{F_{individual\ tire} \cdot r_{effective}}{GR} \quad 5-8$$

Substituting equations 5-4 into 5-8 and the resulting expression into equation 5-7 yields:

$$I_{VDC,motor} = \frac{\left(\frac{\left(\frac{N}{\frac{0.5t_w}{4}} \right) r_{effective}}{GR} \right) \omega_{motor}}{400} \cdot \left(\frac{2\pi}{60} \right)_{RPM \rightarrow Radians} \quad 5-9$$

Note: equations presented are for one individual electric motor and must be repeated for each of the eight wheel stations to form an eight element array of VDC currents, I_{VDC} .

The total current applied to each of the wheels, I_{total} , is then described by the following relationships:

two front axles (no VDC intervention):

$$I_{total,R1} = I_{total,L1} = I_{total,R2} = I_{total,L2} = I_{driver,motor} \quad 5-10$$

two rear axles:

$$I_{total,R3} = I_{total,L3} = I_{total,R4} = I_{total,L4} = I_{VDC,motor} + I_{driver,motor} \quad 5-11$$

Note: The subscript motor here is used as a place holder and corresponds to the particular

motor for which the equation is being used. Additionally, the sign of I_{VDC} is dictated by the sign of the desired yaw moment, N .

5.6.2 Control Allocation – Rear Wheel Steer Angle Distribution

Control allocation for rear wheel steering is straight forward and can be described by the following relationship as functions of the rear axle steer angle commanded by the upper controller, $\delta_{4,ctrl}$:

$$\delta_{R3} = \delta_{L3} = k_{4 \rightarrow 3} \cdot \delta_{4,ctrl} \quad 5-12$$

$$\delta_{R4} = \delta_{L4} = \delta_{4,ctrl} \quad 5-13$$

Note: The ratio between the 3rd and 4th axles taken identical to the 1st and 2nd ratio, $k_{1 \rightarrow 2} = k_{4 \rightarrow 3}$, in order to allow for the implementation of a mirrored front steering rack design for the rear of the vehicle. An in-depth redesign of the steering system (front and rear) and suspension kinematics would be required for implementation in an actual vehicle. This is not in the scope of this work.

5.6.3 Slip Controller

An ON/OFF slip controller is integrated within the lower controller and monitors wheel slip at each wheel station; it's output can either be, 1 (ON), or 0 (OFF). When the wheel slip exceeds the threshold value of 20 percent, the current signal from the lower controller, $I_{total,motor}$, for the slipping motor is multiplied by a zero signal from the slip controller and no torque, positive or negative, is produced. When the wheel slip, i , returns below the threshold value, the required current is multiplied by one and allowed to pass to the motor. Equation 1-1 (repeated here for continuity) is used to calculate the slip for each wheel. Figure 5-10 displays the slip controller architecture for one electric motor/wheel combination.

$$i = \left(1 - \frac{V_t}{r_{effective} \omega_{tire}} \right) * 100\% \quad 1-1$$

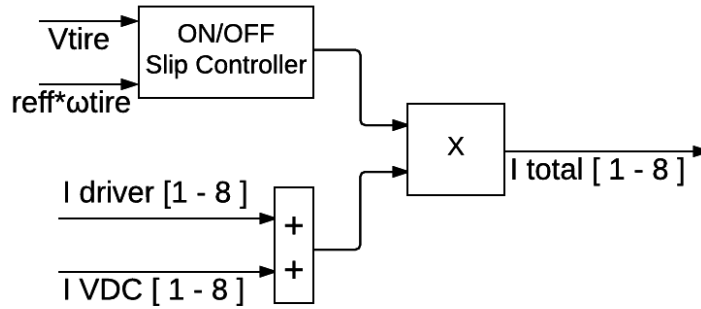


Figure 5-10 Slip Controller Architecture

5.7 SUMMARY

A vehicle dynamics control system has been proposed for the control of an 8 x 8 heavy vehicle with active torque vectoring and steering control capabilities on the two rear axles. The control architecture is composed of several components. Active control is initiated when the vehicle is moving forward between speeds of 0 and 110 kph. The controller is not active when the vehicle is in reverse for safety reasons.

A speed controller manipulates all eight individual electric motor currents to track desired vehicle forward speed via a PI controller. A vehicle dynamics controller is used to manipulate the vehicle performance. It is composed of two controllers: a two DOF LPV H_∞ controller scheduled using vehicle speed for medium and high speed maneuvers; a feedforward ZSS speed dependent rear steer angle controller for turning circle reduction and maneuverability improvement at low speeds. The H_∞ controller is used to track a reference model by manipulating torque distribution and steering angles on the two rear axles. The ZSS controller uses a mathematical relationship to determine the steering ratio between the front and rear axles and does not alter electric motor torque (no torque vectoring in this control mode). A maximum rear steer angle is introduced to mathematically represent the physical constraints of the vehicle's rear wheel wells. Switching between the two controllers is accomplished using activation functions modelled using Gaussian distributions.

The lower controller translates the desired yaw moment about the center of gravity from the upper controller into individual electric motor currents. This current is then combined

with the driver demanded electric motor current and sent to the electric motors. It also distributes the rear steering angle command between the third and fourth axles. A simple on/off controller is used to ensure the slip ratio of each electric motor does not exceed 20%.

CHAPTER 6

RESULTS AND DISCUSSION

6.1 CONTROLLER PERFORMANCE EVALUATION METHODOLOGY

Standard test maneuvers have been simulated using the TruckSim full vehicle model to test the proposed control system. Four different aspects of the control strategy have been evaluated:

1. H_{∞} controller performance is evaluated by comparing controlled and uncontrolled vehicles in double lane change, slalom, sine with dwell, J-Turn and constant radius circle events at various speeds and road friction coefficients.
2. A turning circle evaluation is performed to evaluate the performance of the zero side slip (ZSS) controller in reducing the turning circle of the vehicle
3. H_{∞} controller and ZSS controller are compared to determine a suitable switching speed range for the Gaussian activation functions
4. ZSS controller is tested during low speed double lane change and slalom events to ensure it can be used for low speed maneuvering in addition to being used for turning circle reduction

Table 6-1 lists the various simulations conducted.

Table 6-1 Event List for Controller Evaluation

SIMULATION EVENT		SPEED (kph)	ADDITIONAL INFORMATION
6.2 DYNAMIC TESTING OF THE TWO DOF H_∞ CONTROLLER			
6.2.1	Double Lane Change (NATO AVTP-1 03-160W)	100	μ=0.85
		80	μ=0.85 μ=0.35
6.2.2	30m Constant Step Slalom (NATO AVTP-1 03-30)	65	μ=0.85
		40	μ=0.85 μ=0.35
6.2.3	FMVSS 126 ESC (Sine with dwell)	80	μ=0.85 μ=0.35
6.2.4	J-Turn (120 deg steering wheel input)	80	μ=0.85
		50	μ=0.85 μ=0.35
6.2.5	Constant Radius Circle	50	μ=0.85
6.3 TURNING CIRCLE EVALUATION OF ZSS CONTROLLER			
6.3.3	Turning Circle Reduction	Crawl (< 5)	Max rear steer angles, δ _{4,ZSS,max} , compared: <ul style="list-style-type: none"> • δ_{4,ZSS,max} = Unlimited • 5 < δ_{4,ZSS,max} < 20 • δ_{4,max} = 0 (vehicle with no rear steer)
6.4 SWITCHING SPEED EVALUATION			
6.4.1	Double Lane Change (NATO AVTP-1 03-160W)	80	μ=0.85; H _∞ vs ZSS
6.4.2		60	μ=0.85; H _∞ vs ZSS
6.4.3		40	μ=0.85; H _∞ vs ZSS
6.4.4	30m Constant Step Slalom (NATO AVTP-1 03-30)	40	μ=0.85; H _∞ vs ZSS
6.5 LOW SPEED DYNAMIC EVALUATION OF ZSS CONTROLLER			
6.5.1	Double Lane Change (NATO AVTP-1 03-160W)	30	μ=0.85; ZSS vs No Control
6.5.2			μ=0.35; ZSS vs No Control
6.5.3	30m Constant Step Slalom (NATO AVTP-1 03-30)	30	μ=0.85; ZSS vs No Control
6.5.4			μ=0.35; ZSS vs No Control

6.2 DYNAMIC TESTING OF THE TWO DOF H_{∞} CONTROLLER

The dynamic tests were selected based on standards used in the industry to evaluate heavy vehicles. Speeds used during the tests were chosen to represent the entire range of operation of the LPV H_{∞} controller. Several maneuvers are run at extremely high speeds for this type of vehicle to ensure that the controller is able to deal with those types of scenarios. Events were run on an average dry road with road friction coefficient of 0.85. The majority of tests are then repeated on a low friction surface (0.35μ) to ensure robustness to varying road friction coefficients. Extremely high speed maneuvers were not run on lower friction surfaces as this is not considered a realistic vehicle operation scenario.

6.2.1 Double Lane Change (NATO AVTP-1 03-160W)

The NATO AVTP-1 03-160W double lane change maneuver is used to assess the transient lateral dynamics of a vehicle. The maneuver consists of a lane change with a relatively quick return to the original lane. Figure 6-1 describes the layout of the test course used.

NATO AVTP 03-160 W Lane-Change Test Course Layout
(AVTP = Allied Vehicle Testing Publication)

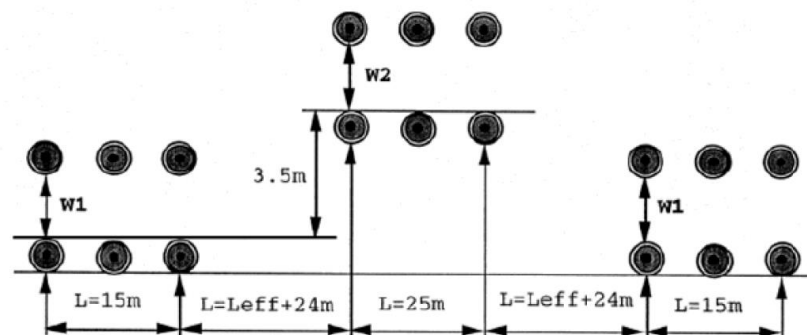


Figure 6-1 NATO AVTP-1 03-160W Double Lane Change (Courtesy GDLS-C)

6.2.1.1 Results – Double Lane Change (100 kph; $\mu=0.85$)

Vehicle speed of the controlled and uncontrolled vehicle were both maintained at approximately 100 kph as shown in Figure 6-2. A fluctuation in vehicle speed for both vehicles can be observed. It should be noted that both vehicles came into contact with the

cones and failed the maneuver. 100 kph is an extremely high speed for this combination of vehicle and maneuver. However, this test is used to showcase how the controller performed during an extreme emergency maneuver double lane change.

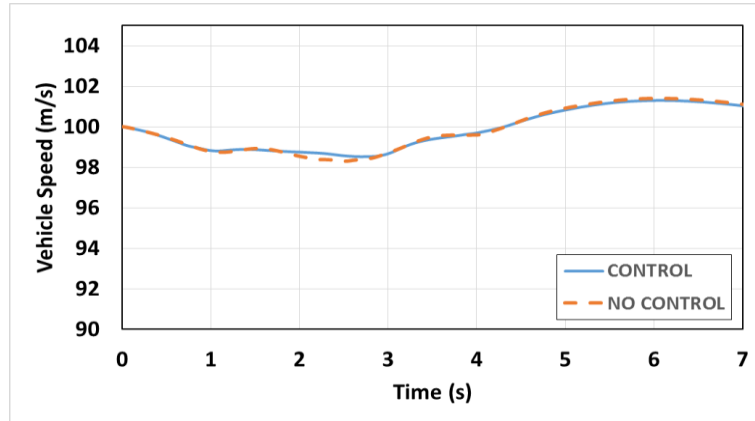


Figure 6-2 Vehicle Speeds during DLC at 100 kph ($\mu=0.85$)

Steering wheel angles of the controlled and uncontrolled vehicles are shown in Figure 6-3.

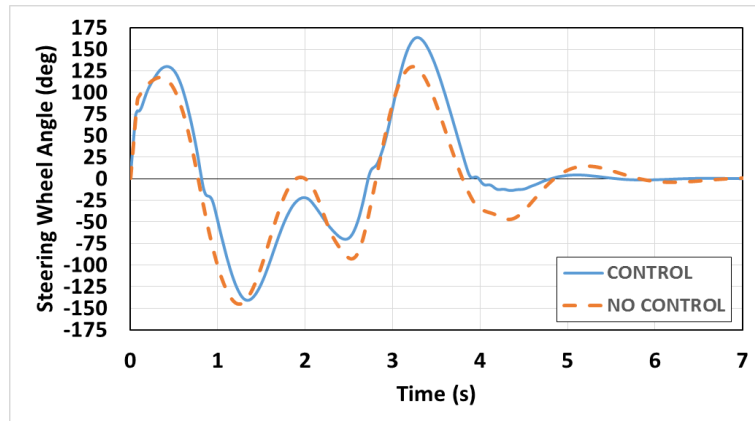
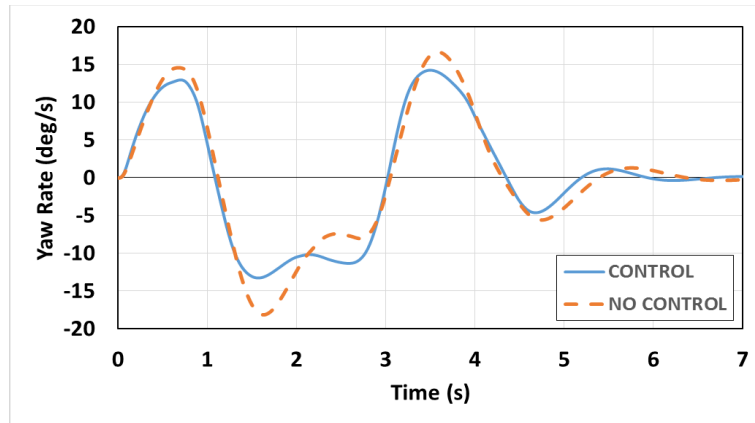


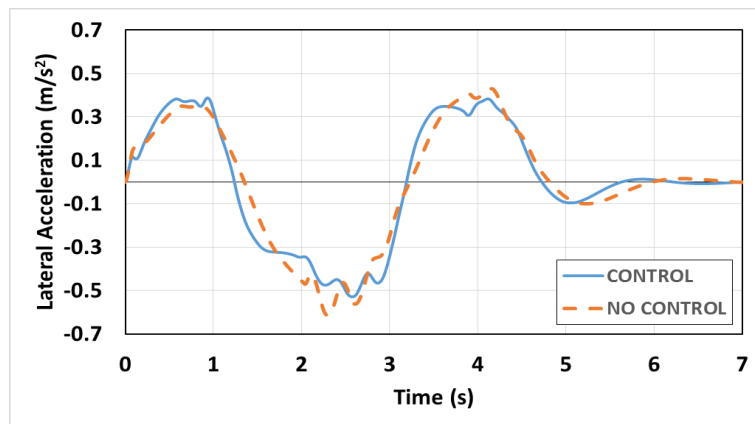
Figure 6-3 Steering Wheel Angles during DLC at 100 kph ($\mu=0.85$)

The controller was able to reduce steering effort between seconds 2 and 3. A considerable reduction in steering effort near the end of the maneuver between seconds 4 and 6 was observed. Marginally higher steering angles were required at 0.5 seconds and 3.5 seconds.

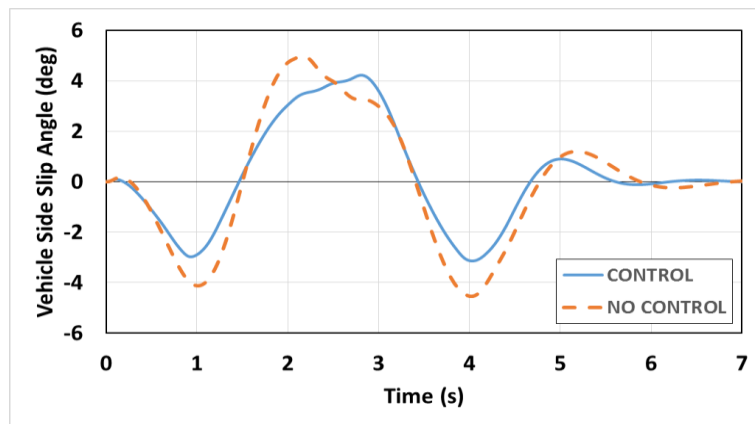
Vehicle yaw rates, lateral accelerations and side slip angles are shown in Figure 6-4.



(a)



(b)



(c)

Figure 6-4 Yaw Rate (a) Lateral Acceleration (b) and Vehicle Side Slip Angle (c) during DLC at 100 kph ($\mu=0.85$)

The controlled vehicle was able to significantly reduce yaw rate and vehicle side slip angle peaks. Lateral accelerations peaks were also slightly reduced as compared to the

uncontrolled vehicle. Rate of change of the three vehicle responses was also reduced leading to a more stable and easily controllable vehicle

Figure 6-5 shows the uncontrolled vehicle overshooting at various points in the maneuver.

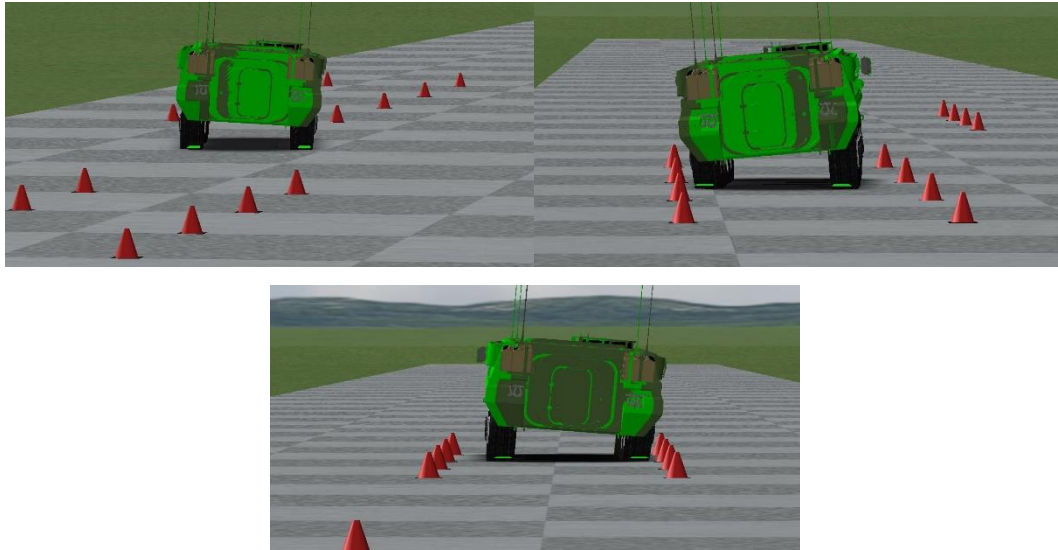


Figure 6-5 Uncontrolled (dark green) vs Controlled (light green) Vehicle during DLC at 100 kph ($\mu=0.85$) [Gate 1, 2 and 3 from Top Left to Bottom]

Controller yaw rate reference signal tracking is shown in Figure 6-6.

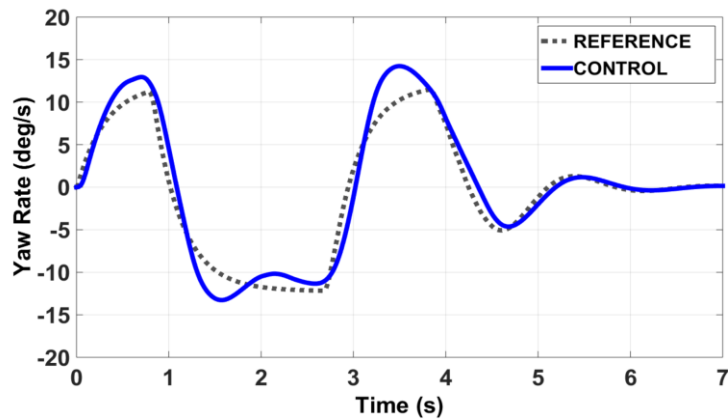
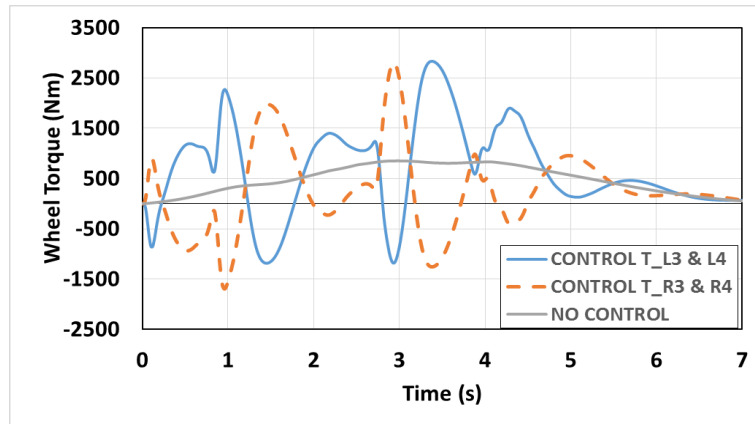


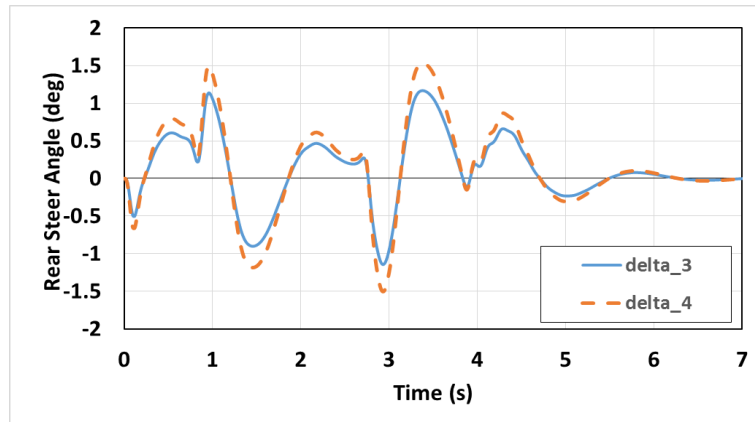
Figure 6-6 H_{∞} Yaw Rate Reference Signal Tracking during DLC at 100 kph ($\mu=0.85$)

The H_{∞} controller was able to accurately track the yaw rate reference signal during the maneuver. Slight overshoot is observed and can be attributed to the extremely high speed at which the maneuver was attempted. Considering extreme nature of this event at this speed for this type of vehicle, reference tracking is quite good.

Wheel torque and rear steer angles on the rear axles of the controlled vehicle are shown in Figure 6-7.



(a)



(b)

Figure 6-7 Wheel Torque (a) and Rear Steer Angles (b) during DLC at 100 kph ($\mu=0.85$)

A maximum wheel torque differential of approximately 4000 Nm was observed. The maximum rear steer angles during the maneuver were 1.5 and 1.1 degrees for the fourth and third axle respectively. Rear steer angles were generally in the same direction as the front steering angles.

6.2.1.2 Results – Double Lane Change (80 kph; $\mu=0.85$)

Vehicle speed of the controlled and uncontrolled vehicle were both maintained at approximately 80 kph as shown in Figure 6-8.

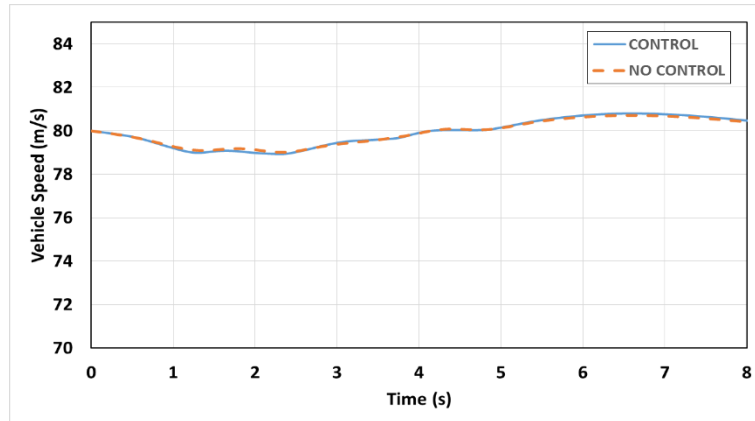


Figure 6-8 Vehicle Speeds during DLC at 80 kph ($\mu=0.85$)

The H_{∞} controller did not have any effect on vehicle speed as compared to the uncontrolled vehicle.

Steering wheel angles of the controlled and uncontrolled vehicles are shown in Figure 6-9.

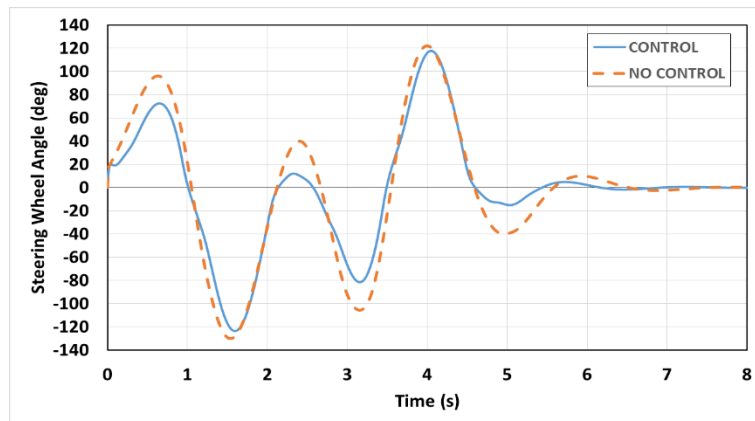
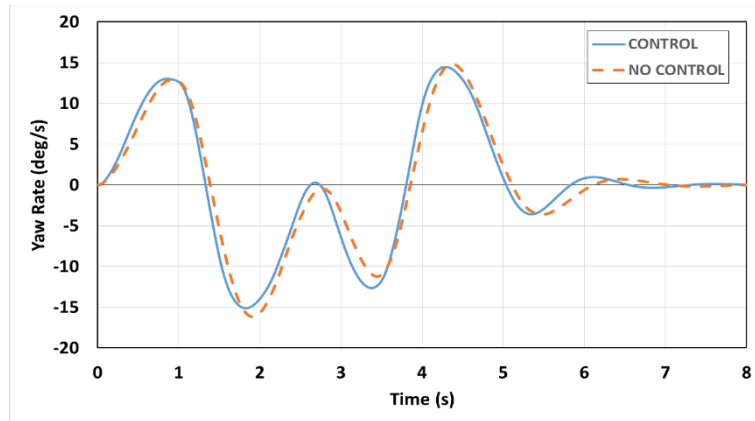


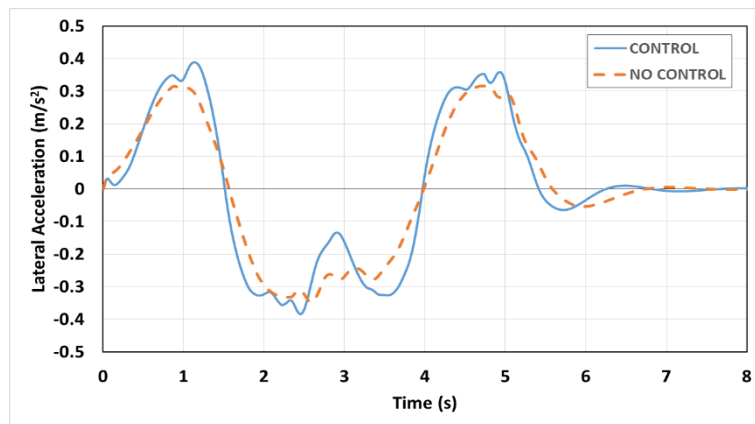
Figure 6-9 Steering Wheel Angles during DLC at 80 kph ($\mu=0.85$)

A significant reduction in steering effort can be observed for the controlled vehicle. Certain peak steering wheel angles have been reduced in excess of 50%. The rate of change of the steering wheel angle has also been reduced. This demonstrates a vehicle that is much easier to maneuver and requires less action on the part of the driver in turning the steering wheel.

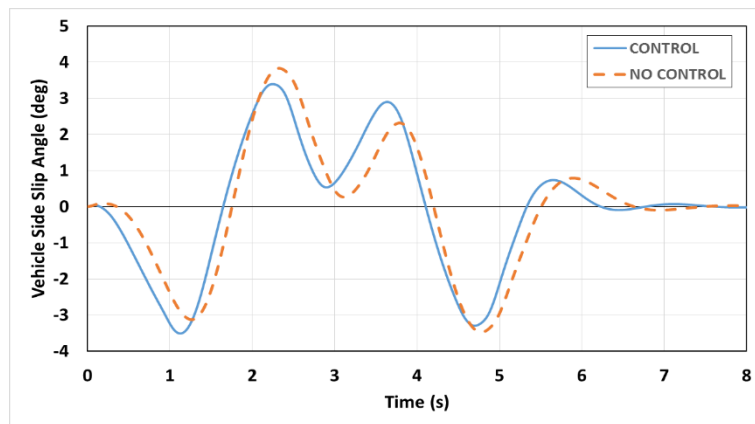
Vehicle yaw rates, lateral accelerations and side slip angles are shown in Figure 6-10.



(a)



(b)



(c)

Figure 6-10 Yaw Rate (a) Lateral Acceleration (b) and Vehicle Side Slip Angle (c) during DLC at 80 kph ($\mu=0.85$)

Yaw rate peak values were relatively unchanged between controlled and uncontrolled vehicles. However, the rate at which yaw rate was generated was higher. A phase shift was

observed between controlled and uncontrolled vehicles. This indicated a controlled vehicle with increased maneuverability. Minor increases in peak lateral accelerations were observed for the controlled vehicle. Again, a phase shift is observed in the generation of lateral acceleration. Vehicle side slip angle is relatively unchanged other than the marginally higher peak values observed at approximately 1 and 3.5 seconds for the controlled vehicle. The phase shift observed in the plot of vehicle slip angle is the most significant. The phase shifts in all three vehicle responses shows an increase in vehicle performance with no significant detriment to vehicle stability.

Controller yaw rate reference signal tracking is shown in Figure 6-11.

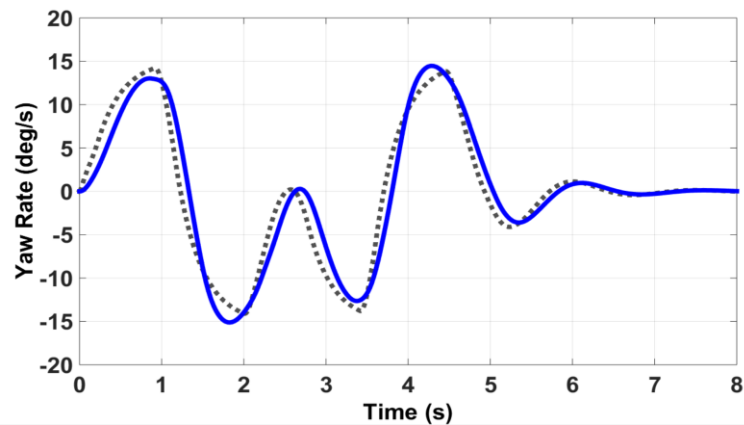
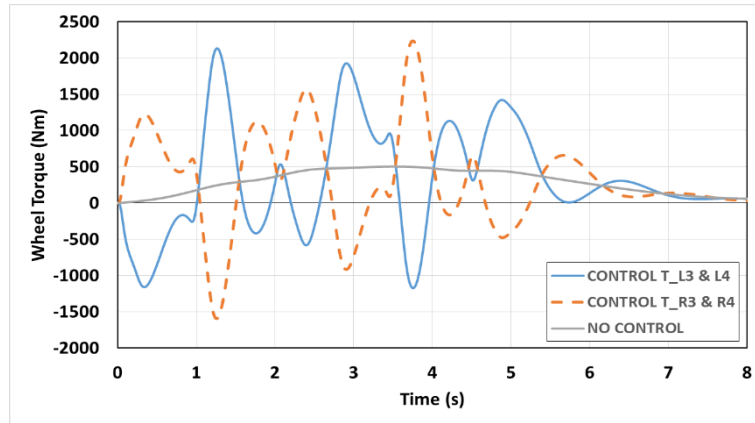


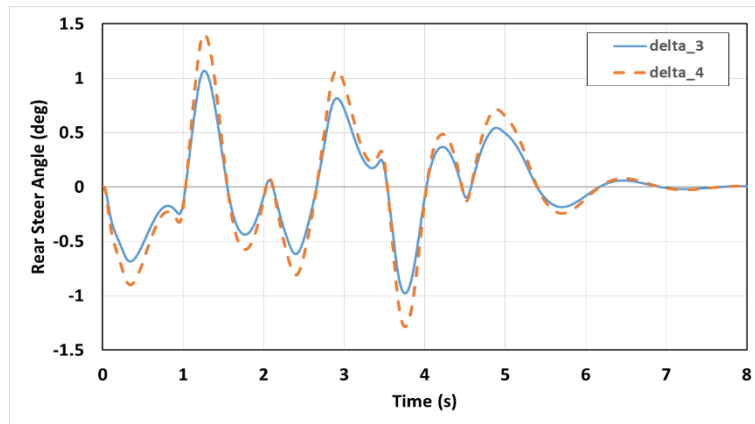
Figure 6-11 H_{∞} Yaw Rate Reference Signal Tracking during DLC at 80 kph ($\mu=0.85$)

Excellent yaw rate reference tracking was observed during the double lane change at 80 kph for the controlled vehicle.

Wheel torque and rear steer angles on the rear axles of the controlled vehicle are shown in Figure 6-12.



(a)



(b)

Figure 6-12 Wheel Torque (a) and Rear Steer Angles (b) during DLC at 80 kph ($\mu=0.85$)

A maximum wheel torque differential of approximately 3500 Nm was observed. The maximum rear steer angles during the maneuver were 1.4 and 1.0 degrees for the fourth and third axle respectively. The direction of the rear wheel steer angles was similar to those observed for the double lane change at 100 kph.

6.2.1.3 Results – Double Lane Change (80 kph; $\mu=0.35$)

Vehicle speed of the controlled and uncontrolled vehicle were both maintained at approximately 80 kph as shown in Figure 6-13. The uncontrolled vehicle becomes unstable which causes larger fluctuations in vehicle speed. This can be attributed to the low road friction coefficient used during this test.

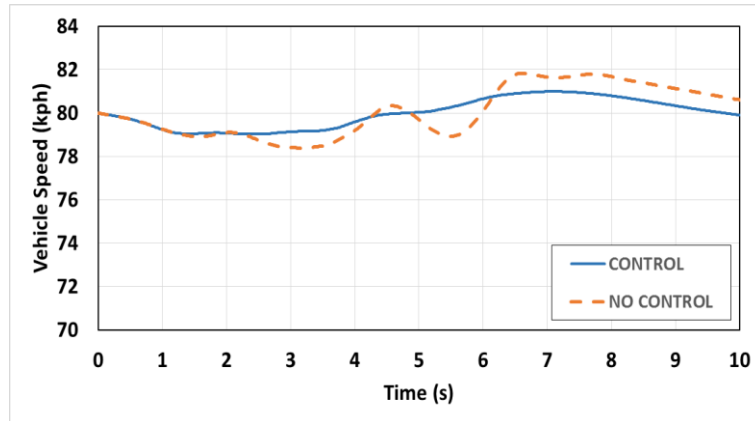


Figure 6-13 Vehicle Speeds during DLC at 80 kph ($\mu=0.35$)

Steering wheel angles of the controlled and uncontrolled vehicles are shown in Figure 6-14.

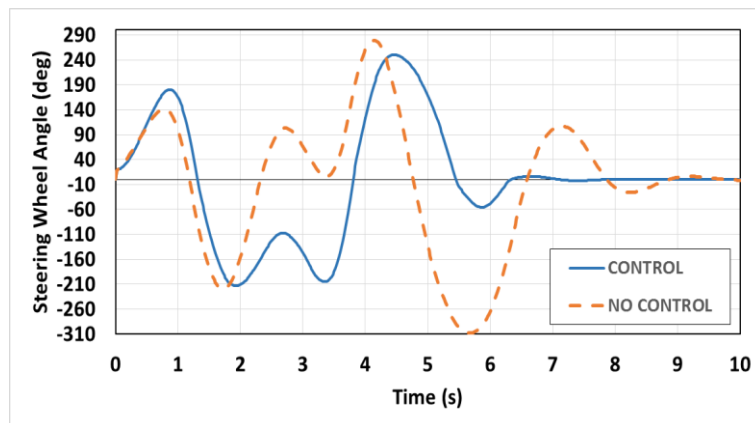
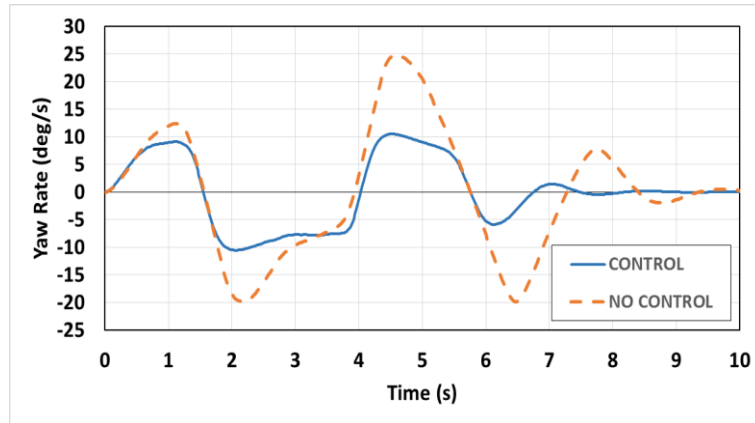


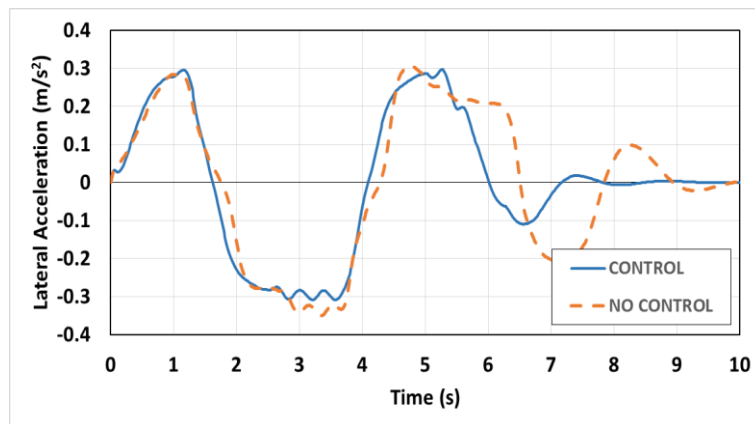
Figure 6-14 Steering Wheel Angles during DLC at 80 kph ($\mu=0.35$)

The steering wheel effort is greatly reduced for the controlled vehicle. The most significant improvement is observed between 2 and 4 seconds where the controlled vehicle's steering wheel angle varies from approximately -210 to -110 degrees and back again. In the same time interval, the uncontrolled vehicle's steering angle varied from -210 to 90 before descending to approximately 0 degrees.

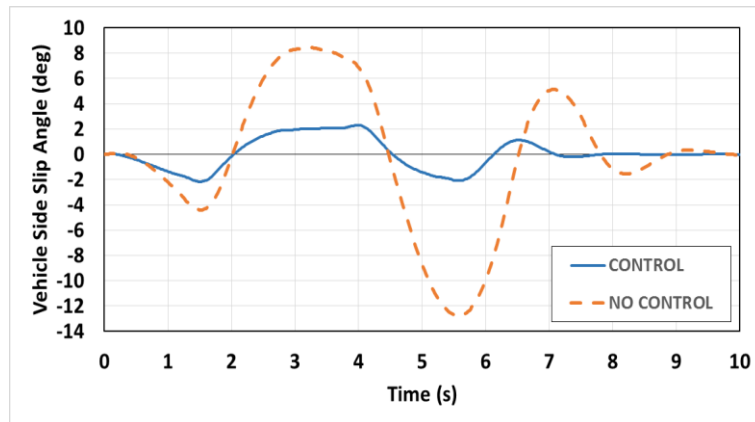
Vehicle yaw rates, lateral accelerations and side slip angles are shown in Figure 6-15.



(a)



(b)



(c)

Figure 6-15 Yaw Rate (a) Lateral Acceleration (b) and Vehicle Side Slip Angle (c) during DLC at 80 kph ($\mu=0.35$)

The proposed controller is able to greatly dampen vehicle yaw rate and vehicle side slip peak responses during the double lane change on the low road friction surface. Reduction in peak lateral acceleration values was also observed but to a lesser extent.

Figure 6-16 shows the uncontrolled vehicle overshooting at various points in the maneuver. It is clear that the controller significantly increased vehicle directional stability on the lower friction surface.

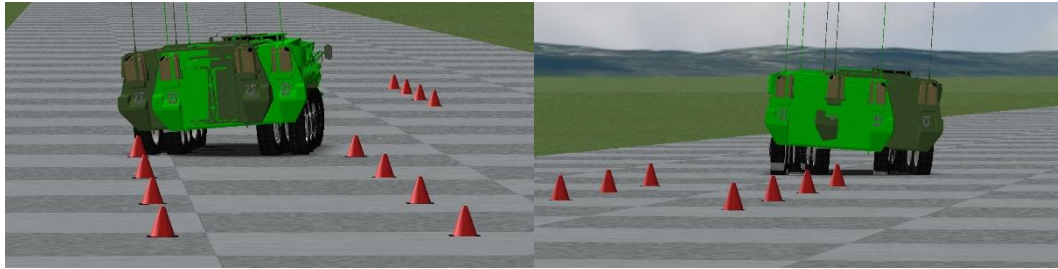


Figure 6-16 Uncontrolled (dark green) vs Controlled (light green) Vehicle during DLC at 80 kph ($\mu=0.35$) [Gate 2 and 3 from Left to Right]

Controller yaw rate reference signal tracking is shown in Figure 6-17. Overshoot is observed. This is considered acceptable as the effects of torque vectoring and rear wheel steering rely on tire force generation. With such a low road friction coefficient, the ability to generate tire forces is greatly reduced and leads to the observed overshooting. The main goal of a low friction surface test is to ensure that the controller is robust to changes in road friction and that vehicle stability is guaranteed and enhanced as compared to the uncontrolled vehicle. In these respects, the controller performance is excellent.

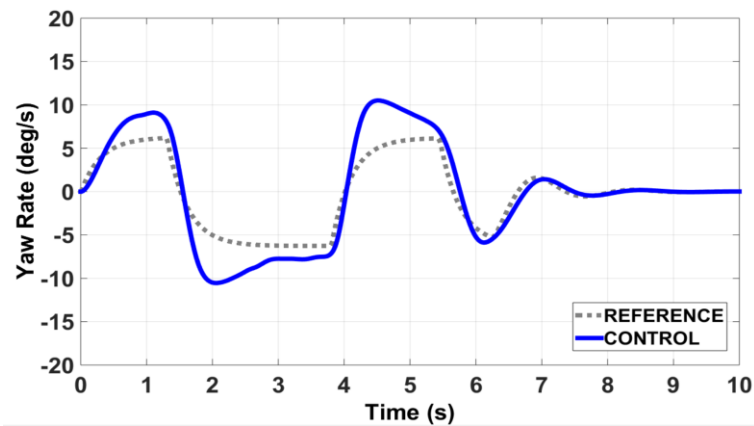
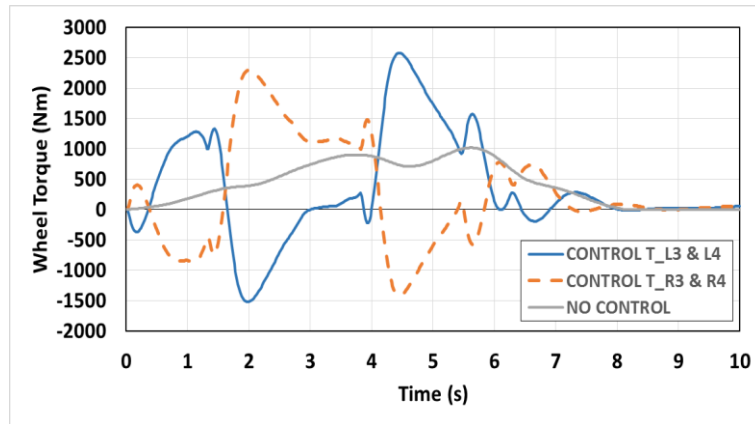
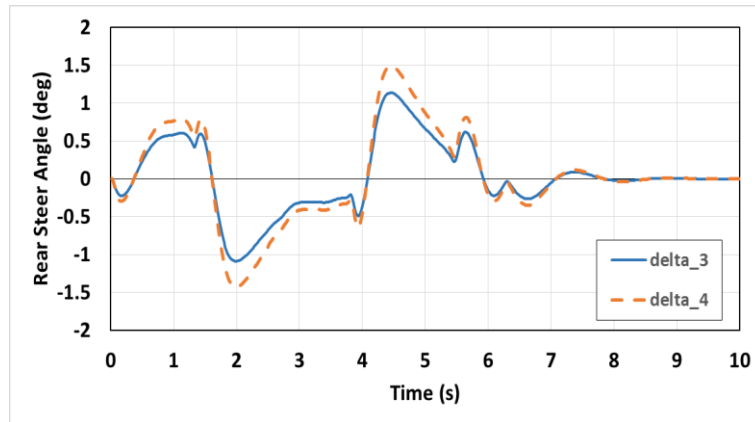


Figure 6-17 H_{∞} Yaw Rate Reference Tracking during DLC at 80 kph ($\mu=0.35$)

Wheel torque and rear steer angles on the rear axles of the controlled vehicle are shown in Figure 6-18.



(a)



(b)

Figure 6-18 Wheel Torque (a) and Rear Steer Angles (b) during DLC at 80 kph ($\mu=0.35$)

A maximum wheel torque differential of approximately 4000 Nm was observed. The maximum rear steer angles observed during the maneuver 1.5 and 1.1 degrees for the fourth and third axle respectively. The rear steering angles were generated in the same direction as the front steering angles.

6.2.2 30m Constant Step Slalom (NATO AVTP-1 03-30)

The vehicle was tested on a NATO AVTP-1 03-30 constant step slalom. Constant cone spacing of 30 meters was maintained for each pair of cones. The width between each pair

of cones was set to five meters. The test course dimensions and layout are shown in Figure 6-19.

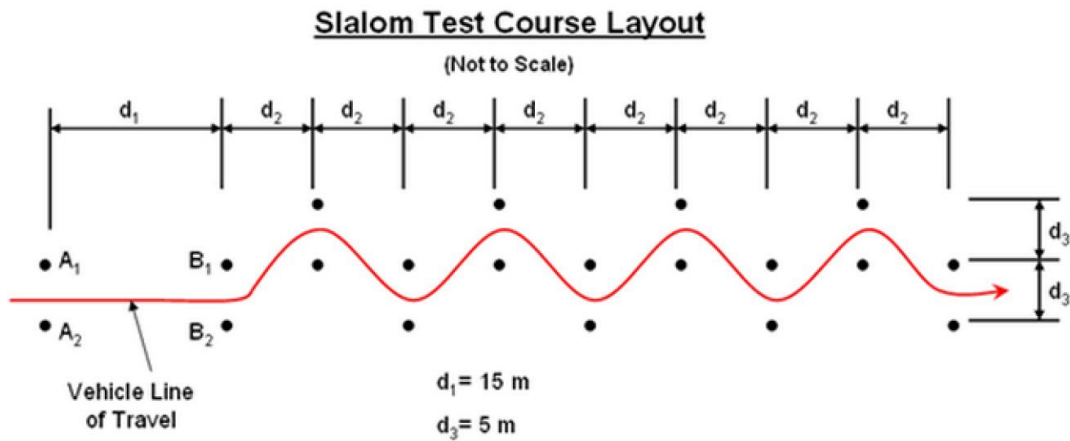


Figure 6-19 NATO AVTP-1 03-30 Constant Step Slalom Test Course Specifications

6.2.2.1 Results - Constant Step Slalom (65 kph; $\mu=0.85$)

Vehicle speed of the controlled and uncontrolled vehicles were both maintained at approximately 65 kph as shown in Figure 6-20. The uncontrolled vehicle lost stability and left the event area explaining the significant drop in speed at approximately 14 seconds.

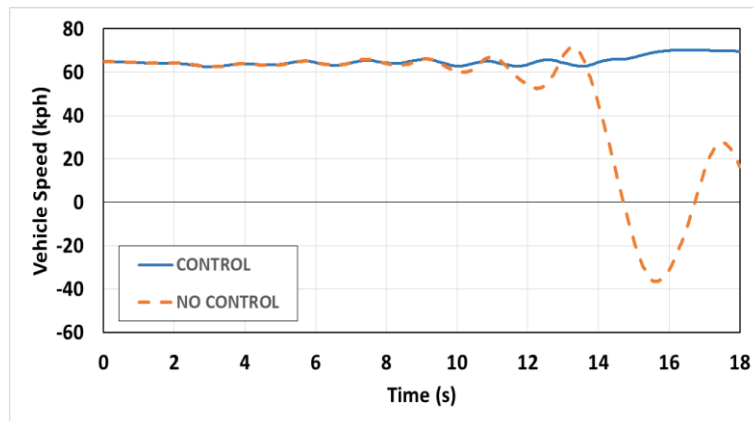


Figure 6-20 Vehicle Speeds during Slalom at 65 kph ($\mu=0.85$)

Steering wheel angles of the controlled and uncontrolled vehicles are shown in Figure 6-21.

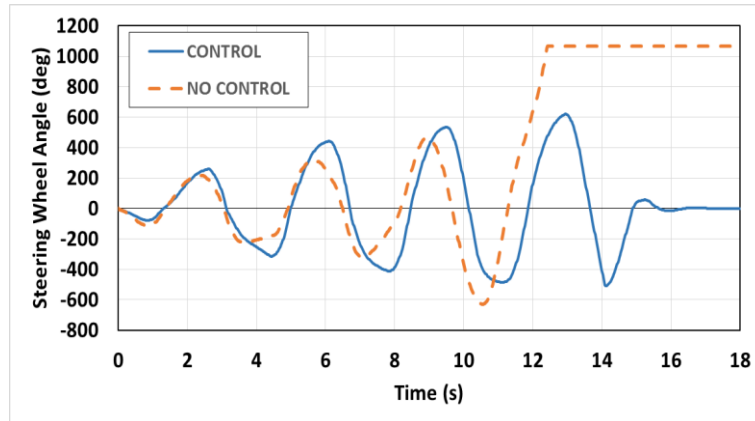


Figure 6-21 Steering Wheel Angles during Slalom at 65 kph ($\mu=0.85$)

The proposed controller is able to significantly reduce the steering wheel effort beginning at approximately 10 seconds. Before 10 seconds steering effort is increased as compared to the uncontrolled vehicle. Rear steer angles requested by the controller are in the same direction as the front steer angles. This can be interpreted as the controller trying to induce understeer in order to increase stability. As the controlled vehicle has a greater tendency to understeer this leads to the observed increased steering effort. Peak steering wheel angles after 10 seconds have been greatly reduced. The uncontrolled vehicle's steering wheel becomes locked at 12 seconds as the driver tries to control the vehicle.

The uncontrolled vehicle loses stability and leaves the event area as shown in Figure 6-22.

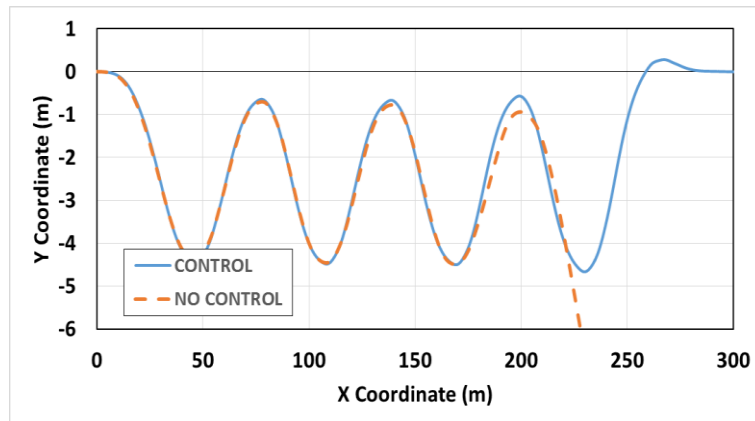
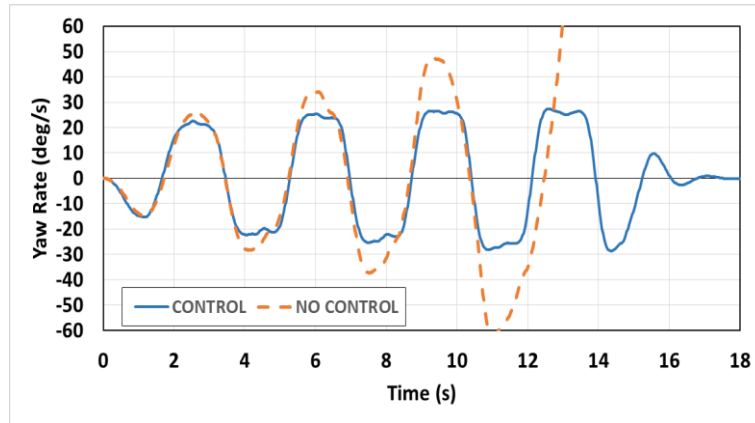
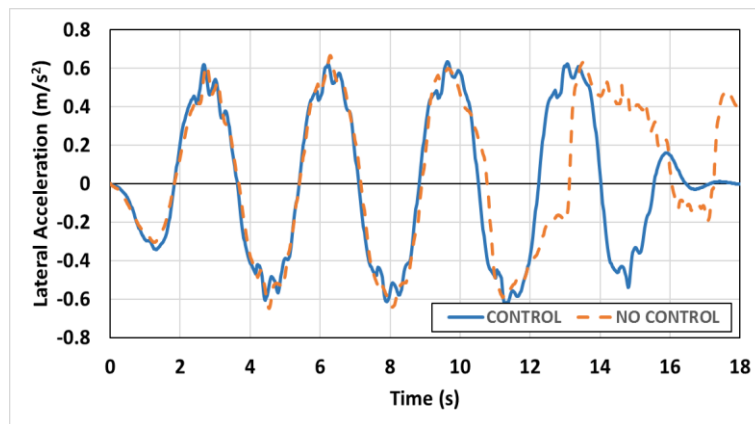


Figure 6-22 Vehicle Trajectory during Slalom at 65 kph ($\mu=0.85$)

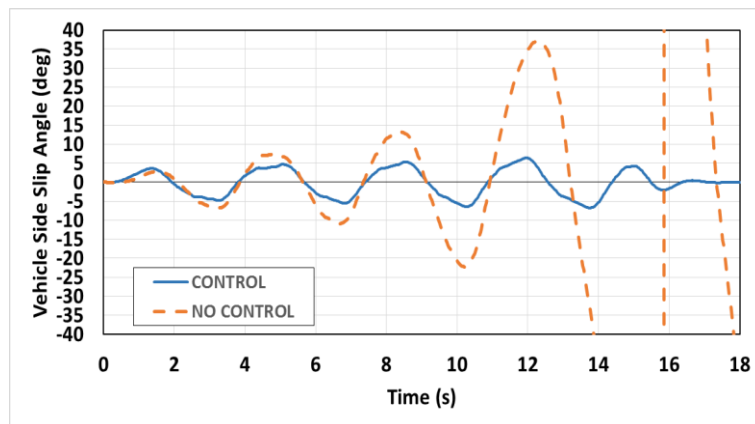
Vehicle yaw rates, lateral accelerations and side slip angles are shown in Figure 6-23.



(a)



(b)



(c)

Figure 6-23 Yaw Rate (a) Lateral Acceleration (b) and Vehicle Side Slip Angle (c) during Slalom at 65 kph ($\mu=0.85$)

The proposed controller is able to greatly dampen vehicle yaw rate and vehicle side slip peak responses during the double lane change at low road friction coefficient. The

controlled vehicle did not show a steady increase in yaw rate and vehicle side slip response amplitudes like the uncontrolled vehicle did. No effect is observed in vehicle lateral acceleration.

Figure 6-24 shows the uncontrolled vehicle overshooting and leaving the event area during the maneuver.

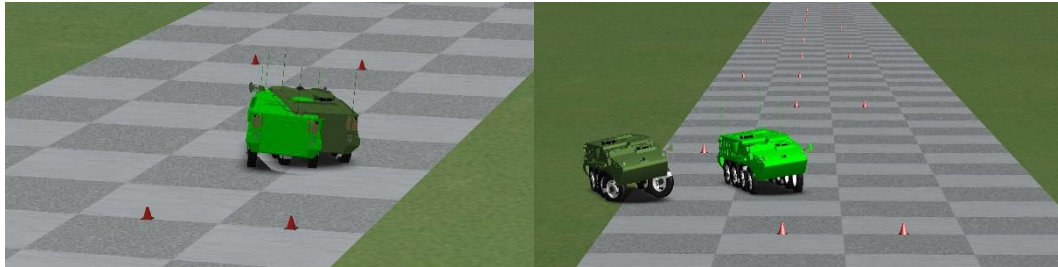


Figure 6-24 Uncontrolled (dark green) vs Controlled (light green) Vehicle during Slalom at 65 kph ($\mu=0.85$)

Controller yaw rate reference signal tracking is shown in Figure 6-25. Overshoot is observed but considered acceptable. This can be attributed to the relatively high speed at which the maneuver was attempted for this type of vehicle.

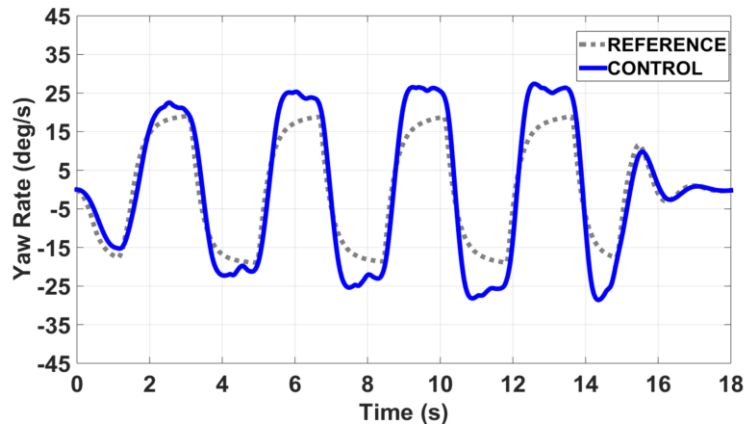
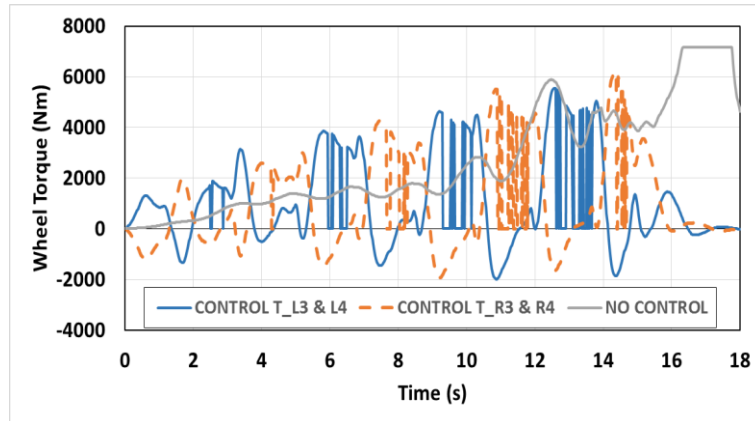
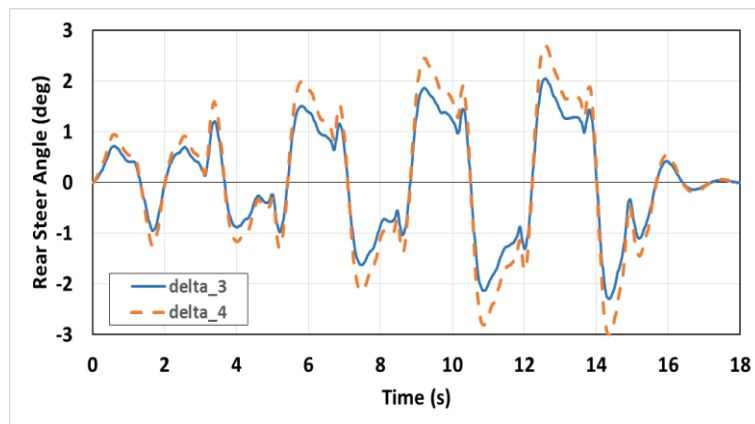


Figure 6-25 H_{∞} Yaw Rate Reference Tracking during Slalom at 65 kph ($\mu=0.85$)

Wheel torque and rear steer angles on the rear axles of the controlled vehicle are shown in Figure 6-26.



(a)



(b)

Figure 6-26 Wheel Torque (a) and Rear Steer Angles (b) during Slalom at 65 kph ($\mu=0.85$)

A maximum wheel torque differential of approximately 7800 Nm was observed. Slip controller intervened during the maneuver. This can be seen when the wheel torque suddenly drops to zero Nm during the event. Intervention occurred on both sides of the vehicle when either side tire normal load was significantly decreased due to lateral load transfer during the event. The maximum rear steer angles observed during the maneuver 3 and 2.3 degrees for the fourth and third axle respectively. Rear steering angles were generally in the same direction as the front steering angles. It should be noted that the torque vectoring and rear steer angles commanded for this maneuver were the highest of any of the maneuvers attempted.

6.2.2.2 Results - Constant Step Slalom (40 kph; $\mu=0.85$)

Vehicle speed of the controlled and uncontrolled vehicle were both maintained at approximately 40 kph as shown in Figure 6-27. The proposed controller had no effect on vehicle speed.

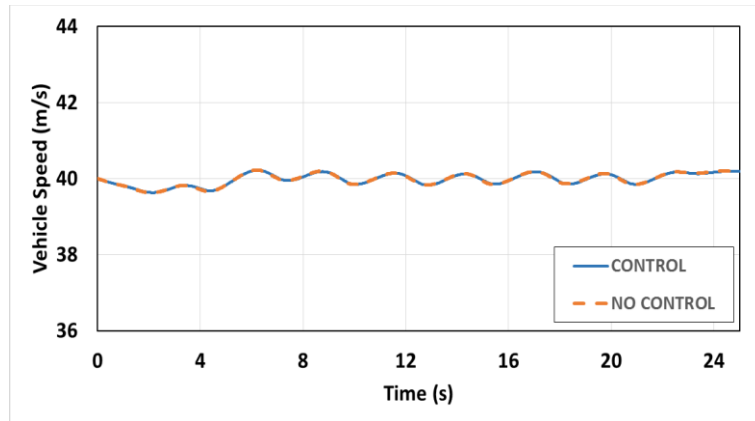


Figure 6-27 Vehicle Speeds during Slalom at 40 kph ($\mu=0.85$)

Steering wheel angles of the controlled and uncontrolled vehicles are shown in Figure 6-28.

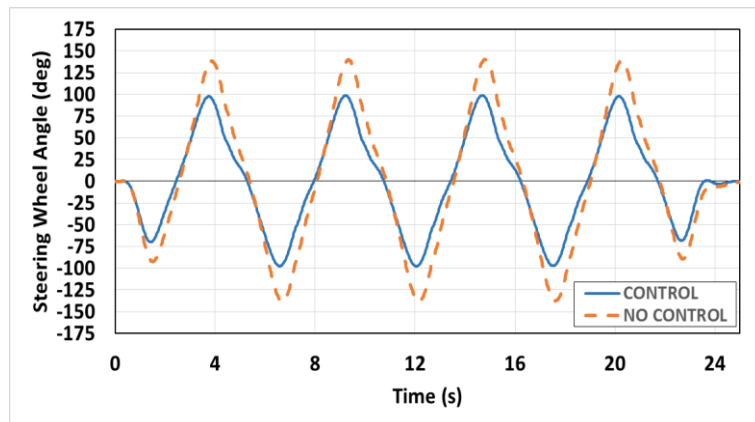
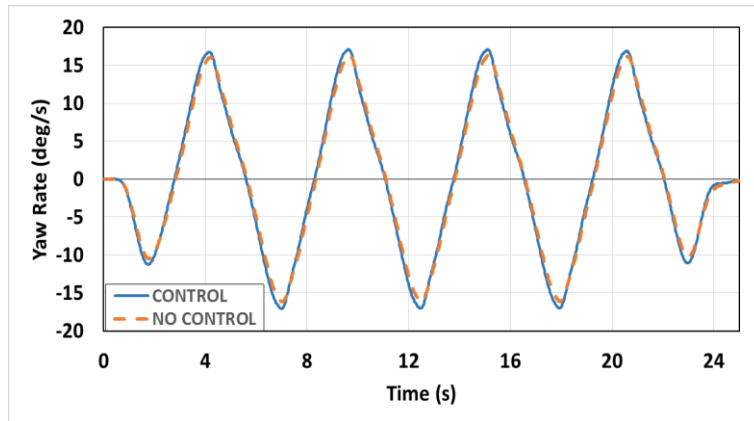


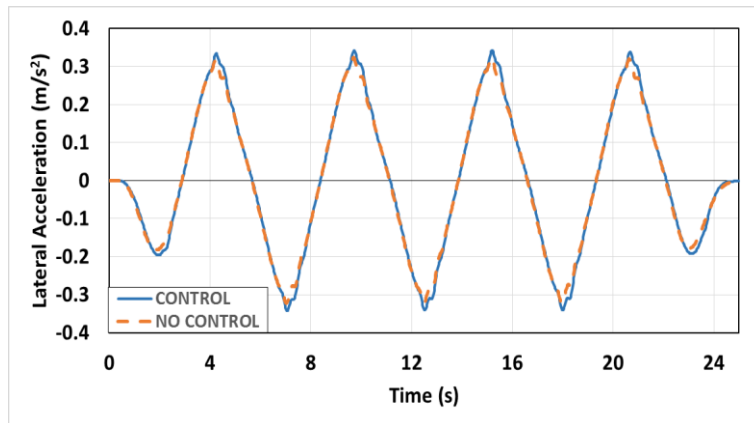
Figure 6-28 Steering Wheel Angles during Slalom at 40 kph ($\mu=0.85$)

The proposed controller significantly reduced steering wheel effort. A maximum reduction of approximately 30% was observed in the steering wheel angle. Steering wheel rate of change was also reduced. The controlled vehicle proved much easier for the driver to maneuver through the slalom course.

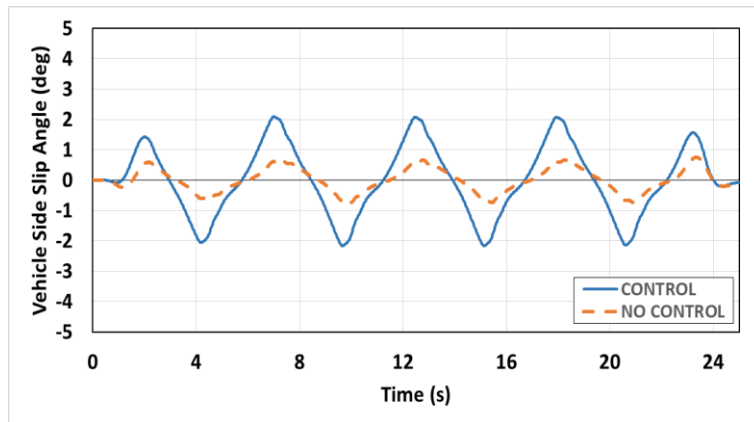
Vehicle yaw rates, lateral accelerations and side slip angles are shown in Figure 6-29.



(a)



(b)



(c)

Figure 6-29 Yaw Rate (a) Lateral Acceleration (b) and Vehicle Side Slip Angle (c) during Slalom at 40 kph ($\mu=0.85$)

There was no significant change in yaw rate and lateral acceleration responses observed between the controlled and uncontrolled vehicles. Vehicle side slip angles were increased for the controlled vehicle as well as the rate of change of the side slip confirming that the controlled vehicle was more maneuverable than the uncontrolled vehicle at 40 kph.

Controller yaw rate reference signal tracking is shown in Figure 6-30.

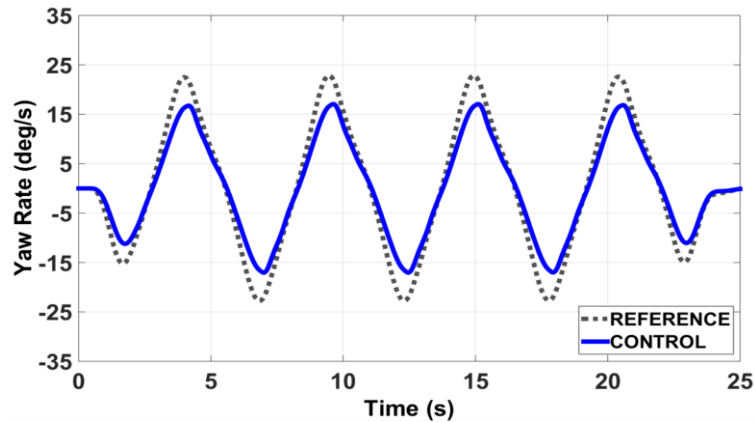
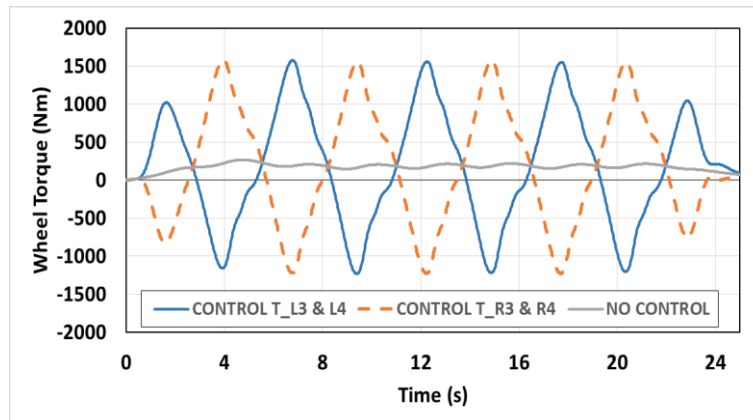


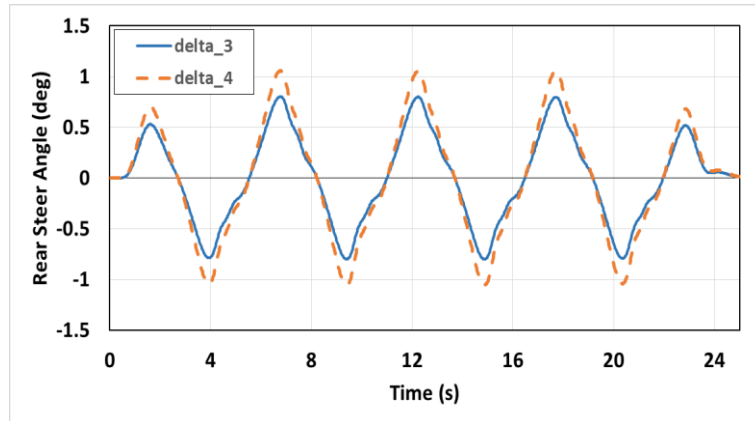
Figure 6-30 H_{∞} Yaw Rate Reference Tracking during Slalom at 40 kph ($\mu=0.85$)

The controller was able to successfully track the reference signal during the 40 kph slalom maneuver. Although peak values were slightly lower than the yaw rate reference model. This can be attributed to the highly transient nature of the slalom course and the significant yaw inertia of the test vehicle.

Wheel torque and rear steer angles on the rear axles of the controlled vehicle are shown in Figure 6-31.



(a)



(b)

Figure 6-31 Wheel Torque (a) and Rear Steer Angles (b) during Slalom at 40 kph ($\mu=0.85$)

A maximum wheel torque differential of approximately 2500 Nm was observed. The maximum rear steer angles observed during the maneuver 1 and 0.76 degrees for the fourth and third axle respectively. Rear steer angles were in the opposite direction of the front axle steer angles.

6.2.2.3 Results - Constant Step Slalom (40 kph; $\mu=0.35$)

Vehicle speed of the controlled and uncontrolled vehicle were both maintained at approximately 40 kph as shown in Figure 6-32. The proposed controller had no effect on vehicle speed.

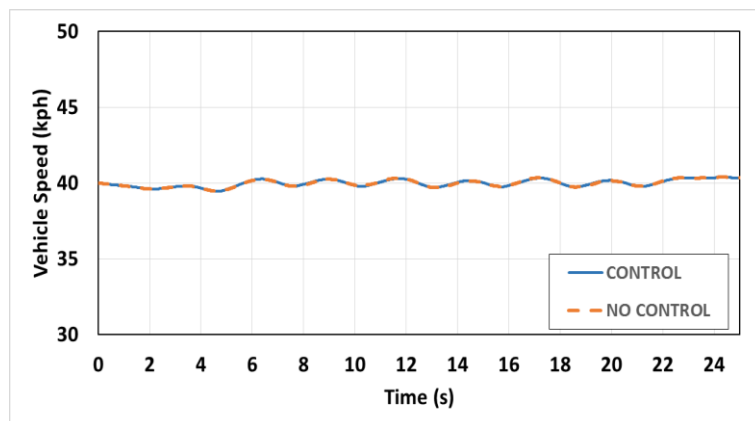


Figure 6-32 Vehicle Speeds during Slalom at 40 kph ($\mu=0.35$)

Steering wheel angles of the controlled and uncontrolled vehicles are shown in Figure 6-33.

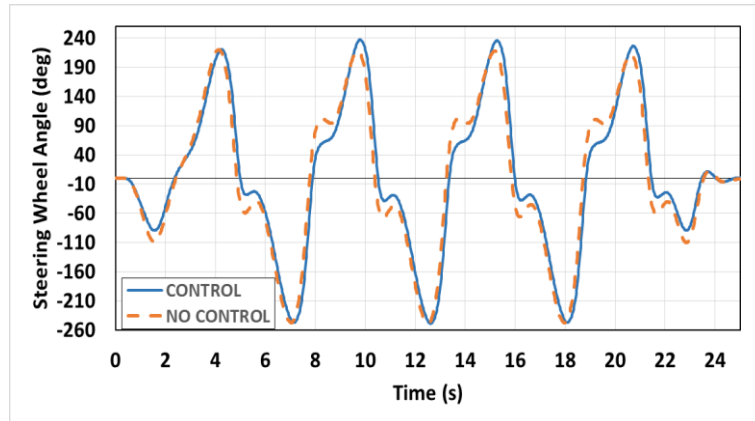
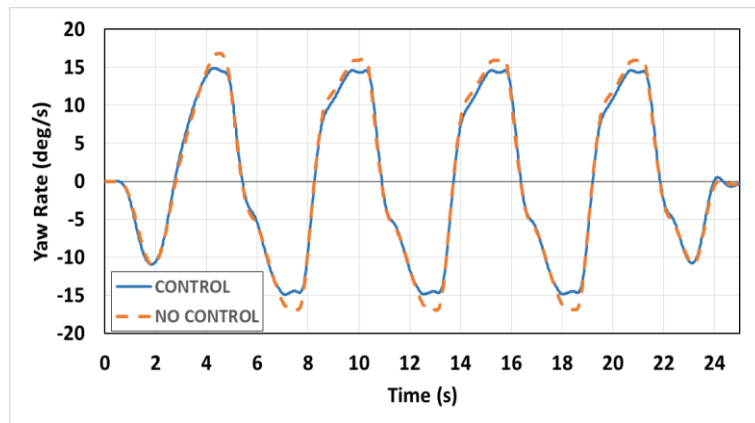


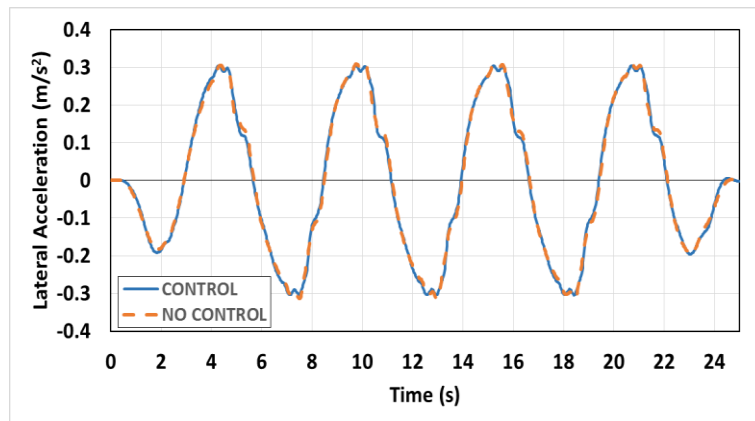
Figure 6-33 Steering Wheel Angles during Slalom at 40 kph ($\mu=0.35$)

Steering effort was approximately the same for the controlled and uncontrolled vehicles. No significant differences were observed.

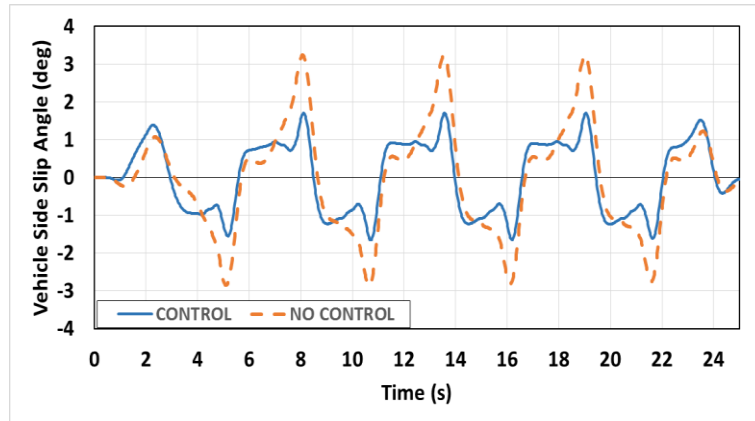
Vehicle yaw rates, lateral accelerations and side slip angles are shown in Figure 6-34.



(a)



(b)



(c)

Figure 6-34 Yaw Rate (a) Lateral Acceleration (b) Vehicle Side Slip Angle (c) during Slalom at 40 kph ($\mu=0.35$)

A slight decrease in peak values of vehicle yaw rate were observed for the controlled vehicle. The controller greatly reduced vehicle side slip angle on the low friction surface. There was no significant effect on lateral acceleration.

Controller yaw rate reference signal tracking is shown in Figure 6-35.

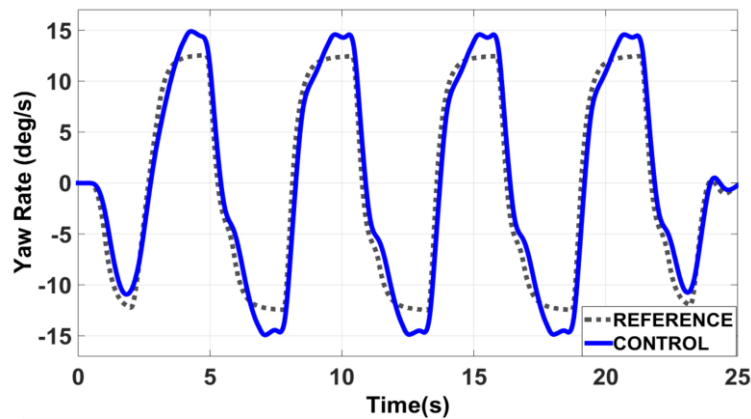
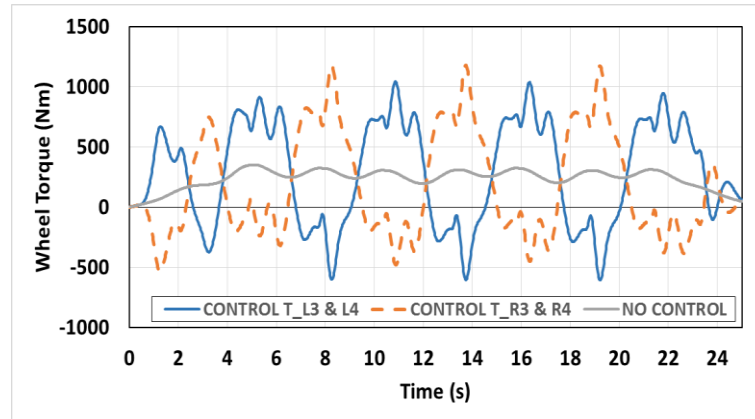


Figure 6-35 H_{∞} Yaw Rate Reference Tracking during Slalom at 40 kph ($\mu=0.35$)

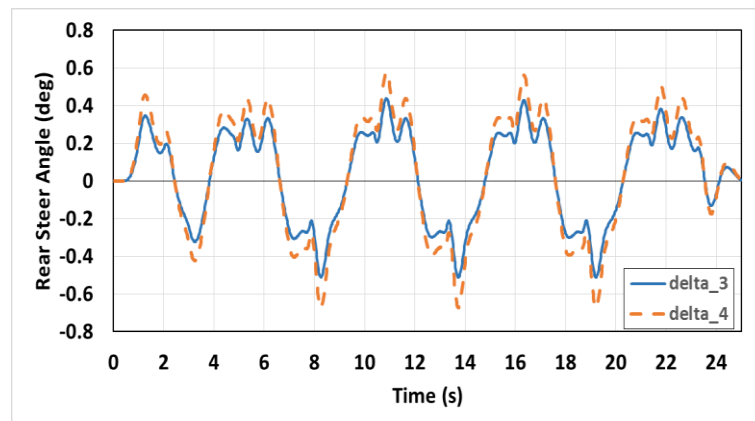
Slight overshoot was observed in the controller yaw rate reference tracking. This is considered acceptable as the effects of torque vectoring and rear wheel steering rely on tire force generation. With such a low road friction coefficient, the ability to generate tire forces is greatly reduced and leads to the observed overshooting. The main goal of a low friction surface test is to ensure that the controller is robust to changes in road friction and that

vehicle stability is guaranteed and enhanced as compared to the uncontrolled vehicle. In these respects, the controller performance is excellent.

Wheel torque and rear steer angles on the rear axles of the controlled vehicle are shown in Figure 6-36.



(a)



(b)

Figure 6-36 Wheel Torque (a) and Rear Steer Angle (b) during Slalom at 40 kph ($\mu=0.35$)

A maximum wheel torque differential of approximately 2000 Nm was observed. The maximum rear steer angles observed during the maneuver 0.6 and 0.45 degrees for the fourth and third axle respectively. Rear steer angles were in the same direction as the front axle steer angles.

6.2.3 FMVSS 126 ESC

A modified version of Federal Motor Vehicle Safety Standard (FMVSS) No. 126 [46] has been used to evaluate controller performance. The test consists of a steering wheel input and not a test course that needs to be followed. The input consists of a sine wave with a 0.7 Hz frequency and a 400 millisecond delay in the second half of the wave. Peak steering wheel angle values of 234 degrees are used. The steering wheel input as function of time is shown in Figure 6-37.

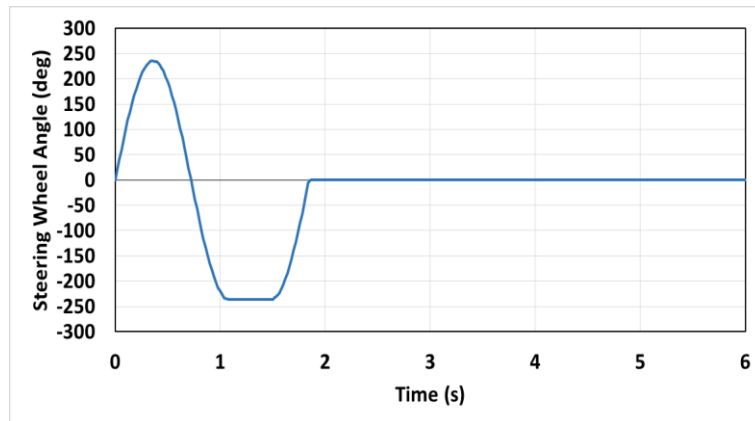


Figure 6-37 Steering Wheel Input during FMVSS Maneuvers

6.2.3.1 Results - FMVSS 126 ESC (80 kph; $\mu=0.85$)

Vehicle speed of the controlled and uncontrolled vehicle were both maintained at approximately 80 kph as shown in Figure 6-38. Due to the very extreme nature of this event, vehicle speeds fluctuated in higher ranges than other simulated events.

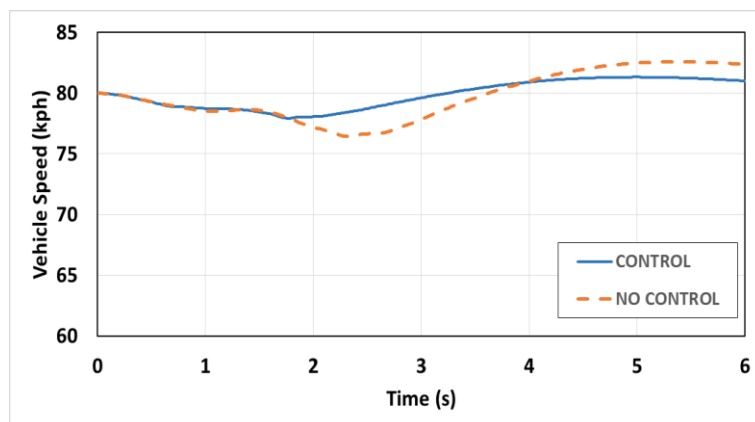
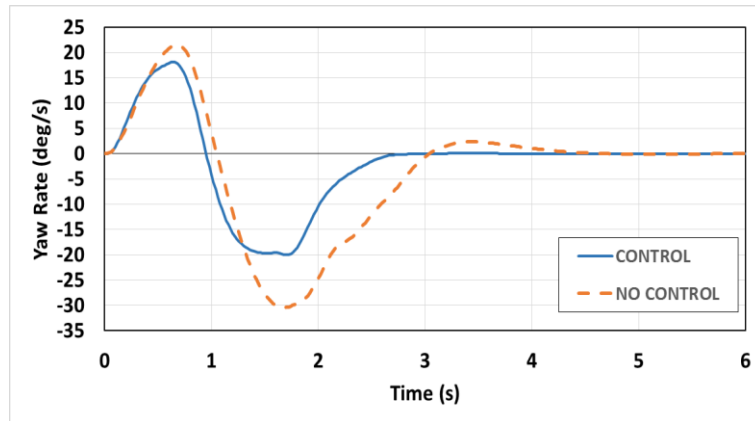
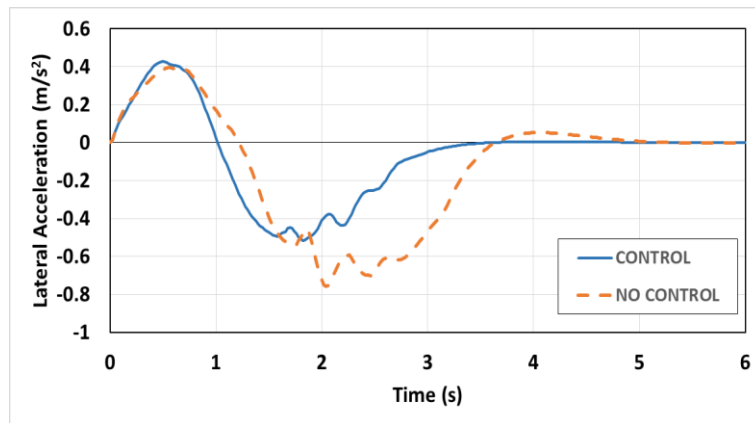


Figure 6-38 Vehicle Speeds during FMVSS at 80 kph ($\mu=0.85$)

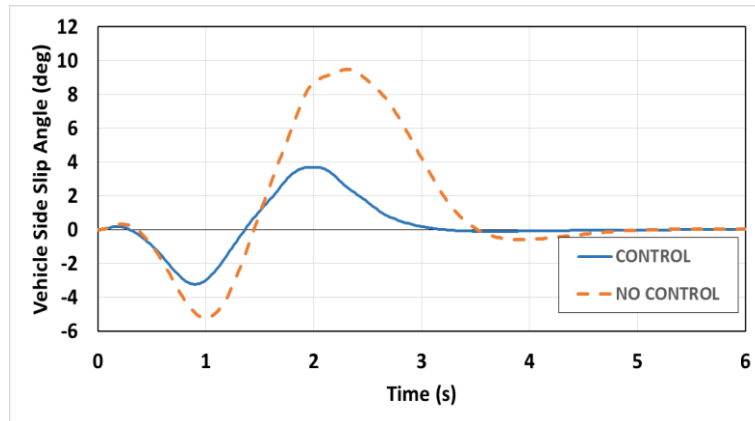
Vehicle yaw rates, lateral accelerations and side slip angles are shown in Figure 6-39.



(a)



(b)



(c)

Figure 6-39 Yaw Rate (a) Lateral Acceleration (b) and Vehicle Side Slip Angle (c) during FMVSS at 80 kph ($\mu=0.85$)

The proposed H_∞ controller was able to greatly increase vehicle stability during the maneuver. Vehicle yaw rates, lateral acceleration and vehicle side slip angle were greatly damped as compared to the uncontrolled vehicle.

Controller yaw rate reference signal tracking is shown in Figure 6-40.

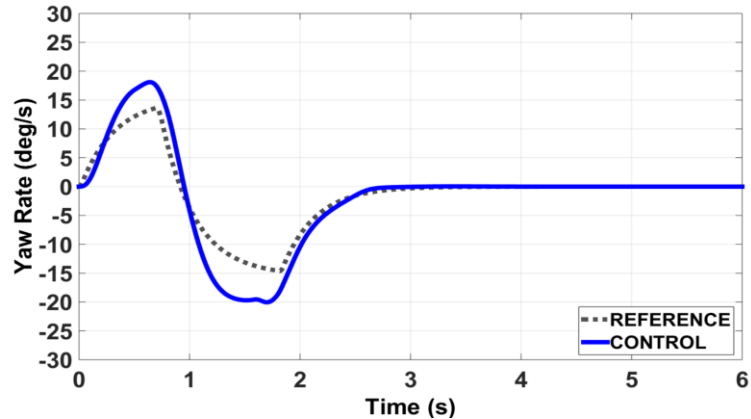
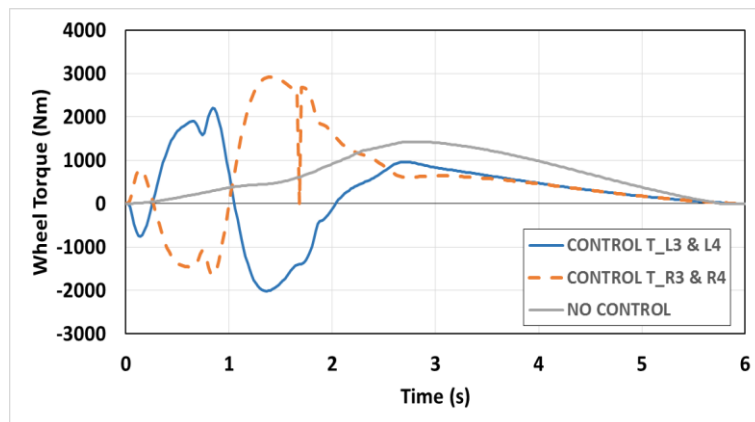


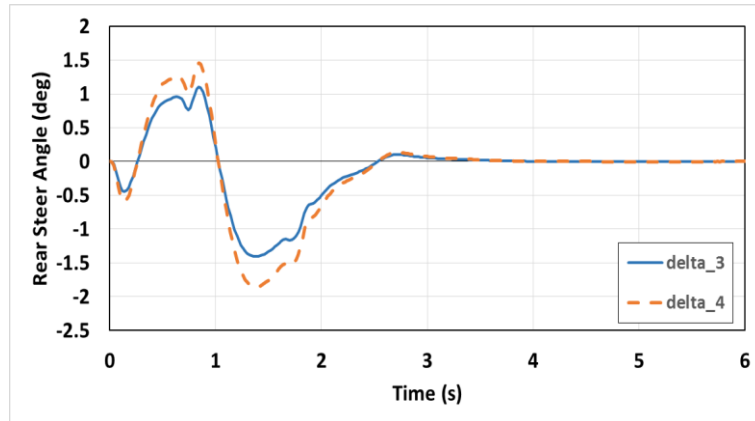
Figure 6-40 H_∞ Yaw Rate Reference Tracking during FMVSS at 80 kph ($\mu=0.85$)

The H_∞ controller was able to accurately track the yaw rate reference signal during the maneuver. Overshoot is observed and can be attributed to the extremely high speed at which the maneuver was attempted for a vehicle of this weight and inertia. Considering the severity of the FMVSS maneuver at 80 kph, reference tracking is considered acceptable.

Wheel torque and rear steer angles on the rear axles of the controlled vehicle are shown in Figure 6-41.



(a)



(b)

Figure 6-41 Wheel Torque (a) and Rear Steer Angles (b) during FMVSS at 80 kph ($\mu=0.85$)

A maximum wheel torque differential of approximately 5000 Nm was observed. The maximum rear steer angles observed during the maneuver 1.8 and 1.4 degrees for the fourth and third axle respectively. Rear steer angles were in the same direction as the front axle steer angles.

6.2.3.2 Results - FMVSS 126 ESC (80 kph; $\mu=0.35$)

Vehicle speed of the controlled and uncontrolled vehicle were both maintained at approximately 80 kph as shown in Figure 6-42. Due to the very extreme nature of this event and low road friction coefficient, vehicle speeds fluctuated in higher ranges than other simulated events.

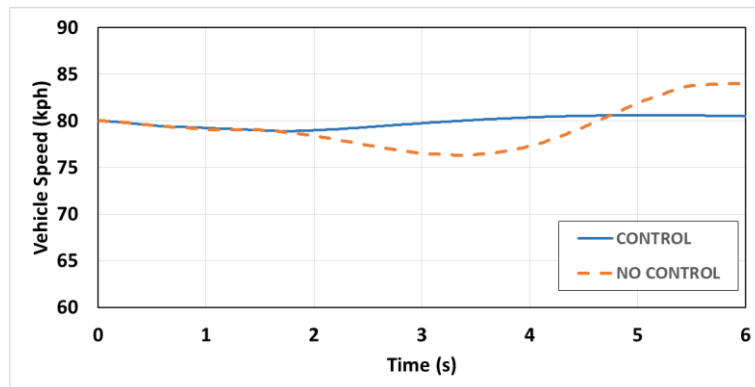
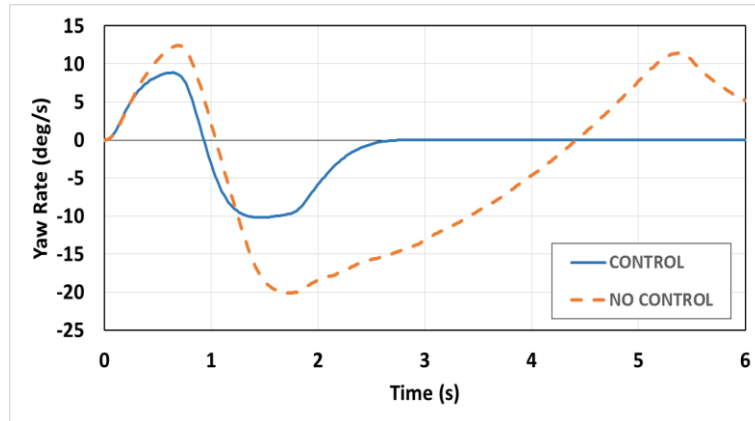
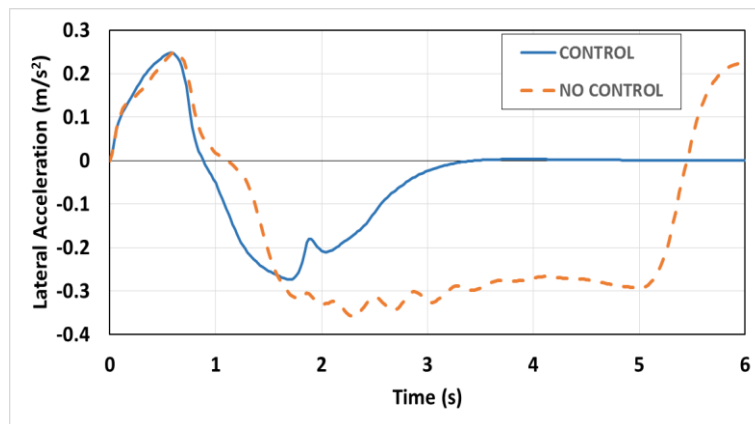


Figure 6-42 Vehicle Speeds during FMVSS at 80 kph ($\mu=0.35$)

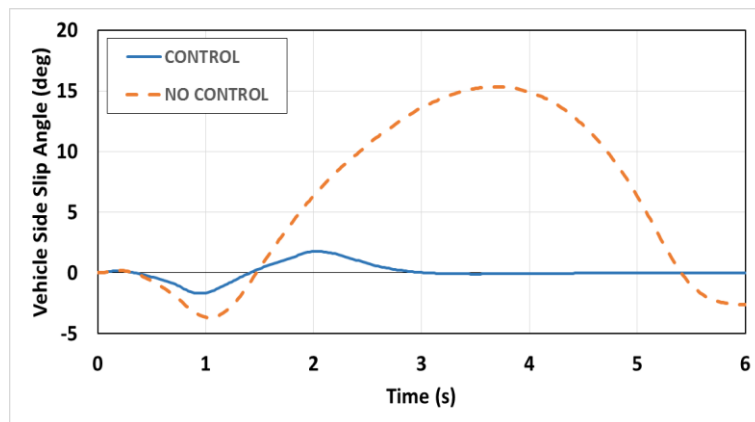
Vehicle yaw rates, lateral accelerations and side slip angles are shown in Figure 6-43.



(a)



(b)



(c)

Figure 6-43 Yaw Rate (a) Lateral Acceleration (b) and Vehicle Side Slip Angle (c) during FMVSS at 80 kph ($\mu=0.35$)

The proposed H_{∞} controller was able to greatly increase vehicle stability during the simulation. Vehicle yaw rates, lateral acceleration and vehicle side slip angle were greatly

damped as compared to the uncontrolled vehicle. This confirms that the controller is robust for low road friction coefficients.

Controller yaw rate reference signal tracking is shown in Figure 6-44.

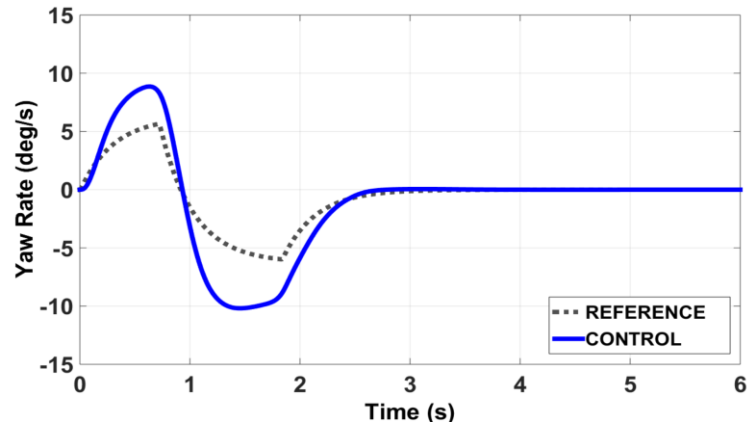
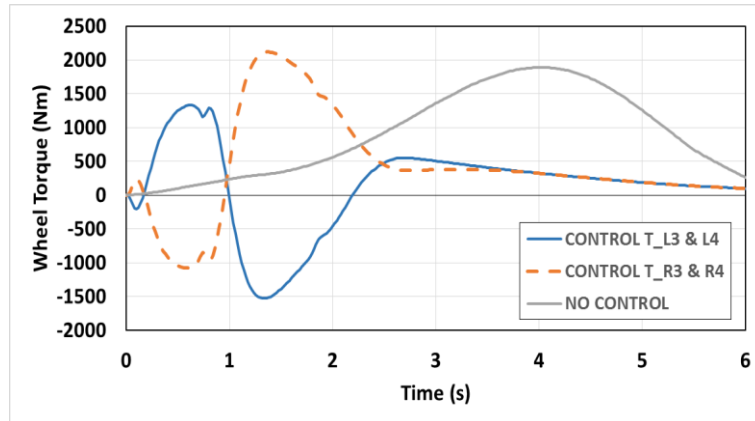


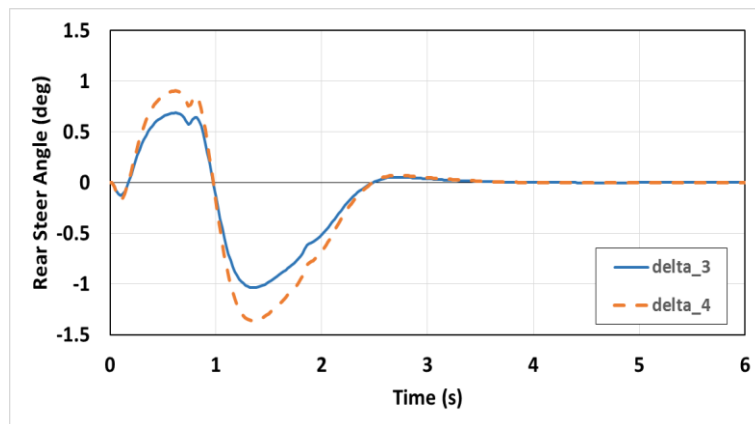
Figure 6-44 H_{∞} Yaw Rate Reference Tracking during FMVSS at 80 kph ($\mu=0.35$)

The H_{∞} controller was able to accurately track the yaw rate reference signal during the maneuver. Overshoot is observed and can be attributed to the extremely high speed at which the maneuver was attempted for a vehicle of this weight and inertia. Additionally, with such a low road friction coefficient, the ability to generate tire forces is greatly reduced and leads to the observed overshooting. The main goal of a low friction surface test is to ensure that the controller is robust to changes in road friction and that vehicle stability is guaranteed and enhanced as compared to the uncontrolled vehicle. In these respects, the controller performance is excellent.

Wheel torque and rear steer angles on the rear axles of the controlled vehicle are shown in Figure 6-45.



(a)



(b)

Figure 6-45 Wheel Torque (a) and Rear Steer Angles (b) during FMVSS at 80 kph ($\mu=0.85$)

A maximum wheel torque differential of approximately 3500 Nm was observed. The maximum rear steer angles observed during the maneuver 1.3 and 1.0 degrees for the fourth and third axle respectively. Rear steer angles were in the same direction as the front axle steer angles.

6.2.4 J-Turn (120 deg step steer input)

A J-Turn test has been used to evaluate vehicle path tracking ability when a sudden steering wheel angle input is applied. The step steering wheel input is shown in Figure 6-46.

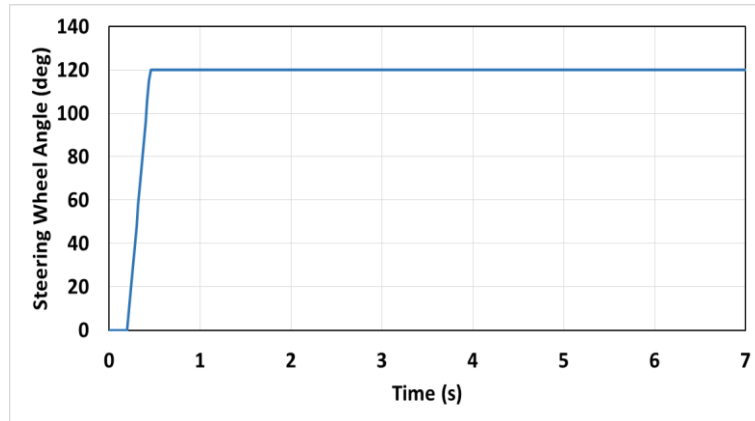


Figure 6-46 Step Steering Wheel Input for J-Turn Maneuver

6.2.4.1 Results – J-Turn (80 kph; $\mu=0.85$)

Vehicle speed of the controlled and uncontrolled vehicle were both maintained at approximately 80 kph as shown in Figure 6-47.

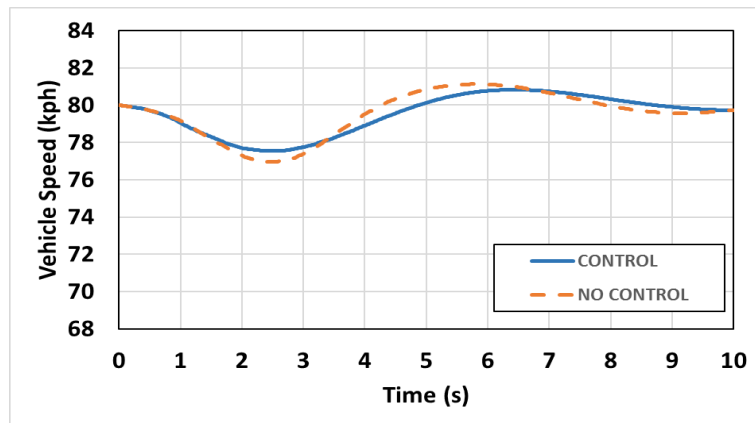


Figure 6-47 Vehicle Speeds during J-Turn at 80 kph ($\mu=0.85$)

The controlled and uncontrolled vehicle paths are shown in Figure 6-48.

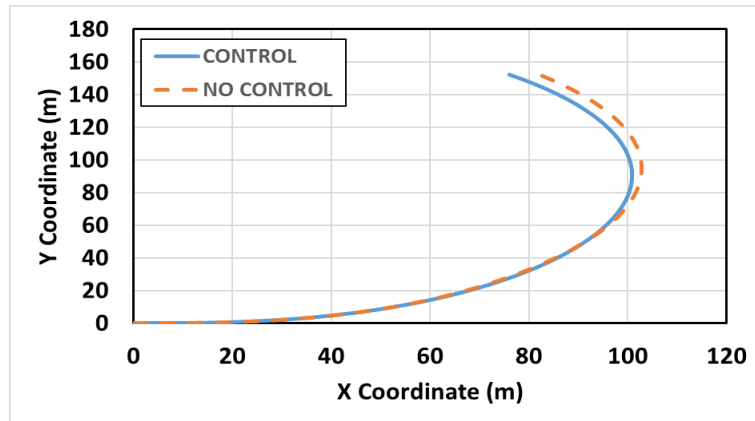


Figure 6-48 Vehicle Trajectory during J-Turn at 80 kph ($\mu=0.85$)

The controlled vehicle was able to follow a path with a smaller radius of curvature than the uncontrolled vehicle. This increase in maneuverability is shown in Figure 6-49.

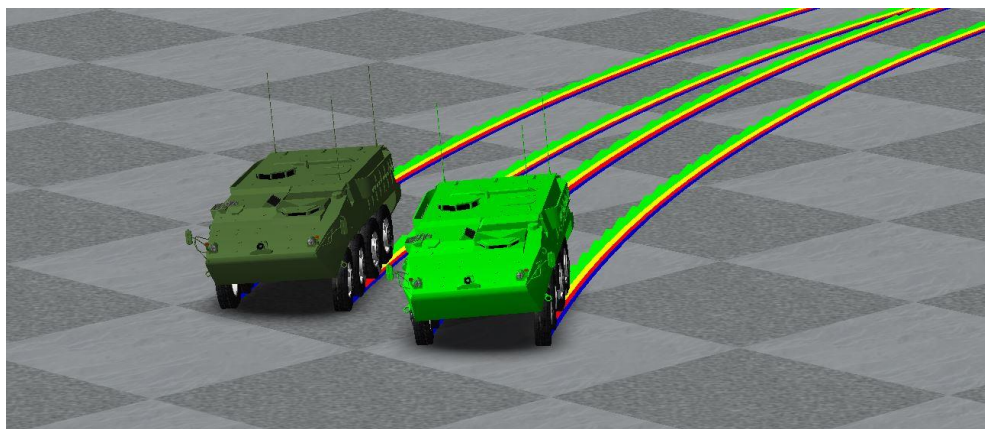
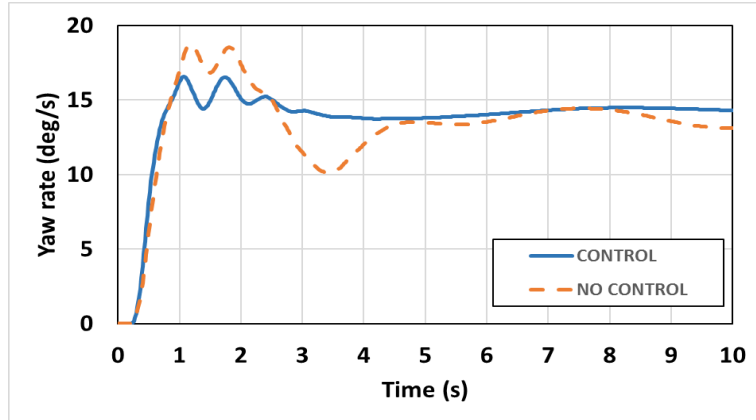
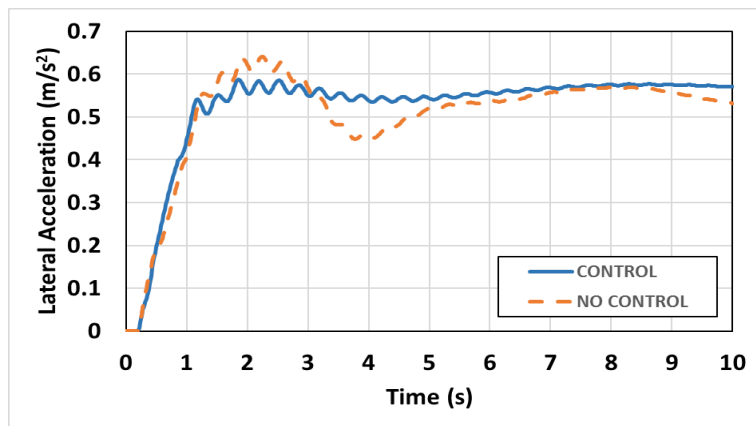


Figure 6-49 Turning Radius of the uncontrolled (dark green) and controlled (light green) vehicles during J-Turn at 80 kph ($\mu=0.85$)

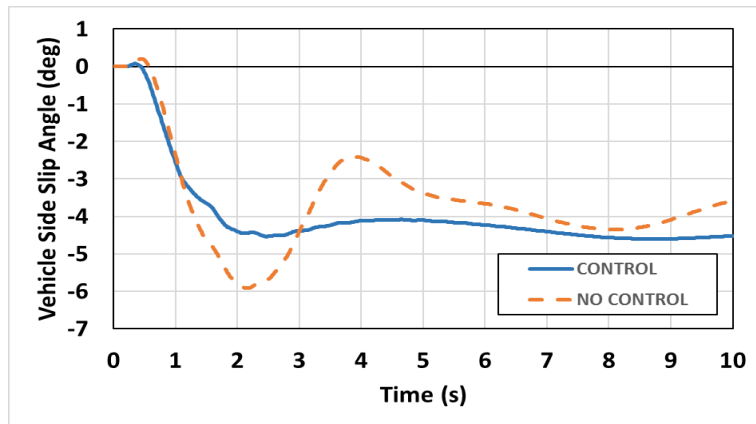
Vehicle yaw rates, lateral accelerations and side slip angles are shown in Figure 6-50.



(a)



(b)



(c)

Figure 6-50 Yaw Rate (a) Lateral Acceleration and Vehicle Side Slip Angle (c) during J-Turn at 80 kph ($\mu=0.85$)

Vehicle yaw rate and lateral acceleration peak transient values were reduced and reached steady state quicker with less oscillation. Vehicle side slip angle was reduced as well and was greatly damped as compared to the uncontrolled vehicle.

Controller yaw rate reference signal tracking is shown in Figure 6-51.

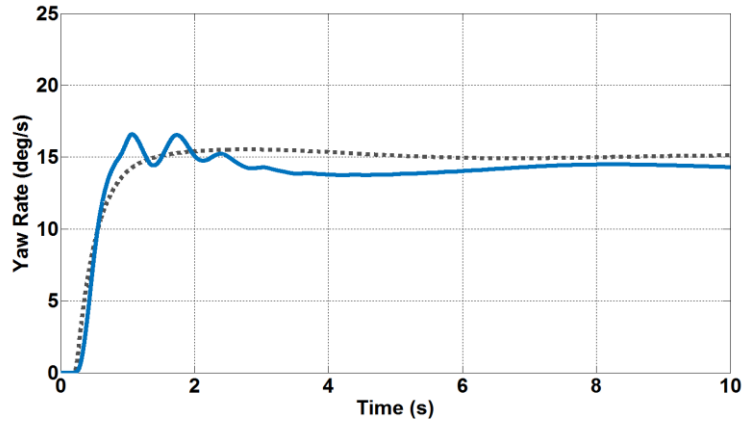
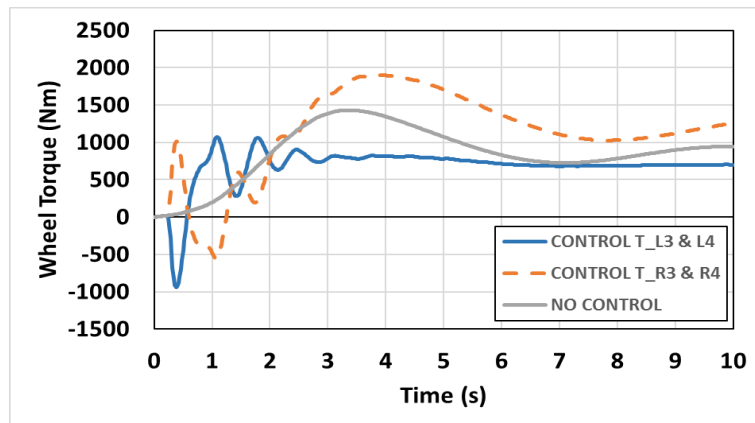


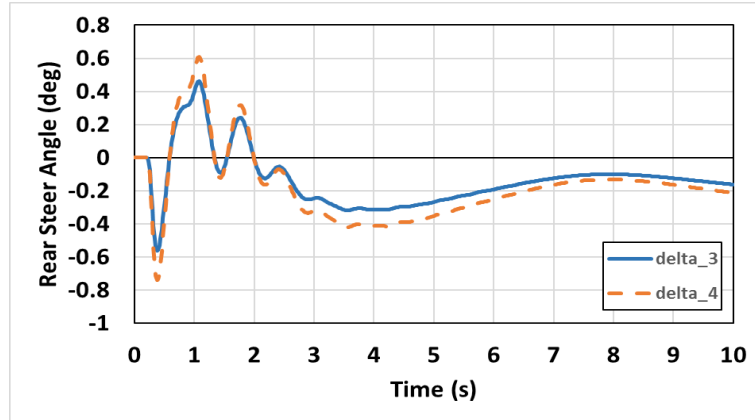
Figure 6-51 H_{∞} Yaw Rate Reference Tracking during J-Turn at 80 kph ($\mu=0.85$)

The proposed controller successfully tracked the yaw rate reference signal during the event. The steady state error was found to be within the 15% tolerance specified in the H_{∞} weighting functions for error tracking.

Wheel torque and rear steer angles on the rear axles of the controlled vehicle are shown in Figure 6-52.



(a)



(b)

Figure 6-52 Wheel Torque (a) and Rear Steer Angles (b) during J-Turn at 80 kph ($\mu=0.85$)

A maximum wheel torque differential of approximately 1500 Nm was observed. The maximum rear steer angles observed during the maneuver 0.7 and 0.5 degrees for the fourth and third axle respectively. Rear steer angles were mostly in the opposite direction of the front axle steer angles.

6.2.4.2 Results – J-Turn (50 kph; $\mu=0.85$)

Vehicle speed of the controlled and uncontrolled vehicle were both maintained at approximately 50 kph as shown in Figure 6-53.

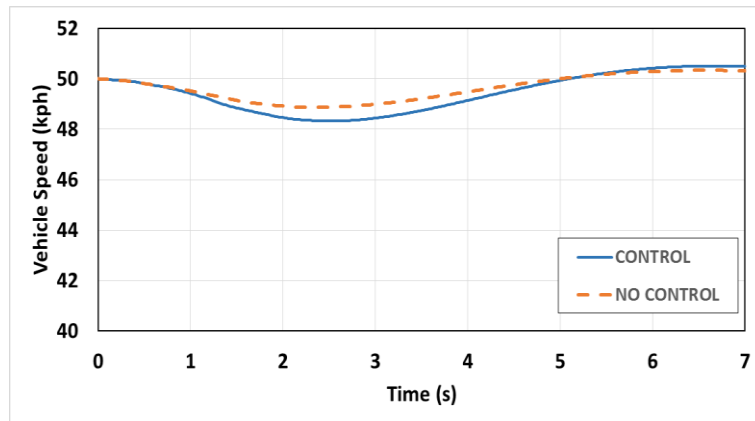


Figure 6-53 Vehicle Speeds during J-Turn at 50 kph ($\mu=0.85$)

The controlled vehicle is able to turn tighter than the uncontrolled vehicle as shown in Figure 6-54.

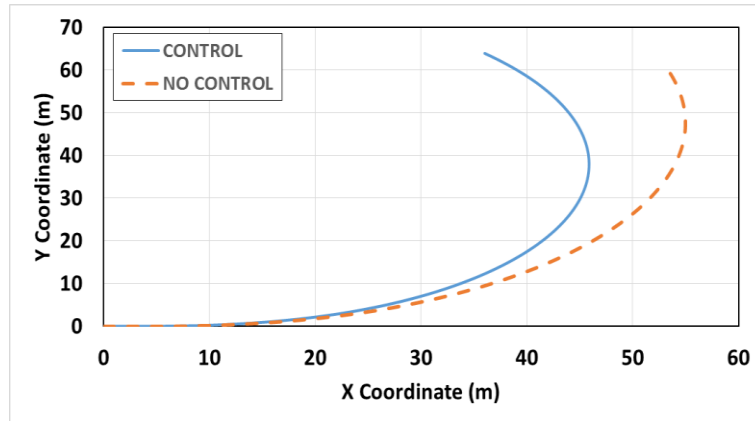


Figure 6-54 Vehicle Trajectory during J-Turn at 50 kph ($\mu=0.85$)

The controlled vehicle was able to follow a path with a smaller radius of curvature than the uncontrolled vehicle. The proposed controller is able to increase vehicle maneuverability during the 50 kph J-Turn maneuver on the high friction surface. The increase in maneuverability is shown in Figure 6-55.

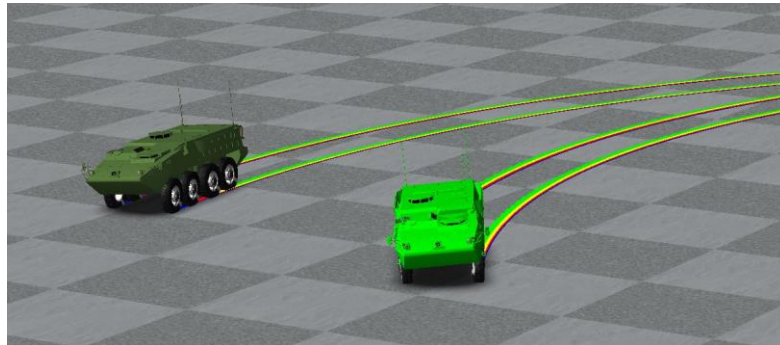
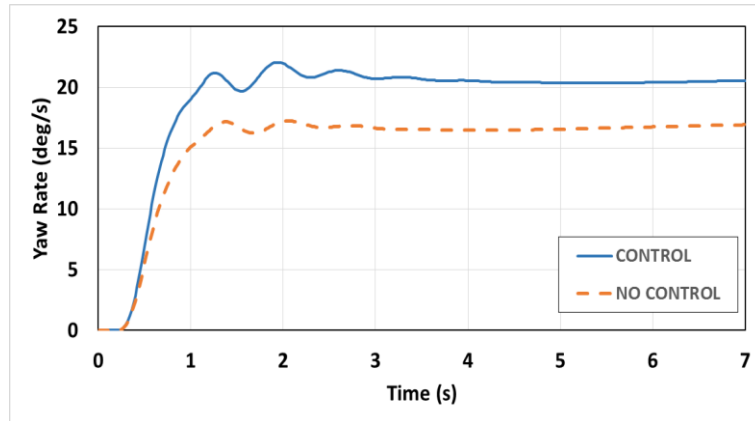
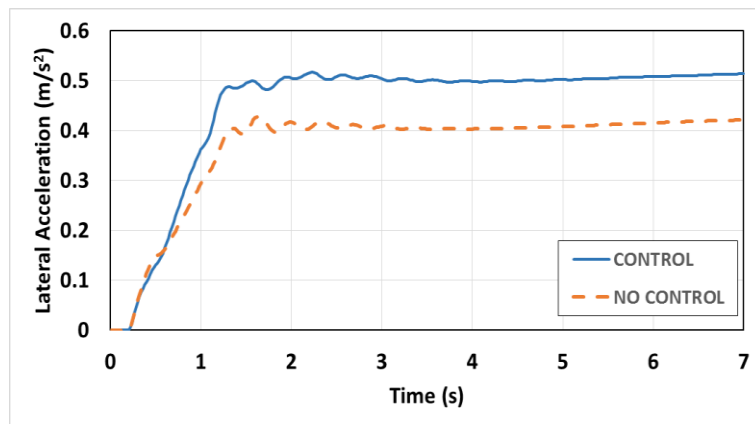


Figure 6-55 Turning Radius of the uncontrolled (dark green) and controlled (light green) vehicles during J-Turn at 50 kph ($\mu=0.85$)

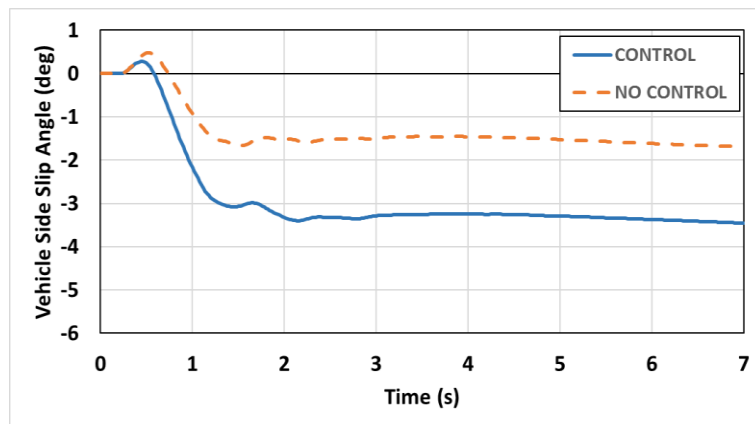
Vehicle yaw rates, lateral accelerations and side slip angles are shown in Figure 6-56.



(a)



(b)



(c)

Figure 6-56 Yaw Rate (a) Lateral Acceleration and Vehicle Side Slip Angle (c) during J-Turn at 50 kph ($\mu=0.85$)

The controlled vehicle was able to generate higher peak values of yaw rate, lateral acceleration and vehicle side slip angle responses for the same steering wheel input as the

uncontrolled vehicle. The slopes of the yaw rate, lateral acceleration and vehicle side slip angle responses also increased meaning that the vehicle time delays have been reduced. There was no negative effect with respect to vehicle stability.

Controller yaw rate reference signal tracking is shown in Figure 6-57.

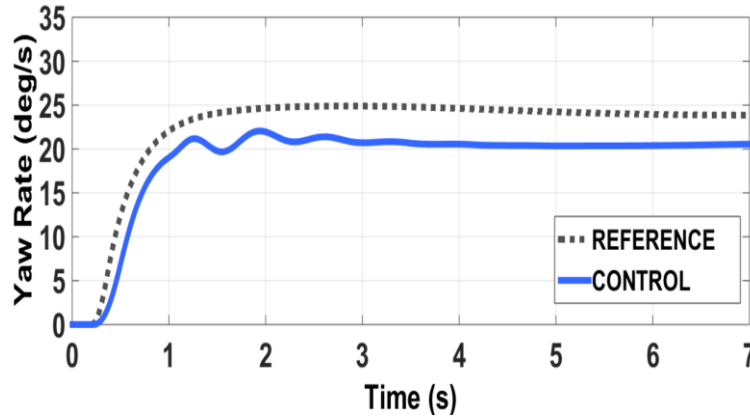
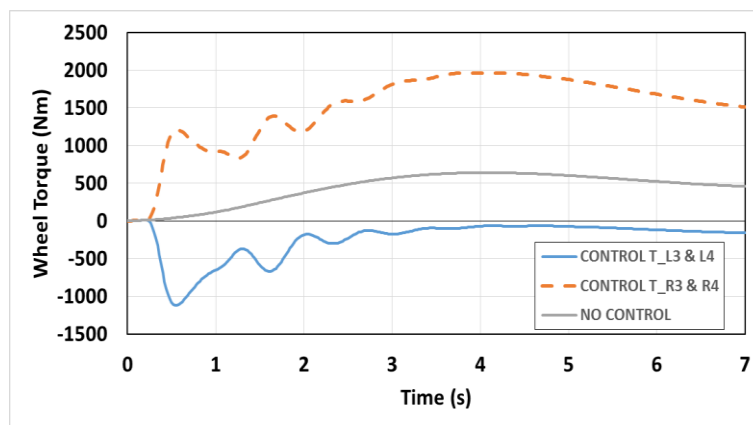


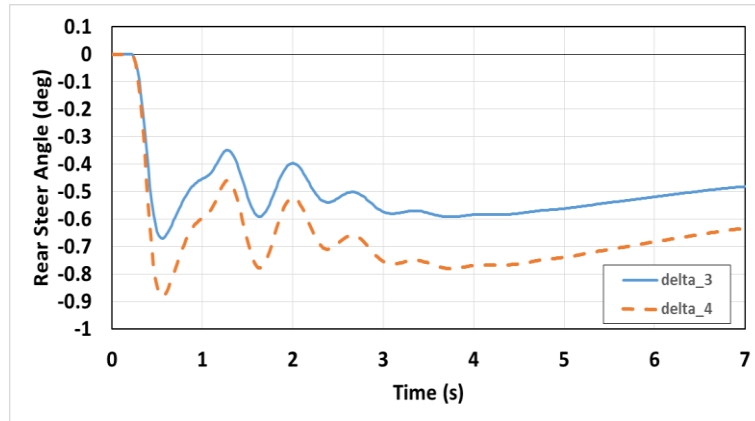
Figure 6-57 H_{∞} Yaw Rate Reference Tracking during J-Turn at 50 kph ($\mu=0.85$)

The proposed controller successfully tracked the yaw rate reference signal during the event. The steady state error was found to be within the 15% tolerance specified in the H_{∞} weighting functions for error tracking.

Wheel torque and rear steer angles on the rear axles of the controlled vehicle are shown in Figure 6-58.



(a)



(b)

Figure 6-58 Wheel Torque (a) and Rear Steer Angles (b) during J-Turn at 50 kph ($\mu=0.85$)

A maximum wheel torque differential of approximately 3400 Nm was observed. The maximum rear steer angles observed during the maneuver 0.9 and 0.7 degrees for the fourth and third axle respectively. Rear steer angles were in the opposite direction of the front axle steer angles.

6.2.4.3 Results – J-Turn (50 kph; $\mu=0.35$)

Vehicle speed of the controlled and uncontrolled vehicle were both maintained at approximately 50 kph as shown in Figure 6-59.

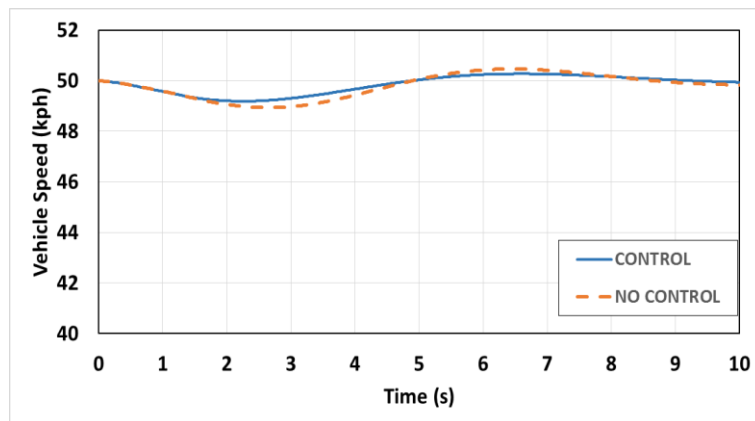


Figure 6-59 Vehicle Speeds during J-Turn at 50 kph ($\mu=0.35$)

The controlled vehicle takes a wider more stable path than the uncontrolled vehicle as shown in Figure 6-60.

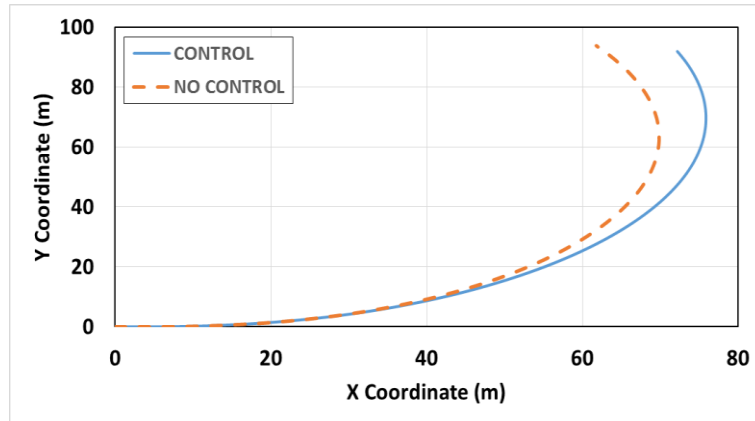
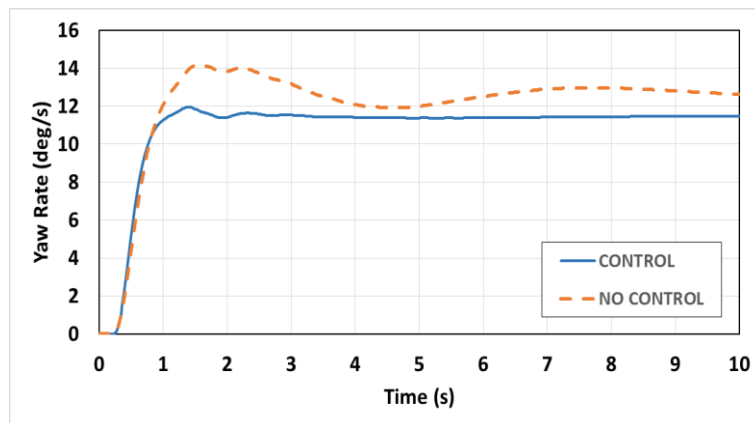
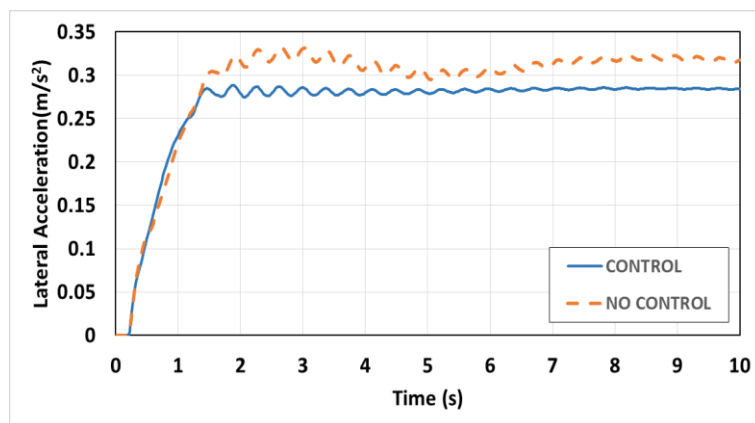


Figure 6-60 Vehicle Trajectory during J-Turn at 50 kph ($\mu=0.35$)

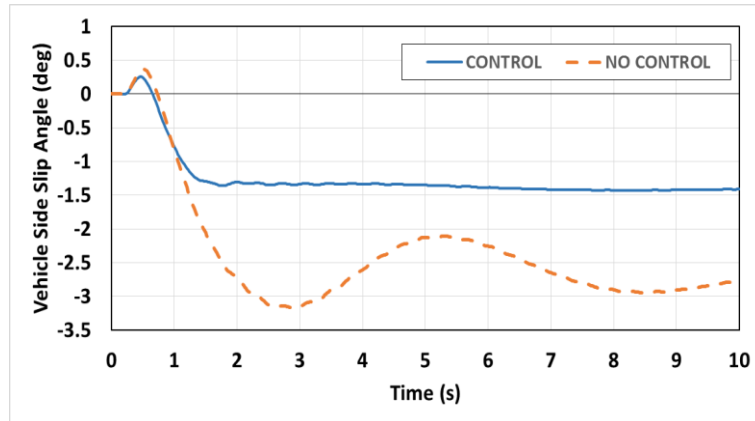
Vehicle yaw rates, lateral accelerations and side slip angles are shown in Figure 6-61.



(a)



(b)



(c)

Figure 6-61 Yaw Rate (a) Lateral Acceleration (b) and Vehicle Side Slip Angle (c) during J-Turn at 50 kph ($\mu=0.35$)

Vehicle yaw rate and lateral acceleration peak steady state values were reduced and reached steady state quicker with less oscillation. Vehicle side slip angle was reduced as well and was greatly damped as compared to the uncontrolled vehicle. The proposed controller has increased vehicle stability on the low friction surface. The same event at the same speed but higher road friction coefficient yielded a controlled vehicle that was more maneuverable with higher peak vehicle dynamic responses.

Controller yaw rate reference tracking shown in Figure 6-62.

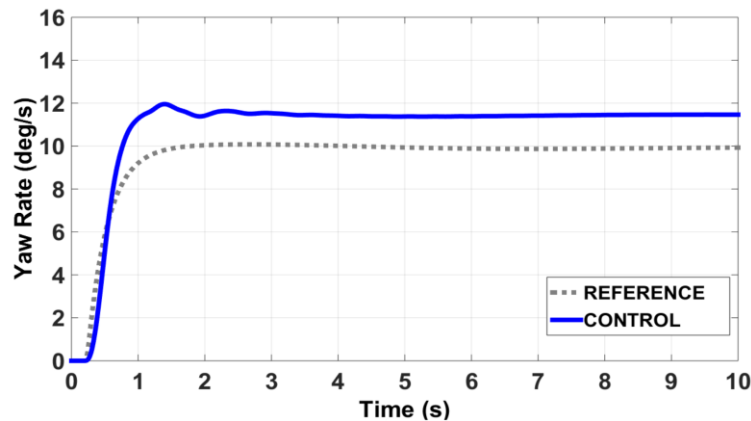
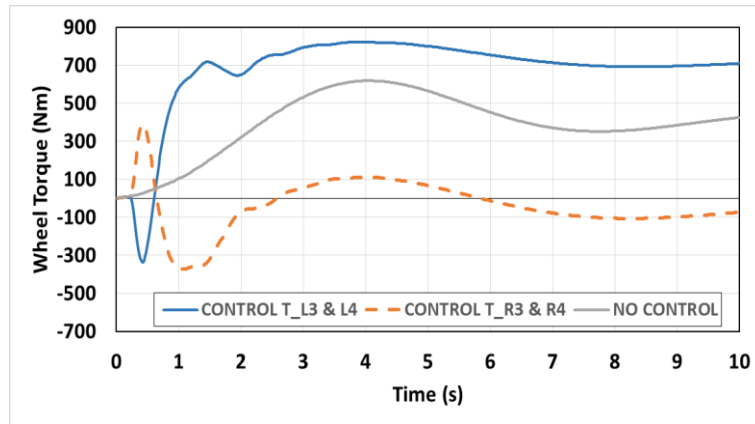


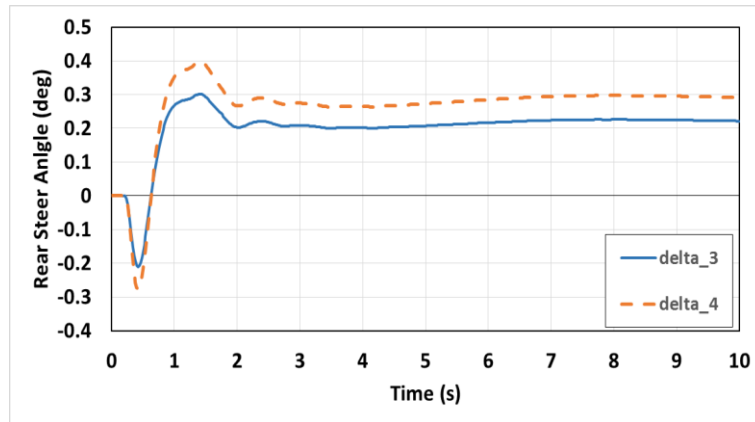
Figure 6-62 H_∞ Yaw Rate Reference Tracking during J-Turn at 50 kph ($\mu=0.35$)

The proposed controller successfully tracked the yaw rate reference signal during the event. The steady state error was found to be within the 15% tolerance specified in the H_∞ weighting functions for error tracking.

Wheel torque and rear steer angles on the rear axles of the controlled vehicle are shown in Figure 6-63.



(a)



(b)

Figure 6-63 Wheel Torque (a) and Rear Steer Angles (b) during J-Turn at 50 kph ($\mu=0.35$)

A maximum wheel torque differential of approximately 1100 Nm was observed. The maximum rear steer angles observed during the maneuver 0.4 and 0.3 degrees for the fourth and third axle respectively. Rear steer angles were mostly in the same direction as the front axle steer angles. The control signal values were the lowest of all events and speeds tested.

6.2.5 Constant Radius Circle (100 ft)

A 100ft radius circle was used to compare the directional stability of the controlled and uncontrolled vehicles. The layout of the 100ft radius circle are shown in Figure 6-64.

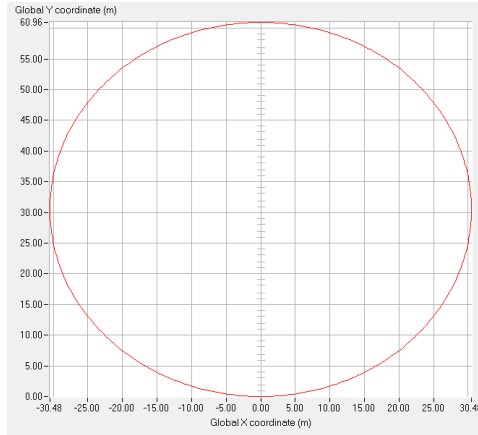


Figure 6-64 100 ft Constant Radius Circle Test Track

6.2.5.1 Results – Constant Radius Circle (50 kph; $\mu=0.85$)

Vehicle speed of the controlled and uncontrolled vehicle were both maintained at approximately 50 kph as shown in Figure 6-65. An initial dip in vehicle speed for both vehicle is observed. The uncontrolled vehicle has difficulty maintaining the 50 kph event speed from 4 to 8 seconds.

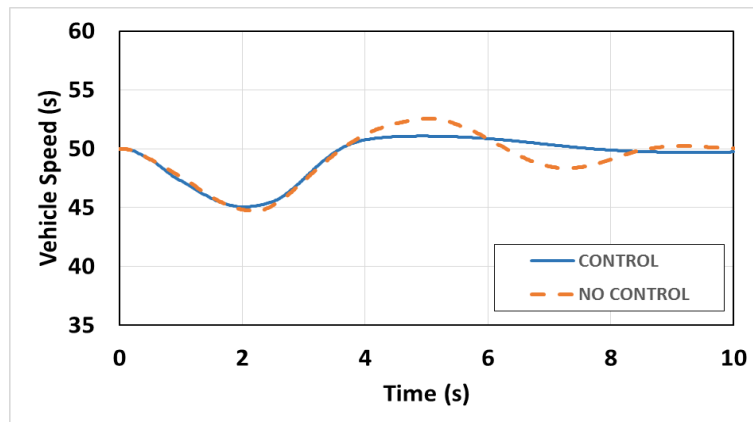
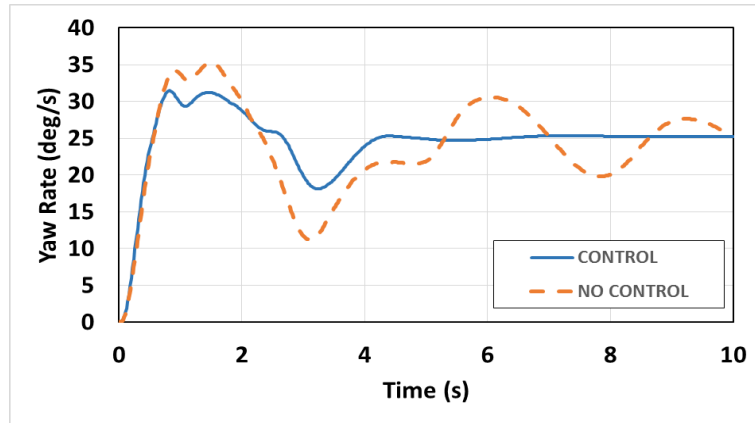
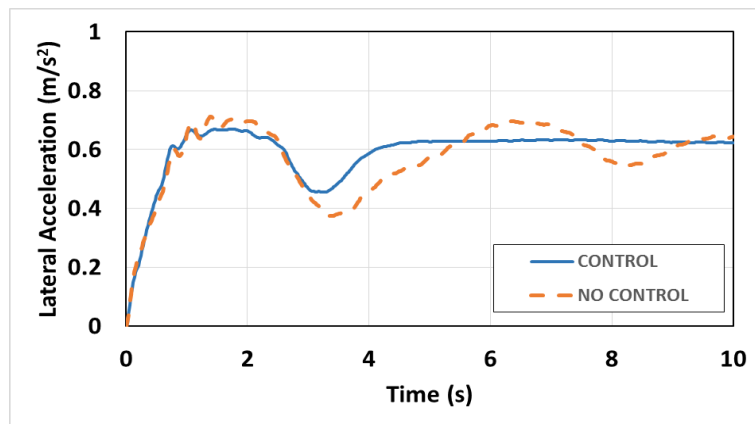


Figure 6-65 Vehicle Speeds during Constant Radius Turn at 50 kph ($\mu=0.85$)

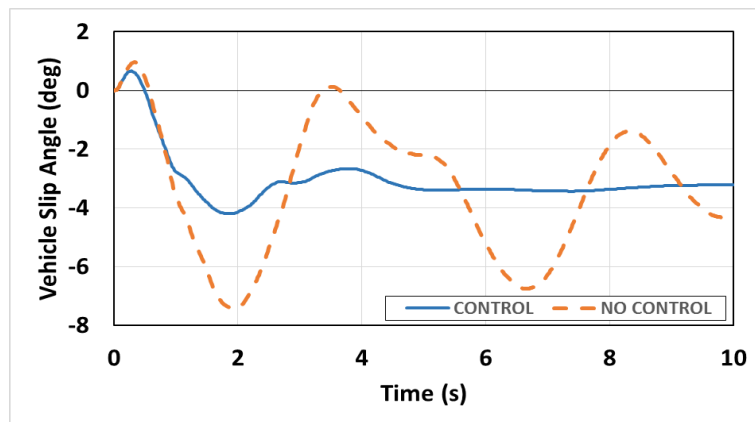
Vehicle yaw rates, lateral accelerations and side slip angles are shown in Figure 6-66.



(a)



(b)



(c)

Figure 6-66 Yaw Rate (a) Lateral Acceleration (b) and Vehicle Side Slip Angle (c) during Constant Radius Circle at 50 kph ($\mu=0.85$)

Vehicle yaw rate and side slip angle peak values were significantly reduced. Lateral acceleration peak values were slightly reduced. In all three cases, the vehicle responses

exhibited almost no oscillations and reached steady state whereas the uncontrolled vehicle continued its oscillations during the event and never reached steady state.

Figure 6-67 shows the uncontrolled vehicle leaving the test track during the maneuver.

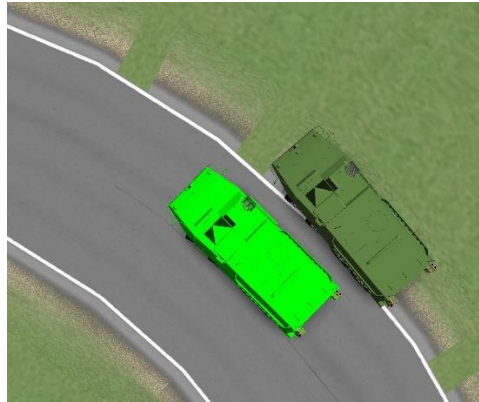


Figure 6-67 Uncontrolled (dark green) Vehicle leaving Test Track during maneuver

Controller yaw rate reference signal tracking is shown in Figure 6-68.

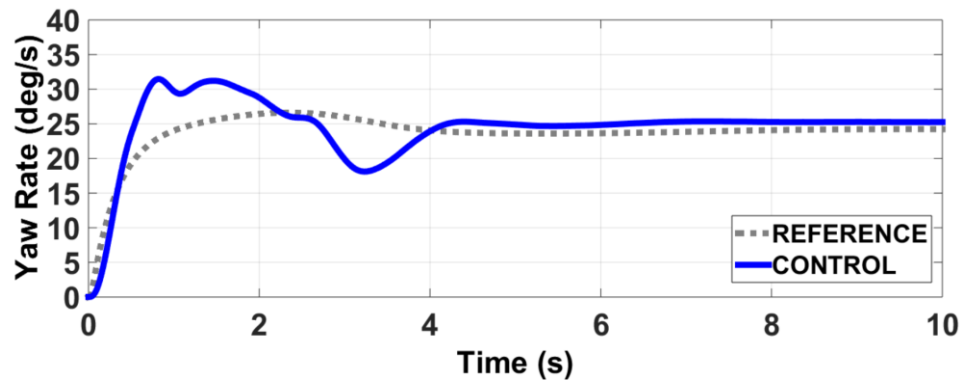
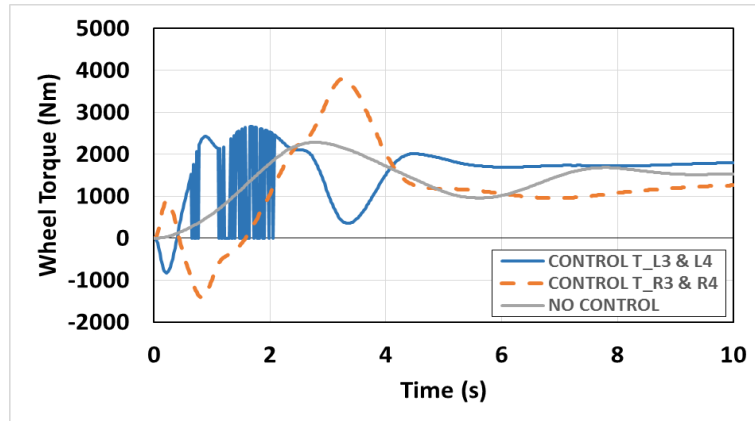


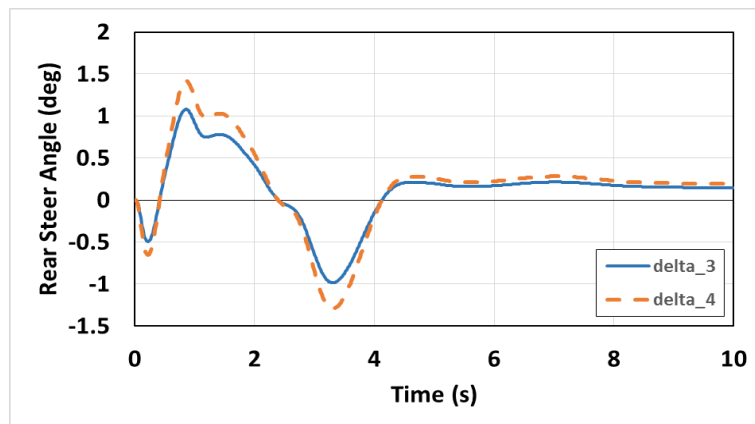
Figure 6-68 H_{∞} Yaw Rate Reference Tracking during Constant Radius Circle at 50 kph ($\mu=0.85$)

The proposed controller successfully tracked the yaw rate reference signal during the event. The steady state error was found to be within the 15% tolerance specified in the H_{∞} weighting function for error tracking.

Wheel torque and rear steer angles on the rear axles of the controlled vehicle are shown in Figure 6-69.



(a)



(b)

Figure 6-69 Wheel Torque (a) and Rear Steer Angles (b) during Constant Radius Circle at 50 mph ($\mu=0.85$)

A maximum wheel torque differential of approximately 3800 Nm was observed. Slip controller intervention is observed between approximately 0.5 and 2 seconds on the left side motors. The maximum rear steer angles observed during the maneuver 1.4 and 1.0 degrees for the fourth and third axle respectively. Rear steer angles were in the opposite and same direction to that of the front axle steer angles.

6.3 TURNING CIRCLE EVALUATION OF ZSS CONTROLLER

Turning circle is of major concern for large multi-wheeled vehicles in situations that require high maneuverability such as when operating in narrow city streets, parking and repositioning for transportation. A turning circle reduction test was conducted to determine

the effectiveness of the zero side slip (ZSS) controller in manipulating the turning circle of the 8 x 8 combat vehicle through actuation of the third and fourth axle wheel angles.

6.3.1 Turning Circle Test - Methodology

The test was conducted by turning the steering wheel to full lock at 0 kph. The vehicle then began to “crawl” (speed less than five kilometers per hour) until one full circle had been completed as shown in Figure 6-70. The outside front tire path is recorded and used in calculating the curb-to-curb turning circle diameter of the vehicle.

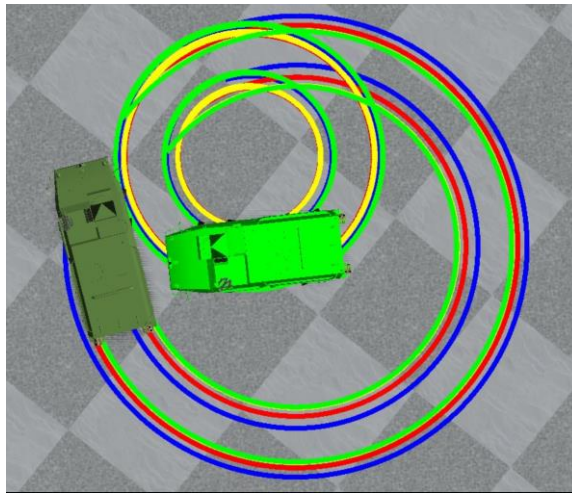


Figure 6-70 Turning Circle Reduction Evaluation Test (uncontrolled vehicle (dark green) controlled (light green))

6.3.2 Maximum Rear Steer Angle

The ZSS controller commands 26 degrees of fourth axle and 19.7 degrees of third axle wheel angles in the opposite direction of the front wheels when the steering wheel is locked and the vehicle is crawling forward. The proposed ZSS controller method does not account for physical constraints in the wheel wells of the vehicle. Without a limit on the controller’s maximum rear wheel angles a conflict was observed between the hull of the vehicle and the tires on the rear axle as circled in red in Figure 6-71.

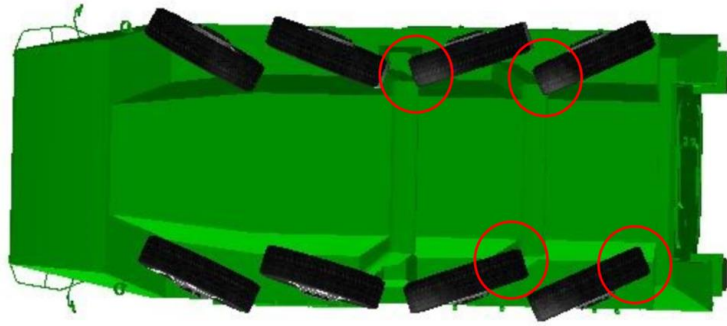


Figure 6-71 ZSS - No Limit Rear Wheel Angles

A saturation block was implemented in the controller in order to account for these physical limitations (see section 5.5.2). The hull at the rear of the vehicle is wider than the front portion of the vehicle hull to allow for increased interior volume and maximum rear hatch dimensions for easier ingress and egress. The maximum front wheel steer angle is 29 degrees. A fourth axle rear wheel steer angle of 26 degrees is too high for the wider rear portion of the hull and must be constrained. Several different maximum fourth axle steering values were tested in order to establish a relationship between turning circle and rear steer angle.

Note: Accurate values for maximum rear wheel steer angles on the two rear axles can only be determined through a detailed suspension and hull design study and is not in the scope of this work. Therefore, an assumption has to be made as to the maximum allowable rear steer angle.

6.3.3 Results – Turning Circle Reduction Test

The uncontrolled vehicle with no steering on the third and fourth axles is compared to the ZSS controller with various limits on the fourth axle rear wheel steer angles. The third axle wheel angles are in turn limited as they are related through a fixed ratio of 0.76 to the fourth axle. The uncontrolled vehicle with no rear axle steering exhibited a turning circle of 18 meters. The ZSS controller with no limit on rear axle wheel angles demonstrated a 10.2 meter turning circle but allowed the tires to contact the hull. The ZSS controller with 20, 17, 15, 10 and 5 degree maximum rear wheel steer angles achieved turning circles of 11.5,

12.5, 12.7, 14.5 and 16.5 meters respectively. The outside first axle tire paths are plotted for each iteration in Figure 6-72.

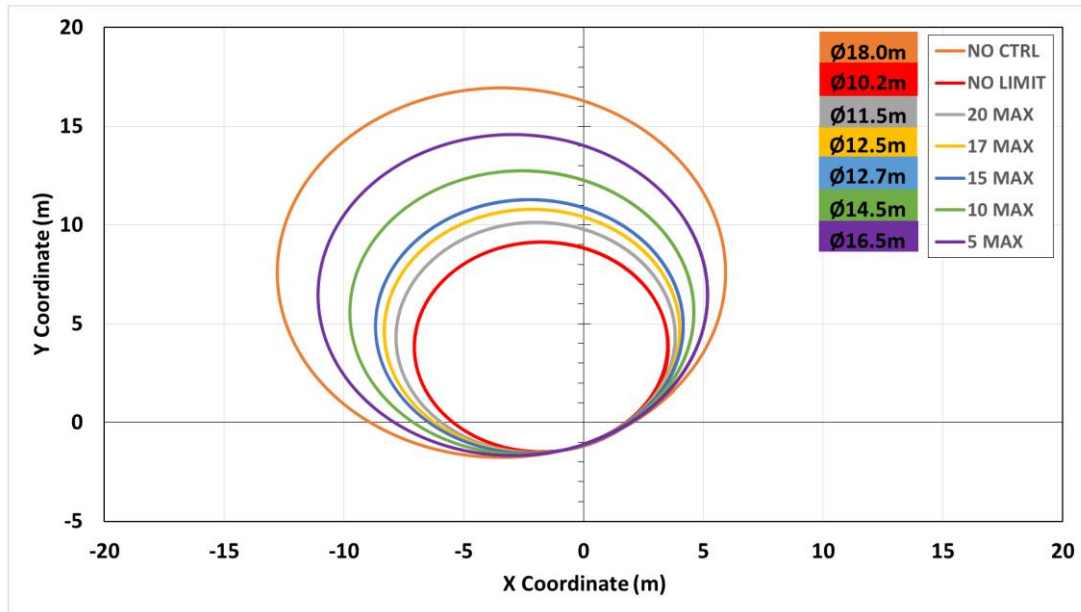


Figure 6-72 Turning Circle Diameter Reduction Results for Various Maximum Rear Wheel Steer Angles

The ZSS controller demonstrated the ability to greatly influence the turning circle diameter. Ideally, unrestricted rear wheel steer angles of 26 and 19.7 degrees for the fourth and third axle rear wheel steer angles respectively provide the maximum reduction of 7.8 meters in turning circle diameter. Due to physical constraints of the current vehicle hull, a compromise is proposed. Maximum rear axle wheel steer angles of 17 and 12.9 degrees for the fourth and third axles respective allow for a turning circle of 12.5 meters. The proposed limited ZSS controller is able to reduce the vehicle turning circle by 5.5 meters representing a reduction of approximately 30%.

6.4 SWITCHING SPEED EVALUATION

H_{∞} controller and ZSS controllers have been compared during NATO double lane change events at 80, 60 and 40 kph and NATO constant step slalom at 40 kph in order to determine a suitable speed range at which to switch between control methods allowing each controller to work within its most effective speed range.

6.4.1 Results – H_∞ vs ZSS Ctrl - Double Lane Change (80 kph; $\mu=0.85$)

Vehicle speed of the ZSS and H_∞ controlled vehicles was maintained at approximately 80 kph as shown in Figure 6-73.

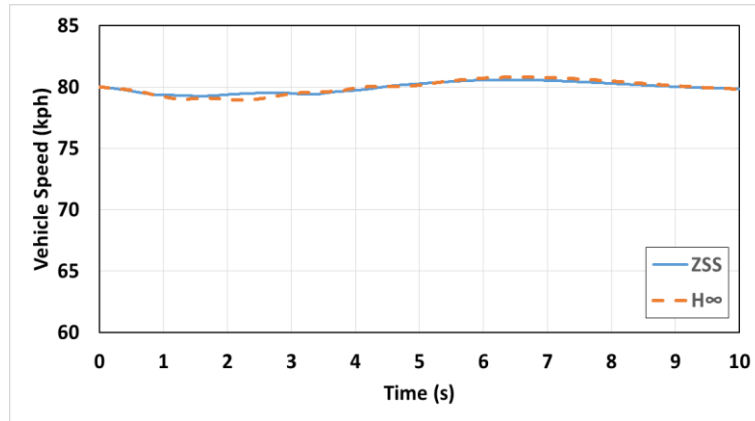


Figure 6-73 Vehicle Speeds during DLC at 80 kph ($\mu=0.85$)

Steering wheel angles of the controlled vehicles are shown in Figure 6-74.

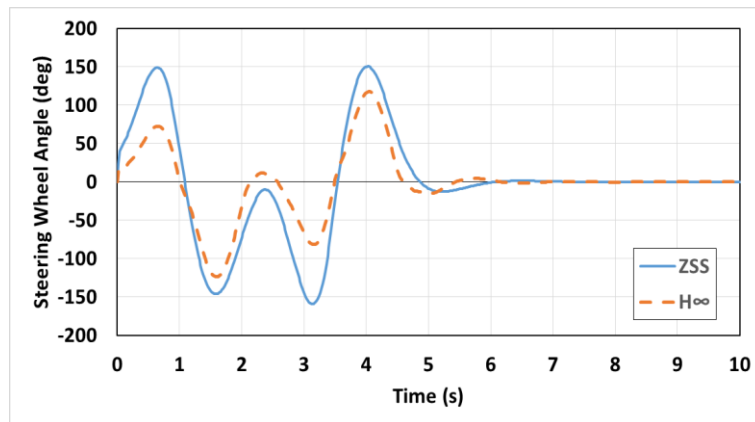


Figure 6-74 Steering Wheel Angles during DLC at 80 kph ($\mu=0.85$)

The H_∞ controlled vehicle required significantly less steering effort in order to complete the double lane change maneuver at 80 kph. At approximately 0.5 and 3 seconds the peak steering angle is 50% lower than the angle required by the ZSS controlled vehicle. A lower rate of change of steering angle was also observed.

The ZSS controlled vehicle failed the double lane change. Figure 6-75 shows the ZSS controlled vehicle coming into contact with the double lane change cones at each gate in

the maneuver. This automatically disqualifies the ZSS controller for use at high speeds as the driver does not expect a conventional vehicle to behave in such a way. The H_∞ controller tracks a yaw rate generated by a conventional vehicle model and will therefore always behave in a manner that will not surprise the driver.

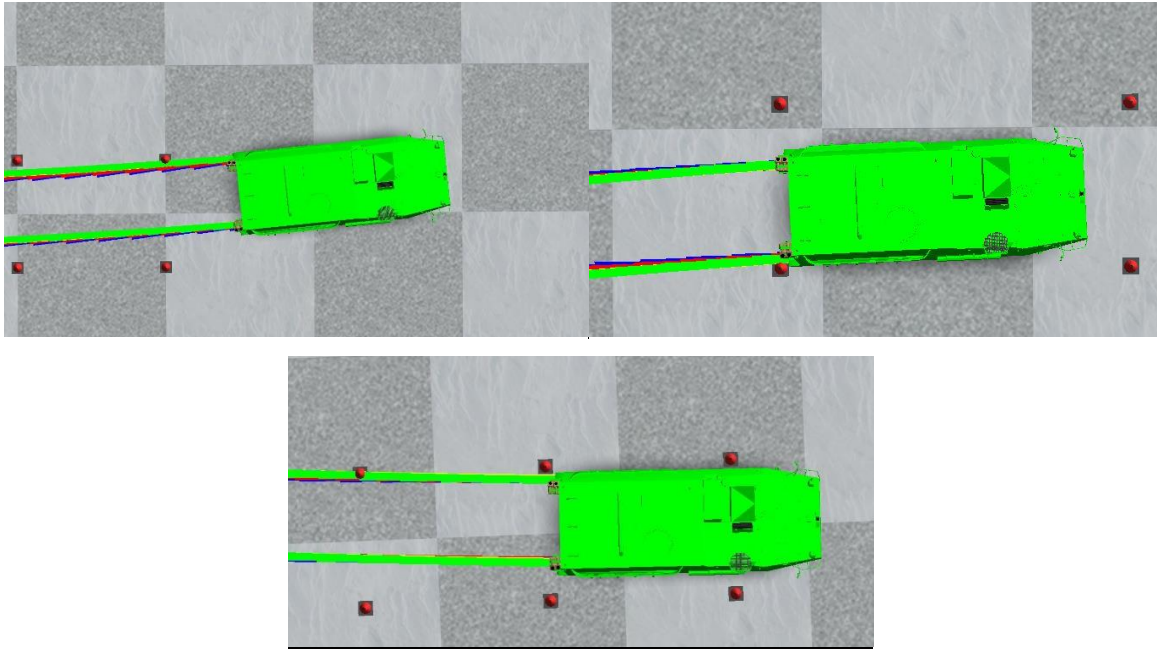
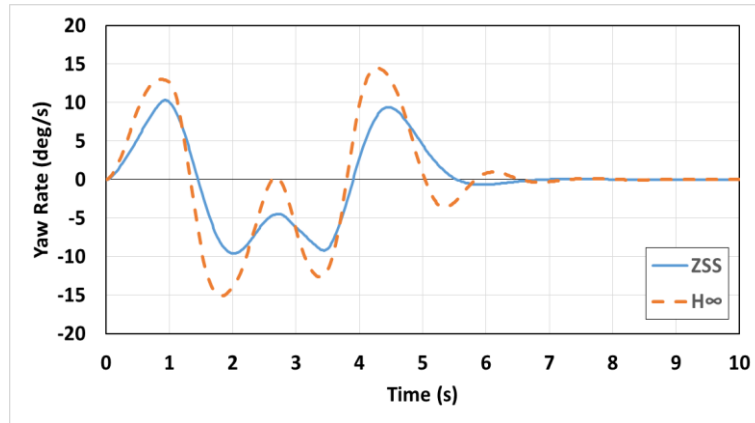
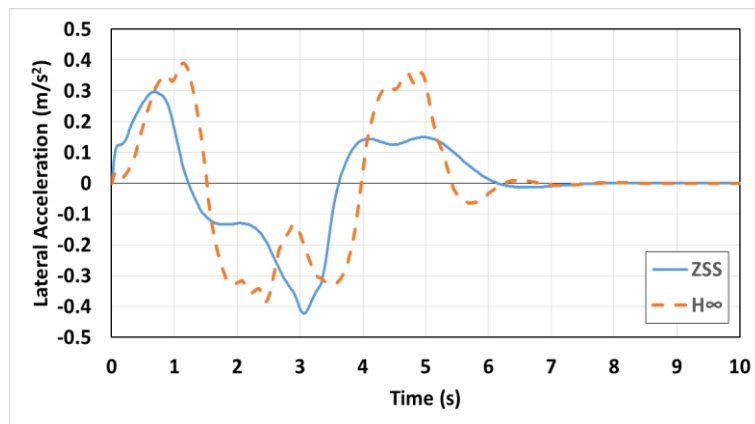


Figure 6-75 ZSS Controlled Vehicle Failing by Cone Contact during DLC at 80 kph ($\mu=0.85$)

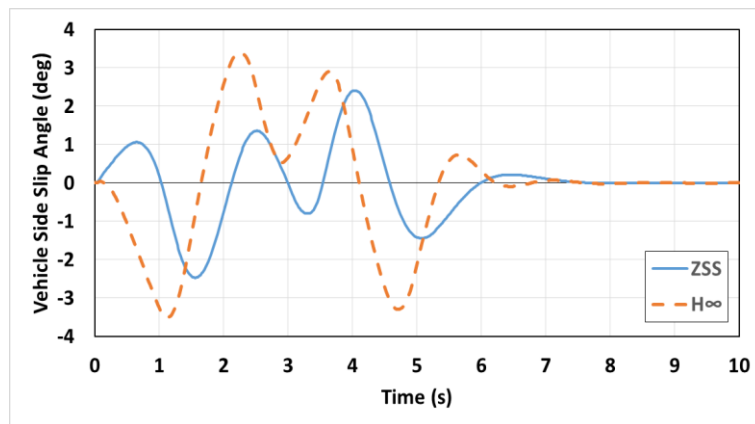
Vehicle yaw rates, lateral accelerations and side slip angles are shown in Figure 6-76. The yaw rate, lateral acceleration and vehicle side slip angle responses of the ZSS controller are significantly overdamped as compared to the H_∞ controller and result in the failure of the maneuver as the vehicle is less responsive to driver inputs.



(a)



(b)



(c)

Figure 6-76 Yaw Rate (a) Lateral Acceleration (b) and Vehicle Side Slip Angle (c) during DLC at 80 kph ($\mu=0.85$)

Rear steer angles on the rear axes of the controlled vehicles are shown in Figure 6-77.

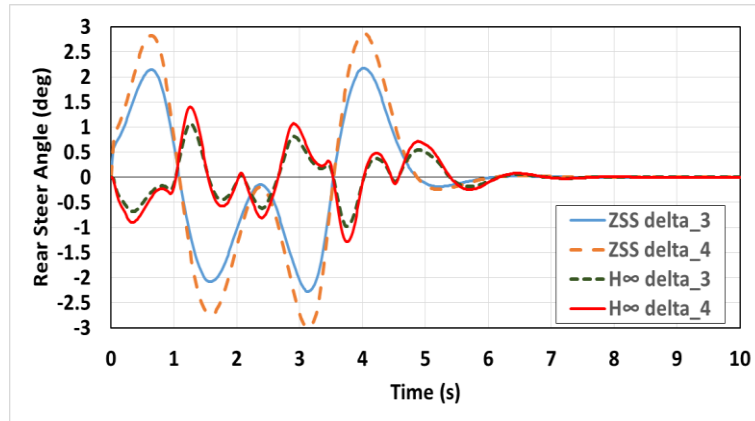


Figure 6-77 Rear Steer Angles of ZSS and H_{∞} Controllers during DLC at 80 kph ($\mu=0.85$)

The ZSS controller algorithm applied steering to the rear axle in the direction of the front wheels. The H_{∞} controller applied rear axle steering in the opposite direction to the front wheels. The H_{∞} controller's peak rear steer angles observed during the maneuver were approximately 1.5 and 1.1 degrees for the fourth and third axle respectively. The ZSS controller's peak rear steer angles observed during the maneuver were approximately 3 and 2.2 degrees for the fourth and third axle respectively.

6.4.2 Results – H_{∞} vs ZSS Ctrl - Double Lane Change (60 kph; $\mu=0.85$)

Vehicle speed of the ZSS and H_{∞} controlled vehicles was maintained at approximately 60 kph as shown in Figure 6-78.

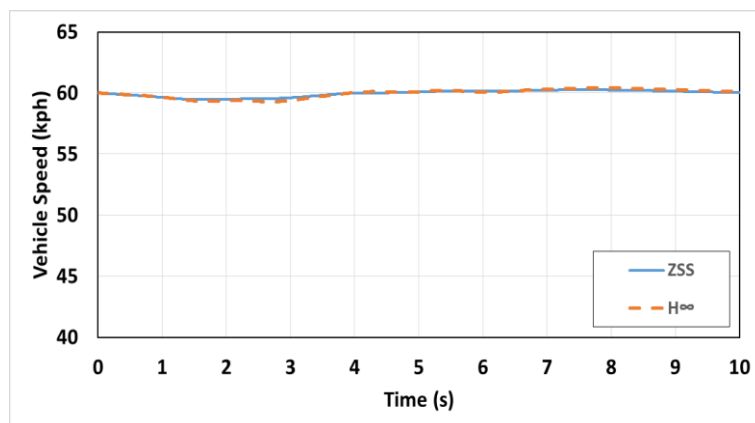


Figure 6-78 Vehicle Speeds during DLC at 60 kph ($\mu=0.85$)

Steering wheel angles of the controlled vehicles are shown in Figure 6-79.

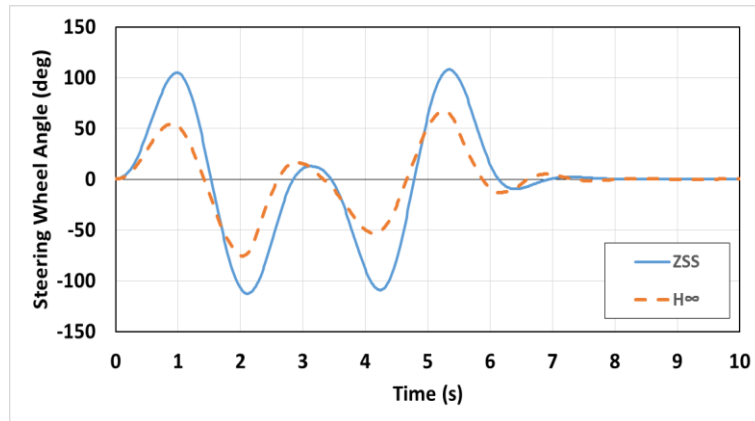
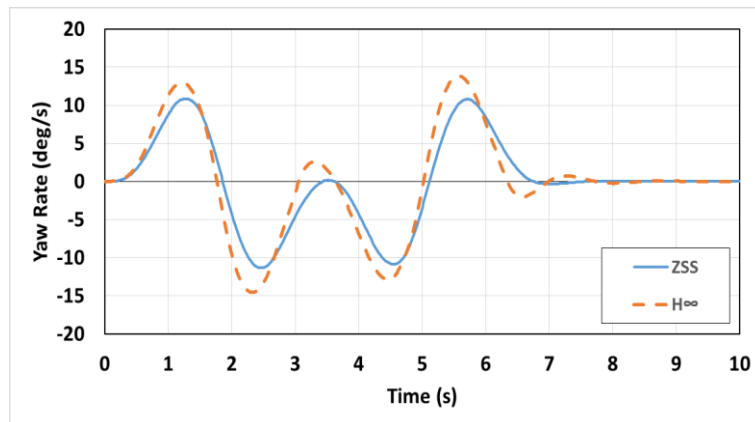


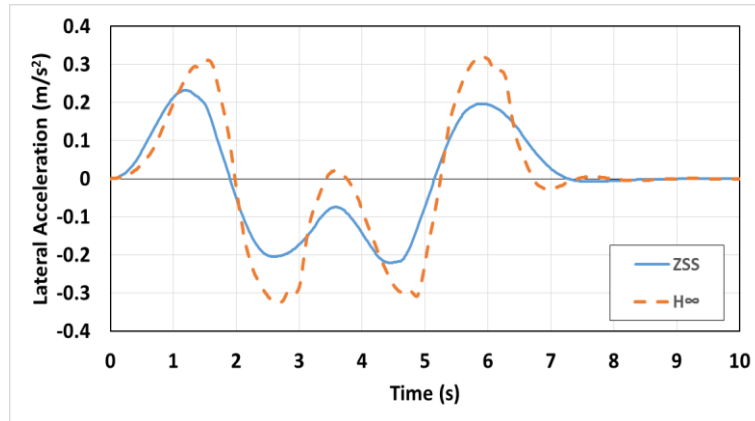
Figure 6-79 Steering Wheel Angles during DLC at 60 kph ($\mu=0.85$)

The H_{∞} controlled vehicle required significantly less steering effort in order to complete the double lane change maneuver at 60 kph as was observed during at 80 kph as well. At approximately 1 and 4.3 seconds the peak steering angle is approximately 50% lower than the angle required by the ZSS controlled vehicle. Therefore, the ZSS controller is deemed inappropriate for use at speeds of 60kph or above as compared to the H_{∞} controller. A lower rate of change of steering angle was also observed.

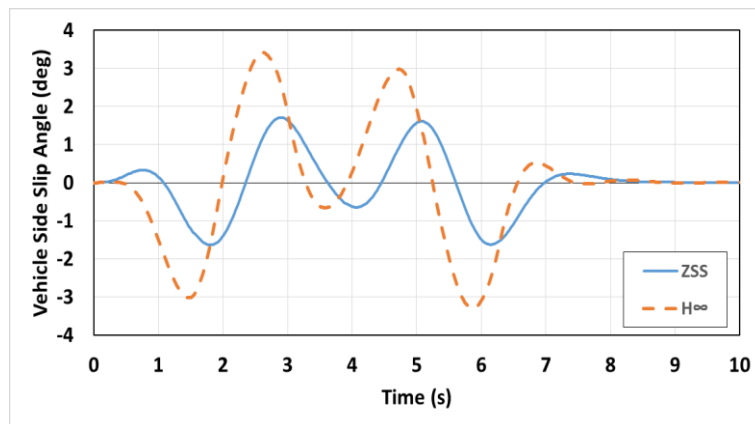
Vehicle yaw rates, lateral accelerations and side slip angles are shown in Figure 6-80.



(a)



(b)



(c)

Figure 6-80 Yaw Rate (a) Lateral Acceleration (b) and Vehicle Side Slip Angle during DLC at 60 kph ($\mu=0.85$)

The yaw rate, lateral acceleration and vehicle side slip angle responses of the ZSS controller are significantly overdamped as compared to the H_∞ controller and result in a significantly less maneuverable vehicle that is difficult to control similar to the results obtained at 80 kph.

Rear steer angles on the rear axles of the controlled vehicles are shown in Figure 6-81.

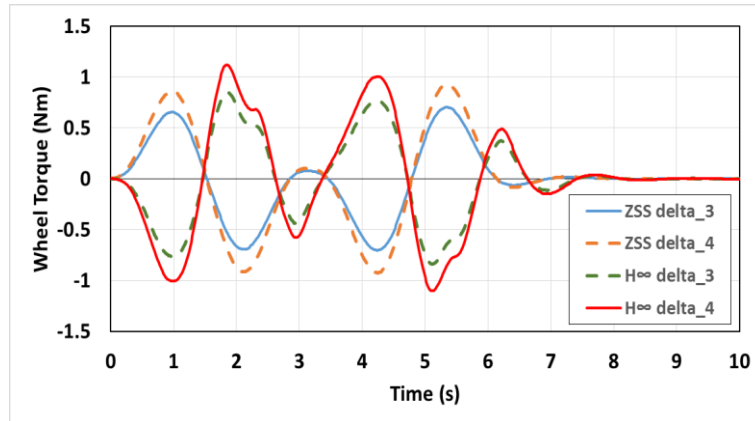


Figure 6-81 Rear Steer Angles of ZSS and H_{∞} Controllers during DLC at 60 kph ($\mu=0.85$)

The ZSS controller algorithm applied steering to the rear axle in the direction of the front wheels. The H_{∞} controller applied rear axle steering in the opposite direction to the front wheels. The H_{∞} controller’s peak rear steer angles observed during the maneuver were approximately 1.1 and 0.8 degrees for the fourth and third axle respectively. The ZSS controller’s peak rear steer angles observed during the maneuver were approximately 0.9 and 0.7 degrees for the fourth and third axle respectively.

6.4.3 Results – H_{∞} vs ZSS Ctrl - Double Lane Change (40 kph; $\mu=0.85$)

Vehicle speed of the ZSS and H_{∞} controlled vehicle was maintained at approximately 40 kph as shown in Figure 6-82.

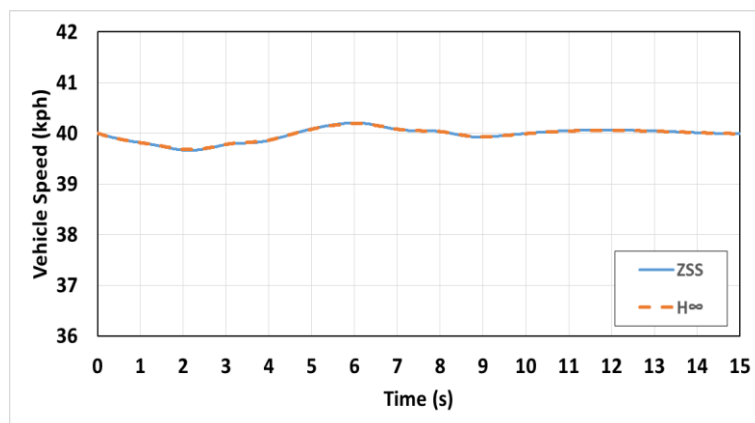


Figure 6-82 Vehicle Speeds during DLC at 40 kph ($\mu=0.85$)

Steering wheel angles of the controlled vehicles are shown in Figure 6-83.

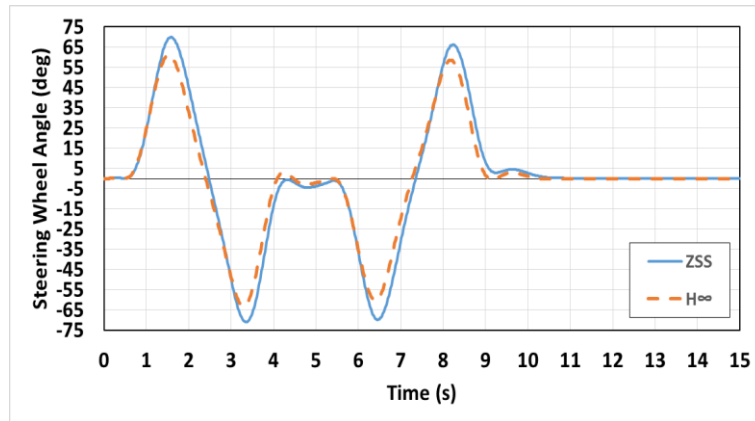
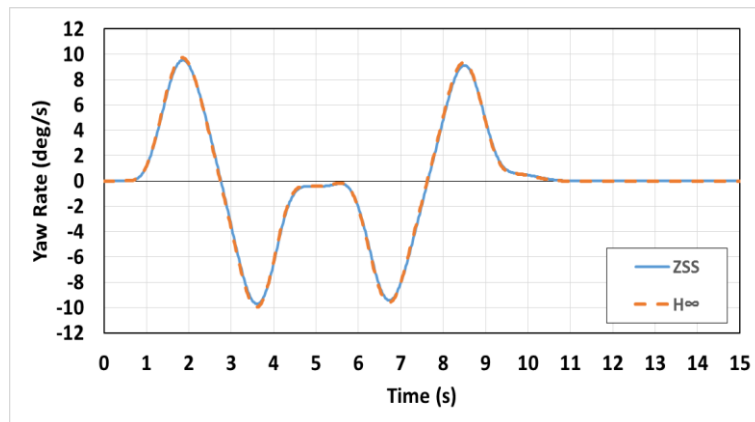


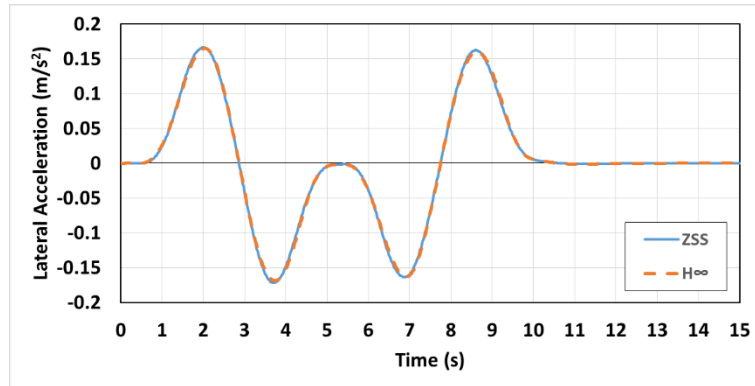
Figure 6-83 Steering Wheel Angles during DLC at 40 kph ($\mu=0.85$)

As observed at 80 and 60 kph, the steering wheel effort for the H_∞ controlled vehicle was lower. In this case however, the discrepancy between ZSS and H_∞ was significantly less pronounced. With the H_∞ controlled vehicle peak steering angles that were less than 10 degrees lower than the ZSS controlled vehicle. A lower rate of change of steering angle was also observed. Nevertheless, due to the lower steering effort required and the fact that the H_∞ controller contains yaw rate feedback for increased safety it is favored at 40 kph.

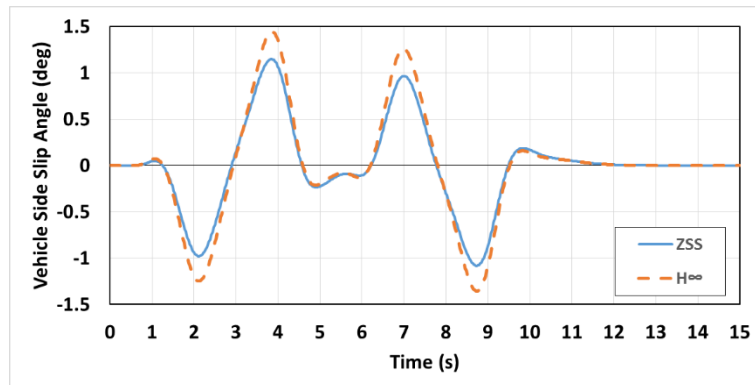
Vehicle yaw rates, lateral accelerations and side slip angles are shown in Figure 6-84.



(a)



(b)



(c)

Figure 6-84 Yaw Rate (a) Lateral Acceleration (b) Vehicle Side Slip Angle (c) during DLC at 40 kph ($\mu=0.85$)

There were no significant differences between the yaw rate and lateral acceleration of the two vehicle during the double lane change at 40 kph indicating that the gap in performance between H_{∞} and ZSS controllers is dependent on vehicle speed. A slight different in peak vehicle side slip angles was observed which correlates with the slightly lower steering effort required by the H_{∞} controller

Rear steer angles on the rear axles of the controlled vehicles are shown in Figure 6-85.

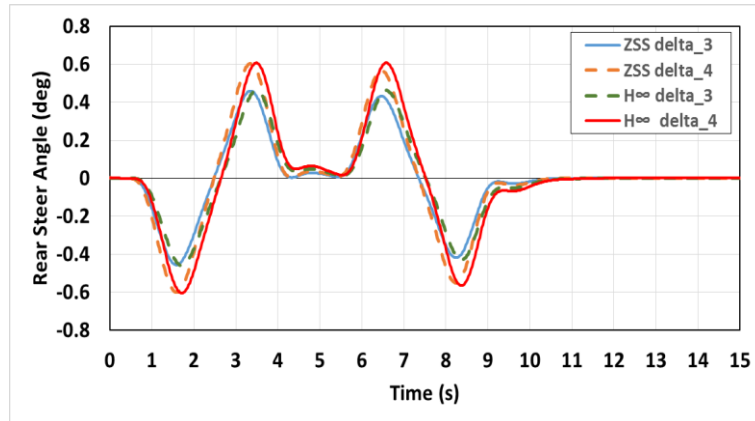


Figure 6-85 Rear Steer Angles of ZSS and H_{∞} Controllers during DLC at 40 kph ($\mu=0.85$)

Both the ZSS and H_{∞} controllers applied steering to the rear axle in the opposite direction of the front wheels. Both the H_{∞} and ZSS controller's peak rear steer angles were approximately 0.6 and 0.4 degrees for the fourth and third axle respectively. It is interesting to note that both controllers demand almost identical rear steering values at 40 kph while conducting the double lane change maneuver.

6.4.4 Results – H_{∞} vs ZSS Ctrl – Const. Step Slalom (40 kph; $\mu=0.85$)

Vehicle speed of the ZSS and H_{∞} controlled vehicle was maintained at approximately 80 kph as shown in Figure 6-86.

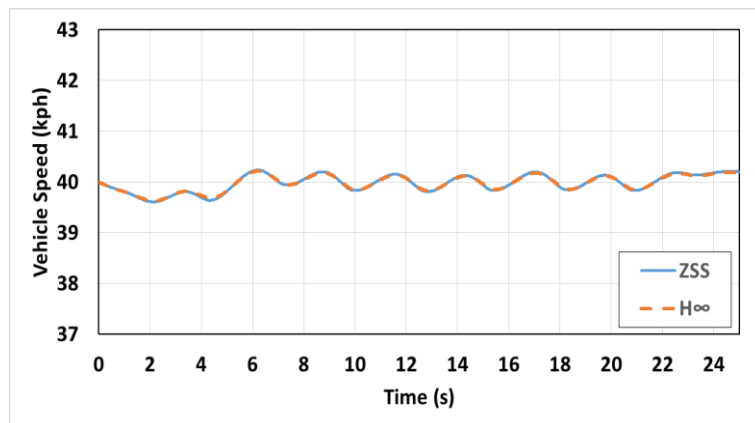


Figure 6-86 Vehicle Speeds during Slalom at 40 kph ($\mu=0.85$)

Steering wheel angles of the controlled vehicles are shown in Figure 6-87.

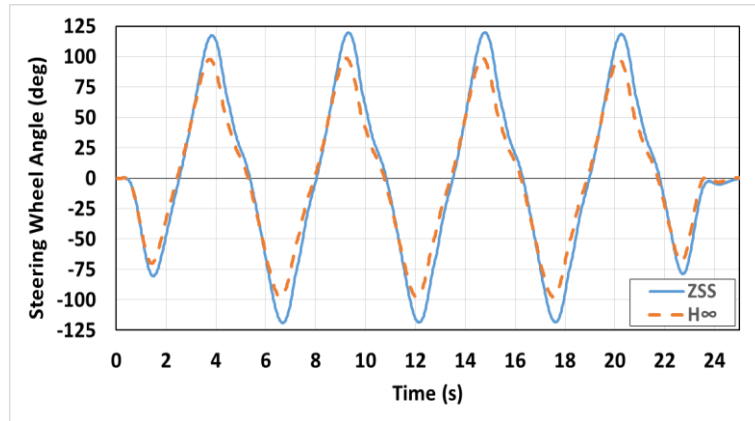
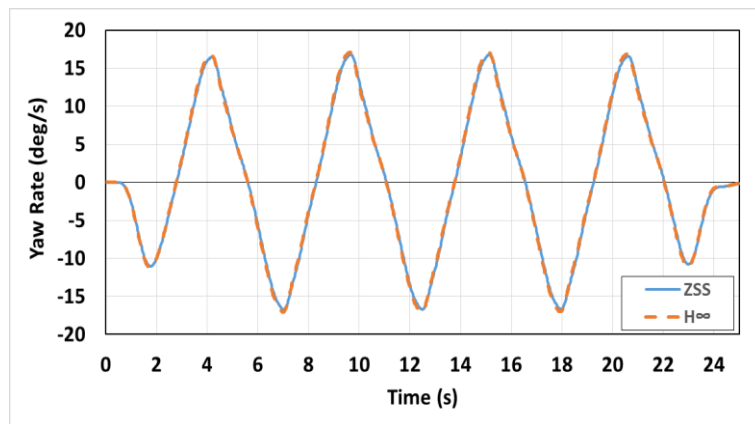


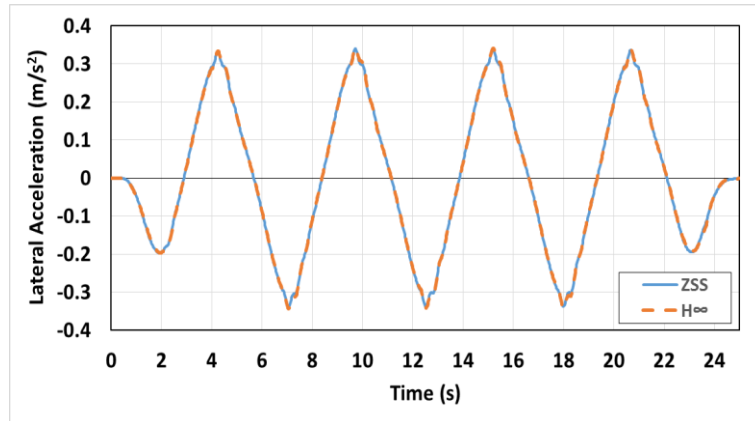
Figure 6-87 Steering Wheel Angles during Slalom at 40 kph ($\mu=0.85$)

Steering effort for the H_∞ controlled vehicle is significantly reduced as compared to the ZSS controlled vehicle. Peak steering angles were reduced by approximately 25%. A lower steering angle rate was also observed for the H_∞ controlled vehicle. Again the H_∞ provides the more effective control during the 40 kph maneuver.

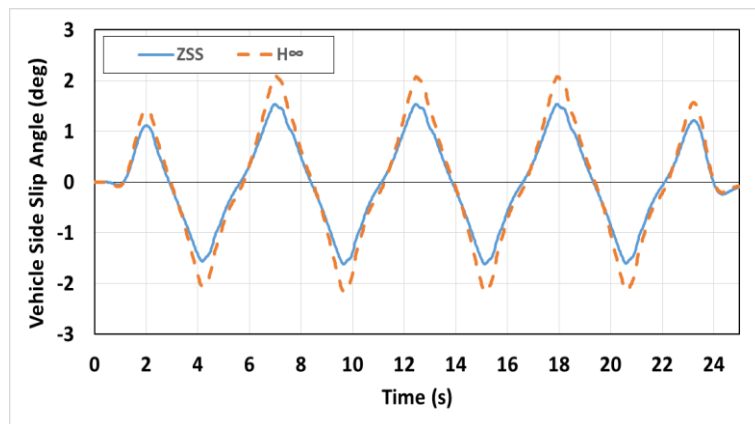
Vehicle yaw rates, lateral accelerations and side slip angles are shown in Figure 6-88.



(a)



(b)



(c)

Figure 6-88 Yaw Rate (a) Lateral Acceleration (b) and Vehicle Side Slip Angle (c) during Slalom at 40 kph ($\mu=0.85$)

There was no significant difference in yaw rate and lateral acceleration for the H_∞ and ZSS controlled vehicles. Vehicle side slip angle was slightly higher for the H_∞ controlled vehicle.

Rear steer angles on the rear axles of the controlled vehicles are shown in Figure 6-89.

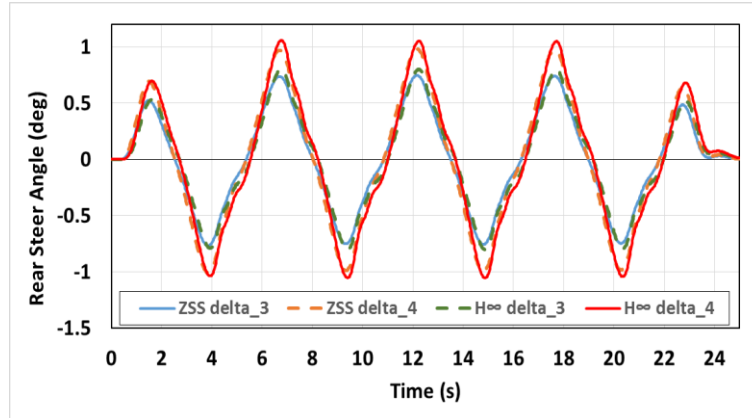


Figure 6-89 Rear Steer Angles of ZSS and H_{∞} Controllers during Slalom at 40 kph ($\mu=0.85$)

Both the ZSS and H_{∞} controllers applied steering to the rear axle in the opposite direction of the front wheels. Both the H_{∞} and ZSS controller's peak rear steer angles were approximately 1.1 and 0.8 degrees for the fourth and third axle respectively. It is interesting to note that both controllers behave almost identical rear steer angles at 40 kph in the slalom event similar to the results for the double lane change at 40 kph.

6.5 LOW SPEED DYNAMIC EVALUATION OF ZSS CONTROLLER

The previous sections have determined that the ZSS controller is:

- effective at crawling speeds in reducing vehicle turning circle
- not well suited for higher speed maneuvers as compared to the H_{∞} controller
- not as effective at reducing steering effort as the H_{∞} controller above 40 kph

This section will determine the viability of the ZSS controller for low speed maneuvering by comparing the uncontrolled and ZSS controlled vehicles in a low speed double lane change and slalom maneuvers at 30 kph for varying road friction coefficients.

6.5.1 Results –ZSS Controller – Double Lane Change (30 kph; $\mu=0.85$)

Vehicle speed of the controlled and uncontrolled vehicles was maintained at approximately 30 kph as shown in Figure 6-90.

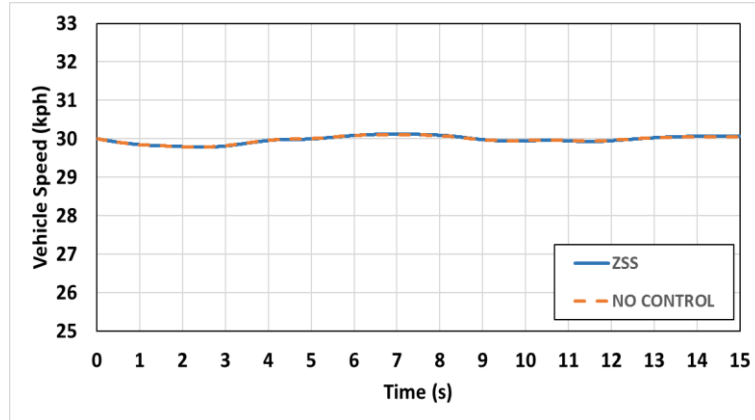


Figure 6-90 Vehicle Speeds during DLC at 30 kph ($\mu=0.85$)

Steering wheel angles of the controlled vehicles are shown in Figure 6-91.

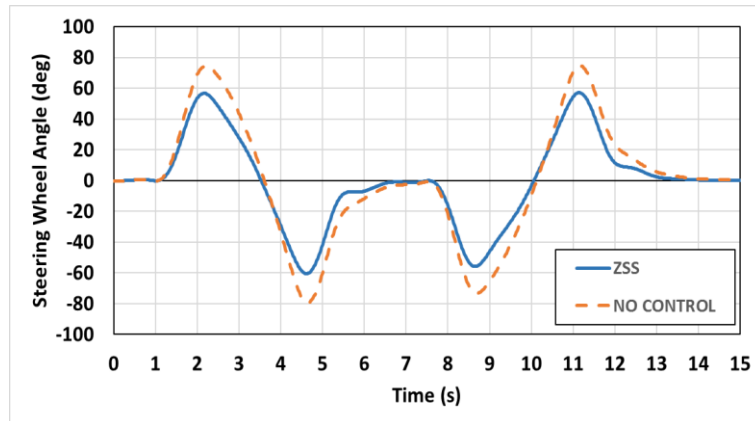
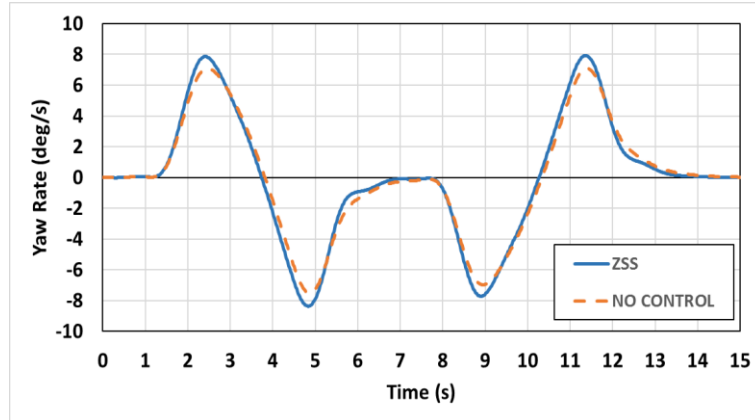


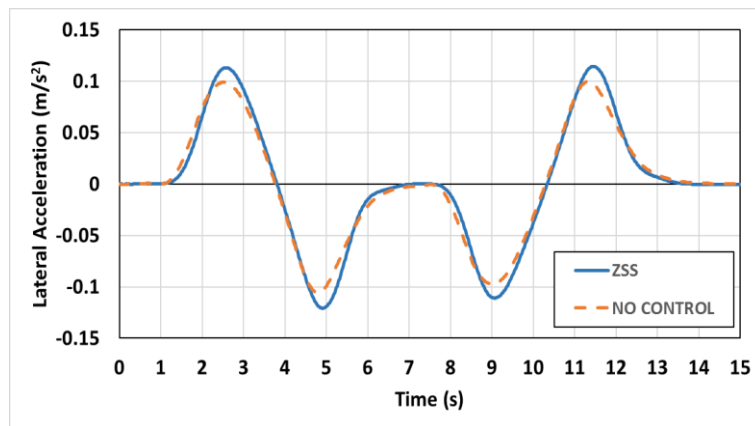
Figure 6-91 Steering Wheel Angles during DLC at 30 kph ($\mu=0.85$)

The ZSS controller successfully reduced steering effort during the double lane change at 30 kph. The peak steering angle values have been reduced by approximately 25%. Steering angle rate has also been reduced most notably between 2.2 and 4.5 and 8.7 and 11.2 seconds. Steering rate is also slightly reduced.

Vehicle yaw rates and lateral accelerations are shown in Figure 6-92.



(a)



(b)

Figure 6-92 Yaw rate (a) and Lateral Acceleration (b) during DLC at 30 ($\mu=0.85$)

Vehicle yaw rate and lateral acceleration peaks were marginally higher for the ZSS controlled vehicle.

Rear steer angles on the rear axles of the controlled vehicle are shown in Figure 6-93.

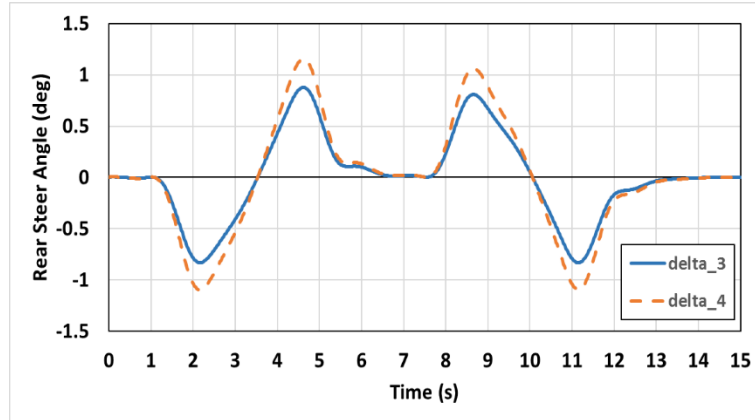


Figure 6-93 Rear Steer Angles during DLC at 30 kph ($\mu=0.85$)

ZSS controller's peak rear steer angles were approximately 1.1 and 0.8 degrees for the fourth and third axle respectively. The rear steer angles were of opposite direction to the front axle steer angles.

6.5.2 Results –ZSS Controller – Double Lane Change (30 kph; $\mu=0.35$)

Vehicle speed of the controlled and uncontrolled vehicles was maintained at approximately 30 kph as shown in Figure 6-94.

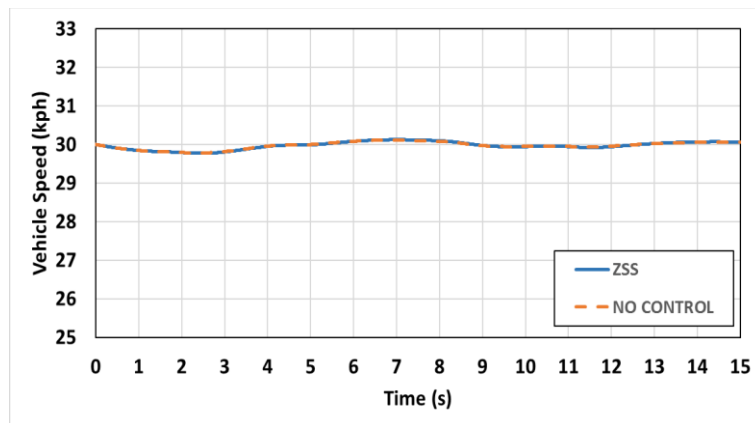


Figure 6-94 Vehicle Speeds during DLC at 30 kph ($\mu=0.35$)

Steering wheel angles of the controlled vehicles are shown in Figure 6-95.

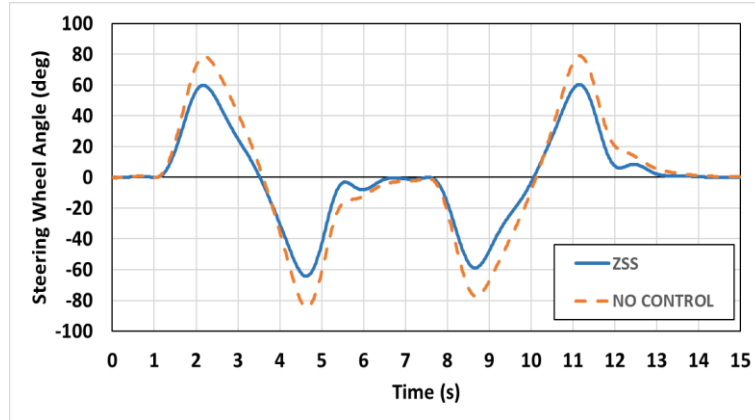
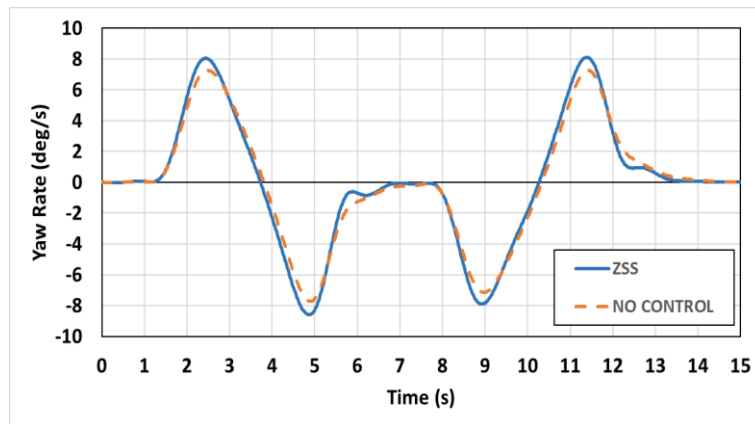


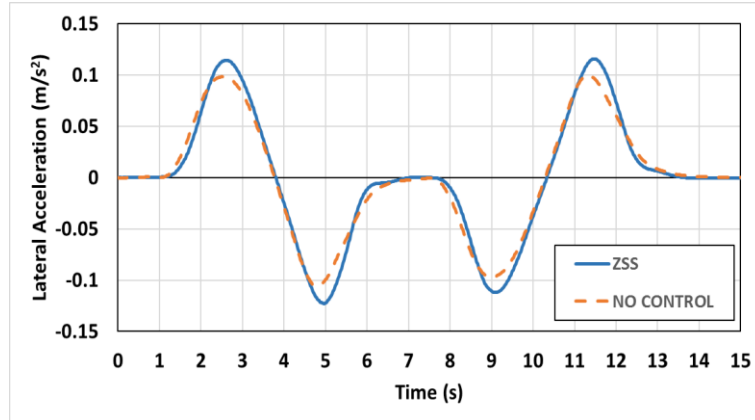
Figure 6-95 Steering Wheel Angles during DLC at 30 kph ($\mu=0.35$)

The ZSS controller successfully reduced steering effort during the double lane change at 30 kph. The peak steering angle values have been reduced by approximately 25%. Steering angle rate has also been reduced most notably between 2.2 and 4.5 and 8.7 and 11.2 seconds.

Vehicle yaw rates and lateral accelerations are shown in Figure 6-96.



(a)



(b)

Figure 6-96 Yaw rate (a) and Lateral Acceleration (b) during DLC at 30 kph ($\mu=0.35$)

Vehicle yaw rate and lateral acceleration peaks were marginally higher for the ZSS controlled vehicle.

Rear steer angles on the rear axles of the controlled vehicles are shown in Figure 6-97.

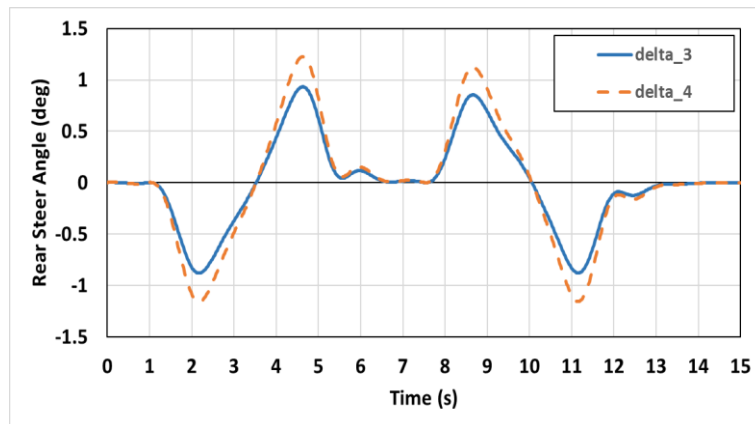


Figure 6-97 Rear Steer Angles during DLC at 30 kph ($\mu=0.35$)

ZSS controller's peak rear steer angles were approximately 1.3 and 1 degrees for the fourth and third axle respectively. The rear steer angles were of opposite direction to the front axle steer angles.

6.5.3 Results –ZSS Controller – Slalom (30 kph; $\mu=0.85$)

Vehicle speed of the controlled and uncontrolled vehicles was maintained at approximately 30 kph as shown in Figure 6-98.

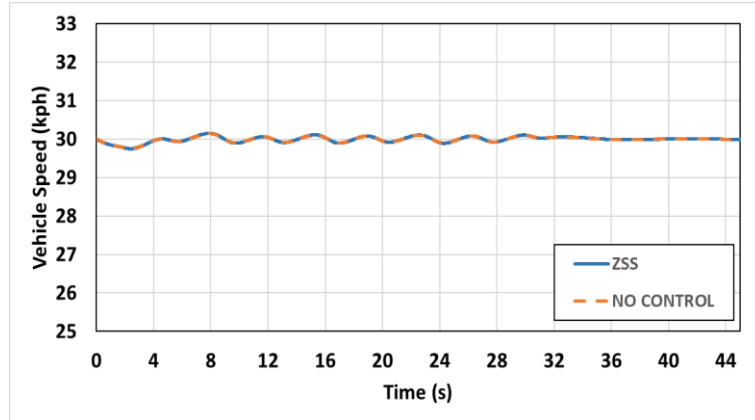


Figure 6-98 Vehicle Speeds during Slalom at 30 kph ($\mu=0.85$)

Steering wheel angles of the controlled vehicles are shown in Figure 6-99.

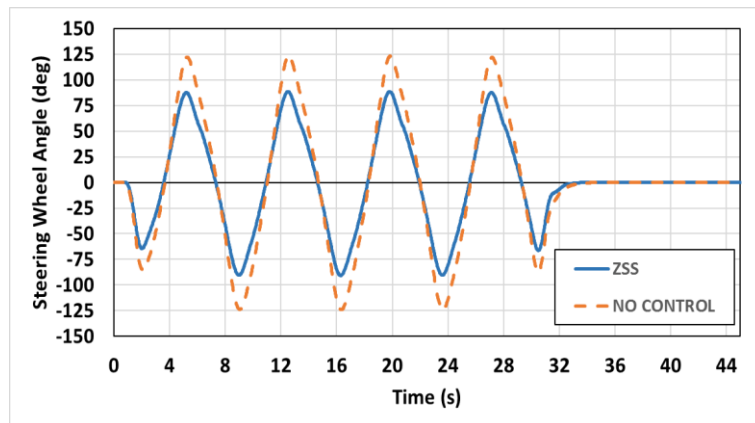
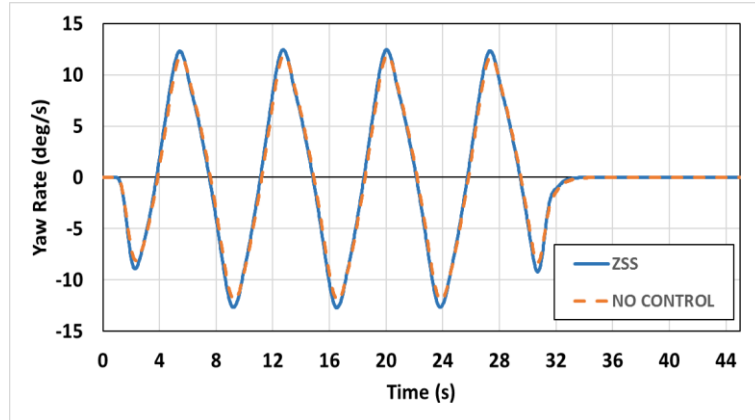


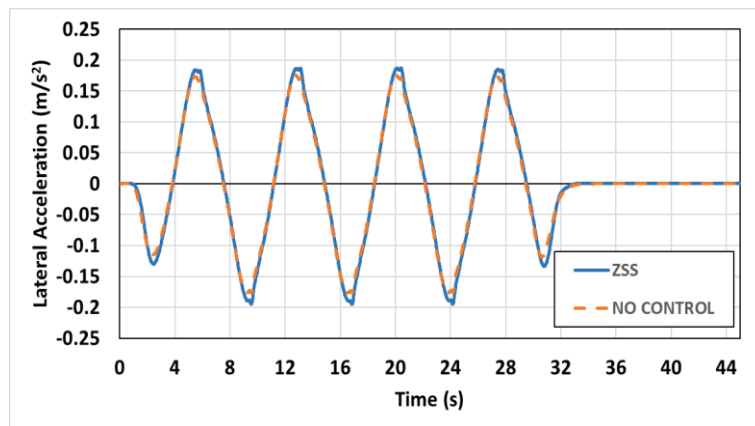
Figure 6-99 Steering Wheel Angles during Slalom at 30 kph ($\mu=0.85$)

The ZSS controller successfully reduced steering effort during the constant step slalom at 30 kph. The peak steering angle values have been reduced by approximately 30%. Steering angle rate has also been marginally reduced.

Vehicle yaw rates and lateral accelerations are shown in Figure 6-100.



(a)



(b)

Figure 6-100 Yaw Rate (a) and Lateral Acceleration (b) during Slalom at 30 kph ($\mu=0.85$)

Vehicle yaw rate and lateral acceleration peaks were largely unchanged with ZSS controller during the constant step slalom at 30 kph.

Rear steer angles on the rear axles of the controlled vehicles are shown in Figure 6-101.

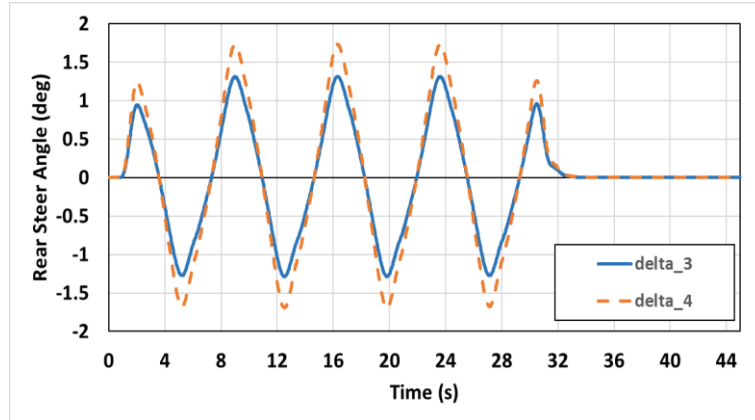


Figure 6-101 Rear Steer Angles during Slalom at 30 kph ($\mu=0.85$)

ZSS controller's peak rear steer angles were approximately 1.6 and 1.2 degrees for the fourth and third axle respectively. The rear steer angles were of opposite direction to the front axle steer angles.

6.5.4 Results –ZSS Controller – Slalom (30 kph; $\mu=0.35$)

Vehicle speed of the controlled and uncontrolled vehicles was maintained at approximately 30 kph as shown in Figure 6-102.

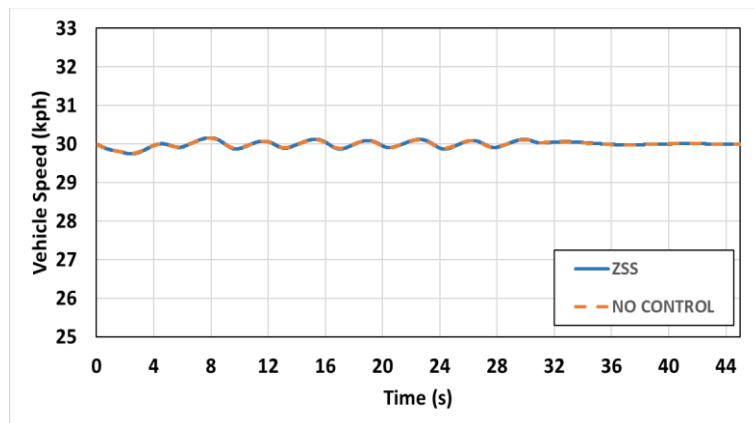


Figure 6-102 Vehicle Speeds during Slalom at 30 kph ($\mu=0.35$)

Steering wheel angles of the controlled vehicles are shown in Figure 6-103.

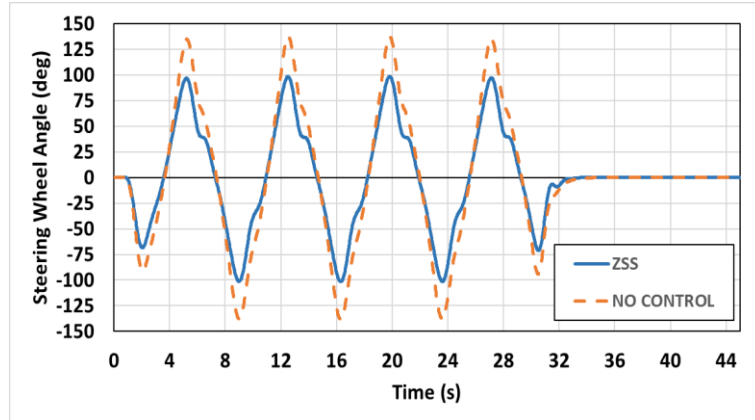
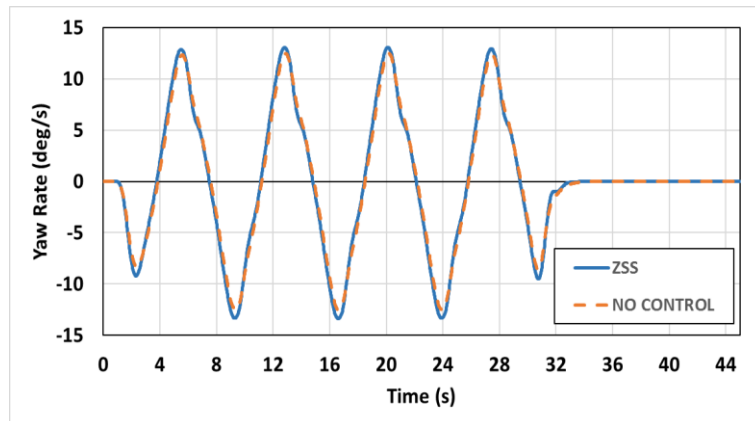


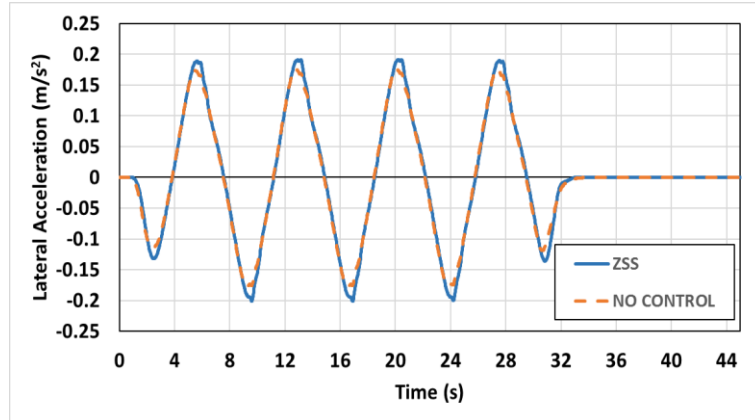
Figure 6-103 Steering Wheel Angles during Slalom at 30 kph ($\mu=0.35$)

The ZSS controller successfully reduced steering effort during the constant step slalom at 30 kph. The peak steering angle values have been reduced by approximately 30%. Steering angle rate has also been marginally reduced.

Vehicle yaw rates, lateral accelerations and side slip angles are shown in Figure 6-104.



(a)



(b)

Figure 6-104 Yaw rate (a) and Lateral Acceleration (b) during Slalom at 30 kph ($\mu=0.35$)

Vehicle yaw rate and lateral acceleration peaks were largely unchanged with ZSS controller during the maneuver.

Rear steer angles on the rear axles of the controlled vehicles are shown in Figure 6-105.

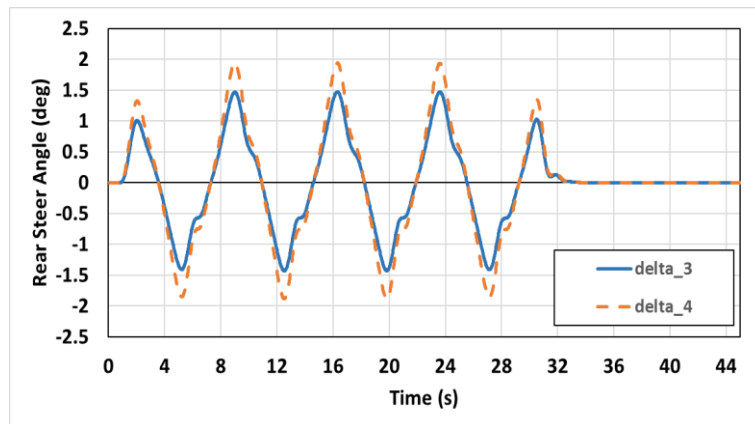


Figure 6-105 Rear Steer Angles during Slalom at 30 kph ($\mu=0.35$)

ZSS controller's peak rear steer angles were approximately 2 and 1.5 degrees for the fourth and third axle respectively. The rear steer angles were of opposite direction to the front axle steer angles.

6.6 SUMMARY

This chapter presented the results of the proposed vehicle dynamic control system in various dynamic events. A comparison between the vehicle equipped with the proposed control system, H_∞ and ZSS controllers, and uncontrolled vehicle was conducted to evaluate performance at various speeds, dynamic events and road friction coefficients (0.35 and 0.85 μ)

6.6.1 Conclusions - H_∞ Controller Dynamic Performance

The H_∞ controller was able to greatly improve dynamic performance on the double lane change, slalom, FMVSS 126 ESC, J-Turn and constant radius circle maneuvers on both low and high friction surfaces and is suitable for use on the 8 x 8 combat vehicle.

The controller demonstrated:

- Robustness for various vehicle speeds within the scheduling parameter range, 40 to 100 kph events.
- Increased vehicle stability in high speed/highly demanding maneuvers by attenuating peak yaw rates, lateral accelerations and vehicle side slip responses. Steady state responses were obtained in a shorter time span and were maintained throughout the maneuvers. This effect was most prominent on the low friction surfaces and very demanding events on high friction surfaces. This confirms that the proposed controller is both robust to low friction surfaces and, more importantly, that it maintains vehicle stability in emergency/highly demanding maneuvers. The most notable results were obtained in the FMVSS 126 ESC at 80 kph for both 0.35 and 0.85 μ surfaces and the 65 kph slalom on 0.85 μ surface.
- Effectiveness in greatly decreasing steering effort in path following events (double lane change and slalom). The greatest impact was observed in the 80 kph double lane change on both 0.35 and 0.85 μ surfaces and in the 65 and 40 kph slalom events on 0.85 μ surface. Peak steering wheel angles were decreased by 50% or more in some cases.

- Increased vehicle mobility during the J-Turn events at 50 kph on 0.85 μ surface by decreasing yaw rate, lateral acceleration and vehicle side slip time delays and increasing peak steady state values. This resulted in a tighter turning circle for the same steering input. When the event was repeated on a low friction surface, the controller demonstrated lower peak vehicle responses and maintained stability through a longer turning circle as compared to the uncontrolled vehicle. The same damping effect was observed when the J-Turn was simulated at 80 kph on a high friction surface, again vehicle responses were attenuated and vehicle stability was maintained.
- Good yaw rate reference signal tracking through all events. Overshoot was observed for high speed/highly demanding maneuvers on the lower friction surfaces which is acceptable given the nature of the simulated events. Steady state error was confirmed to fall within the 15% error specified during controller synthesis via the yaw rate error weighting functions.
- The proposed PI speed controller did negatively affect vehicle forward speed tracking during any of the events
- Average wheel torque differentials during the various dynamic events of 3500 – 4000 Nm. The highest torque differential, 7800 Nm, occurred during the 65 kph slalom event on the 0.85 μ surface. The lowest torque differential, 1100 Nm, occurred during the J-Turn at 50 kph on the 0.35 μ surface.
- Average rear axle steering angles during the various dynamic events of 1.5 – 1 degrees for the fourth axle and 1.1 – 0.7 degrees for the third axle. The highest rear axle steering angles, 3 and 2.3 degrees, for the fourth and third axles respectively occurred during the 65 kph slalom event on the 0.85 μ surface. The lowest rear axle steering angles, 0.4 and 0.3 degrees, for the fourth and third axles respectively occurred during the J-Turn at 50 kph on the 0.35 μ surface. The H_∞ controller turned the rear wheels in both the same and opposite direction of the front steering angles depending on the event and speed.

6.6.2 Conclusions – Turning Circle Reduction Performance

ZSS controller proved very effective for turning circle reduction. The following observations were made:

- Rear steer angles required a limit due to physical space allowed for tire angles on the rear two axles of the vehicle. Maximum angles of 20, 17, 15, 10 and 5 degrees were tested resulting in turning circle diameters of 11.5, 12.5, 12.7, 14.5 and 16.5 meters respectively.
- A maximum angle of 17 degrees for the fourth axle and 13 degrees for the third axle is recommended
- The developed ZSS turning circle reduction controller with limited rear steer angles provided a turning circle diameter of 12.5m representing a reduction of 30% from the baseline vehicle with no rear steering capability.

6.6.3 Conclusions – Switching Speed Evaluation

Switching speed evaluation was conducted by comparing the ZSS and H_{∞} controllers in a double lane change maneuver at 80, 60 and 40 kph and a slalom maneuver at 40 kph. The ZSS controller was not as effective as the H_{∞} and was therefore found not to be suitable for speeds between 40 and 80 kph.

The following observations were made:

- The ZSS controller is not suitable for use at speed of 80 kph. During the double lane change at 80 kph the ZSS controlled vehicle demonstrated heavy understeering behaviour which resulted in the vehicle failing the maneuver by contacting cones at every gate in the event. The ZSS controlled commanded rear wheel steer angles in the same direction as the front steering angles which led to the heavy understeer. This agrees with the literature on ZSS control at high speeds. Steering effort was greatly increased for the ZSS controller.
- The ZSS controller is not suitable for use at speed of 60 kph. During the double lane change, the vehicle equipped with the ZSS controller required steering effort peak values that were twice as high as those for of the H_{∞} controlled vehicle. Again

the H_∞ controller commanded rear steer angles in the opposite direction of the front steer angles where the ZSS controller commanded them in the same direction as the front steer angles.

- The gap in performance between the ZSS and H_∞ controllers was greatly decreased in double lane change at 40 kph. Only a marginally lower steering effort was observed for the H_∞ . Vehicle responses were almost identical. It is interesting to note that the rear steer angles commanded by both controllers were both in the opposite direction of the front wheels and of the same magnitude. This explains the similar performance demonstrated by the controllers during this event.
- The H_∞ controller was much more effective than the ZSS during the slalom at 40 kph. Peak steering efforts were reduced by 25%. Rear steer angles were identical in both direction and magnitude for both controllers. Concluding that the lower steering effort observed can be attributed to the additional torque vectoring capability of the H_∞ controller.
- The upper limit cut-off speed for the ZSS controller was found to be lower than 40 kph.

6.6.4 Conclusions – Low Speed Dynamic Evaluation of ZSS Controller

More testing was required to determine the cut-off speed for the ZSS controller. The ZSS controlled and uncontrolled vehicle were compared during double lane change and slalom events at 30 kph on both 0.35 and 0.85 μ to determine the suitability of using the ZSS during low speed maneuvering. The ZSS controller was deemed suitable for use during low speed (<30 kph) maneuvering.

The following observations were made:

- For both the double lane change and slalom at 30 kph on both the 0.35 and 0.85 μ surfaces, the ZSS controller was able to greatly increase vehicle maneuverability by decreasing steering angle peaks by approximately 25% and demonstrating slight increases in peak values of yaw rate and lateral acceleration.
- There was no evidence to indicate that the ZSS controller caused any additional instability at 30 kph on high and low friction surfaces and is therefore considered

suitable for turning circle reduction and low speed maneuverability. Speeds below 30 kph on the maneuvers will yield similar results.

- The switching speed range used for the Gaussian activation functions was determined to be 30 to 40 kph. Until speeds of 30 kph the ZSS turning circle reduction controller will be used to control the vehicle. No torque vectoring is used. At speeds between 30 and 40 kph. The rear steer angle commanded by the ZSS controller will be phased out while the rear steer angles and torque vectoring commands from the H_∞ controller will be phased in. At speeds of 40 kph and above, only the H_∞ controller will be active ensuring proper reference tracking for vehicle stability at higher speeds.
- Maximum rear steer angles of 2 and 1.5 degrees for the fourth and third axles respectively were observed during the slalom event at 30 kph with a road friction coefficient of 0.35 μ .
- The ZSS controller steered the rear axles in the opposite direction of the front axles for all maneuvers which attributed the increase in maneuverability.

CHAPTER 7

CONCLUSIONS & FUTURE WORK

7.1 ACCOMPLISHMENTS

This thesis proposes a vehicle dynamics controller for vehicle stability, maneuverability and turning circle reduction. The proposed control scheme is composed of two distinct controllers, each with their own range of operation based on vehicle speed. A feedforward zero side slip (ZSS) controller actuates the third and fourth axle steering angles. It is used for maneuvering at speeds of 30 kph and below and for turning circle reduction. A two DOF LPV H_∞ controller that monitors steering wheel angle and yaw rate error uses both the rear axle steering and torque vectoring to enhance vehicle dynamics at speeds above 40 kph. The proposed control scheme is evaluated by running simulations using a validated TruckSim full vehicle model in co-simulation with the proposed control scheme in Simulink. Events used for testing included NATO double lane change, NATO constant step slalom, FMVSS 126 ESC, J-Turn and constant radius circle. Two road friction coefficients were tested, 0.35 and 0.85 μ .

The following goals have been accomplished:

- An externally modelled electric powertrain has been developed and implemented with the TruckSim full vehicle model.
- A control scheme based on speed dependent switching between feedforward ZSS and two DOF LPV H_∞ controller has been proposed. Gaussian activation functions have been used for switching purposes. A simple on/off slip controller is also included. A switching speed range of 30 to 40 kph was determined using full vehicle simulations.
- The proposed control scheme has been successfully implemented in MATLAB/Simulink in co-simulation with TruckSim and the electric powertrain in order to test the performance of the vehicle dynamics control system.
- A ZSS feedforward controller has been implemented for low speed (30 kph and below) maneuverability and turning circle reduction. Peak steer angle reductions

of 25% were observed. Curb-to-curb vehicle turning circle was reduced by 30% for a final turning circle of 12.5m with maximum allowable rear steer angles of 17 and 13 degrees for the fourth and third axles respectively.

- The two DOF LPV H_∞ controller was found to increase vehicle stability at high speed and/or low friction maneuvers. Steering angle peak values and rates of change of the steering angle have been reduced allowing for a more easily controlled vehicle. Yaw rate, lateral acceleration and vehicle side slip angle peaks have been successfully damped for high speed/low friction events.
- The two DOF LPV H_∞ controller was also found to increase vehicle maneuverability on higher friction surfaces during less aggressive maneuvers. Higher peak values of yaw rate, lateral acceleration and vehicle side slip as well as shorter time delays were observed during simulation. No negative impact to vehicle stability was observed.
- Good yaw rate reference tracking was observed in all cases.
- The yaw rate reference generator with road friction saturation was critical in allowing for an increase in both maneuverability and stability. The algorithm enables a flexible yaw rate signal that adapts to vehicle speed, steering and road friction coefficient.
- The highest torque differential (7800 Nm) occurred during the 65 kph slalom event on the 0.85 μ surface. The lowest torque differential (1100 Nm) occurred during the J-Turn at 50 kph on the 0.35 μ surface.
- The maximum rear steer angles commanded by the H_∞ controller were 3 and 2.3 degrees for the fourth and third axles respective which occurred during the 65 kph slalom event on the 0.85 μ surface.
- The maximum rear steer angles commanded by the ZSS controller were 2 and 1.5 degrees for the fourth and third axles respectively were observed during the slalom event at 30 kph with a road friction coefficient of 0.35 μ .

7.2 GENERAL CONCLUSIONS

The widespread adoption of active safety control systems in automotive applications in the last several decades including anti-lock braking (ABS) systems, traction control systems (TCS) and electronic stability control systems (ESC) has allowed for great improvement in vehicle safety. Advancements in powertrain and control systems technologies have led to the rise of more complex and effective systems including torque vectoring and rear wheel steering. The above control systems have been proven in real life passenger car applications and are currently in production. Work was conducted to explore the benefits of applying these control systems to an 8 x 8 combat vehicle.

A general reintroduction of the fundamental working foundations of vehicle dynamics and control theory including tire dynamics, vehicle lateral dynamics and control system configurations was presented.

A literature review of the body of work conducted on torque vectoring and rear wheel steering with respect to its effectiveness in influencing vehicle dynamic behaviour, its implementation in four-wheeled vehicles, electric vehicles and multi-wheeled vehicles was presented. An emphasis was placed on linear parameter-varying H_∞ controller implementations. A great deal of work was reviewed that demonstrated the effectiveness of torque vectoring and active steering systems on influencing vehicle dynamic behaviour. Various linear control methods have been proposed to control non-linear vehicle responses utilizing feedforward, feedback control or both. Positive results have been demonstrated by all studies. The most popular methods of control include PID, fuzzy logic, MPC, LQR, sliding mode and H_∞ . However, an optimal method has not been proposed. Several studies concluded that due to the uncertainties involved with vehicle dynamics, robust control strategies should be used. H_∞ control was found to be well suited to the control of multiple actuation systems as it exhibits robustness and disturbance rejection. LPV H_∞ control has been widely used for multiple input multiple output systems with good results. Feedforward turning circle reduction strategies were also covered.

Four different vehicle models were derived for use in this work. A validated non-linear TruckSim vehicle model of the 8 x 8 combat vehicle was presented and used for controller

performance evaluation using the developed externally modelled electric powertrain implemented in Simulink. A linear plant model based on differential equations of the yaw rate and side slip responses of a bicycle model including external yaw moment and third and fourth axle steering terms was used for H_∞ controller synthesis. A linear steady state bicycle model without external yaw moment or rear steering was used in conjunction with a first order time delay and saturation function based on vehicle speed and road friction coefficient to generate the yaw rate reference signal required for reference signal tracking in the H_∞ controller. The zero side slip (ZSS) method was developed for the four axle bicycle model and used for turning circle reduction and low speed maneuverability improvement.

The theory behind linear parameter-varying (LPV) H_∞ control synthesis was presented. This theory was then used in order to develop the two DOF LPV H_∞ controller with scheduling parameters based on vehicle speed. The controller consists of a feedforward and feedback components utilising mixed sensitivity weighting functions for good reference tracking and to minimize the yaw rate error signal due to disturbances and uncertainties. A 15% limit on steady state error performance weighting function was used for the error signal. Use of rear steering control was limited to frequencies between 1 and 10 Hz where it is difficult for the driver to intervene on his own.

The proposed vehicle dynamics control system is activated when the vehicle is moving forward between speeds of 0 and 110 kph. The controller is not active when the vehicle is in reverse for safety reasons. The system is composed of a PI speed controller that manipulates all eight electric motor currents evenly in order to maintain desired forward speed. The upper controller consists of the presented two DOF LPV H_∞ controller (speeds of 40 kph and above) and the ZSS controller (speeds of 30 kph and below). Switching is accomplished using two Gaussian distribution functions, one for each controller output. The functions transition from the ZSS controller's rear steer signal to the H_∞ controller's rear steering and torque vectoring signals between 30 kph to 40 kph. The lower controller translates the desired yaw moment about the center of gravity from the upper controller into individual electric motor currents to implement torque vectoring. This current is then combined with the PI speed controller electric motor current and sent to the electric

powertrain. The lower controller also distributes the rear steering angle command between the third and fourth axles for the ZSS and H_∞ controllers. A simple on/off slip controller is used to ensure the slip ratio of each wheel does not exceed 20%.

Various simulations were run in order to evaluate the proposed control systems performance. The performance of the H_∞ controller was tested on NATO double lane change, NATO slalom, FMVSS 126 ESC, J-Turn and constant radius circle maneuvers for speeds ranging from 40 kph to 100 kph. Two road friction coefficients were used, 0.85 and 0.35 μ . The ZSS controller ability to reduce turning circle was evaluated by locking the steering wheel and allowing the vehicle to turn one full turning circle diameter and comparing the result with the uncontrolled vehicle. Gaussian distribution switching speed range was determined by comparing the performance of the H_∞ and ZSS controllers through a NATO double lane change at speeds between 40 and 80 kph and a NATO slalom maneuver at 40 kph for low and high road friction coefficients. Low speed NATO double lane change and NATO slalom maneuvers at 30 kph for high and low friction surfaces were used to determine the viability of using the ZSS to maneuver at low speeds.

The control system was found to increase vehicle stability at high speed and/or low friction maneuvers. Steering angle peaks and rate of change were reduced allowing for a more easily controlled vehicle. Yaw rate, lateral acceleration and vehicle side slip angle peaks were successfully damped for high speed/low friction events. The control system was also found to increase vehicle maneuverability on higher friction surfaces during less aggressive maneuvers. Vehicle stability was not adversely affected.

Good reference tracking was observed in all cases. The yaw rate reference generator with road friction saturation was critical in allowing for an increase in both maneuverability and stability. The algorithm enables a flexible yaw rate signal that adapts to vehicle speed, steering and road friction coefficient.

Turning circle reduction with maximum allowable rear steer angles of 17 and 13 degrees for the fourth and third axles respectively allow for a 30% reduction in turning circle diameter for a final turning circle diameter of 12.5m.

The ZSS controller was found to be inappropriate for high speed maneuvering. Ideal switching speed range was found to be between 30 and 40 kph. The ZSS controller was found to increase vehicle maneuverability at speeds of 30 kph by reducing steering angle peaks by 25%.

7.3 FUTURE WORK

The use of parameter-dependent weighting functions could be explored during controller synthesis in order to determine their effect on controller performance.

An online road friction estimator should be developed and implemented for all simulations conducted in order to determine the feasibility and reliability of online road friction coefficient estimation.

Reference generation is a critical component in any reference tracking controller as has been shown here. Several authors have proposed more complex reference models involving offline optimization. A reference model with all available actuation systems is run for all possible values of the control systems the vehicle will be equipped with. This allows for the creation of a large area of possible lateral acceleration vs steering curve values. The designer is free to choose the shape and characteristics of this curve allowing for the complete modification of the controlled vehicle's behaviour. This reference model should be implemented with the proposed control system here and the simulations rerun for comparison purposes.

The effect of implementing a more complex optimal lower controller to distribute rear wheel steer angle and torque vectoring commands could be explored. Care should be taken to ensure the proposed system is implementable on an actual vehicle. Simulations comparing the lower controller from this work with a more complex lower controller should be explored in order to determine if there are any performance gains to be had.

The proposed control system should be implemented in a driver-in-the-loop full vehicle simulator in order to determine the effect of a human driver on controller performance and how the controller affects driver feedback and confidence during various maneuvers.

Finally, work should be conducted to convert the proposed control system to discrete time implementation. Issues such as fault detection and sensor noise should be addressed. Online computational power required should be investigated with either hardware-in-the-loop simulations or implementation on an actual 8 x 8 combat vehicle in order to document controller performance under real world testing conditions.

PUBLICATIONS

D'Urso, P., El-Gindy, M., "Development of H_{∞} Control Strategy for a Multi-Wheeled Combat Vehicle – A Literature Survey", *International Journal of Vehicle Performance (IJVP)*, 2016 (Submitted)

D'Urso, P., El-Gindy, M., " H_{∞} Vehicle Dynamics Control of an 8 x 8 Combat Vehicle Using Rear Wheel Steering and Torque Vectoring", *International Journal of Vehicle Systems Modelling and Testing (IJVSMT)*, 2016 (Submitted)

Note: Publication(s) mentioned above have been written in whole or in part by the author and are included in this work. All writing, data and research conducted in this work and publication(s) was completed by the author. Co-authors reviewed and provided technical support when required.

REFERENCES

- [1] L. Systems. (2016, June 03). *Products - Light Armoured Vehicles - LAV III*. Available: <http://www.gdlsCanada.com/products/light-armoured-vehicles/lav-iii.php>
- [2] IIHS. (2016, June 03). *Stability control could prevent a third of fatal crashes*. Available: <http://www.iihs.org/iihs/news/desktopnews/electronic-stability-control-could-prevent-nearly-one-third-of-all-fatal-crashes-and-reduce-rollover-risk-by-as-much-as-80-effect-is-found-on-single-and-multiple-vehicle-crashes>
- [3] M. Blundell and D. Harty, *The Multibody Systems Approach to Vehicle Dynamics*. Coventry: Elsevier, 2015.
- [4] D. Karnopp, *Vehicle Dynamics, Stability, and Control*. Boca Raton: CRC Press, 2013.
- [5] G. Mastinu and M. Ploechl, *Road and Off-Road Vehicle System Dynamics Handbook*. Boca Raton: CRC Press, 2014.
- [6] J. Y. Wong, *Theory of Ground Vehicles*. Hoboken: John Wiley & Sons, Inc., 2008.
- [7] A. Reid, "Development and Optimization of a Wide Base FEA Truck Tire Model for Prediction of Tire-Road Interactions," *University of Ontario Institute of Technology*, p. 123, 2015.
- [8] E. Bedner, Fulk, D., and Hac, A., "Exploring the Trade-Off of Handling Stability and Responsiveness with Advanced Control Systems," *SAE Technical Paper*, p. 14, 2007.
- [9] H. Kim, S. Lee, and J. K. Hedrick, "Active yaw control for handling performance improvement by using traction force," *International Journal of Automotive Technology*, vol. 16, pp. 457-464, 2015.
- [10] W. F. Milliken and D. L. Milliken, *Race Car Vehicle Dynamics*: Society of Automotive Engineers, 1995.
- [11] S. o. A. Engineers, "Vehicle Dynamics Terminology," ed. Warrendale, PA: SAE International, 2008, p. 73.
- [12] S. Sano, Y. Furukawa, and S. Shiraishi, "Four Wheel Steering System with Rear Wheel Steer Angle Controlled as a Function of Steering Wheel Angle," *SAE Technical Paper Series*, vol. V-95-86, p. 16, 1986.
- [13] S. Skogestad, I. Postlethwaite, and S. Skogestad, *Multivariable feedback control: Analysis and design*, 2 ed. United States: Wiley, John & Sons, 2005.
- [14] N. S. Nise, *Control systems engineering* vol. Seventh. Hoboken, NJ: John Wiley & Sons, Inc, 2015.
- [15] EVBud. (June 8). *Rimac concept One Supercar*. Available: <http://evbud.com/news/505/>
- [16] K. U. Sawase, Yuichi; Miura, Takami;, "Left-Right Torque Vectoring Technology as the Core of Super All Wheel Control (S-AWC)," *Mitsubishi Technical Review*, 2006.
- [17] M. Hancock, R. Williams, T. Gordon, and M. C. Best, "A comparison of braking and differential control of road vehicle yaw-sideslip dynamics," *Proceedings of the Institution of Mechanical Engineers, Part D: Journal of Automobile Engineering*, vol. 219, pp. 309-327, 2005.

- [18] A. G. Ulsoy, H. Peng, and M. Çakmakci, *Automotive control systems*: Cambridge University Press, 2012.
- [19] Y. Furukawa and M. Abe, "Advanced chassis control systems for vehicle handling and active safety," *Vehicle System Dynamics*, vol. 28, pp. 59-86, 1997.
- [20] M. Nagai, Y. Hirano, and S. Yamanaka, "Integrated Control of Active Rear Wheel Steering and Direct Yaw Moment Control," *Vehicle System Dynamics*, vol. 27, pp. 357-370, 1997.
- [21] M. Yamamoto, "Active control strategy for improved handling and stability," SAE Technical Paper 0148-7191, 1991.
- [22] K. Shimada and Y. Shibahata, "Comparison of three active chassis control methods for stabilizing yaw moments," SAE Technical Paper 0148-7191, 1994.
- [23] K. U. Sawase, Yuichi, "Improvement of Vehicle Dynamics by Right-and-Left Torque Vectoring System in Various Drivetrains," *Mitsubishi Motors Technical Review*, 2008.
- [24] M. K. Aripin, Y. Md Sam, K. A. Danapalasingam, K. Peng, N. Hamzah, and M. F. Ismail, "A Review of Active Yaw Control System for Vehicle Handling and Stability Enhancement," *International Journal of Vehicular Technology*, vol. 2014, pp. 1-15, 2014.
- [25] A. B. Hac, Mark, "Improvements in Vehicle Handling Through Integrated Control of Chassis Systems," *International Journal of Vehicle Autonomous Systems*, vol. 1, pp. 83-110, 2002.
- [26] J. Kasac, J. Deur, B. Novakovic, M. Hancock, and F. Assadian, "Optimization of global chassis control variables," in *Proceedings of the 17th World Congress: the International Federation of Automatic Control Seoul, Korea*, 2008, pp. 2081-2086.
- [27] J. Yamakawa and K. Watanabe, "A method of optimal wheel torque determination for independent wheel drive vehicles," *Journal of Terramechanics*, vol. 43, pp. 269-285, 2006.
- [28] K. Jalali, T. Uchida, J. McPhee, and S. Lambert, "Development of an Integrated Control Strategy Consisting of an Advanced Torque Vectoring Controller and a Genetic Fuzzy Active Steering Controller," *SAE International Journal of Passenger Cars - Electronic and Electrical Systems*, vol. 6, pp. 222-240, 2013.
- [29] K. Jalali, T. Uchida, J. McPhee, and S. Lambert, "Development of an advanced fuzzy active steering controller and a novel method to tune the fuzzy controller," *SAE Int J Passenger Cars Electron Electr Syst*, vol. 6, pp. 241-254, 2013.
- [30] E. Siampis, E. Velenis, and S. Longo, "Rear wheel torque vectoring model predictive control with velocity regulation for electric vehicles," *Vehicle System Dynamics*, vol. 53, pp. 1555-1579, 2015.
- [31] B. Li, H. Du, and W. Li, "Optimal Distribution Control Of Non-Linear Tire Force Of Electric Vehicles With In-Wheel Motors," *Asian Journal of Control*, vol. 18, pp. 69-88, Jan 2016.
- [32] T. Bunte, S. Kaspar, S. Hohmann, and J. Brembeck, "Inverse model based torque vectoring control for a rear wheel driven battery electric vehicle," in *IFAC World Congress*, 2014.
- [33] N. Bajcinca and T. Bunte, "A novel control structure for dynamic inversion and tracking tasks," in *Proc. of 16th IFAC World Congress, Prague*, 2005.

- [34] L. S. De Novellis, Aldo; Gruber, Patrick; Shead, Leo; and V. H. Ivanov, Kristian;, "Torque Vectoring for Electric Vehicles with Individually Controlled Motors: State-of-the-Art and Future Developments," 2012.
- [35] V. A. Ivanov, Klaus; Savitski, Dzmitry;, "Torque Vectoring for improving mobility of all-terrain electric vehicles," 2012.
- [36] L. De Novellis, A. Sorniotti, P. Gruber, J. Orus, J.-M. Rodriguez Fortun, J. Theunissen, *et al.*, "Direct yaw moment control actuated through electric drivetrains and friction brakes: Theoretical design and experimental assessment," *Mechatronics*, vol. 26, pp. 1-15, 2015.
- [37] A. Jackson, D. Crolla, A. Woodhouse, and M. Parsons, "Improving performance of a 6× 6 off-road vehicle through individual wheel control," SAE Technical Paper 0148-7191, 2002.
- [38] B. Chen, C. Yu, and W. Hsu, "Optimal steering control for six-wheeled vehicle," in *Proceeding of International Symposium on Advanced Vehicle Control*, 2006, pp. 605-610.
- [39] S. An, H. Lee, W. Cho, G. Jung, K. Yi, and K. Lee, "Development of steering algorithm for 6WS military vehicle and verification by experiment using a scale-down vehicle," in *Proc. Int. Symp. Advanced Vehicle Control*, 2006.
- [40] S.-J. An, K. Yi, G. Jung, K. I. Lee, and Y.-W. Kim, "Desired yaw rate and steering control method during cornering for a six-wheeled vehicle," *International Journal of Automotive Technology*, vol. 9, pp. 173-181, 2008.
- [41] W. Kim, K. Yi, and J. Lee, "An optimal traction, braking, and steering coordination strategy for stability and manoeuvrability of a six-wheel drive and six-wheel steer vehicle," *Proceedings of the Institution of Mechanical Engineers, Part D: Journal of automobile engineering*, vol. 226, pp. 3-22, 2011.
- [42] W. G. K. Kim, J. Y.; YI, K., "Drive Control System Design for Stability and Maneuverability of a 6WD/6WS Vehicle," *International Journal of Automotive Technology*, vol. 12, pp. 67-74, 2011.
- [43] R. Rajamani, *Vehicle dynamics and control*: Springer Science & Business Media, 2011.
- [44] 이대옥 and 여승태, "A Study on Maneuvering Control Algorithm Based on All-wheel Independent Driving and Steering Control for Special Purpose 6WD/6WS Vehicles," *Journal of the Korea Institute of Military Science and Technology*, vol. 16, pp. 240-249, 2013.
- [45] W. Kim, K. Yi, and J. Lee, "Drive control algorithm for an independent 8 in-wheel motor drive vehicle," *Journal of Mechanical Science and Technology*, vol. 25, pp. 1573-1581, 2011.
- [46] H. Ragheb, "Torque Control Strategy for Off-Road Vehicle Mobility," Doctor of Philosophy (PhD), University of Ontario Institute of Technology, Oshawa, Canada, 2014.
- [47] D.-W. Gu, P. H. Petkov, and M. M. Konstantinov, "Robust Control Design with MATLAB®," *Advanced Textbooks in Control and Signal Processing*, 2013.
- [48] G. Kaiser, "Torque Vectoring-Linear Parameter-Varying Control for an Electric Vehicle," Doctor of Philosophy (PhD), Technischen Universität Hamburg-Harburg, Heidelberg, Germany, 2015.

- [49] Q. Lu, A. Sorniotti, P. Gruber, J. Theunissen, and J. De Smet, "H ∞ loop shaping for the torque-vectoring control of electric vehicles: Theoretical design and experimental assessment," *Mechatronics*, vol. 35, pp. 32-43, 2016.
- [50] T. Goggia, A. Sorniotti, L. D. Novellis, A. Ferrara, A. Pennycott, P. Gruber, *et al.*, "Integral sliding mode for the yaw moment control of four-wheel-drive fully electric vehicles with in-wheel motors," *International Journal of Powertrains*, vol. 4, pp. 388-419, 2015.
- [51] S. Horiuchi, N. Yuhara, and A. Takei, "Two degree of freedom/H ∞ controller synthesis for active four wheel steering vehicles," *Vehicle System Dynamics*, vol. 25, pp. 275-292, 1996.
- [52] H. Lv, N. Chen, and P. Li, "Multi-objective H ∞ optimal control for four-wheel steering vehicle based on yaw rate tracking," *Proceedings of the Institution of Mechanical Engineers, Part D: Journal of Automobile Engineering*, vol. 218, pp. 1117-1123, 2004.
- [53] B. A. Güvenç, T. Bünte, D. Odenthal, and L. Güvenç, "Robust two degree-of-freedom vehicle steering controller design," *Control Systems Technology, IEEE Transactions on*, vol. 12, pp. 627-636, 2004.
- [54] B. A. Güvenç, B. A. Güvenç, and S. Karaman, "Robust yaw stability controller design and hardware-in-the-loop testing for a road vehicle," *Vehicular Technology, IEEE Transactions on*, vol. 58, pp. 555-571, 2009.
- [55] M. Canale, L. Fagiano, M. Milanese, and P. Borodani, "Robust vehicle yaw control using an active differential and IMC techniques," *Control Engineering Practice*, vol. 15, pp. 923-941, 2007.
- [56] G. Kaiser, Q. Liu, C. Hoffmann, M. Korte, and H. Werner, "Torque vectoring for an electric vehicle using an LPV drive controller and a torque and slip limiter," in *Decision and Control (CDC), 2012 IEEE 51st Annual Conference on*, 2012, pp. 5016-5021.
- [57] Q. Liu, G. Kaiser, S. Boonto, H. Werner, F. Holzmann, B. Chretien, *et al.*, "Two-degree-of-freedom LPV control for a through-the-road hybrid electric vehicle via torque vectoring," in *Decision and Control and European Control Conference (CDC-ECC), 2011 50th IEEE Conference*, Orlando, USA, 2011, pp. 1274-1279.
- [58] G. Yin, R. Wang, and J. Wang, "Robust control for four wheel independently-actuated electric ground vehicles by external yaw-moment generation," *International Journal of Automotive Technology*, vol. 16, pp. 839-847, 2015.
- [59] P. Gáspár, Z. Szabó, and J. Bokor, "The design of an integrated control system in heavy vehicles based on an LPV method," in *Decision and Control, 2005 and 2005 European Control Conference. CDC-ECC'05. 44th IEEE Conference*, Seville, Spain, 2005, pp. 6722-6727.
- [60] C. Poussot-Vassal, O. Sename, S. Fergani, M. Doumiati, and L. Dugard, "Global chassis control using coordinated control of braking/steering actuators," *Robust Control and Linear Parameter Varying approaches: application to vehicle dynamics*, pp. 237-266, 2013.
- [61] D. Selmanaj, M. Corno, O. Sename, and S. Savaresi, "Advantages of rear steer in LTI and LPV vehicle stability control," in *Decision and Control (CDC), 2013 IEEE 52nd Annual Conference*, 2013, pp. 3523-3528.

- [62] M. Doumiati, O. Sename, L. Dugard, J.-J. Martinez-Molina, P. Gaspar, and Z. Szabo, "Integrated vehicle dynamics control via coordination of active front steering and rear braking," *European Journal of Control*, vol. 19, pp. 121-143, 2013.
- [63] C. Poussot-Vassal, "Robust LPV multivariable Automotive Global Chassis Control," Institut National Polytechnique de Grenoble-INPG, 2008.
- [64] Y. Furukawa, N. Yuhara, S. Sano, H. Takeda, and Y. Matsushita, "A review of four-wheel steering studies from the viewpoint of vehicle dynamics and control," *Vehicle System Dynamics*, vol. 18, pp. 151-186, 1989.
- [65] Y. Lin, "Improving vehicle handling performance by a closed-loop 4ws driving controller," SAE Technical Paper 0148-7191, 1992.
- [66] K. Bayar and Y. S. Unlusoy, "Steering strategies for multi-axle vehicles," *International Journal of Heavy Vehicle Systems*, vol. 15, pp. 208-236, 2008.
- [67] J. C. Whitehead, "Four wheel steering: Maneuverability and high speed stabilization," SAE Technical Paper 0148-7191, 1988.
- [68] M. Canale and L. Fagiano, "Comparing rear wheel steering and rear active differential approaches to vehicle yaw control," *Vehicle System Dynamics*, vol. 48, pp. 529-546, 2010.
- [69] (2016, 16 June). *LAV III UP*. Available: <http://www.network54.com/Forum/169232/thread/1359659835/LAV+III+UP>
- [70] D. E. Williams, "Generalised multi-axle vehicle handling," *Vehicle System Dynamics*, vol. 50, pp. 149-166, 2012.
- [71] P. Gahinet, A. Nemirovskii, A. J. Laub, and M. Chilali, "The LMI control toolbox," in *IEEE conference on decision and control*, 1994, pp. 2038-2038.
- [72] O. Sename, P. Gaspar, and J. Bokor, *Robust control and linear parameter varying approaches: application to vehicle dynamics* vol. 437: Springer, 2013.
- [73] J.-O. Hahn, R. Rajamani, and L. Alexander, "GPS-based real-time identification of tire-road friction coefficient," *IEEE Transactions on Control Systems Technology*, vol. 10, pp. 331-343, 2002.
- [74] K. Yi, K. Hedrick, and S.-C. Lee, "Estimation of tire-road friction using observer based identifiers," *Vehicle System Dynamics*, vol. 31, pp. 233-261, 1999.
- [75] J. Wang, L. Alexander, and R. Rajamani, "Friction estimation on highway vehicles using longitudinal measurements," *Journal of dynamic systems, measurement, and control*, vol. 126, pp. 265-275, 2004.
- [76] R. Rajamani, G. Phanomchoeng, D. Piyabongkarn, and J. Y. Lew, "Algorithms for real-time estimation of individual wheel tire-road friction coefficients," *IEEE/ASME Transactions on Mechatronics*, vol. 17, pp. 1183-1195, 2012.
- [77] K. B. Singh and S. Taheri, "Estimation of tire-road friction coefficient and its application in chassis control systems," *Systems Science & Control Engineering*, vol. 3, pp. 39-61, 2015.